Electronic Thesis and Dissertation Repository

1-24-2016 12:00 AM

Surface Modification of Electrode Materials for Lithium-Ion Batteries

Biwei Xiao, *The University of Western Ontario*

Supervisor: Prof. Xueliang (Andy) Sun, *The University of Western Ontario*
A thesis submitted in partial fulfillment of the requirements for the Doctor of Philosophy degree in Mechanical and Materials Engineering
© Biwei Xiao 2016

Abstract

The development of lithium-ion batteries (LIBs) has been hampered by the intrinsic limitations of the electrode materials. High-performance LIBs demand electrode materials with fast lithium/electron diffusion rate, stable surface chemistry and high specific capacity. Surface modification by atomic layer deposition (ALD) is an essential method to optimize the performance of the electrode materials. The research in this thesis aims at achieving high-performance LIBs *via* surface modification and understanding the mechanisms *via* synchrotron radiation.

Firstly, by applying ALD $FePO_4$ on $LiNi_{0.5}Mn_{1.5}O_4$ (LNMO), we successfully alleviated the electrolyte decomposition under high voltage by using the electrochemically active $FePO_4$ as a buffer layer. By coating the high energy $Li_{1.2}Mn_{0.54}Co_{0.13}Ni_{0.13}O_2$ (HENMC) with $AlPO_4$, we demonstrated higher thermal resistance compared with the most widely used Al_2O_3 as the coating material.

The irreversible phase change in cathode materials is an intrinsic property that is difficult to be addressed by simple coating, therefore, we extended the practice of ALD to accurately control the surface composition by post annealing TiO_2 coated LNMO. We demonstrated the effectiveness of creating a surface layer of spinel $TiMn_2O_4$-like structure and Ti-doped LNMO sub-surface, which protect the material surface from the electrolyte attack and prevent the intrinsic phase change simultaneously.

To understand how the structure evolves, we used synchrotron radiation to study the behavior of HENMC in the initial cycle and 450th cycle in an in-situ manner. The in-situ X-ray absorption (XAS) has been demonstrated to be an outstanding method to track the change of transition metals while the cell is under operation. We found that the Ni and Co have lost their electrochemical activity after long-term cycling due to the phase segregation.

We also studied the surface behaviors of graphene nanoribbons (GNRs) synthesized from chemically unzipped carbon nanotubes and the correlation with the electrochemical performance used as anode materials. We found that defects, surface area and surface functional groups introduced by the chemical treatment play pivotal roles.

In summary, the discoveries in this thesis provide important methods and unveil critical understandings to achieve high-performance LIBs.

Keywords

Co-Authorship Statement

1.

Title: Unravelling the Role of Electrochemically Active $FePO_4$ Coating by Atomic Layer Deposition for Increased High-voltage Stability of $LiNi_{0.5}Mn_{1.5}O_4$ Cathode Material

Authors: B. Xiao, J. Liu, Q. Sun, B. Wang, M. Banis, D. Zhao, Z. Wang, R. Li, X. Cui, T.-K. Sham and X. Sun

The final version of this manuscript has been published in **Advanced Science**, 2015, 1500022

Biwei Xiao: carried out all of the experiments; finished the draft with following modifications

Jian Liu: carried out the ALD process and helped revise the manuscript

Qian Sun: helped organize the experiment and discuss the results

Biqiong Wang: helped run synchrotron XPS at the PGM beamline of CLS

Dong Zhao: helped run the XAS at the SGM beamline of CLS

Zhiqiang Wang: helped discuss the synchrotron results

Ruying Li: helped organize experiments

Xiaoyu Cui: helped discuss the XPS results

T.-K Sham: helped organize the synchrotron results

Xueliang Sun: supervisor, helped organize the whole story and funding supports.

2.

Title: Highly Stable $Li_{1.2}Mn_{0.54}Co_{0.13}Ni_{0.13}O_2$ Enabled by Novel Atomic Layer Deposited $AlPO_4$ Coating

Authors: B. Xiao, B. Wang, J. Liu, K. Kaliyappan, Q. Sun, M. Banis, G. Dadheech, M. Balogh, M. Cai, T.-K Sham, R. Li and X. Sun

The final version of this manuscript has been submitted for publishing

Biwei Xiao: carried out all of the experiments; finished the draft with following modifications

Biqiong Wang: carried out following ALD process and helped revise the manuscript

Jian Liu: carried out the ALD process and helped revise the manuscript

Karthikeyan Kaliyappan: helped material synthesis and revise the manuscript

Qian Sun: helped organize the experiment and discuss the results

Mohammad N. Banis: helped XRD results collection and revise the manuscript

Gayatri Dadheech: helped organize the experiment and revise the manuscript

Michael Balogh: helped HRTEM training

Mei Cai: helped organize the experiment and revised the manuscript

Ruying Li: helped organize experiments

T.-K Sham: helped organize the synchrotron results

Xueliang Sun: supervisor, helped organize the whole story and funding supports.

3.

Title: Atomic-scale Manipulation of Spinel Lithium Nickel Manganese Surface by Tetrahedrally-coordinated Ti as High Performance Cathode Material

Authors: B. Xiao, H. Liu, J. Liu, Q. Sun, B. Wang, K. Kaliyappan, Y. Liu, C. Langford, R. Li, T.-K Sham, G. Botton, M. Cai and X. Sun

The final version of this manuscript has been submitted for publishing

Biwei Xiao: carried out all of the experiments; finished the draft with following modifications

Hanshuo Liu: carried out HAADF-STEM measurements and related discussions, contributed equally to this manuscript.

Jian Liu: carried out the ALD process and helped revise the manuscript

Qian Sun: helped organize the experiment and discuss the results

Biqiong Wang: helped with ALD process

Karthikeyan Kaliyappan: helped collect samples and discussions

Yulong Liu: helped carry out the XRD measurements

Ruying Li: helped organize experiments

Tsun-Kong Sham: helped organize the synchrotron results

Gianluigi Botton: helped organize the HAADF-STEM results

Mei Cai: helped organize the manuscript

Xueliang Sun: supervisor, helped organize the whole story and funding supports

4.

Title: Insight into the Structure Evolution of Li-rich NMC via In-situ X-ray Absorption Spectroscopy

Authors: B. Xiao, M. Banis, Q. Sun, Y. Liu, M. Cai, T.-K Sham, R. Li and X. Sun

The final version of this manuscript is under preparation

Biwei Xiao: carried out all of the experiments; finished the draft with following modifications

Mohammad N. Banis: helped carry out in-situ XAS measurement and following data analysis

Qian Sun: helped data analysis

Yulong Liu: carried out the XRD measurements

Mei Cai: helped organize the experiments

Tsun-Kong Sham: helped organize the synchrotron results

Ruying Li: helped organize experiments

Xueliang Sun: supervisor, helped organize the whole story and funding supports

5.

Title: Graphene Nanoribbons Derived from the Unzipping of Carbon Nanotubes: Controlled Synthesis and Superior Lithium Storage Performance

Authors: Biwei Xiao, Xifei Li, Xia Li, Biqiong Wang, Craig Langford, Ruying Li and Xueliang Sun

The final version of this manuscript has been published in **Journal of Physical Chemistry C**, 2014, 118. 881-890

Biwei Xiao: carried out all of the experiments; finished the draft with following modifications

Xifei Li: helped organize the experiments and revised the manuscript

Xia Li: helped FTIR and BET measurement

Biqiong Wang: helped RAMAN data collection

Craig Langford: helped revise the manuscript

Ruying Li: helped organize the experiments

Xueliang Sun: supervisor, helped organize the whole story and funding supports

6.

Title: Surface Behaviors and Modifications of Cathode Materials for Lithium-ion Batteries

Authors: Biwei Xiao and Xueliang Sun

The final version of this manuscript is to be submitted for publishing

Biwei Xiao: wrote the whole review

Xueliang Sun: supervisor, helped organize the whole review and funding supports

I hear and I forget. I see and I remember. I do and I understand.

- *Xunzi*

不闻不若闻之，闻之不若见之，见之不若知之，知之不若行之，学至于行之而止

矣。

- *荀子*

Acknowledgements

This Ph.D work was accomplished in Dr. Sun's Nanomaterials and Energy Lab at the University of Western Ontario in London, Canada. I would like to thank everyone that has helped me throughout the past five years.

I would like to express my sincere gratitude to my supervisor Prof. Xueliang (Andy) Sun, a professor at the Department of Mechanical & Materials Engineering of University of Western Ontario, Canada Research Chair, Fellow of the Canadian Academy of Engineering and the Royal Society of Canada. Dr Sun's dedication to the lab, his diligence, brilliance, patience and kindness have greatly inspired me. I'm really grateful to Dr. Sun for allowing to work in General Motors as an intern for two summers. Without Dr. Sun's continuous support and encouragement, I would not have been able to accomplish my Ph.D work.

I would also like to thank Mrs. Ruying (Kathy) Li, she is the wife of Dr. Sun and a research engineer in our lab. I cannot forget her maternal care to me and her patient help to my life and my research, she was always the one I seek comfort when I feel depressed and frustrated. The incentive talks have been a strong support for me in the past five years.

I am also grateful to Dr. Mei Cai, a technical fellow and a lab manager of the General Motors (GM). She provided me with the opportunities to carry out internships in GM during the summers of 2015 and 2016. The experience in GM helped me gain knowledge of the connections between academic to industry, it will benefit my career without any doubt. I also appreciate my GM supervisor Mrs. Gayatri Dadheech and other GM colleagues, Dr. Mahmoud Abdelhamid, Dr. Qiangfeng Xiao, Dr. Xingcheng Xiao, Dr. Li Yang and Mr. Michael Balogh et al. for their help in training and discussing.

Sincerely thanks to Prof. Tsun-Kong Sham, Dr. Yun-Mui Yiu and Dr. Zhiqiang Wang in the Department of Chemistry for their help in my synchrotron radiation-related work. I would also like to acknowledge the beamline scientists of Canadian Light Sources (CLS), Dr. Ning Chen, Dr. Yongfeng Hu, Dr. Qunfeng Xiao, Dr. Xiaoyu Cui et al. for their kind help throughout those sleepless days and nights in CLS. Thanks to Prof. Gianluigi Botton and Miss Hanshuo Liu from McMaster University for their help in HAADF-STEM characterizations and discussions.

the airport. I would not have made it this far without their understanding, supports and encouragements. I love you all!

<div align="right">

Biwei Xiao

CMLP 1325, University of Western Ontario

September 23rd, 2016

</div>

Table of Content

List of Tables

List of Figures

List of Appendices

List of Abbreviations

2D: two-dimensional

3D: three-dimensional

A

AB: Acetylene black

AC: Alternating current

ALD: Atomic layer deposition

B

BET: Brunauer–Emmett–Teller

C

CCEM: Canadian Centre for Electron Microscopy

CE: Coulombic efficiency

CFI: Canada Foundation for Innovation

CLS: Canadian Light Sources

CNTs: Carbon nanotubes

CRC: Canada Research Chair

CV: Cyclic voltammetry

D

DEC: Diethyl carbonate

DEMS: Differential electrochemical mass spectrometry

DFT: Density function theory

DMC: Dimethyl carbonate

DSC: Differential scanning calorimetry

<div align="center">

E

</div>

EDS: Energy dispersive spectroscopy

EELS: Electron energy loss spectroscopy

EIS: Electrochemical impedance spectroscopy

EMC: Ethylmethy carbonate

EXAFS: Extended X-ray absorption fine structure

<div align="center">

F

</div>

FTIR: Fourier-transformed infrared spectroscopy

FLY: Fluorescence yield

FYI: Fluorescence yield

<div align="center">

G

</div>

GM: General Motors

GNRs: Graphene nanoribbons

<div align="center">

H

</div>

HAADF: High-angle annular dark-field imaging

HENMC: High energy lithium nickel manganese cobalt oxide

HOMO: Highest occupied molecular orbital

HXMA: Hard X-ray MicroAnalysis

I

ICE: Initial coulombic efficiency

L

LFP: Lithium iron phosphate

LIB: Lithium ion battery

LMO: Lithium manganese oxide

LNMO: Lithium nickel manganese oxide

LMRNMC: Lithium manganese rich nickel manganese cobalt oxide

LUMO: Lowest unoccupied molecular orbital

M

MCMB: MesoCarbon MicroBeads

MLD: Molecular layer deposition

MWCNTs: Multi-walled carbon nanotubes

N

NCA: Lithium nickel cobalt aluminum oxide

NMC: Lithium nickel manganese cobalt oxide

NMP: N-Methyl-2-pyrrolidone

NSERC: National science & engineering research center

P

PANi: Polyaniline

PC: Propylene carbonate

PE: Polyethylene

PEDOT: Poly(3,4-ethylenedioxythiophene)

PP: Polypropylene

PPy: Polypyrrole

PT: Polythiophene

PVDF: Polyvinylidene fluoride

<div align="center">

S

</div>

SAED: Selected area electron diffraction

SEI: Solid electrolyte interphase

SEM: Scanning electron microscopy

SGM: Spherical grating monochromator

STEM: Scanning transmission electron microscopy

SXRD: Synchrotron X-ray diffraction

SXRMB: Soft X-ray microcharacterization beamline

<div align="center">

T

</div>

TEY: Total electron yield

TEM: Transmission electron microscopy

TGA: Thermogravimetric analysis

TM: Transition metal

TMA: Trimethy aluminum

TMPO: Trimethyl phosphate

TOF-SIMS: Time-of-flight secondary ion mass spectrometry

U

UWO: University of Western Ontario

V

VLSPGM: Variable line spacing plane grating monochromator

X

XANES: X ray absorption near edge spectroscopy

XAS: X ray absorption spectroscopy

XPS: X ray photoelectron spectroscopy

XRD: X ray diffraction

Chapter 1

1 Background Review

1.1 General Introduction

The abusive consumption of fossil fuels releases greenhouse gases like carbon dioxide and methane to the atmosphere and traps heat, causing global warming. With regard to these impacts, the development of sustainable energy is exceptionally imperative. Renewable energies will not have the anticipated impact unless we find an efficient way to store and use the electricity produced by them. Therefore, high-performance energy-storage devices with high energy and power density are highly demanded for electricity-consuming products. Electrochemical batteries have been considered as the most qualified candidate, taking into account the safety, power density, cost, longevity and efficiency, rechargeable lithium-ion batteries (LIBs) are hitherto the most successful technique. The extensive application of LIBs not only resides in the vast portable electronics market, but also expedites the revolution of electrical vehicles. Although LIBs-driven hybrid vehicles are already commercially available in some companies, much more efforts are yet required to devote in order to achieve the energy density, safety and cost as the United States Advanced Battery Consortium Goals for Advanced Batteries for EVs – CY 2020 Commercialization has stated.[1-5]

LIBs have attracted massive attention after being commercialized by SONY in 1991 due to their high energy density, good performance and long cycling life compared to conventional Ni-H, Ni-Cd, and Pb-acid batteries,[6] the drastically growing demand for LIBs during the last two decades have stimulated enormous investigations on the development of high performance electrode materials. A practical LIB usually comprises three functional components, the cathode, anode and electrolyte. Figure 1.1 shows a schematic illustration of the working principle of a Lithium-ion battery, where lithium ions de-intercalate from the cathode materials and migrate through the separator to the anode materials during discharge, electron flows along the external circuit and power up devices, during charge, the process is reversed. Primary prototype of LIBs was the $LiCoO_2/Li$

system, where $LiCoO_2$ was the cathode material and the lithium metal was the anode material. The charge/discharge cycle was achieved on the basis of lithium intercalation and de-intercalation from the $LiCoO_2$ layered structure. The metallic lithium was later replaced by carbonaceous materials in secondary LIBs due to safety issues. In addition to the carbonaceous materials, a myriad of other materials were reported to be eligible as anode materials, such as Sn, Si, $Li_4Ti_5O_{12}$, metal oxides etc.[7] In sharp contrast to the diversity of anode materials, the cathode materials are much less developed, even though the intercalation chemistry has been comprehensively studied over centuries, the categories of cathode materials are rather scarce.[8]
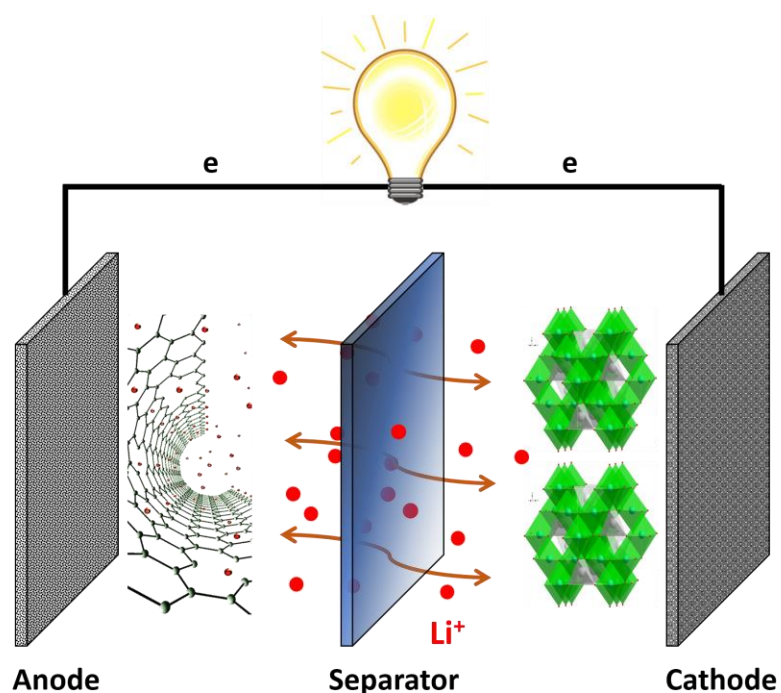
Figure 1.1 Schematic illustration of the working principle of a Lithium ion battery

Primary groups of cathode materials include the layered $LiCoO_2$, spinel $LiMn_2O_4$, poly-anion $LiFePO_4$ and their derivatives. Fig. 1.2a shows the cost components of a representative graphite/NMC333 ($LiNi_{1/3}Mn_{1/3}Co_{1/3}O_2$ – a derivative of $LiCoO_2$) cell in 2013 according to the United States Department of Energy,[9] within the six major parts of a battery, the cathode costs 38%, the most critical reasons are the difficulty of materials manufacturing and the low abundance of cobalt, manganese and nickel that dominate the

current LIBs market. Hence, the relatively slow development of cathode materials is the major barrier for future low-cost LIBs. Six main types of cathode materials are illustrated in Figure 1.2b based on the specific discharge capacity vs voltage. Energy density of a specific type of cathode material is calculated on voltage multiplying capacity, therefore, in order to achieve high energy density, researchers are looking for cathode materials that offer either high voltage or high discharge capacity. The chart shows two cathode materials that are of great potential. The spinel LNMO with a working capacity of around 120 mAhg^{-1} and a voltage of 5 V and the Li-rich NMC with a working capacity of around 250 mAhg^{-1} and a voltage of 4 V. Figure 1.2c-e show the crystal structures of typical cathode materials: olivine LiFePO$_4$, spinel LiMn$_2$O$_4$ and layered LiCoO$_2$.
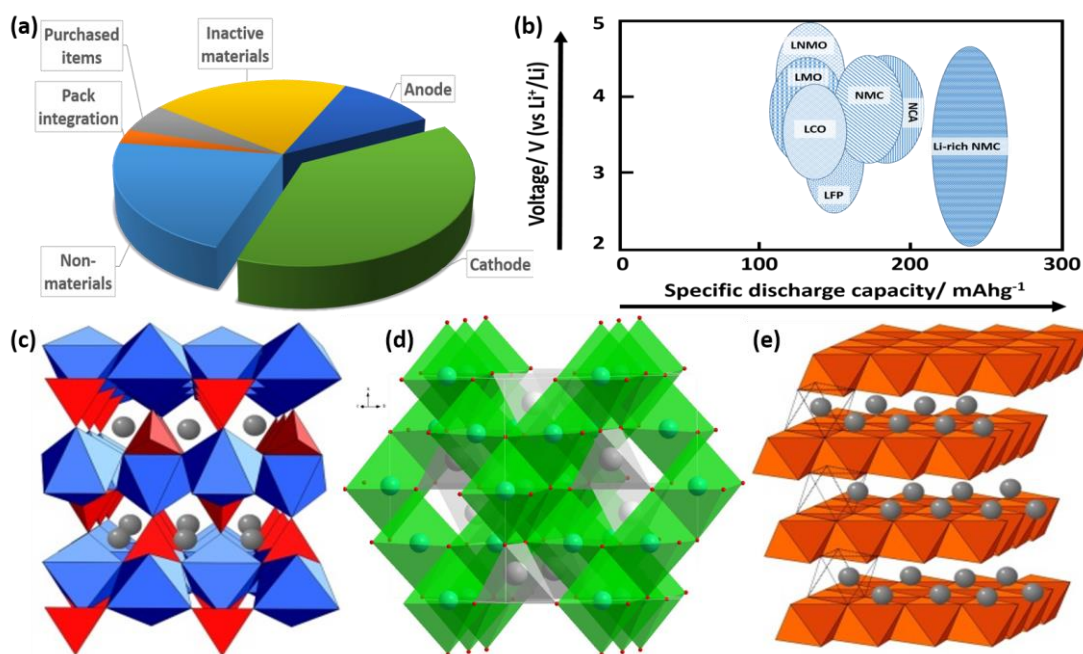
Figure 1.2 (a) The cost components of a representative graphite/NMC333 battery in 2013; (b) voltage vs capacity chart of main cathode materials (LNMO: LiNi$_{0.5}$Mn$_{1.5}$O$_4$, LMO: LiMn$_2$O$_4$, LFO: LiFePO$_4$, NMC: LiNi$_{1/3}$Co$_{1/3}$Mn$_{1/3}$O$_2$ up to 4.3 V, NCA: LiNi$_{0.8}$Co$_{0.15}$Al$_{0.05}$O$_2$) (c) crystal structure of LiFePO$_4$ (d) crystal structure of LiMn$_2$O$_4$ and (e) crystal structure of LiCoO$_2$

In order to maximize the efficiency of a cathode material, researches have been dedicated to the exploration of advanced materials, the development of various synthetic methods

and the modification of existing materials.[10-14] While all of these directions have been under rigorous investigation, the topic will always end up with a critical concern – the materials surface. The surface is where lithium ions or electrons diffusion ends in the material and transfer into the electrolyte or conductive agents, thus the majority of the side reactions happen here due to non-equilibrium diffusion.[15, 16] Attempts of surface modification aimed at adjusting the surface chemical or physical properties have been made within the past decades, but the underlying mechanisms have not yet been fully unraveled. In this chapter, we present a comprehensive review of surface modification methods on cathode materials by starting with an understanding of the fundamental origins of the surface behaviors, followed by possible explanations to how surface modification work and a prospect of advanced surface modification methods.

1.2 Surface Behaviors of Cathode Materials

1.2.1 Surface Phase Reconstruction

1.2.1.1 Layered $LiMeO_2$ (Me = Co, Mn, Ni)

Owing to the considerable voltage and capacity and easy scalability, $LiCoO_2$ has been registered as the most successful cathode material so far. Layered $LiCoO_2$ belongs to a rhombohedral space group $R\bar{3}m$ with edge-sharing CoO_6 octahedra, which gives CoO_2 sheets.[17] Lithium ions reside in between the CoO_2 sheets so that the electrochemical deintercalation forms Li_xCoO_2.[18] Despite the theoretical capacity of $LiCoO_2$ is calculated to be 272 $mAhg^{-1}$, in practical, $LiCoO_2$ can only be deintercalated to $Li_{0.5}CoO_2$ within a cut-off voltage of 4.5 V, hence only half of the theoretical capacity can be reversible.[18] The reason is that $LiCoO_2$ undergoes phase transition from layered to quasi-spinel (QS) structure when half of the lithium is deintercalated. It is suggested that the transition is due to the migration of Co ions into Li planes because of the higher thermal diffusivity.[19] Dahn et al. initially reported the synthesis of QS-$LiCoO_2$ (or in some cases written as $Li_{1+y}Co_2O_4$) in space group $Fd\bar{3}m$ at low temperature (400 ^oC), the thermodynamic stability of which is lower than that of layered $LiCoO_2$.[20] Various approaches to synthesizing $LiCoO_2$ with both layered and quasi-spinel configurations were reviewed by Antonelli.[21] In-depth study of the two phases revealed that the QS-$LiCoO_2$

shows much lower capacity and higher polarization than layered $LiCoO_2$, thus turning out to be an inferior candidate for battery materials.[20] X-ray absorption near-edge spectra (XANES) confirmed that there are intermediate phases between the layered and spinel structures due to the higher oxidation state of spinel $LiCoO_2$,[22] it was thereafter found to be $Li_xCo_{1-x}[Co_2]O_4$ by Thackeray et al.[23]

The formation of spinel phase in layered $LiCoO_2$ was found to initiate from the surface and extends to the bulk upon intensive cycling, extended voltage window and operation under high temperature. Transmission electron microscopy (TEM) studies revealed that there are dislocations and internal strains within the lattice of $LiCoO_2$ even at low cycle numbers, the accumulation of these defects is directly responsible for long term capacity fade.[24, 25] The presence of strains indicates that the interlayer spacing within $LiCoO_2$ lattice has been changed, which is in accordance with the in-situ X-ray diffraction (XRD) study carried out by Dahn et al.[19] A recent study found that post-thermal treatment of $LiCoO_2$ forms a thin spinel $Li_xCo_2O_4$ film on the surface and improves the performance significantly since the spinel phase is strongly conductive.[26] This report is however contradictive to previous studies, probably due to the different formation mechanisms of this phase.

The layered to spinel phase change has also been observed in other species of metal oxide cathodes such as $LiNiO_2$ and $LiMnO_2$, which are iso-structures of layered $LiCoO_2$ as shown in Figure 1.3a.[27-29] Each of these ending members of $LiMeO_2$ (Me = Ni, Co, Mn) possesses its unique advantages as a cathode material. Nevertheless, other than the structural transition, these materials suffer from severe Jahn-Teller distortion, which is another chief factor of the capacity decay.[30, 31] In the case of $LiNiO_2$, the low spin Ni^{3+} ion has a $t_{2g}^6 e_g^1$ electronic configuration, the Jahn-Teller distortion can be induced by the e_g energy level, resulting in the structural destruction due to internal stress.[31] Earliest observation of the Jahn-Teller distortion of $LiNiO_2$ was reported by Delmas et al. in 1995.[30] Two Ni-O bond lengths with 1.91Å and 2.09 Å were found to exist in $LiNiO_2$ by employing extended x-ray absorption fine structure (EXAFS). Unlike Ni^{3+}, the electronic configuration of Co^{3+} can be expressed as t_{2g}^6, with one less valence electron, therefore, the Jahn-Teller distortion in $LiCoO_2$ is not as profound as $LiNiO_2$.[31] In regard

of this, plenty of efforts have been dedicated to the investigation of dopants induced suppression, such as Al, Co, Mn, Cr etc.[32, 33] The fundamental principle is to lower the concentration of the Jahn-Teller effective ions, for instance, doping $LiNiO_2$ with Co to form $LiCo_{0.5}Ni_{0.5}O_2$ has been suggested to change the Ni electronic configuration from $t_{2g}^6 e_g^1$ to $t_{2g}^6 e_g^2$, which is Jahn-Teller inactive.[34, 35]

The attempts of doping fundamental layered metal oxides introduce numerous derivatives, which are of remarkable value now. Among them, $LiNi_xMn_yCo_{1-x-y}O_2$ (NMC) and $LiNi_{0.8}Co_{0.15}Al_{0.05}O_2$ (NCA) have found applications in current electrical vehicles. The high operational voltage and specific capacity have made these materials outperform many other cathode materials.[36-40]
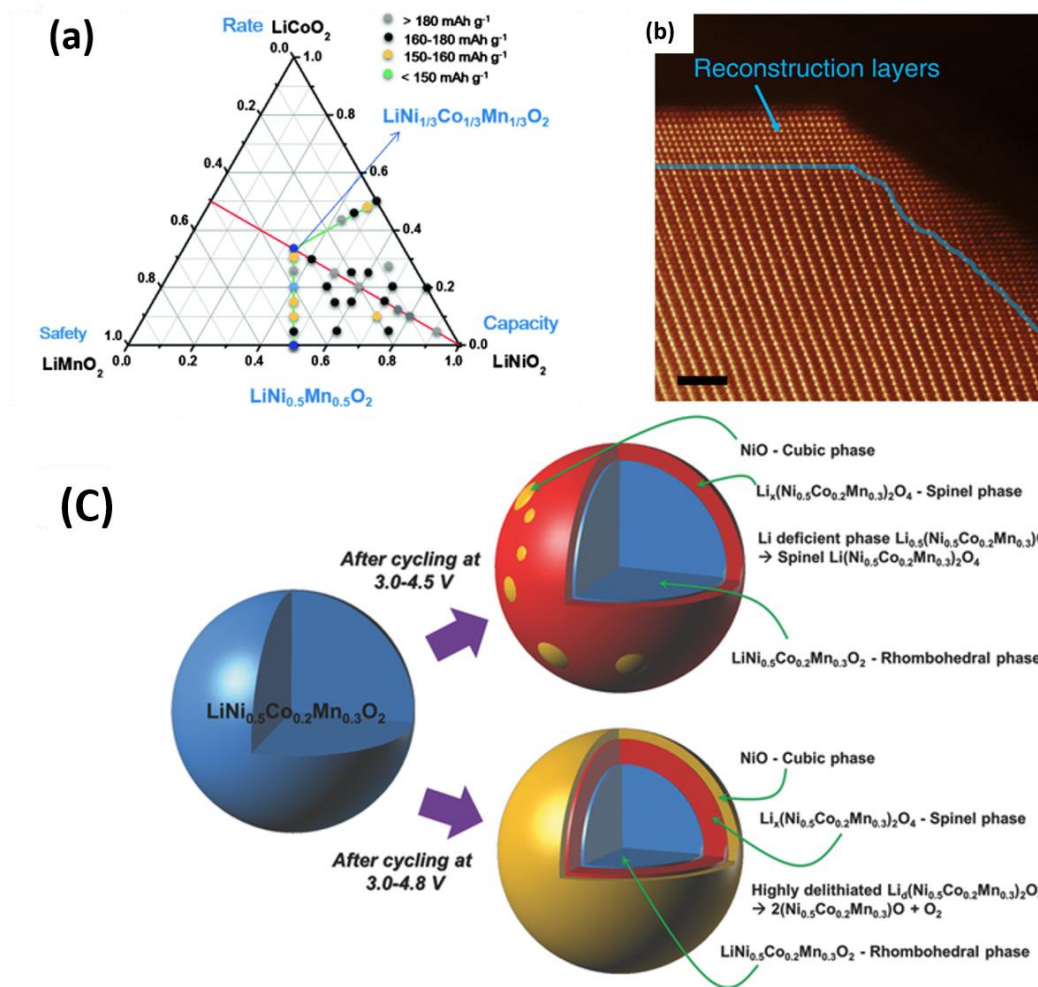
Figure 1.3 (a) Compositional phase diagram of LiMnO₂-LiNiO₂-LiCoO₂ (Reproduced from ref. [41] with permission, copyright 2015 Wiley-VCH); (b) reconstructed surface layer after 1st cycle within 2.0-4.7 V (Reproduced from ref. [37] with permission, copyright 2014 Nature Publishers); (c) Degradation mechanism of Ni-rich LiNi₀.₅Co₀.₂Mn₀.₃O₂ (Reproduced from ref. [42] with permission, copyright 2014 Wiley-VCH)

Within the category of NMC layered cathode materials, $LiNi_{1/3}Mn_{1/3}Co_{1/3}O_2$ with a ratio of 1:1:1 (NMC111) has been most studied since it combines the rate performance of $LiCoO_2$, safety of $LiMnO_2$ and capacity of $LiNiO_2$ as has been illustrated in Figure 1.3a, the surface reconstruction upon aggressive exposure to electrolyte has, however, also been reported in these materials, as shown in Figure 1.3b.[37] In an attempt to achieve high energy density cathode materials for EVs, Ni-rich NMC with high capacity has become a

focus in recent years. The rich Ni content in the material, however, involves safety issues and preparation difficulty.[42] Due to the close ionic radii and charge with Li^+, Ni^{2+} in Ni-rich NMC materials has been found to show very high degree of interlayer mixing with the Li^+, which results in strong phase segregation and capacity fade.[43] Figure 1.3c shows a schematic illustration of the degradation mechanism of a $LiNi_{0.5}Co_{0.2}Mn_{0.3}O_2$ (NMC523) material. In this study, different degradation mechanism from NMC111 was proposed, specifically, O3 to O1 phase transformation was supposed to be the major reason of capacity fade in NMC111 due to the formation of stacking fault. However, no such phase transformation was observed in NMC523, probably due to the higher Ni-Li site exchange since the Ni percentage in NMC523 is much higher. These studies have unambiguously pointed out that the stabilization of Ni in Ni-rich NMC cathodes is the key to stabilized performance. A possible strategy is to design a Ni rich bulk and Mn rich surface NMC material, this gradient concentration has proven to be effective in controlling the surface Ni disorder.[44-46]

1.2.1.2   Layered Lithium-rich Oxides Layered $LiMeO_2$ (Me = Co, Mn, Ni)

Lithium-rich layered oxides are controversially recognized as either the solid solutions or nano-domains of Li_2MnO_3 (monoclinic, C2/m) and $LiMeO_2$ (Me = transition metals) (rhombohedral, $R\overline{3}m$).[47] The crystalline structure of a typical Li-rich layered NMC material is shown in Figure 1.4a(i), lithium ions occupy part of the transition metals and result in off-stoichiometric lithium content compared with conventional NMC based materials.[48, 49] It has drawn much attention because of the high capacity (above 250 $mAhg^{-1}$) and high voltage. Dissimilar with other layered materials, this material shows an anomalous voltage plateau at ~4.5 V during the first charge, where all of the transition metals should have reached their final oxidation state. Early researches speculated that the mysterious charge plateau was originated from the removal of lithium and oxygen, but direct observation was not reported until 2006.[50] By using in situ differential electrochemical mass spectrometry (DEMS), P. Bruce et al. found that there was O_2 release when the material was initially charged to above 4.2 V. The lithiation/de-lithiation process of Li-rich NMC under different cutoff voltages is illustrated in Figure 1.4a. When the cell

is charged to a cutoff voltage of 4.2 V, the whole process resembles a conventional NMC that the lithium ions from the lithium ion layer are removed. However, at a voltage above 4.2 V, the lithium ions that reside in the octahedrally coordinated transition metal layer get extracted, associated with the loss of O^{2-}, which is subsequently oxidized to O_2 and is responsible for the "anomalous plateau". The oxygen vacancies de-stabilize the transition metals, in particular Ni ions, resulting in the diffusion of transition metals into the lithium ion layers and form a spinel phase that blocks lithium ions transportation.[51] Once the O_2 gas is released, a series of side reactions take place. Yabuuchi et al. combined synchrotron X-ray diffraction (SXRD), X-ray absorption spectroscopy (XAS), X-ray photoelectron spectroscopy (XPS) and time-of-flight secondary ion mass spectroscopy (TOF-SIMS) to investigate the surface behaviours of Li_2MnO_3-$LiCo_{1/3}Ni_{1/3}Mn_{1/3}O_2$. The released O_2 may undergo oxygen reduction reaction at the material surface and form Li_2CO_3 which is responsible for the disappearance of the reversible capacity of the surface redox reactions during the first several cycles.[52] On the other hand, O_2 gas facilitates the decomposition of electrolyte under high voltage and results in undesirable solid electrolyte interphase (SEI) growth, low initial coulombic efficiency and impedance buildup. In addition, O_2 release potentially increases the risk of battery thermal runaway and leads to safety concern.[53, 54]

Aside from the oxygen formation, severe voltage decay has also been observed in this type of cathode materials as has been shown in Figure 1.4b. The voltage decay leads to the drop of cell energy density,[55] it is supposed to be the major factor that should be addressed in order to commercialize lithium rich NMC. Gu et al. examined the phase distribution of $Li_{1.2}Ni_{0.2}Mn_{0.6}O_2$ and found that Ni was highly inhomogeneous, as shown in Figure 1.4c, whereas the Mn was rather uniform. This observation proves that phase segregation exists in cycled Li-rich layered materials, which is possibly the reason of low capacity and poor rate capability.[56-58] The sluggish lithium diffusion across the surface caused by the phase segregation is directly responsible for the voltage decay, therefore strategies aimed at suppressing voltage fade are mostly focused on surface phase change suppression. In addition, corrosion induced pits are often found in heavily cycled particles and the formation of these pits evidently happens on specific crystallographic facets. The surface topographical change can be a reason of capacity fade in lithium rich materials. Extra

diffraction spots are always observed in extensively cycled particles, as can be seen from Figure 1.4d, which is also an evidence of cation migration.
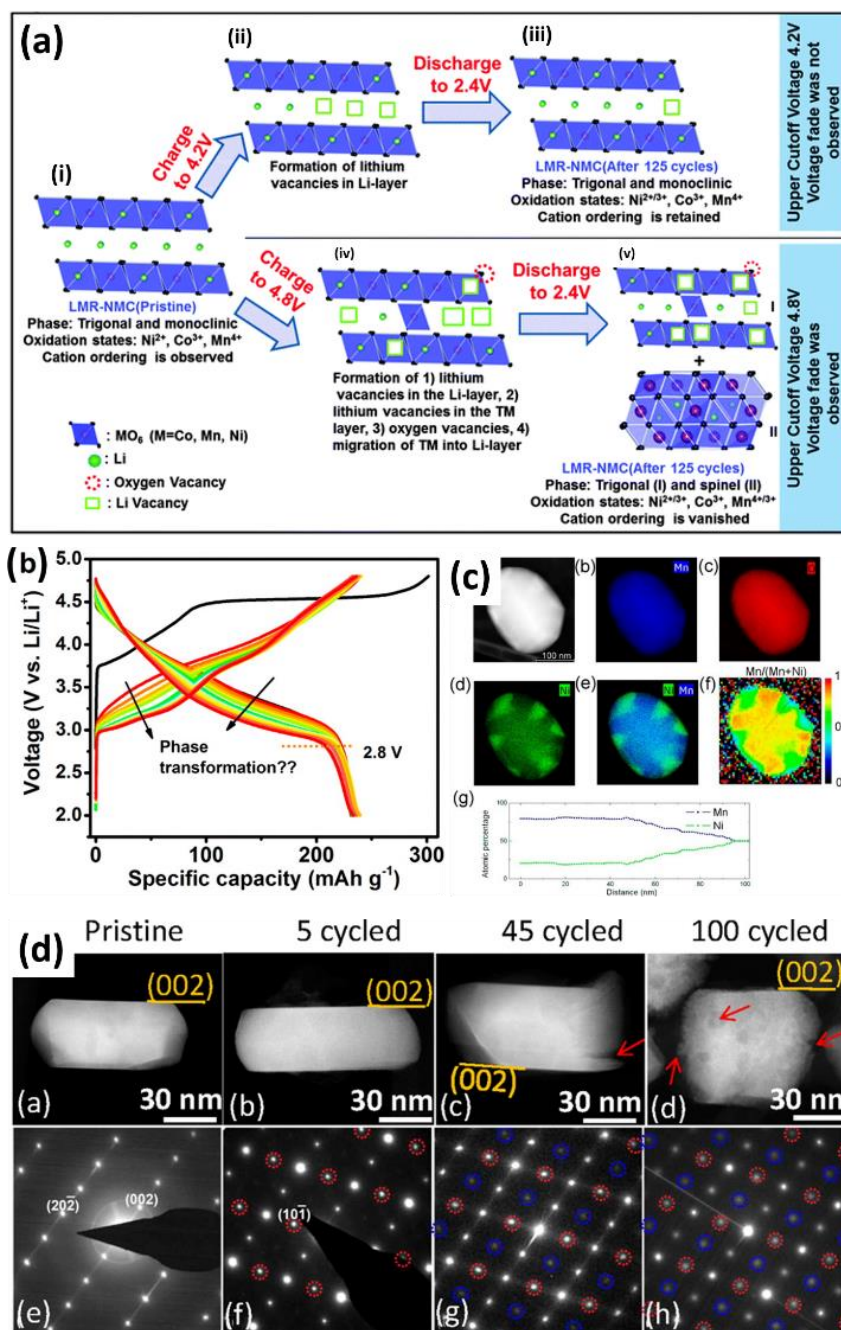
Figure 1.4 (a) Proposed phase changes in a lithium rich NMC under different cutting-off voltages; (Reproduced from ref. [51] with permission, copyright 2013 Royal Society of Chemistry); (b) Typical charge/discharge curves of lithium rich NMC showing voltage decay; (Reproduce from ref.[59] with permission, copyright 2015

American Chemical Society) (c) HAADF Z-contrast image and XEDS maps showing non-uniform distribution of elements in a cycled lithium-rich NMC particle. (Reproduced from ref. [56] with permission, copyright 2013 American Chemical Society) (d) Low magnification STEM-HAADF images and corresponding [010] zone axis SAED patterns of the lithium rich cathodes after different cycles (Reproduced from ref. [60] with permission, copyright 2015 American Chemical Society)

1.2.1.3 Spinel $LiMn_2O_4$

The spinel type $LiMn_2O_4$ belongs to space group symmetry of $Fd\overline{3}m$, in which Mn shows an average valence of 3.5, indicating the coexistence of Mn^{3+} and Mn^{4+}.[61] However, the equilibrium can be easily broken by Li^+ insertion or temperature change, causing the Jahn-Teller distortion of Mn^{3+} at the octahedral sites. The onset of Jahn-Teller distortion at 4.0 V has been regarded as the principal origin of capacity loss.[62, 63] Study on the surface structure of $LiMn_2O_4$ revealed that the net valence differs from the bulk, with more Mn^{3+} in presence due to the non-equipoised dynamics of Li^+ insertion (C-rate controlled) and extraction (diffusion-controlled) at the surface.[64, 65] This was suggested to result in the formation of $Li_2Mn_2O_4$, which is much less electrochemically reactive.[66] Nonetheless, the phase transition from cubic to tetragonal induced by the Mn^{3+} Jahn-Teller distortion was speculated to generate phase boundary at the particle surfaces and thwart the diffusion of Li^+. Similar with the strategies of doping alien elements in layered $LiMeO_2$, the doping of $LiMn_2O_4$ has also been a vastly studied topic aimed at suppressing the Jahn-Teller distortion.[61, 65] Of the various doping elements, introducing Ni to form $P4_332$ $LiNi_{0.5}Mn_{1.5}O_4$ is the most successful one, due to the electrochemical reactivity of Ni^{2+} and the disappearance of Mn^{3+}.[67] Furthermore, the incorporation of Ni^{2+} provides two voltage plateaus at about 4.7 V (Ni^{2+}/Ni^{3+}, Ni^{3+}/Ni^{4+}), making it a very promising high power cathode material. Even though trace Mn^{3+} was reported in oxygen-deficient $LiNi_{0.5}Mn_{1.5}O_{4-\delta}$ with space group $Fd\overline{3}m$, the Jahn-Teller distortion is much more suppressed.[68-70]

1.2.2   Stress-induced Cracking

Mechanical cracking is most reported in anode materials that suffer from tremendous volume expansion upon lithiation, such as Si and Sn. The cathode materials, however, are also found to develop cracks upon high rate cycling when the lithium ions do not have sufficient time to diffuse homogeneously, ending up with extra stress in particles.[71, 72] On a brittle cathode material, the C-rate that initiates cracks decreases with increasing particle size.[73, 74] The internal stress of electrode materials during preparation and phase change (such as Jahn-Teller distortion, O_2 release) induced stress can also help develop cracks at the materials bulk and keep propagating.[75] In addition, if the volume expansion of cathode materials is non-elastic deformation, it will lose contact with binders and conductive carbon, forming gaps in between. The occurrence of cracks segregates part of the materials from the electrolyte and leads to the increase of impedance and subsequent battery failure. An in-situ SEM study on $LiNi_{0.8}Co_{0.15}Al_{0.05}O_2$ shows direct visual evidence of the cracks development and separation of active materials from electrolyte, as shown in Figure 1.5a-d. Surprisingly, such cracks development started even from the first cycle, indicating that the prevention of cracking in cathode materials is very necessary. A schematic diagram showing the segregation consequence of the cracking towards lithium diffusion is presented in Figure 1.5e. Zhang et al. investigated the crack formation on lithium rich layered $Li[Li_{0.2}Ni_{0.2}Mn_{0.6}]O_2$.[76] Micro-cracks were found in deeply cycled particles due to the large strain caused by simultaneous removal of lithium and oxygen, ending up with pulverized surface structures. The surface Mn ions were found to have been reduced as revealed by electron energy loss spectroscopy (EELS), indicating the break of surface structural consistency.
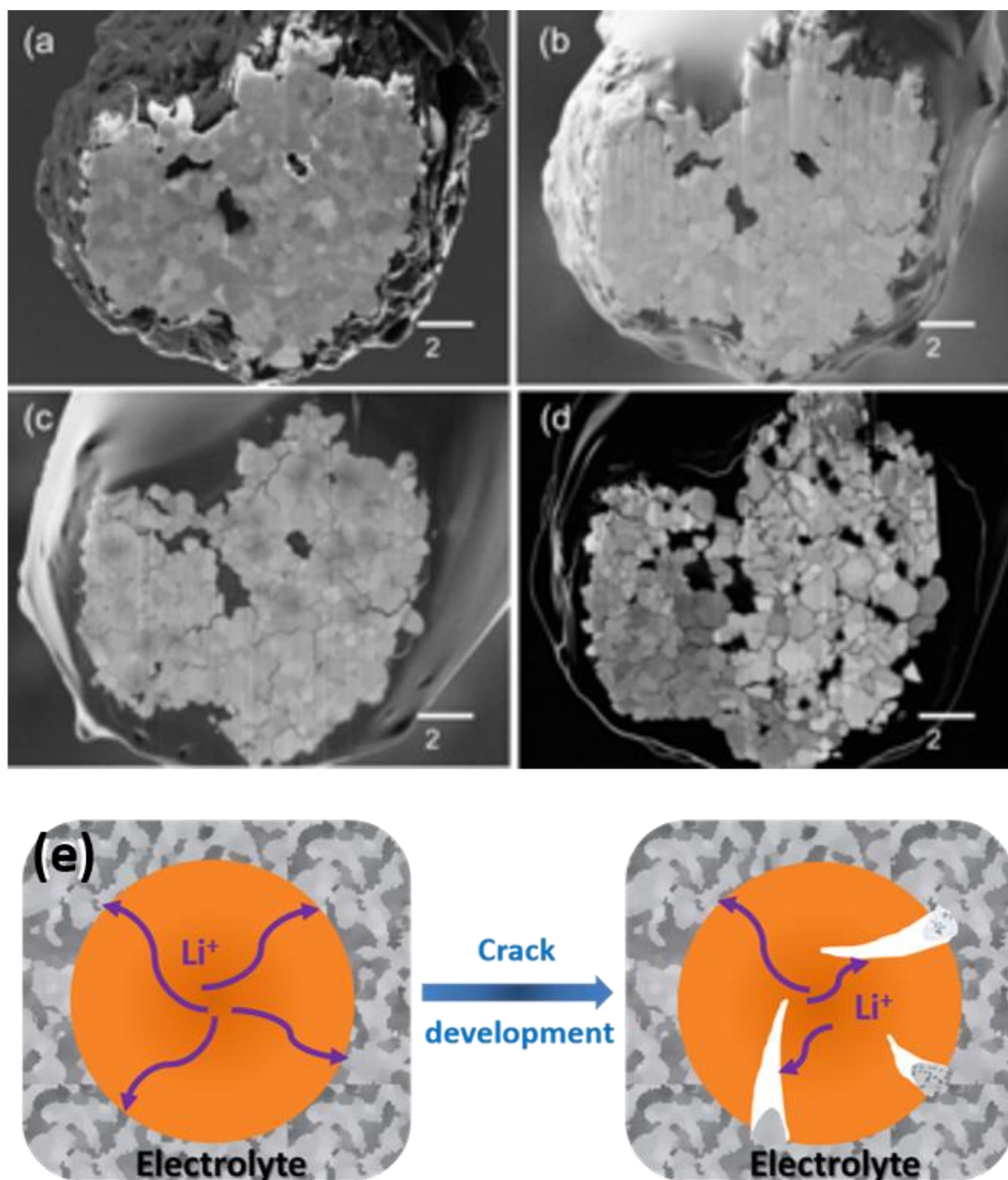
Figure 1.5 SEM images of LiNi$_{0.8}$Co$_{0.15}$Al$_{0.05}$O$_2$ particle cracking after (a) 1; (b) 2; (c) 3; (d) 4 electrochemical cycles; (Reproduced from ref. [77] with permission, copyright WILEY-VCH 2013) (e) Schematic illustration of the segregation consequences of cracks towards the lithium ions diffusion

1.2.3　　Electrolyte Decomposition and Transition Metal Dissolution

1.2.3.1　　Electrolyte Decomposition

Electrolytes for LIBs are generally liquid or solid with electrical conductivity below 10^{-10} S/cm and lithium ion conductivity above 10^{-4} S/cm.[78] Organic carbonate esters based blends, including ethylene carbonate (EC), diethylene carbonate (DEC), propylene carbonate (PC), dimethylene carbonate (DMC) and ethylmethyl carbonate (EMC) are widely used as electrolyte solvents,[79] $LiPF_6$ is the common salt currently.[80] The operation voltage windows of these solvents are typically from 1.0 V to 4.7 V vs. Li/Li^+,[81, 82] therefore any cathode materials that require a voltage cutoff value above 4.7 V (in practical 4.5 V due to the catalytic effect of cathode materials) inevitably involve the oxidation decomposition of electrolyte. The consequence of the electrolyte decomposition is the formation of a passivation SEI layer, comprising inorganic salts such as Li_2CO_3, LiF, and organic species like poly(ethylene carbonate).[83-85] Due to the oxidation nature of the metal oxide cathode materials, the decomposition of electrolyte may be accompanied with gas evolution such as CO_2.[86-88] The SEI layer is normally electrically insulating yet lithium conductive.[89, 90] Much efforts have been dedicated to expanding the electrolyte redox window, such as the fluorination of solvents in order to lower the highest occupied molecular orbital (HOMO) and lowest occupied molecular orbital (LUMO) of organic carbonate esters.[91] The SEI formation causes irreversible capacity loss at the first several cycles, in this sense, it is unfavorable to the battery performance.

The intricacy of SEI growth is far from being resolved thus far.[84] Despite the capacity consumption during the electrolyte decomposition, the oxidation of electrolyte on the surface of cathode materials requires continuous electron transfer,[78, 92] the electrically insulating layer can keep the electrolyte from being further oxidized, an SEI layer with certain thickness and considerable stability is therefore desired.[79, 93] In order to mitigate the electrolyte decomposition, the introduction of sacrificial electrolyte additives has been extensively reported.[94] As the electrolyte decomposition mechanisms on anode and cathode are reduction and oxidation reactions respectively, the additive selection is distinct. In most cases, the additives act as facilitator of the decomposition and stabilize the SEI.

Lithium bos(oxalato) borate (LiBOB), glutaric anhydride, 2,5-dihydrofuran, γ-butyrolactone, 2-(Pentafluorophenyl)-tetrafluoro-1,3,2-benzodioxaborole, 1,1-Difluoro-1-alkenes, vinyl ethylene carbonate, tris_hexafluoro-iso-propyl_phosphate et al. have been reported as suitable additives for cathode materials.[95-102] The inspirational role of SEI has motivated researchers to develop the surface coating technique, i.e., instead of generating an SEI layer, an artificial layer is intentionally deposited onto electrode particles.[103]

1.2.3.2   Transition Metal Dissolution

Nonetheless, the decomposition issue is not the only problem that pertains to the electrolyte. Practically, there are traces of moisture in the electrolyte or on the surface of cathode materials. The $LiPF_6$ salt may undergo the reaction: $LiPF_6 \rightleftharpoons LiF + PF_5$, followed by the hydrolysis of PF_5: $PF_5 + H_2O \rightarrow POF_3 + 2HF$ according to Aurbach and Heider's theory.[88, 104] The HF from the hydrolysis of PF_5, along with the inherent HF in the $LiPF_6$ salt, triggers obscure side reactions on the cathode materials.[79, 105, 106] Taking spinel $LiMn_2O_4$ as an example, it was found that cathode materials containing more Mn^{3+} tend to suffer from higher manganese dissolution into the electrolyte.[107, 108] The Mn^{3+} tends to undergo a disproportional reaction: $2Mn^{3+} \rightarrow Mn^{2+} + Mn^{4+}$, where the Mn^{4+} remains on the material surface and Mn^{2+} dissolves into the electrolyte. Aoshima and colleagues studied the mechanism of capacity fading in manganese spinels and concluded that the dissolved Mn^{2+} tend to form a layer of MnF_2 and ramsdellite-$Li_{0.5}MnO_2$ on the surface of cathode, and another layer of metal Mn on the anode, the synergetic deterioration of both cathode and anode is responsible for the capacity fading.[66, 109-111] A more recent study by Kanno and coworkers found that the dissolution of Mn also differs according to the crystal planes exposed to the electrolyte, the (110) plane was found to be less stable than the (111) plane.[106] The dissolution of Mn is, however, more intense in cathode materials that work under higher voltage such as $LiNi_{0.5}Mn_{1.5}O_4$ and high operation temperatures.[112] The side effect of the Mn dissolution, aside from the loss of active materials, also involves the degradation of the anode part. An "ion-exchange model" was proposed to explain the reaction of Mn on the anode surface as shown in Figure 1.6.[111] In detail, the Mn is supposed to react with the SEI and changes its composition,

by exchanging with the Li^+ in the SEI, it becomes Mn-rich and the lithium diffusion channels are often blocked by the Mn and thus results in impedance growth.
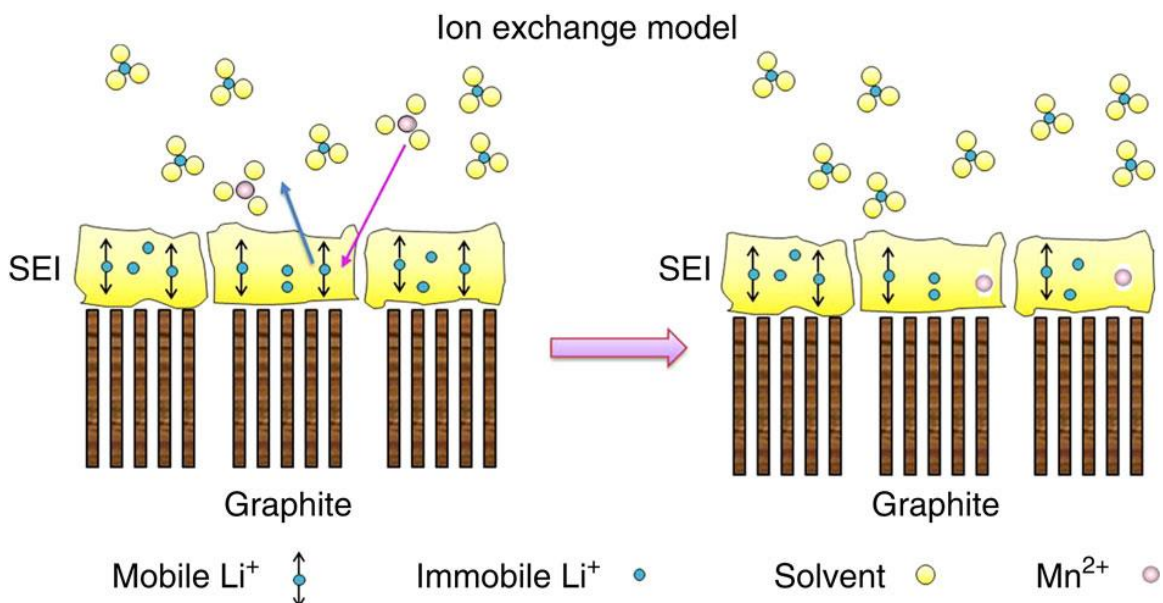
Figure 1.6 Schematic illustration of the Mn-Li exchange model mechanism for the deposition of Mn on graphite in a graphite/LiMn₂O₄ cell (Reproduced from reference [111] with permission, Copyright 2013 Nature Publishers)

1.2.4   Electrical/Li-Ion Conductivity

The kinetics of lithium and electrical diffusion in cathode materials are critical factors during the electrochemical process. The conduction phenomena of Li-ion batteries has been comprehensively reviewed by Fisher et al.[16] and Park et al.[113] The lithium ions diffusion paths in typical layered, spinel and olivine structures and their activation energies are illustrated in Figure 1.7 adopted from Meng's review, details are summarized in Table 1.1.[114] Depending on the diffusion paths and activation energy, various cathode materials manifest different lithium diffusion coefficient.
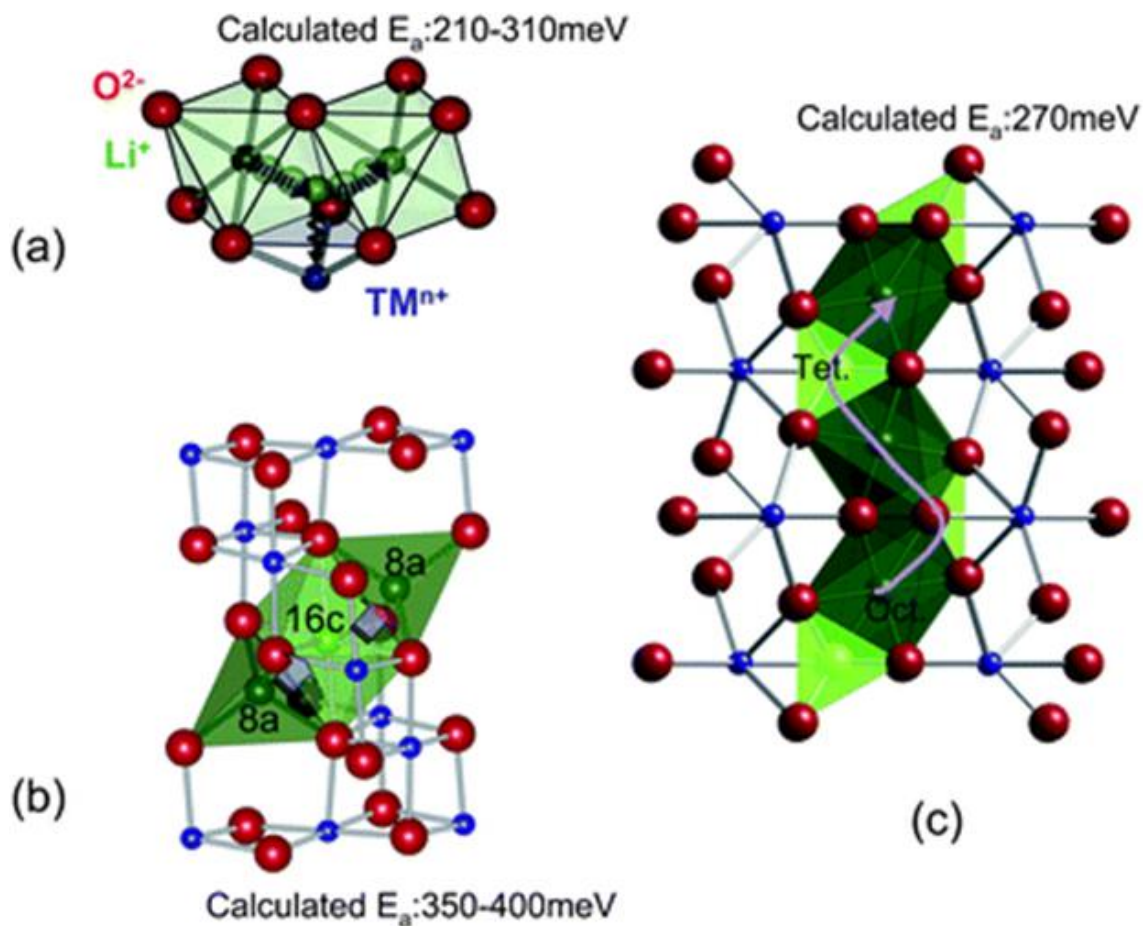
Figure 1.7 Lithium diffusion paths and activation energies calculated via density function theory (DFT) of (a) layered, (b) spinel and (c) olivine structures (Reproduced from ref. [114] with permission, copyright 2009 Royal Society of Chemistry)

Table 1.1 Lithium ions diffusion in various categories of typical cathode materials

Material	Structure	Diffusion path	Activation barrier	Dimensions
$LiMeO_2$	Layered	Oct.→Oct.	210-310 meV	2D
$LiMn_2O_4$	Spinel	Tet.→Oct.→ Tet.	350-400 meV	3D
$LiFePO_4$	Olivine	Oct.→Tet.→Oct.	More than 1 eV	1D

1.3   Roles of Surface Modifications

1.3.1   Surface Modification as Phase Transition Blocker

1.3.1.1   Surface Doping Design

Bulk doping on cathode materials has been studied over decades, the aim of this process is to control the phase change or enhance the diffusion rate within a particle. However, bulk doping elements, usually Ti, Al and so on, are normally electrochemically inactive, restricting the doping to the material surface has therefore become a prevalent topic since minimum capacity sacrifice is expected in this scenario. Cho had conducted tremendous work on the surface protection of $LiCoO_2$ and in most of the cases, the metal ions in the coating oxide materials, such as Al, Zr and Sn were speculated to have migrated into the near surface lattice of the cathode materials, forming a solid solution.[115-118] His early work in 2000 showed that when the surface of $LiCoO_2$ was slightly doped with Al, the c axis would have 1.7% shift during the first cycle whereas the ones with solid solution on the surface showed only 0.14%, which was also observed in their later report on Zr doped surface. This opinion was however opposed by Dahn et al. when they conducted a ZrO_2 coating study on $LiCoO_2$ with careful examination on the structural change, no difference was observed on the coated and bare samples.[119, 120] Therefore, closer investigation on the mechanism through which surface doping works to suppress the phase reconstruction is needed. Recently, Park et al. reported another possible explanation.[121] MgO was deposited onto the surface of $LiCoO_2$ followed by heat treatment under different temperatures. Before electrochemical cycling, the structure remained exactly the same on both the near surface and bulk. However, when the material was cycled, extra diffractions can be observed on the non-coated areas and the bulk, these weak reflections were supposed to be lithium and vacancy ordering, which were not observed in the coated region. Therefore, they concluded that the incorporation of Mg into the $LiCoO_2$ actually occupied the Li sites instead of Co sites and this is the reason why it did not undergo any phase transition. Similar with this study, Cho also reported another possible design of surface solid solution recently, they used Ni^{2+} ions to reside in the Li slabs on the near surface of $LiNi_{0.62}Co_{0.14}Mn_{0.24}O_2$ with a thickness of about 10 nm. This material showed exceptional structural stability especially at elevated temperature.[122] A more recent

study of Cabana and coworkers has adopted Al_2O_3 to modify the surface of $LiMn_2O_4$ nanoparticles and found that an expitaxially grown Mn^{3+}-depleted phase was formed on the surface as shown in Figure 1.8a. The replacement of Mn^{3+} by non-soluble Al^{3+} on the surface has reduced the risk of surface destruction and resulted in significant performance enhancement. Similar study has also been reported by Amine and co-workers.[123]
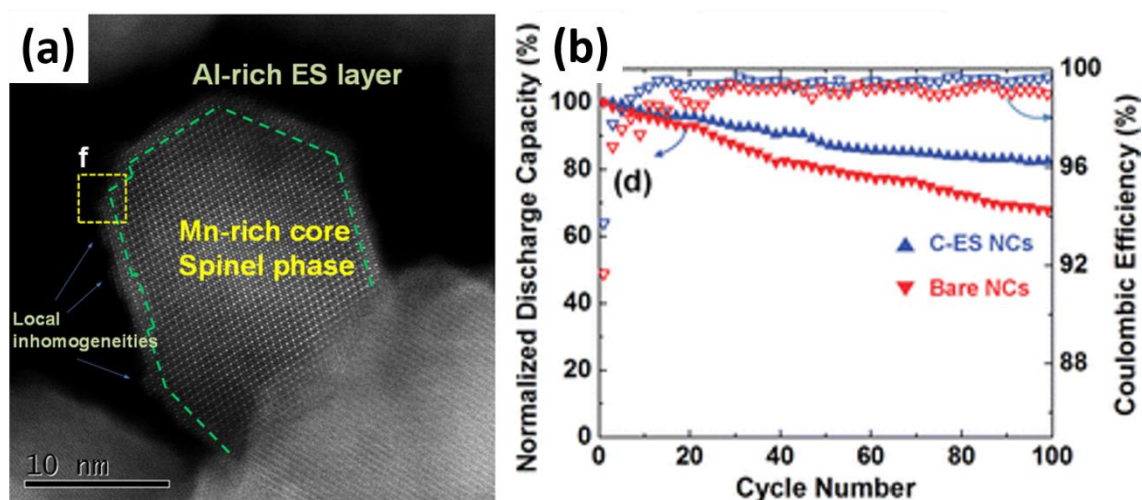
Figure 1.8 (a) High-resolution HAADF image indicating an Al-rich surface on the $LiMn_2O_4$ nanoparticle; (b) Stability test of the bare $LiMn_2O_4$ and Al-modified $LiMn_2O_4$ under 55 ℃. (Reproduced from ref. [124] with permission, copyright 2014 American Chemical Society)

When it comes to the issue of Jahn-Teller distortion caused phase transitions, surface doping design often shows very apparent improvement. Taking $LiMn_2O_4$ as an example, as has been discussed above, the Jahn-Teller distortion is most intense at the material surface where the charge equilibrium is always broken by the lithium diffusion. With respect to this, many researchers believe that modifying only the surface of $LiMn_2O_4$ to replace part of the Jahn-Teller active ions can help avoid performance fade at lowest expense of capacity loss.[125] Chung et al. adopted a coating material composed of $LiM_{0.05}Mn_{1.95}O_4$ (M = Co, Ni) to deposit onto the surface of $LiMn_2O_4$.[126] The slightly doped $LiM_{0.05}Mn_{1.95}O_4$ was supposed to be able to suppress the Jahn-Teller effect. Similar speculation was also proposed by Xiong et al.[127] They found that when Al_2O_3 coated $LiMn_2O_4$ was subject to annealing, the Al that diffused into the surface lattice will help

suppress the Jahn-Teller distortion and the remaining crystalline Al_2O_3 shielded the electrolyte from attacking the Mn. Though many people have reported the feasibility of this surface modification method, there is however still a lack of means to fully unveil the change of surface structure upon such treatment and the role of it towards enhancing the electrochemical performance.

Surface doping design has also been proven to be effective in suppressing the O_2 evolution in lithium-rich materials. Previous discussion has implied that the release of O_2 resulted from the simultaneous leaching of Li_2O from the layer of Li_2MnO_3. It becomes very interesting if hetero atoms are introduced to the surface layers, since the imported ions may impose extra stress to the Li_2MnO_3 and change its behavior under cycling. This speculation was proven by Park et al.[128] in their attempt to improve the performance of a lithium-rich $Li[Li_{0.167}Ni_{0.233}Co_{0.100}Mn_{0.467}Mo_{0.0333}]O_2$. Specifically, a layer of Al_2O_3 or $AlPO_4$ was deposited onto the material surface followed by heat treatment under 600 ^{o}C for 3 h, the Al was, within expectation, found to have diffused into the surface lattice. By applying a pressure sensor in the battery, they found that when the surface was modified, the pressure dropped noticeably, which is due to the suppressed O_2 release. The basic reason was that the Al incorporated into the surface and bonded strongly with the O and simultaneously created smaller domains of $LiMn_2O_3$.

A pillar effect was proposed by Cho et al.[129] They found that by annealing $Mg_2(PO_4)_3$ coated $Li_{1.17}Ni_{0.17}Co_{0.17}Mn_{0.5}O_2$, the Mg can be introduced into the Li (4h) site. The replacement of Li by Mg was responsible for the suppression of voltage fade because it hindered the migration of transition metals into the Li slab. Likewise, Na has been studied as a doping element, the Na ions enlarged the Li^+ slab and helped realize the pinning effect with stabilized structure and faster Li^+ diffusion rate.[130] In addition, partial formation of artificial spinel phase that provides both good lithium and electron conductivity has been reported by annealing carbon materials on lithium rich cathode through carbonthermal reaction or exposure to reducing agent such as hydrazine.[131, 132]

Previous solid doping design was almost focused on the metal ions diffusing into the bulk, there is actually another possible consequence - to have part of the surface lithium or

transition metals diffused into the coating layer to form a second phase. This mechanism was reported by Wu et al.[133] When a layer of electrochemically active MnO_x was applied on the surface of $Li[Ni_{0.2}Li_{0.2}Mn_{0.6}]O_2$ subject to post annealing, they found that the improved performance could be associated with the occurrence of lithium vacancies on the surface because of diffusion into the MnO_x. The partially lithium depleted surface resulted in an oxygen depletion, therefore decreased the chance of O_2 formation. In addition, the MnO_x could provide lithium diffusion channels.[134] Croy et al. carried out a delicate study using X-ray absorption spectroscopy at the metal K-edges.[135] They used a Li-Ni-PO_4 composition to modify the surface of $Li_{1.2}Mn_{0.4}Co_{0.4}O_2$, also followed by annealing.[49] It was found that the Ni after annealing was not in the phase of phosphate any more, instead, it replaced the surface Li in the transition layers and formed a $NiMn_6$ unit that made the Li_2MnO_3 phase more stable. Also, there are reports on treating the lithium-rich material with mild acid or hydrazine to replace part of the surface Li^+ with H^+ or incorporate N into the surface.[136-139]

1.3.1.2   Surface Coating

The role of surface coating towards surface phase transition suppression is actually under debate. In theory, surface phase change that results from cation disorder is an intrinsic behavior, therefore lots of researchers believe that simple coating is not as effective in controlling the phase transition upon electrochemically cycling.[140] AlF_3 coating was one of the few materials that were reported to be effective in mitigating the layered to spinel phase transition in Li-rich cathode materials by increasing the structural stability.[141] Al_2O_3 is a prevalent coating material from atomic layer deposition, therefore its application in surface modification of cathode materials is widely reported. But the effectiveness of Al_2O_3 in controlling the surface phase transition, especially in Li-rich cathode materials, has been under debate. A recent study by Wang's group provided visualized evidence on the suppression of layered to spinel phase transition in Al_2O_3 coated $Li_{1.2}$ $Ni_{0.2}Mn_{0.6}O_2$.[142] Figure 1.9 shows their STEM-EELS results. In a typical uncoated particle, the Mn valence on the surface dropped apparently after only 40 charge/discharge cycles, whereas the coated particles showed rather stable composition. The uncoated particle also showed surface reconstruction with a depth of about 5 nm, however, the coated

sample remained unchanged. The role of coating layers in suppressing the surface change of cathode materials is more complicated than it seems to be and thus more work are required aimed at elucidating this problem.
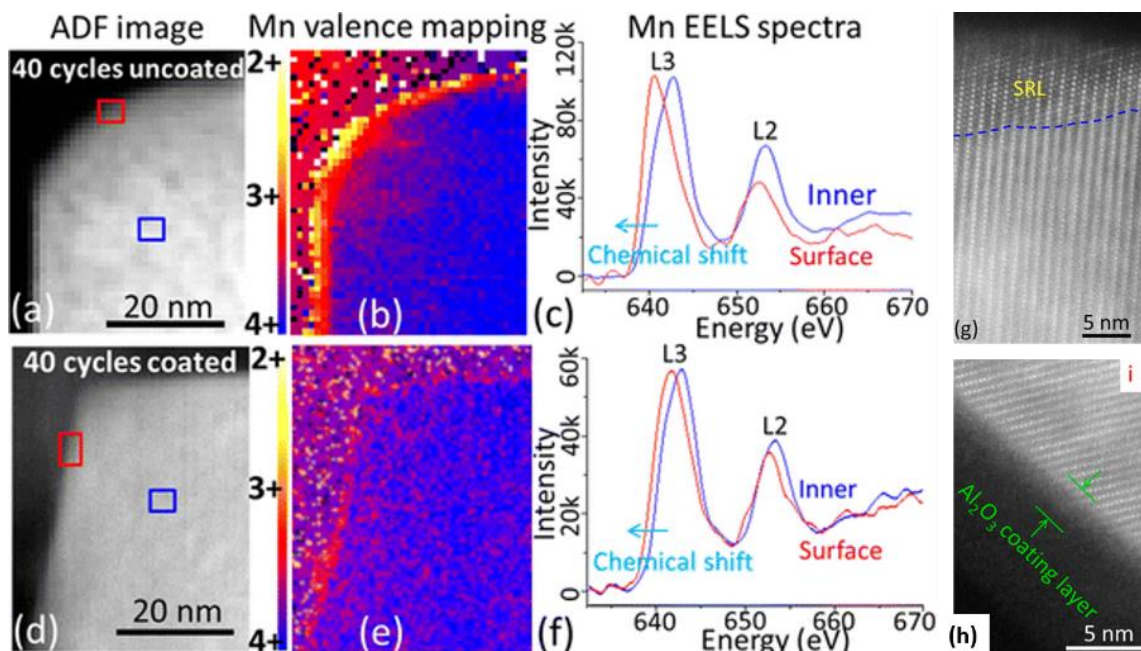
Figure 1.9 STEM-EELS study of Li$_{1.2}$Ni$_{0.2}$Mn$_{0.6}$O$_2$ and Al$_2$O$_3$ coated Li$_{1.2}$Ni$_{0.2}$Mn$_{0.6}$O$_2$ and their corresponding lattice images (Reproduced from ref. [142] with permission, copyright 2016 American Chemical Society)

1.3.2   Surface Modification as A Mechanical Buffer Layer

While there have been enormous reported coating materials aimed at suppressing mechanical cracks in anode, the cathode part is not as profound. The surface modification required for a cracking surface should be able to accommodate the strain upon electrochemical cycling.

Some metallic compounds such as Al$_2$O$_3$ and AlF$_3$ have been studied aimed at suppressing the crack formation inside of particles and were found to be effective.[143-145] But problems may arise since these materials are mostly brittle, too heavy crack formation may result in coating peeling off and lead to performance decay. Taking this into consideration, polymers with better mechanical properties may be better candidate.[146] There has been

some excellent work on coating aimed at suppressing cracks on anode materials such as the self-healing polymers reported by Cui et al.[147] Also, a molecular layer deposition (MLD) has been designed for polymer coating at the molecular level, this can be a potential method to adjust the cathode surfaces.[148] Such polymer coating has to have wide voltage window in order to remain consistent. In addition, since one of the reasons for the cracking formation is the phase transition on the surface, the strategies discussed in last session should also be helpful in avoiding the local cracking occurrence.

1.3.3   Surface Modification as HF Scavenger

The role of surface modification as HF scavenger is quite straightforward, in many cases, metal oxides have been used as surface coating materials in order to neutralize the HF originated from the electrolyte with the following reactions:[119, 149-155]

$$MgO + 2HF \rightarrow MgO + H_2O$$

$$ZnO + 2HF \rightarrow ZnF_2 + H_2O$$

$$TiO_2 + 4HF \rightarrow TiF_4 + 4H_2O$$

$$ZrO_2 + 4HF \rightarrow ZrF_4 + 4H_2O$$

$$Al_2O_3 + 6HF \rightarrow 2AlF_3 + 3H_2O$$
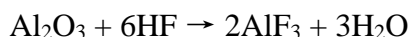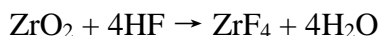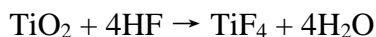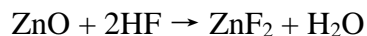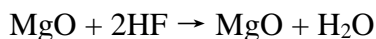
More importantly, the metal fluorides formed in these reactions are very stable in non-aqueous electrolyte, thus shielding the cathode materials from further loss when the surface metal oxides are completely consumed after extensive cycles.[156] The direct use of these metal fluorides or other metal phosphates is therefore also reported owing to their stable nature.[134, 157-160]

HF generation in the system causes transition metal dissolutions. As has been discussed before, transition metal reduction, in particular Mn, is a direct cause of metal dissolution. A study from our group on ALD derived $LiTaO_3$ coated $LiNi_{1/3}Mn_{1/3}Mn_{1/3}O_2$ has proven that the transition metal dissolution can be apparently suppressed by coating, the bare sample demonstrated 20 times higher transition metal dissolution than the sample with only

10 ALD cycles coating after 100 charge/discharge cycles.[161] Also, in our study in protecting $LiNi_{0.5}Mn_{1.5}O_4$ with atomic layer deposition derived $FePO_4$, the surface Mn chemical state after electrochemical cycling was found to be closely related to the performance and the presence of coating. X-ray absorption spectroscopy (XAS) study of Mn was conducted in this report. Transition metal $L_{3,2}$-edge XAS measures the unoccupied density of state of the transitional metal 3d and oxygen 2p bands, provides important information of the oxidation state, the spin state and the metal oxide covalence.[162, 163] The Mn $L_{3,2}$ edge XAS are shown in Figure 1.10a, it can be seen that an obvious peak shift to lower energy happened when the material was electrochemically cycled. The samples without any coating showed much less sharp peak at 646.5 eV as has been marked by the red arrow. The higher intensity indicates that the Mn in the coated sample was at higher oxidation state after cycling. Figure 1.10b shows the stability tests, apparently the sample with higher Mn oxidation state after cycling demonstrated much less intense capacity fade. Therefore, surface coating is effective in suppressing the Mn reduction and subsequent dissolution. A pre-lithiation method that enabled electrolyte reduction reaction manually by charging the cell from relatively lower voltage was reported by Wu and co-workers,[164] they found that the process generated a desirable SEI layer and allowed for full protection over NMC532/CNTs composites from metal dissolution.
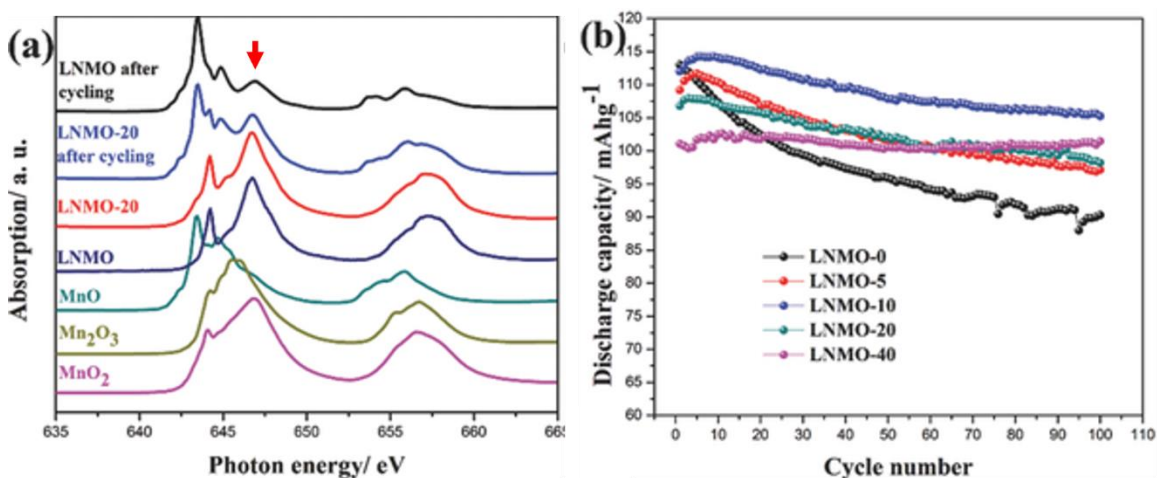
Figure 1.10 (a) XAS results of different LNMO samples and standard manganese oxides; (b) Cyclic stability tests of LNMO with various FePO₄ coating thicknesses (Reproduced from ref. [165] with permission, copyright 2014 WILEY-VCH)

1.3.4 Surface Modification as Metal-oxygen Bond Stabilizer

The dissolution of transition metals originates from the break of metal-oxygen bonds, therefore strengthening the bond at the surface can be a possible strategy to improve the performance. A regular coating diminishes the contact between the cathode materials and the electrolyte to combat with metal dissolution, the electron and ion diffusion is, however, restricted by the coating material. Numerous investigations have been reported on the doping method to deal with the above-mentioned scenarios, however, concerns regarding the loss of active components in the cathode materials arise when it comes to the bulk scale. The principle of surface doping design is more effective in this regard. In fact, surface doping design works at two aspects in terms of metal dissolution suppression, the first one is the stabilization of metal-oxygen bond and the second one is to minimize the amount of susceptible metal ions without affecting the structural integrity.

A systematic study of the role of surface Mg doping on the $LiNi_{0.5}Mn_{1.5}O_4$ cathode material was carried out by Cabana and coworkers using synchrotron soft X-ray absorption spectroscopy (XAS) focusing on the metal $L_{3,2}$-edges and oxygen K-edge.[166] The $LiNi_{0.5}Mn_{1.5}O_4$ charged to a voltage as high as 5 V undergoes very intensive chemical change since the Ni-O bond turns into highly oxidized and unstable state which is prone to be reduced by the electrolyte. Close scrutiny reveals the existence of a new Ni-O bond as a sign of electron depletion on the cathode materials with Mg doped surface and peak intensity ratio changes in both Ni $L_{3,2}$-edges and O K-edge in the surface sensitive total electron yield (TEY) spectra, indicating that the Mg doped surface helps retain a more oxidized surface upon electrochemical cycling, which is a result of more robust Ni-O bond so as to resist severe reduction by the electrolyte. It is worthwhile to note that this research was focusing on Ni-O bond state, more interesting results would be obtained if Mn $L_{3,2}$ edges were taken into consideration, since the reduction of surface Mn and the subsequent Jahn-Teller distortion effect can be tracked easily. The combination of these observation presents important guidelines of the principle through which surface doping design works in terms of stabilizing metal-oxygen bonds.

As has been mentioned above, the mechanism through which surface doping design works also involves the replacement of soluble metal ions on the surface. A representative

example is the formation $LiCo_{1-x}Al_xO_2$ solid solution on the $LiCoO_2$ cathode material surface. Previous discussions have mentioned the role of Al in suppressing surface phase transition in $LiCoO_2$, the incorporated Al, as an insoluble source in non-aqueous electrolyte, also reduces the dissolution of Co. The fundamental principle was presented by Dahéron and coworkers in 2009.[167] They tracked the surface acid-base properties of the $LiCo_{1-x}Al_xO_2$ while adjusting the value of x. To be more specific, NH_3 and SO_2 gases were absorbed onto the surface of $LiCo_{1-x}Al_xO_2$. Depending on the way the N and S are bonded on the Lewis acidic sites, Lewis basic sites and Brönsted acidic sites, they will display different binding energy on the N 1s and S 2p when characterized by XPS. The results showed that the surface basicity will drop drastically when Al is incorporated into the surface to form solid solution. The lower basicity makes the material much less vulnerable in the presence of HF.

1.3.5 Surface Modification as Electronic/Li$^+$ Conductivity Accelerators

Surface coating does not change the inherent electronic and lithium ion conductivity of cathode materials, it actually provides conducting network among individual particles so as to guarantee consecutive mobile channels to maximize the utilization of active materials. The way through which surface modification functions depends on the properties of the materials and how they are deposited.

1.3.5.1 In-situ Deposition of Conductivity Accelerators

The first category of the coating materials involves the substances that are intrinsically conductive. Metals such as Ag, Cu and Al have been studied, but the high cost is not acceptable for scaled-up productions, nevertheless, metals do not always cover the surface of powders well and the acidic nature of electrolyte will certainly dissolve the metal into ions and contaminate the active materials.[168, 169] Additionally, metals are generally mechanically rigid, cracks may happen when volume change of active materials is significant. Similarly, coating some metallic compounds that possess considerable electronic conductivity such as TiN and RuO_2 is also feasible regardless of the cost.[170, 171] Rutile TiO_2 is another possible carbon-free coating material thus can promote the

electrical conductivity profoundly as reported by Wang et al.[172] in their attempts of growing rutile-TiO_2 on the edge of $Li_4Ti_5O_{12}$ as an anode material.

Alternatively, the in-situ growth of conductive polymers has been widely reported. The polymers include polyaniline (PANi), polypropylene (PPy), polythiophene (PT), poly(3,4-ethylenedioxythiophene) (PEDOT), polyimide etc.[146, 173-177] The benefit of the in-situ growth of polymers is that the monomers can be easily nucleated on the surface of powders and get polymerized with the help of catalyst, therefore the thickness is quite uniform.

On the other hand, some carbon-based materials such as graphene, carbon nanotubes (CNTs), graphite and amorphous carbon have been used to form composites with the cathode materials. These carbon-based materials generally help build 3-D conductive network, not many of them were "coated" onto cathode powders. For materials that do not involve dissolution problem such as $LiFePO_4$, using graphene or CNTs to form composites is very effective in improving the electrical conductivity.[178-181] On the other hand, Song and coworkers used a high speed ball milling method to tether very thin and porous graphite layers onto $LiMn_2O_4$, they found that this conformal layer can double the $LiMn_2O_4$ capacity, the coating and performance of this sample is shown in Figure 1.11a-b.[182] Besides, a novel concept of hybrid coating, i.e. a composite coating layer that contain both electrical and lithium conductive substances has been reported, Figure 1.11e shows the mechanism of the hybrid coating, in this study, a coating layer that is composed of Li_3PO_4 and carbon has been investigated, with this type of coating, conductivity and surface stability can be enhanced simultaneously. Therefore the performance of the sample with hybrid coating was significantly improved.
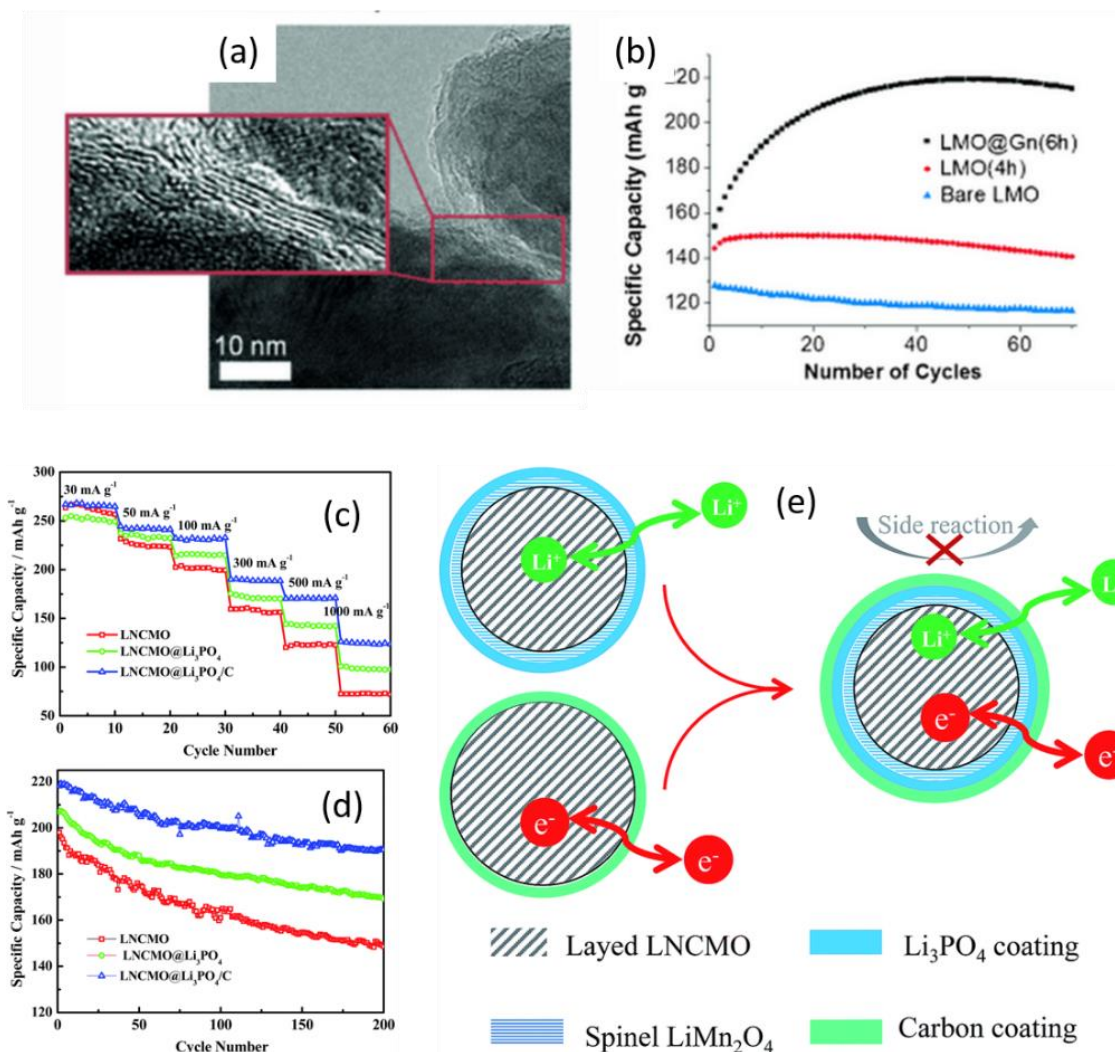
Figure 1.11 (a) Porous Graphite coating of LiMn₂O₄; (b) Discharge capacity of porous graphite coated LiMn₂O₄ with a voltage range of 2.4-4.3 V (Reproduced from ref. [182], copyright 2014 Wiley-VCH) (c) Rate capability test and (d) Stability test of the LNCMO, Li₃PO₄ coated LNCMO and Li₃PO4/C coated LNCMO; (e) Mechanism of the hybrid coating (Reproduced from ref. [183] with permission, copyright Royal Society of Chemistry 2015)

Another category is the deposition of lithium conductive coatings, compounds that are often considered as candidates for solid state electrolyte such as $LiAlO_2$, Li_2ZrO_3, Li_3PO_4, $LaPO_4$, LiPON, lithium boron oxide glass, $LiTaO_3$ et al. have been utilized in order to facilitate the transfer of lithium ions on cathode material surfaces.[184-192]

1.3.5.2   Deposition of Conductivity Accelerators via Post Treatment

The pyrolysis of carbon containing organics *via* either solid state method or chemical vapor deposition has been a proven strategy to improve the performance of cathode materials, particularly on those with poor intrinsic electronic conductivity and are resistant to reduction, such as $LiFePO_4$ and $LiMnPO_4$, this has been comprehensively reviewed by our group.[193] The carbon coating on $LiMeO_x$ (Me = Ni, Mn, Co etc.), however, remains hard to realize because of their oxidation nature, which will be reduced by carbon under high temperature and lead to poor performance. Despite many researchers are attempting to achieve the pyrolysis of organic under temperatures as low as 350 ^{o}C in air without burning up the carbon in short time, the feasibility of this method is under debate.[182, 194-198]

The surface doping design is another reported way that can possibly generate surface conductivity facilitator. For example, Manthiram et al.[199] coated the 5V class cathode material $LiMn_{1.42}Ni_{0.42}Co_{0.16}O_4$ with Al_2O_3 followed by heating at 400-600 ^{o}C for 3h, despite the insulating nature of Al_2O_3, they found that the Al_2O_3 reacted with the cathode surface during annealing and formed $LiAlO_2$, which is a good lithium conductor. Similar behavior was also observed by Zhang et al.[200], in their attempt of coating $Li(Ni_{1/3}Co_{1/3}Mn_{1/3})O_2$ with ZrO_2 via post annealing of $ZrO(NO_3)_2$, the near surface Zr was found to exist in the form of Li_2ZrO_3, which is also a good lithium conductor. In a more complicated case, Yang et al.[201] found that when a $AlPO_4$ layer was coated onto $LiCoO_2$ followed by heat treatment, the surface Li_2CO_3 resulted from lithium over-stoichiometry will react with the $AlPO_4$ and turn into a dual phase of $LiCo_{1-y}Al_yO_2$ at the ~10 nm region and Li_3PO_4 at ~ 100 nm region near the surface, the former was found to be effective in suppressing metal dissolution and the latter one is a proven good lithium conductor. The presence of Li_3PO_4 was the reason why $AlPO_4$ was more effective than Al_2O_3 in improving the capacity retention of $LiCoO_2$ especially at extended voltage ranges.
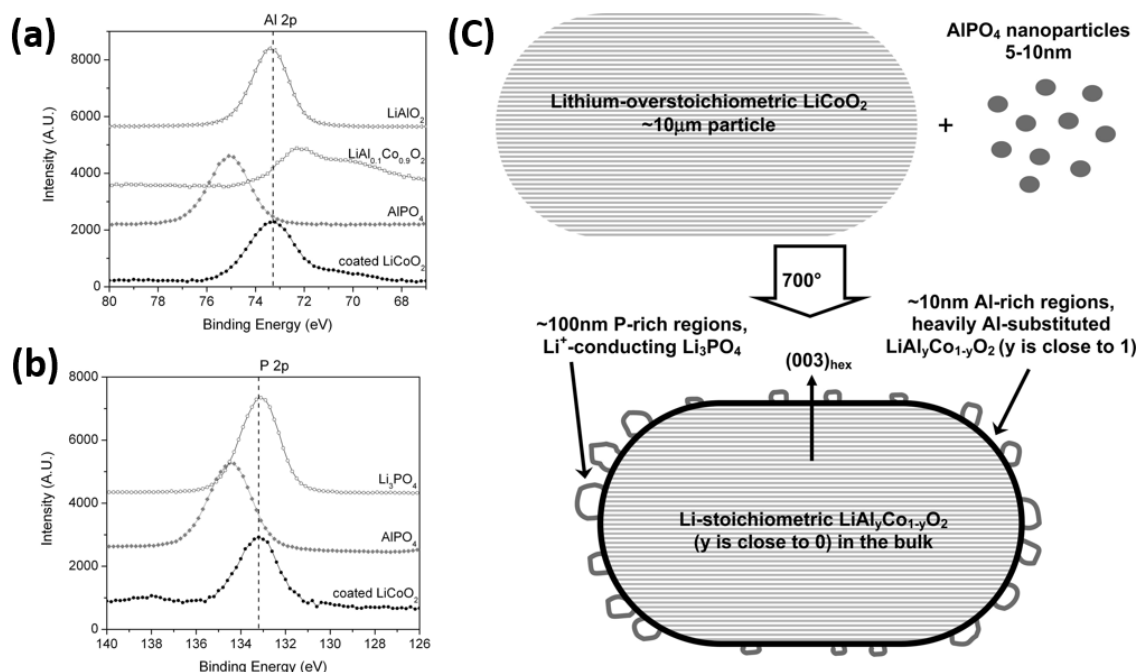
Figure 1.12 XPS spectra of (a) Al 2p and (b) P 2p of AlPO₄ coated LiCoO₂; (c) schematic illustration of the AlPO₄ surface modification mechanism (Reproduced from ref.[201] Copyright 2007 American Chemical Society)

1.3.5.3 Formation of Conductivity Accelerators during Lithiation/ delithiation

When the surface coating material can accommodate the reversible insertion/desertion of lithium ions, they tend to turn into a good lithium accelerator. For example, Ta_2O_5 has been reported to undergo following reaction when cycled:[202]

$$Ta_2O_5 + 10\,Li^+ + 10e \rightarrow 2\,Ta^{5+} + 5\,Li_2O$$

$$Li_2O + Ta_2O_5 \rightarrow 2\,LiTaO_3$$
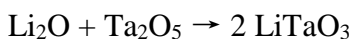
The product $LiTaO_3$ is a well-known solid-state electrolyte at reduced dimensions, Heitjans et al.[203] proved that the $LiTaO_3$ with a particles size of 20 nm demonstrates a lithium ions conductivity of about 3×10^{-6} S cm^{-1}. Our group has successfully synthesized conformal $LiTaO_3$ film *via* atomic layered deposition by the combination of Li_2O and Ta_2O_5, and the $LiTaO_3$ was also employed to protect the cathode material

LiNi$_{1/3}$Mn$_{1/3}$Co$_{1/3}$O$_2$ by precisely adjusting the coating thickness.[161] Similarly, Al$_2$O$_3$, which is a well-known insulator, also experiences lithiation into LiAlO$_2$, turning into a good lithium conductor.

TiO$_2$ is another widely studied coating material that can be reversibly lithiated/delithiated under proper voltage ranges, the resulted LiTiO$_2$ is a good electron conductor, which has been theoretically proven by Wagemaker et al.[204]

In an attempt to theoretically predict the criteria of coating materials screening, Wolverton and co-workers have calculated the thermodynamic principles of cathode coating materials, such as metal oxides and metal fluorides.[205] By assuming the overall conversion reaction of metal oxides and metal fluorides as:

$$M_xO_{1/2} + Li \rightarrow xM + 1/2Li_2O; \quad M_xF + Li \rightarrow xM + LiF$$

respectively, they calculated the density function theory (DFT) voltages of oxides and fluorides compared to the experimental voltages, as shown in Figure 1.13. The higher the lithiation voltage, the more likely the coating gets lithiated during electrochemical cycling. It can be seen that fluorides generally have much higher lithiation voltage than oxides, due to the higher electronegativity of fluorine than oxygen. This chart is an important support for the selection of coating materials in terms of coating lithiation manipulation.
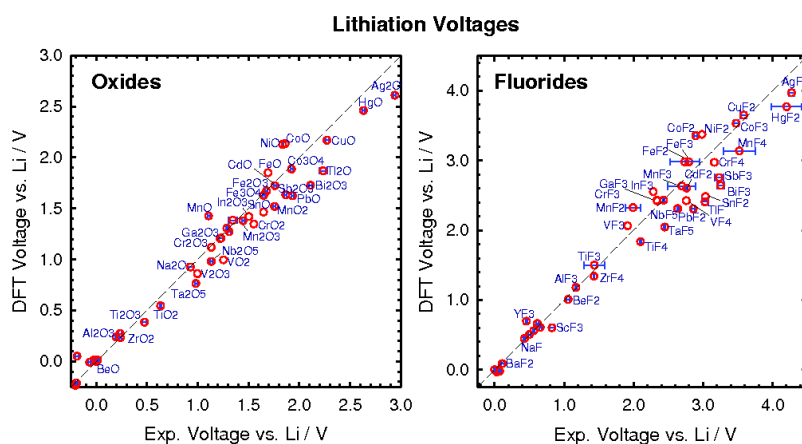
Figure 1.13 Calculated average voltages for oxides and fluorides versus voltages estimated from experimental formation enthalpies (Reproduced from ref. [205] with permission, copyright 2014 Wiley-VCH)

1.4 Methods of Cathode Materials Surface Modifications

Possible surface modification scenarios have been illustrated in Figure 1.14. The various designs of surface modification methods have been repeatedly attested in aforementioned reports, it still remains a question that what is an ideal modification method? Conclusively, it depends on the problem that one attempts to address when applying surface modification. Regular coating might work moderately in suppressing metal dissolution, electrolyte decomposition and improving conductivity, but is of less use when the intrinsic phase change is the issue. The surface coating might be very rough, though electrical and ionic transportation can be less affected, full coverage against acid attacking is however not guaranteed. Surface doping design could help mitigate surface phase transition, improve conductivity and decrease the possibility of metal dissolution, but is restricted by the doping element and controlled doping level, moreover, the doping process is often undergoing an unpredictable scenario. Conformal coatings can protect the electrode at very well controlled manner, but the hermetic nature prohibits electron and lithium diffusion seriously if the coating material is insulating.
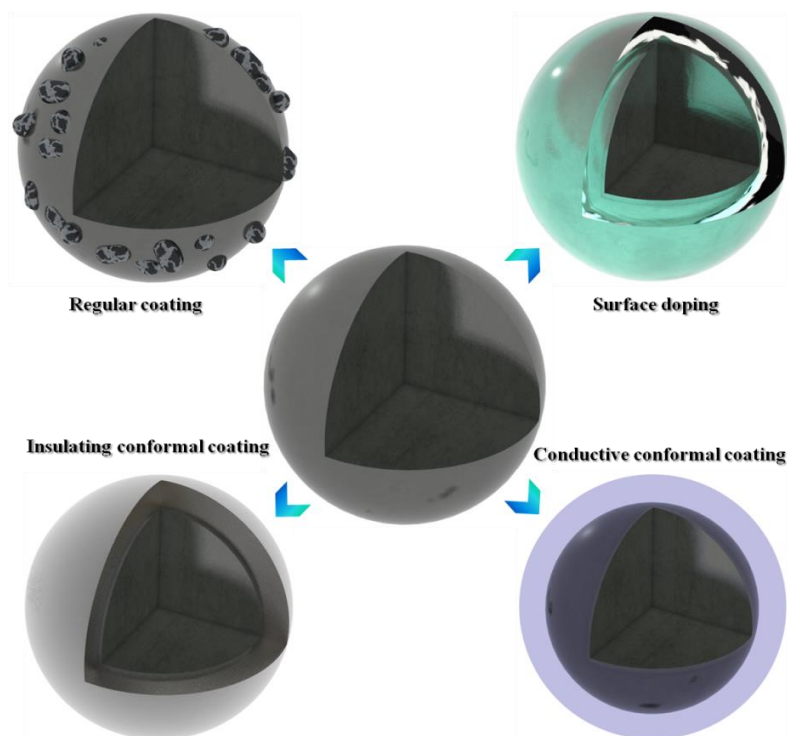
Figure 1.14 Possible ways of surface modification

1.4.1　Atomic Layer Deposition and Its Derivative Methods

Atomic layer deposition (ALD) is a technique used to fabricate conformal coatings with controlled thickness, a representative schematic is shown in Fig. 1.15a using the most widely used Al_2O_3 as an example. In a typical ALD process, the surface of the substrate is initially functionalized with hydroxyl groups, in a following step, trimethylaluminum (TMA) and H_2O are purged into the reacting chamber in sequence and allow the following reactions to take place:

$AlOH + Al(CH_3)_3 \rightarrow Al\text{-}O\text{-}Al(CH_3)_2 + CH_4$ (a)

$Al\text{-}O\text{-}Al(CH_3)_2 + 2H_2O \rightarrow Al\text{-}O\text{-}Al(OH)_2 + 2CH_4$ (b)
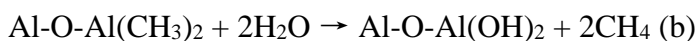
Each of these reactions is a half reaction and this particular advantage enables the self-limiting growth, i. e. deposition at a controllable manner. In addition, the bottom-up growth from atomic level allows ultra-uniform and conformal deposition.[206-210]

Molecular layer deposition (MLD) is another technique analogous to ALD, in which all-organic coating can be deposited, when combining with an ALD process, MLD can generate a hybrid organic-inorganic coating. The process of a typical MLD coating of alucone (aluminum organic) is shown in Fig. 1.15b, in which the only difference from ALD is the replacement of water with ethyl glycol.[211, 212] Though no references can be indexed about the application of MLD in cathode materials surface modifications, its versatile design will certainly find great potential in this area. With the fast development of conductive polymer coatings using MLD,[213, 214] and the pyrolysis of a polymer coating into conductive carbon,[215] it is rationally predicable that MLD will be an extremely powerful technique targeting at cathode materials surface modifications.
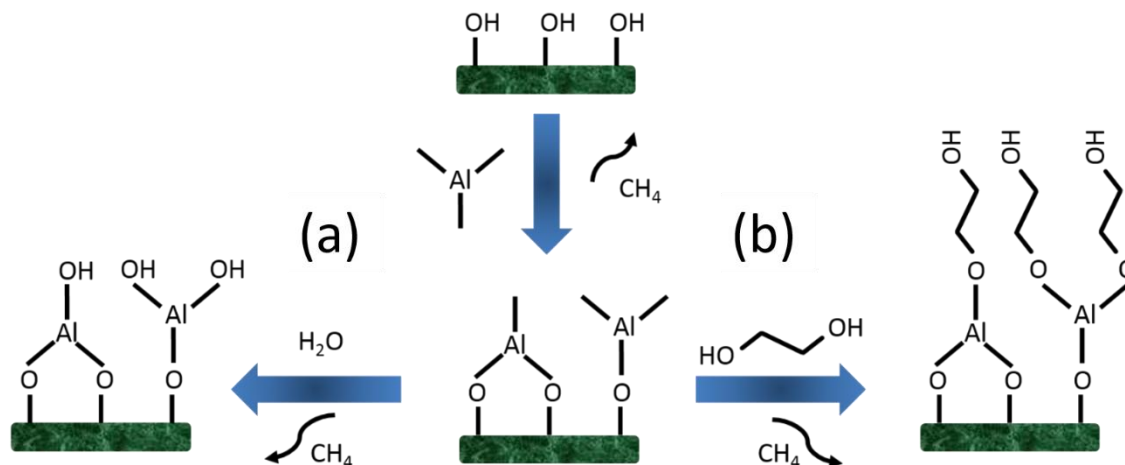
Figure 1.15 Schematic illustration of (a) ALD process of Al$_2$O$_3$ synthesis and (b) MLD process of Alucone synthesis

1.5 Surface Properties of Graphene-based Anode Materials

Because of its extraordinary specific surface area and electrical conductivity, graphene has been extensively employed as both pure anode material and as an additive to tailor material properties. [216-219]

Although these results have proven that graphene can be an outstanding candidate for lithium-ion batteries, graphene microstructure and morphology can nevertheless exert significant effects on the cyclic performance and rate capability of lithium-ion batteries, as demonstrated by recent studies of Sun et al. [217, 220] Hence, developing novel-structured graphene is imperative.

While much research focuses on decreasing the layers of graphene, very few of them provide insight on decreasing the dimension, i.e. creating quasi-one-dimensional graphene nanoribbons (GNRs).

1.5.1 Theoretical Prediction

One of the most notable changes of GNRs is the presence of edge structures in comparison with graphene. The configuration of edges can be either zigzag or armchair. Lithium adsorption at GNRs has been studied by Barone et al. [221] Based on spin-polarized Kohn-

Sham approach within both the local spin density approximation and the generalized gradient approximation, they found that the binding energy of lithium at zigzag edges can be 50% stronger than that of graphene and armchair edges. The Li interaction with center adsorption positions weakens sharply, indicating the confined width of GNRs is very ideal to attain larger ion concentrations.

On the other hand, Barone et al. have also studied the diffusion of Li atoms within GNRs. [222] They concluded that the diffusion of Li atoms along the edge is remarkably faster than the channels along the axis, and two orders of magnitude higher than graphene. In the case of zigzag GNR, the edge effect can be even more profound. While the edges of GNRs display extraordinary Li conductivity, the inner graphene structures, typically within several nano-meters, will show 2D graphene limit.

1.5.2 Graphene Nanoribbons as Anode Material for Lithium-ion Batteries

Upon intensive charge and discharge, some electrode materials may undergo fracture and pulverization, resulting in fading capacity. [223] Although CNTs are well known to have very high Young's modulus, they still suffer from this deficiency during lithiation and de-lithiation. [224] Huang et al. [225] used in situ transmission electron microscopy to study the electrochemical behavior of GNRs and found that the GNRs are mechanically robust upon tension and compression test.

MWCNTs are circumferentially closed cylinders, which is the main reason of the brittle nature during lithiation since there is little space to accommodate the volume change. On the contrary, GNRs are unconfined layers of graphene with weak interlayer coupling and can tolerate even harsher electrochemical reactions. This unique characteristic enables very stable cyclic performance. The initial use of GNRs for lithium-ion batteries anode material was reported by Fahlman et al. [226] They found that the reduced GNRs derived from unzipped CNTs demonstrated slightly higher reversible capacity than conventional MCMB graphite but lower Coulombic efficiency. They also evaluated graphene oxide nanoribbons (GONRs), which is GNRs containing a lot of oxygen-containing functional groups.

1.6   Thesis Objectives

As has been thoroughly reviewed, the existing obstacles in the electrode materials for lithium-ion batteries are mainly divided into 3 categories: 1) the synthesis of high purity material; 2) the modification of the materials surface to enable optimized electrochemical performance and 3) the understanding of how surface modifications benefit the performance of battery materials. The content will be mainly focused on 3 types of electrode materials. In the cathode part, spinel $LiNi_{0.5}Mn_{1.5}O_4$ and layered Li-rich $Li_{1.2}Mn_{0.54}Co_{0.13}Mn_{0.13}O_2$ that have high energy density will be investigated in detail. In the anode part, graphene-based materials will be investigated as an alternative of graphite. As such, the thesis objectives are divided into 5 topics.

(1) To synthesize high purity cathode materials. The synthesis of $LiNi_{0.5}Mn_{1.5}O_4$ and $Li_{1.2}Mn_{0.54}Co_{0.13}Mn_{0.13}O_2$ will be carried out via various methods for high purity. These cathode materials are known to be prone to forming rock salt impurity phases such as NiO during synthesis. The materials will be used as base materials for ALD coating effect study.

(2) To study the effect of ALD coating. Previous researches on surface coating of cathode materials have indicated that in order to achieve high stability without significantly sacrificing the capacity of a cathode material, electrochemically active coatings are desired. In addition, there is a lack of report on using metal phosphates as surface coating material by ALD, even though coating by regular methods has been reported a lot.

(3) To explore surface modification methods on the basis of ALD. ALD is an outstanding method to form uniform coatings, but using ALD coatings followed by annealing to tailor the surface structure has not been reported thus far.

(4) To understand the structural evolution of HENMC based on in-situ XAS of fresh electrode and heavily cycled electrode.

(5) To unveil the surface properties of graphene based anode materials and the effects of these factors on the performance.

1.7 Thesis Organizations

This thesis include seven chapters and satisfies the requirements on Integrated-Article form as outlined in the *Thesis Regulation Guide* by the School of Graduate and Postdoctoral Studies (SGPS) of the University of Western Ontario. Specifically, it consists of the following sequence:

Chapter 1 presents a comprehensive introduction to the current status of research on cathode materials, the problems that pertain to this field of study, the possible explanations to these problems and the methods that researchers have adopted to address these problems. Also, thesis objectives have been listed in this chapter.

Chapter 2 describes the experimental methods and analytical apparatus used in the work of this thesis.

Chapter 3 presents the study of using an electrochemically active amorphous iron phosphate material as coating on spinel $LiNi_{0.5}Mn_{1.5}O_4$ via ALD. The presence of the amorphous iron phosphate suppressed the reduction of Mn upon cycling significantly and helped create a lithium conductive layer through the lithiation of $FePO_4$.

Chapter 4 explores the possibility of using Ti to modify the surface structure of spinel $LiNi_{0.5}Mn_{1.5}O_4$ using ALD. Specifically, TiO_2 was deposited onto LNMO powders by ALD, the samples were subject to post annealing. Systematic studies have been carried out in order to understand the surface structure change. A significant performance improvement was observed in the samples with appropriate coating thickness. This is a first study on tailoring the surface structure of cathode materials via ALD.

Chapter 5 studies the utilization of aluminum phosphate as coating material on Li-rich $Li_{1.2}Mn_{0.54}Co_{0.13}Mn_{0.13}O_2$ *via* ALD. The oxygen release problem in this material may lead to thermal runaway problems, $AlPO_y$ coating was found to be able to increase the thermal stability more than regular Al_2O_3 coating. In addition, the surface change in the ALD process has been systematically studied.

Chapter 6 investigates the behaviors of transition metals in HENMC during the initial cycle and the 450th cycle through in-situ XAS measurements. It was found that the Ni and Co lose their electrochemical activity in the long term cycles whereas Mn can still undergo redox reaction, participation of oxygen in the charge compensation during the 450th cycle was proposed.

Chapter 7 systematically studies the effects of surface functional groups, surface area and defects on the LIBs performance of graphene nanoribbons derived from carbon nanotubes.

Chapter 8 summarizes the results and contributions of this work and provide outlook and future work.

The structure of the work in this thesis has also been illustrated in the following figure.
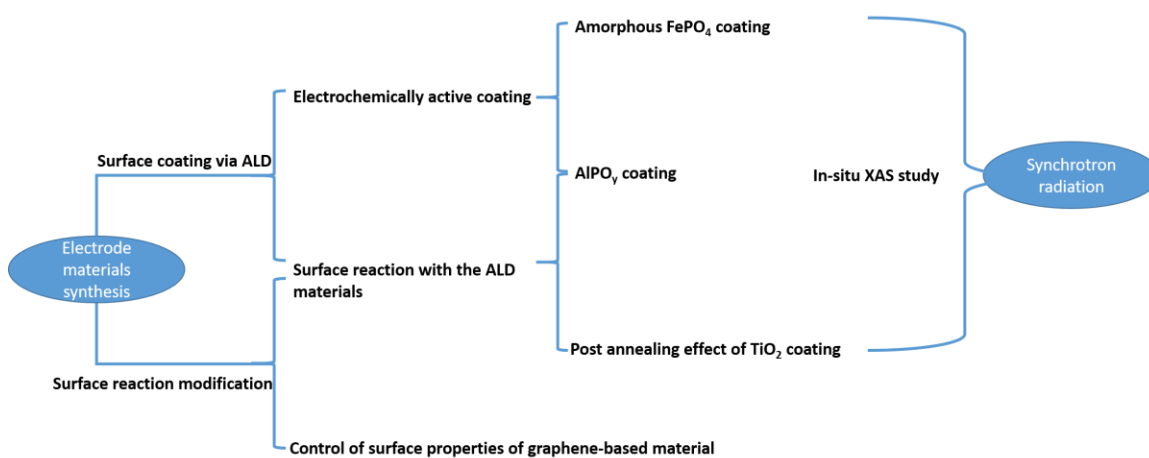
Figure 1.16 Flow chart of the thesis organization

References

[1] B. Scrosati, Challenge of Portable Power, *Nature*, 1995, **373**, 557-558.

[2] J.-M. Tarascon and M. Armand, Issues and Challenges Facing Rechargeable Lithium Batteries, *Nature*, 2001, **414**, 359-367.

[3] J. B. Goodenough and Y. Kim, Challenges for Rechargeable Li Batteries, *Chem. Mater.*, 2010, **22**, 587-603.

[4] J. B. Goodenough, Evolution of Strategies for Modern Rechargeable Batteries, *Acc. Chem. Res.*, 2013, **46**, 1053-1061.

[5] USABC Goals for Advanced Batteries for EVs - CY 2020 Commercialization.

[6] Y. Nishi, The Development of Lithium Ion Secondary Batteries, *Chem. Rec*,, 2001, **1**, 406-413.

[7] N. Nitta, F. X. Wu, J. T. Lee and G. Yushin, Li-Ion Battery Materials: Present and Future, *Mater. Today*, 2015, **18**, 252-264.

[8] J. Cabana, L. Monconduit, D. Larcher and M. R. Palacin, Beyond Intercalation-Based Li-Ion Batteries: The State of the Art and Challenges of Electrode Materials Reacting through Conversion Reactions, *Adv. Mater.*, 2010, **22**, E170-192.

[9] D. Howell, T. Q. Duong, P. W. Faguy and B. Cunnigham, The EV Everywhere Challenge, FY 2013 Annual Progress Report, 2013.

[10] M. S. Whittingham, Lithium Batteries and Cathode Materials, *Chem. Rev.*, 2004, **104**, 4271-4302.

[11] J. M. Tarascon and M. Armand, Issues and Challenges Facing Rechargeable Lithium Batteries, *Nature*, 2001, **414**, 359-367.

[12] M. Armand and J. M. Tarascon, Building Better Batteries, *Nature*, 2008, **451**, 652-657.

[13] P. G. Bruce, B. Scrosati and J. M. Tarascon, Nanomaterials for Rechargeable Lithium Batteries, *Angew. Chem. Int. Ed.*, 2008, **47**, 2930-2946.

[14] M. R. Palacin, Recent Advances in Rechargeable Battery Materials: A Chemist's Perspective, *Chem. Soc. Rev.*, 2009, **38**, 2565-2575.

[15] K. T. Lee, S. Jeong and J. Cho, Roles of Surface Chemistry on Safety and Electrochemistry in Lithium Ion Batteries, *Acc. Chem. Res*., 2013, **46**, 1161-1170.

[16] M. S. Islam and C. A. Fisher, Lithium and Sodium Battery Cathode Materials: Computational Insights into Voltage, Diffusion and Nanostructural Properties, *Chem. Soc. Rev*., 2014, **43**, 185-204.

[17] T. Ohzuku, A. Ueda, M. Nagayama, Y. Iwakoshi and H. Komori, Comparative Study of $LiCoO_2$, $LiNi_{1/2}Co_{1/2}O_2$ and $LiNiO_2$ for 4 Volt Secondary Lithium Cells, *Electrochim. Acta*, 1993, **38**, 1159-1167.

[18] G. G. Amatucci, CoO_2, the End Member of the Li_xCoO_2 Solid Solution, *J. Electrochem. Soc*., 1996, **143**, 1114.

[19] Z. Chen, Z. Lu and J. R. Dahn, Staging Phase Transitions in Li_xCoO_2, *J. Electrochem. Soc*., 2002, **149**, A1604.

[20] E. Rossen, J. Reimers and J. Dahn, Synthesis and Electrochemistry of Spinel LT · $LiCoO_2$, *Solid State Ionics*, 1993, **62**, 53-60.

[21] E. Antolini, $LiCoO_2$: Formation, Structure, Lithium and Oxygen Nonstoichiometry, Electrochemical Behaviour and Transport Properties, *Solid State Ionics*, 2004, **170**, 159-171.

[22] S. Kang, Electrochemical and Structural Properties of HT-$LiCoO_2$ and LT- $LiCoO_2$ Prepared by the Citrate Sol-Gel Method, *Solid State Ionics*, 1999, **120**, 155-161.

[23] Y. Shao-Horn, S. A. Hackney, A. J. Kahaian and M. M. Thackeray, Structural Stability of $LiCoO_2$ at 400°C, *J. Solid State Chem*., 2002, **168**, 60-68.

[24] H. Wang, Tem Study of Electrochemical Cycling-Induced Damage and Disorder in $LiCoO_2$ Cathodes for Rechargeable Lithium Batteries, *J. Electrochem. Soc*., 1999, **146**, 473.

[25] H. Gabrisch, R. Yazami and B. Fultz, A Transmission Electron Microscopy Study of Cycled LiCoO$_2$, *J. Power Sources*, 2003, **119**, 121, 674-679.

[26] J.-H. Shim, K.-S. Lee, A. Missyul, J. Lee, B. Linn, E. C. Lee and S. Lee, Characterization of Spinel Li$_x$Co$_2$O$_4$-Coated LiCoO$_2$ prepared with Post-Thermal Treatment as a Cathode Material for Lithium Ion Batteries, *Chem. Mater.*, 2015, **27**, 3273-3279.

[27] T. Ohzuku, Electrochemistry and Structural Chemistry of LiNiO$_2$ (R3m) for 4 Volt Secondary Lithium Cells, *J. Electrochem. Soc.*, 1993, **140**, 1862.

[28] A. R. Armstrong, N. Dupre, A. J. Paterson, C. P. Grey and P. G. Bruce, Combined Neutron Diffraction, NMR, and Electrochemical Investigation of the Layered-to-Spinel Transformation in LiMnO$_2$, *Chem. Mater.*, 2004, **16**, 3106-3118.

[29] P. Kalyani and N. Kalaiselvi, Various Aspects of Linio2chemistry: A Review, *Sci. Tech. Adv. Mater.*, 2005, **6**, 689-703.

[30] A. Rougier, C. Delmas and A. V. Chadwick, Non-Cooperative Jahn-Teller Effect in LiNiO$_2$: An EXAFS Study, *Solid State Commun.*, 1995, **94**, 123-127.

[31] M. Arroyo y de Dompablo, C. Marianetti, A. Van der Ven and G. Ceder, Jahn-Teller Mediated Ordering in Layered Li$_x$MO$_2$ Compounds, *Phys. Rev. B*, 2001, **63**, 14, 144107

[32] J. Kim, B. H. Kim, Y. H. Baik, P. K. Chang, H. S. Park and K. Amine, Effect of (Al, Mg) Substitution in LiNiO$_2$ Electrode for Lithium Batteries, *J. Power Sources*, 2006, **158**, 641-645.

[33] R. Sathiyamoorthi, P. Shakkthivel, S. Ramalakshmi and Y.-G. Shul, Influence of Mg Doping on the Performance of LiNiO$_2$ Matrix Ceramic Nanoparticles in High-Voltage Lithium-Ion Cells, *J. Power Sources*, 2007, **171**, 922-927.

[34] A. W. Moses, H. G. G. Flores, J.-G. Kim and M. A. Langell, Surface Properties of LiCoO$_2$, LiNiO$_2$ and LiNi$_{1-x}$Co$_x$O$_2$, *Appl. Surf. Sci.*, 2007, **253**, 4782-4791.

[35] J. M. Wang, J. P. Hu, C. Y. Ouyang, S. Q. Shi and M. S. Lei, Cobalt Suppressed Jahn–Teller Effect in for Lithium Ion Batteries, *Solid State Commun*., 2011, **151**, 234-237.

[36] S. Muto, Y. Sasano, K. Tatsumi, T. Sasaki, K. Horibuchi, Y. Takeuchi and Y. Ukyo, Capacity-Fading Mechanisms of $LiNiO_2$-Based Lithium-Ion Batteries, *J. Electrochem. Soc*., 2009, **156**, A371.

[37] F. Lin, I. M. Markus, D. Nordlund, T. C. Weng, M. D. Asta, H. L. Xin and M. M. Doeff, Surface Reconstruction and Chemical Evolution of Stoichiometric Layered Cathode Materials for Lithium-Ion Batteries, *Nat. Commun*., 2014, **5**, 3529.

[38] R. Robert, C. Villevieille and P. Novák, Enhancement of the High Potential Specific Charge in Layered Electrode Materials for Lithium-Ion Batteries, *J. Mater. Chem. A*, 2014, **2**, 8589.

[39] T. Nonaka, C. Okuda, Y. Seno, K. Koumoto and Y. Ukyo, X-Ray Absorption Study on $LiNi_{0.8}Co_{0.15}Al_{0.05}O_2$ Cathode Material for Lithium-Ion Batteries, *Ceram. Int*., 2008, **34**, 859-862.

[40] T. Nonaka, C. Okuda, Y. Seno, Y. Kondo, K. Koumoto and Y. Ukyo, Surface-Sensitive X-Ray Absorption Study on $LiNi_{0.8}Co_{0.15}Al_{0.05}O_2$ Cathode Material for Lithium-Ion Batteries, *J. Electrochem. Soc*., 2007, **154**, A353.

[41] W. Liu, P. Oh, X. Liu, M. J. Lee, W. Cho, S. Chae, Y. Kim and J. Cho, Nickel-Rich Layered Lithium Transition-Metal Oxide for High-Energy Lithium-Ion Batteries, *Angew. Chem. Int. Ed*., 2015, **54**, 4440-4457.

[42] S. K. Jung, H. Gwon, J. Hong, K. Y. Park, D. H. Seo, H. Kim, J. Hyun, W. Yang and K. Kang, Understanding the Degradation Mechanisms of $LiNi_{0.5}Co_{0.2}Mn_{0.3}O_2$ Cathode Material in Lithium Ion Batteries, *Adv. Energy. Mater*., 2014, **4**, 1300787

[43] P. F. Yan, J. M. Zheng, D. P. Lv, Y. Wei, J. X. Zheng, Z. G. Wang, S. Kuppan, J. G. Yu, L. L. Luo, D. Edwards, M. Olszta, K. Amine, J. Liu, J. Xiao, F. Pan, G. Y. Chen, J. G. Zhang and C. M. Wang, Atomic-Resolution Visualization of Distinctive Chemical Mixing

Behavior of Ni, Co, and Mn with Li in Layered Lithium Transition-Metal Oxide Cathode Materials, *Chem. Mater.*, 2015, **27**, 5393-5401.

[44] B.-B. Lim, S.-J. Yoon, K.-J. Park, C. S. Yoon, S.-J. Kim, J. J. Lee and Y.-K. Sun, Advanced Concentration Gradient Cathode Material with Two-Slope for High-Energy and Safe Lithium Batteries, *Adv. Funct. Mater.*, 2015, **25**, 4673-4680.

[45] Y. K. Sun, Z. Chen, H. J. Noh, D. J. Lee, H. G. Jung, Y. Ren, S. Wang, C. S. Yoon, S. T. Myung and K. Amine, Nanostructured High-Energy Cathode Materials for Advanced Lithium Batteries, *Nat. Mater.*, 2012, **11**, 942-947.

[46] Y. K. Sun, S. T. Myung, B. C. Park, J. Prakash, I. Belharouak and K. Amine, High-Energy Cathode Material for Long-Life and Safe Lithium Batteries, *Nat. Mater.*, 2009, **8**, 320-324.

[47] A. K. Shukla, Q. M. Ramasse, C. Ophus, H. Duncan, F. Hage and G. Chen, Unravelling Structural Ambiguities in Lithium- and Manganese-Rich Transition Metal Oxides, *Nat. Commun.*, 2015, **6**, 8711.

[48] S. H. Kang and M. M. Thackeray, Stabilization of $xLi_2MnO_3 \cdot (1-x)LiMO_2$ Electrode Surfaces (M=Mn, Ni, Co) with Mildly Acidic, Fluorinated Solutions, *J. Electrochem. Soc.*, 2008, **155**, A269.

[49] S.-H. Kang and M. M. Thackeray, Enhancing the Rate Capability of High Capacity $xLi_2MnO_3 \cdot (1-x)LiMO_2$ (M=Mn, Ni, Co) Electrodes by Li–Ni–PO_4 Treatment, *Electrochem. Commun.*, 2009, **11**, 748-751.

[50] A. R. Armstrong, M. Holzapfel, P. Novak, C. S. Johnson, S. H. Kang, M. M. Thackeray and P. G. Bruce, Demonstrating Oxygen Loss and Associated Structural Reorganization in the Lithium Battery Cathode $Li[Ni_{0.2}Li_{0.2}Mn_{0.6}]O_2$, *J. Am. Chem. Soc.*, 2006, **128**, 8694-8698.

[51] D. Mohanty, A. S. Sefat, J. Li, R. A. Meisner, A. J. Rondinone, E. A. Payzant, D. P. Abraham, D. L. Wood III, and C. Daniel, Correlating Cation Ordering and Voltage Fade

in a Lithium-Manganese-Rich Lithium-Ion Battery Cathode Oxide: A Joint Magnetic Susceptibility and Tem Study, *Phys. Chem. Chem. Phys*., 2013, **15**, 19496-19509.

[52] N. Yabuuchi, K. Yoshii, S. T. Myung, I. Nakai and S. Komaba, Detailed Studies of a High-Capacity Electrode Material for Rechargeable Batteries, Li_2MnO_3-$LiCo_{(1/3)}Ni_{(1/3)}Mn_{(1/3)}O_2$, *J. Am. Chem. Soc*., 2011, **133**, 4404-4419.

[53] N. Dupre, M. Cuisinier, E. Legall, D. War and D. Guyomard, Contribution of the Oxygen Extracted from Overlithiated Layered Oxides at High Potential to the Formation of the Interphase, *J. Power Sources*, 2015, **299**, 231-240.

[54] S.-M. Bak, K.-W. Nam, W. Chang, X. Yu, E. Hu, S. Hwang, E. A. Stach, K.-B. Kim, K. Y. Chung and X.-Q. Yang, Correlating Structural Changes and Gas Evolution During the Thermal Decomposition of Charged $Li_xNi_{0.8}Co_{0.15}Al_{0.05}O_2$ cathode Materials, *Chem. Mater*., 2013, **25**, 337-351.

[55] Y. Wu, C. Ma, J. Yang, Z. Li, L. F. Allard, C. Liang and M. Chi, Probing the Initiation of Voltage Decay in Li-Rich Layered Cathode Materials at the Atomic Scale, *J. Mater. Chem. A*, 2015, **3**, 5385-5391.

[56] M. Gu, A. Genc, I. Belharouak, D. Wang, K. Amine, S. Thevuthasan, D. R. Baer, J.-G. Zhang, N. D. Browning, J. Liu and C. Wang, Nanoscale Phase Separation, Cation Ordering, and Surface Chemistry in Pristine $Li_{1.2}Ni_{0.2}Mn_{0.6}O_2$ for Li-Ion Batteries, *Chem. Mater*., 2013, **25**, 2319-2326.

[57] M. Gu, I. Belharouak, J. Zheng, H. Wu, J. Xiao, A. Genc, K. Amine, S. Thevuthasan, D. R. Baer, J. G. Zhang, N. D. Browning, J. Liu and C. Wang, Formation of the Spinel Phase in the Layered Composite Cathode Used in Li-Ion Batteries, *ACS Nano*, 2013, **7**, 760-767.

[58] A. Boulineau, L. Simonin, J. F. Colin, C. Bourbon and S. Patoux, First Evidence of Manganese-Nickel Segregation and Densification Upon Cycling in Li-Rich Layered Oxides for Lithium Batteries, *Nano Lett*., 2013, **13**, 3857-3863.

[59] J. Zheng, P. Xu, M. Gu, J. Xiao, N. D. Browning, P. Yan, C. Wang and J.-G. Zhang, Structural and Chemical Evolution of Li- and Mn-Rich Layered Cathode Material, *Chem. Mater.*, 2015, **27**, 1381-1390.

[60] P. Yan, A. Nie, J. Zheng, Y. Zhou, D. Lu, X. Zhang, R. Xu, I. Belharouak, X. Zu, J. Xiao, K. Amine, J. Liu, F. Gao, R. Shahbazian-Yassar, J. G. Zhang and C. M. Wang, Evolution of Lattice Structure and Chemical Composition of the Surface Reconstruction Layer in $Li_{1.2}Ni_{0.2}Mn_{0.6}O_2$ Cathode Material for Lithium Ion Batteries, *Nano Lett.*, 2015, **15**, 514-522.

[61] J. M. Tarascon, E. Wang, F. K. Shokoohi, W. R. Mckinnon and S. Colson, The Spinel Phase of $LiMn_2O_4$ as a Cathode in Secondary Lithium Cells, *J. Electrochem. Soc.*, 1991, **138**, 2859-2864.

[62] Y. Shao-Horn, S. A. Hackney, A. J. Kahaian, K. D. Kepler, E. Skinner, J. T. Vaughey and M. M. Thackeray, Structural Fatigue in Spinel Electrodes in $Li/Li_x[Mn_2]O_4$ Cells, *J. Power Sources*, 1999, **81**, 82, 496-499.

[63] K. Y. Chung and K. B. Kim, Investigation of Structural Fatigue in Spinel Electrodes Using in Situ Laser Probe Beam Deflection Technique, *J. Electrochem. Soc.*, 2002, **149**, A79-A85.

[64] K. Y. Chung, W.-S. Yoon, H. S. Lee, X.-Q. Yang, J. McBreen, B. H. Deng, X. Q. Wang, M. Yoshio, R. Wang, J. Gui and M. Okada, Comparative Studies between Oxygen-Deficient $LiMn_2O_4$ and Al-Doped $LiMn_2O_4$, *J. Power Sources*, 2005, **146**, 226-231.

[65] K. Y. Chung and K.-B. Kim, Investigations into Capacity Fading as a Result of a Jahn–Teller Distortion in 4V $LiMn_2O_4$ Thin Film Electrodes, *Electrochim. Acta*, 2004, **49**, 3327-3337.

[66] T. Eriksson, T. Gustafsson and J. O. Thomas, Surface Structure of $LiMn_2O_4$ Electrodes, *Electrochem. Solid St.*, 2002, **5**, A35.

[67] R. Alcántara, M. Jaraba, P. Lavela, J. L. Tirado, P. Biensan, A. de Guibert, C. Jordy and J. P. Peres, Structural and Electrochemical Study of New $LiNi_{0.5}Ti_xMn1._{5-x}O_4$ spinel Oxides for 5-V Cathode Materials, *Chem Mater.*, 2003, **15**, 2376-2382.

[68] J. H. Kim, S. T. Myung, C. S. Yoon, S. G. Kang and Y. K. Sun, Comparative Study of $LiNi_{0.5}Mn_{1.5}O_{4-\delta}$ and $LiNi_{0.5}Mn_{1.5}O_4$ cathodes Having Two Crystallographic Structures: Fd̄3m and P4$_3$32, *Chem. Mater.*, 2004, **16**, 906-914.

[69] J.-H. Kim, N. P. W. Pieczonka, Z. Li, Y. Wu, S. Harris and B. R. Powell, Understanding the Capacity Fading Mechanism in $LiNi_{0.5}Mn_{1.5}O_4$/Graphite Li-Ion Batteries, *Electrochim. Acta*, 2013, **90**, 556-562.

[70] P. V. Sushko, K. M. Rosso, J.-G. Zhang, J. Liu and M. L. Sushko, Oxygen Vacancies and Ordering of D-Levels Control Voltage Suppression in Oxide Cathodes: The Case of Spinel $LiNi_{0.5}Mn_{1.5}O_{4-\delta}$, *Adv. Funct. Mater.*, 2013, **23**, 5530-5535.

[71] R. Deshpande, Y. Qi and Y.-T. Cheng, Effects of Concentration-Dependent Elastic Modulus on Diffusion-Induced Stresses for Battery Applications, *J. Electrochem. Soc.*, 2010, **157**, A967.

[72] R. Deshpande, Y.-T. Cheng and M. W. Verbrugge, Modeling Diffusion-Induced Stress in Nanowire Electrode Structures, *J. Power Sources*, 2010, **195**, 5081-5088.

[73] K. Zhao, M. Pharr, J. J. Vlassak and Z. Suo, Fracture of Electrodes in Lithium-Ion Batteries Caused by Fast Charging, *J. Appl. Phys.*, 2010, **108**, 073517.

[74] W. H. Woodford, Y.-M. Chiang and W. C. Carter, "Electrochemical Shock" of Intercalation Electrodes: A Fracture Mechanics Analysis, *J. Electrochem. Soc.*, 2010, **157**, A1052.

[75] A. Ito, D. Li, Y. Sato, M. Arao, M. Watanabe, M. Hatano, H. Horie and Y. Ohsawa, Cyclic Deterioration and Its Improvement for Li-Rich Layered Cathode Material $Li[Ni_{0.17}Li_{0.}2Co_{0.07}Mn_{0.56}]O_2$, *J. Power Sources*, 2010, **195**, 567-573.

[76] J. Zheng, M. Gu, J. Xiao, P. Zuo, C. Wang and J. G. Zhang, Corrosion/Fragmentation of Layered Composite Cathode and Related Capacity/Voltage Fading During Cycling Process, *Nano Lett*., 2013, **13**, 3824-3830.

[77] D. J. Miller, C. Proff, J. G. Wen, D. P. Abraham and J. Bareño, Observation of Microstructural Evolution in Li Battery Cathode Oxide Particles by in Situ Electron Microscopy, *Adv. Energy Mater*., 2013, **3**, 1098-1103.

[78] J. B. Goodenough and Y. Kim, Challenges for Rechargeable Li Batteries, *Chem. Mater*., 2010, **22**, 587-603.

[79] K. Xu, Nonaqueous Liquid Electrolytes for Lithium-Based Rechargeable Batteries, *Chem. Rev*., 2004, **104**, 4303-4418.

[80] V. Aravindan, J. Gnanaraj, S. Madhavi and H. K. Liu, Lithium-Ion Conducting Electrolyte Salts for Lithium Batteries, *Chemistry*, 2011, **17**, 14326-14346.

[81] X. R. Zhang, R. Kostecki, T. J. Richardson, J. K. Pugh and P. N. Ross, Electrochemical and Infrared Studies of the Reduction of Organic Carbonates, *J. Electrochem. Soc*., 2001, **148**, A1341-A1345.

[82] M. Egashira, H. Takahashi, S. Okada and J. Yamaki, Measurement of the Electrochemical Oxidation of Organic Electrolytes Used in Lithium Batteries by Microelectrode, *J. Power Sources*, 2001, **92**, 267-271.

[83] S. Shi, P. Lu, Z. Liu, Y. Qi, L. G. Hector, Jr., H. Li and S. J. Harris, Direct Calculation of Li-Ion Transport in the Solid Electrolyte Interphase, *J. Am. Chem. Soc.*, 2012, **134**, 15476-15487.

[84] M. Winter, The Solid Electrolyte Interphase – the Most Important and the Least Understood Solid Electrolyte in Rechargeable Li Batteries, *Z. Phys. Chem*., 2009, **223**, 1395-1406.

[85] D. Aurbach, B. Markovsky, G. Salitra, E. Markevich, Y. Talyossef, M. Koltypin, L. Nazar, B. Ellis and D. Kovacheva, Review on Electrode–Electrolyte Solution Interactions, Related to Cathode Materials for Li-Ion Batteries, *J. Power Sources*, 2007, **165**, 491-499.

[86] K. L. Browning, L. Baggetto, R. R. Unocic, N. J. Dudney and G. M. Veith, Gas Evolution from Cathode Materials: A Pathway to Solvent Decomposition Concomitant to Sei Formation, *J. Power Sources*, 2013, **239**, 341-346.

[87] Y. Kim, Mechanism of Gas Evolution from the Cathode of Lithium-Ion Batteries at the Initial Stage of High-Temperature Storage, *J. Mater. Sci*., 2013, **48**, 8547-8551.

[88] D. Aurbach, Review of Selected Electrode–Solution Interactions Which Determine the Performance of Li and Li Ion Batteries, *J. Power Sources*, 2000, **89**, 206-218.

[89] P. Lu and S. J. Harris, Lithium Transport within the Solid Electrolyte Interphase, *Electrochem. Commun*., 2011, **13**, 1035-1037.

[90] P. Verma, P. Maire and P. Novák, A Review of the Features and Analyses of the Solid Electrolyte Interphase in Li-Ion Batteries, *Electrochim. Acta*, 2010, **55**, 6332-6341.

[91] Z. Zhang, L. Hu, H. Wu, W. Weng, M. Koh, P. C. Redfern, L. A. Curtiss and K. Amine, Fluorinated Electrolytes for 5 V Lithium-Ion Battery Chemistry, *Energy Environ. Sci*., 2013, **6**, 1806.

[92] J. B. Goodenough and Y. Kim, Challenges for Rechargeable Batteries, *J. Power Sources*, 2011, **196**, 6688-6694.

[93] D. D. MacNeil and J. R. Dahn, Can an Electrolyte for Lithium-Ion Batteries Be Too Stable?, *J. Electrochem. Soc*., 2003, **150**, A21.

[94] S. S. Zhang, A Review on Electrolyte Additives for Lithium-Ion Batteries, *J. Power Sources*, 2006, **162**, 1379-1394.

[95] M. Xu, N. Tsiouvaras, A. Garsuch, H. A. Gasteiger and B. L. Lucht, Generation of Cathode Passivation Films Via Oxidation of Lithium Bis(Oxalato) Borate on High Voltage Spinel (LiNi$_{0.5}$Mn$_{1.5}$O$_4$), *J. Phys. Chem. C*, 2014, **118**, 7363-7368.

[96] X.-G. Sun, C. Liao, L. Baggetto, B. Guo, R. R. Unocic, G. M. Veith and S. Dai, Bis(Fluoromalonato)Borate (BFMB) Anion Based Ionic Liquid as an Additive for Lithium-Ion Battery Electrolytes, *J. Mater. Chem. A*, 2014, **2**, 7606.

[97] H. Bouayad, Z. Wang, N. Dupré, R. Dedryvère, D. Foix, S. Franger, J. F. Martin, L. Boutafa, S. Patoux, D. Gonbeau and D. Guyomard, Improvement of Electrode/Electrolyte Interfaces in High-Voltage Spinel Lithium-Ion Batteries by Using Glutaric Anhydride as Electrolyte Additive, *J. Phys. Chem. C*, 2014, **118**, 4634-4648.

[98] T. Kubota, M. Ihara, S. Katayama, H. Nakai and J. Ichikawa, 1,1-Difluoro-1-Alkenes as New Electrolyte Additives for Lithium Ion Batteries, *J. Power Sources*, 2012, **207**, 141-149.

[99] A. von Cresce and K. Xu, Electrolyte Additive in Support of 5 V Li Ion Chemistry, *J. Electrochem. Soc.*, 2011, **158**, A337.

[100] Z. Chen and K. Amine, Bifunctional Electrolyte Additive for Lithium-Ion Batteries, *Electrochem. Commun.*, 2007, **9**, 703-707.

[101] Z. Chen, W. Q. Lu, J. Liu and K. Amine, LiPF$_6$/LiBOB Blend Salt Electrolyte for High-Power Lithium-Ion Batteries, *Electrochim. Acta*, 2006, **51**, 3322-3326.

[102] K. Abe, Y. Ushigoe, H. Yoshitake and M. Yoshio, Functional Electrolytes: Novel Type Additives for Cathode Materials, Providing High Cycleability Performance, *J. Power Sources*, 2006, **153**, 328-335.

[103] S. M. George, B. Yoon and A. A. Dameron, Surface Chemistry for Molecular Layer Deposition of Organic and Hybrid Organic-Inorganic Polymers, *Acc. Chem. Res*., 2009, **42**, 498-508.

[104] U. Heider, R. Oesten and M. Jungnitz, Challenge in Manufacturing Electrolyte Solutions for Lithium and Lithium Ion Batteries Quality Control and Minimizing Contamination Level, *J. Power Sources*, 1999, **81-82**, 119-122.

[105] T. Kawamura, S. Okada and J.-i. Yamaki, Decomposition Reaction of $LiPF_6$-Based Electrolytes for Lithium Ion Cells, *J. Power Sources*, 2006, **156**, 547-554.

[106] M. Hirayama, H. Ido, K. Kim, W. Cho, K. Tamura, J. Mizuki and R. Kanno, Dynamic Structural Changes at $LiMn_2O_4$/Electrolyte Interface During Lithium Battery Reaction, *J. Am. Chem. Soc.*, 2010, **132**, 15268-15276.

[107] W. Choi and A. Manthiram, Comparison of Metal Ion Dissolutions from Lithium Ion Battery Cathodes, *J. Electrochem. Soc.*, 2006, **153**, A1760.

[108] D. H. Jang, Dissolution of Spinel Oxides and Capacity Losses in 4 V Li∕$LiMn_2O_4$ Cells, *J. Electrochem. Soc.*, 1996, **143**, 2204.

[109] T. Aoshima, K. Okahara, C. Kiyohara and K. Shizuka, Mechanisms of Manganese Spinels Dissolution and Capacity Fade at High Temperature, *J. Power Sources*, 2001, **97-8**, 377-380.

[110] D. Kim, S. Park, O. B. Chae, J. H. Ryu, Y. U. Kim, R. Z. Yin and S. M. Oh, Re-Deposition of Manganese Species on Spinel $LiMn_2O_4$ Electrode after Mn Dissolution, *J. Electrochem. Soc.*, 2012, **159**, A193-A197.

[111] C. Zhan, J. Lu, A. Jeremy Kropf, T. Wu, A. N. Jansen, Y. K. Sun, X. Qiu and K. Amine, Mn(II) Deposition on Anodes and Its Effects on Capacity Fade in Spinel Lithium Manganate-Carbon Systems, *Nat. Commun.*, 2013, **4**, 2437.

[112] N. P. W. Pieczonka, Z. Y. Liu, P. Lu, K. L. Olson, J. Moote, B. R. Powell and J. H. Kim, Understanding Transition-Metal Dissolution Behavior in $LiNi_{0.5}Mn_{1.5}O_4$ High-Voltage Spinel for Lithium Ion Batteries, *J. Phys. Chem. C*, 2013, **117**, 15947-15957.

[113] M. S. Park, J. W. Lee, W. Choi, D. Im, S. G. Doo and K. S. Park, On the Surface Modifications of High-Voltage Oxide Cathodes for Lithium-Ion Batteries: New Insight and Significant Safety Improvement, *J. Mater. Chem*., 2010, **20**, 7208-7213.

[114] Y. S. Meng and M. E. Arroyo-de Dompablo, First Principles Computational Materials Design for Energy Storage Materials in Lithium Ion Batteries, *Energy Environ. Sci*., 2009, **2**, 589-609.

[115] J. Cho, Improvement of Structural Stability of $LiCoO_2$ Cathode During Electrochemical Cycling by Sol-Gel Coating of SnO_2, *Electrochem. Solid-State Lett*., 1999, **3**, 362.

[116] J. Cho, Y. J. Kim and B. Park, Novel $LiCoO_2$ cathode Material with Al_2O_3 Coating for a Li Ion Cell, *Chem. Mater*., 2000, **12**, 3788-3791.

[117] J. Cho, Y. J. Kim, T.-J. Kim and B. Park, Zero-Strain Intercalation Cathode for Rechargeable Li-Ion Cell, *Angew. Chem. Int. Ed*., 2001, **40**, 3367-3369.

[118] J. Cho, Y. J. Kim and B. Park, $LiCoO_2$ Cathode Material That Does Not Show a Phase Transition from Hexagonal to Monoclinic Phase, *J. Electrochem. Soc*., 2001, **148**, A1110.

[119] Z. Chen and J. R. Dahn, Effect of a ZrO_2 Coating on the Structure and Electrochemistry of $LiCoO_2$ When Cycled to 4.5 V, *Electrochem. Solid St*., 2002, **5**, A213.

[120] Z. Chen and J. R. Dahn, Studies of $LiCoO_2$ Coated with Metal Oxides, *Electrochem. Solid S*t., 2003, **6**, A221.

[121] J.-H. Shim, S. Lee and S. S. Park, Effects of MgO Coating on the Structural and Electrochemical Characteristics of $LiCoO_2$ as Cathode Materials for Lithium Ion Battery, *Chem. Mater.,* 2014, **26**, 2537-2543.

[122] Y. Cho, P. Oh and J. Cho, A New Type of Protective Surface Layer for High-Capacity Ni-Based Cathode Materials: Nanoscaled Surface Pillaring Layer, *Nano Lett*., 2013, **13**, 1145-1152.

[123] J. Lu, C. Zhan, T. Wu, J. Wen, Y. Lei, A. J. Kropf, H. Wu, D. J. Miller, J. W. Elam, Y. K. Sun, X. Qiu and K. Amine, Effectively Suppressing Dissolution of Manganese from Spinel Lithium Manganate Via a Nanoscale Surface-Doping Approach, *Nat. Commun.*, 2014, **5**, 5693.

[124] C. Kim, P. J. Phillips, L. Xu, A. Dong, R. Buonsanti, R. F. Klie and J. Cabana, Stabilization of Battery Electrode/Electrolyte Interfaces Employing Nanocrystals with Passivating Epitaxial Shells, *Chem. Mater.*, 2015, **27**, 394-399.

[125] R. J. Gummow, A. de Kock and M. M. Thackeray, Improved Capacity Retention in Rechargeable 4 V Lithium/Lithium-Manganese Oxide (Spinel) Cells, *Solid State Ionics*, 1994, **69**, 59-67.

[126] K. Y. Chung, C.-W. Ryu and K.-B. Kim, Onset Mechanism of Jahn-Teller Distortion in 4 V $LiMn_2O_4$ and Its Suppression by $LiM_{0.05}Mn_{0.95}O_4$ (M = Co, Ni) Coating, *J. Electrochem. Soc.*, 2005, **152**, A791.

[127] L. Xiong, Y. Xu, T. Tao, X. Du and J. Li, Double Roles of Aluminium Ion on Surface-Modified Spinel $LiMn_{1.97}Ti_{0.03}O_4$, *J. Mater. Chem.*, 2011, **21**, 4937.

[128] M.-S. Park, J.-W. Lee, W. Choi, D. Im, S.-G. Doo and K.-S. Park, On the Surface Modifications of High-Voltage Oxide Cathodes for Lithium-Ion Batteries: New Insight and Significant Safety Improvement, *J. Mater. Chem.*, 2010, **20**, 7208.

[129] W. Liu, P. Oh, X. Liu, S. Myeong, W. Cho and J. Cho, Countering Voltage Decay and Capacity Fading of Lithium-Rich Cathode Material at 60 °C by Hybrid Surface Protection Layers, *Adv. Energy Mater.*, 2015, **5**, n/a-n/a.

[130] R.-P. Qing, J.-L. Shi, D.-D. Xiao, X.-D. Zhang, Y.-X. Yin, Y.-B. Zhai, L. Gu and Y.-G. Guo, Enhancing the Kinetics of Li-Rich Cathode Materials through the Pinning Effects of Gradient Surface Na^+ Doping, *Adv. Energy Mater.*, 2015, n/a-n/a.

[131] L. Guo, N. Zhao, J. Li, C. He, C. Shi and E. Liu, Surface Double Phase Network Modified Lithium Rich Layered Oxides with Improved Rate Capability for Li-Ion Batteries, *ACS Appl. Mater. Interfaces*, 2015, **7**, 391-399.

[132] Q. Xia, X. Zhao, M. Xu, Z. Ding, J. Liu, L. Chen, D. G. Ivey and W. Wei, A Li-Rich Layered@Spinel@Carbon Heterostructured Cathode Material for High Capacity and High Rate Lithium-Ion Batteries Fabricated Via an in Situ Synchronous Carbonization-Reduction Method, *J. Mater. Chem. A*, 2015, **3**, 3995-4003.

[133] F. Wu, N. Li, Y. Su, H. Lu, L. Zhang, R. An, Z. Wang, L. Bao and S. Chen, Can Surface Modification Be More Effective to Enhance the Electrochemical Performance of Lithium Rich Materials?, *J. Mater. Chem.*, 2012, **22**, 1489.

[134] Y. K. Sun, M. J. Lee, C. S. Yoon, J. Hassoun, K. Amine and B. Scrosati, The Role of AlF_3 Coatings in Improving Electrochemical Cycling of Li-Enriched Nickel-Manganese Oxide Electrodes for Li-Ion Batteries, *Adv. Mater.*, 2012, **24**, 1192-1196.

[135] J. R. Croy, M. Balasubramanian, D. Kim, S.-H. Kang and M. M. Thackeray, Designing High-Capacity, Lithium-Ion Cathodes Using X-Ray Absorption Spectroscopy, *Chem. Mater.*, 2011, **23**, 5415-5424.

[136] G. Xu, J. Li, Q. Xue, X. Ren, G. Yan, X. Wang and F. Kang, Enhanced Oxygen Reducibility of $0.5Li_2MnO_3 \cdot 0.5LiNi_{1/3}Co_{1/3}Mn_{1/3}O_2$ Cathode Material with Mild Acid Treatment, *J. Power Sources*, 2014, **248**, 894-899.

[137] H. Z. Zhang, Q. Q. Qiao, G. R. Li, S. H. Ye and X. P. Gao, Surface Nitridation of Li-Rich Layered $Li(Li_{0.17}Ni_{0.25}Mn_{0.58})O_2$ Oxide as Cathode Material for Lithium-Ion Battery, *J. Mater. Chem.*, 2012, **22**, 13104.

[138] P. Yan, L. Xiao, J. Zheng, Y. Zhou, Y. He, X. Zu, S. X. Mao, J. Xiao, F. Gao, J.-G. Zhang and C.-M. Wang, Probing the Degradation Mechanism of Li_2MnO_3 Cathode for Li-Ion Batteries, *Chem. Mater.*, 2015, **27**, 975-982.

[139] J. Zhang, Z. Lei, J. Wang, Y. NuLi and J. Yang, Surface Modification of $Li_{1.2}Ni_{0.13}Mn_{0.54}Co_{0.13}O_2$ by Hydrazine Vapor as Cathode Material for Lithium-Ion Batteries, *ACS Appl. Mater. Interfaces*, 2015, **7**, 15821-15829.

[140] I. Bloom, L. Trahey, A. Abouimrane, I. Belharouak, X. Zhang, Q. Wu, W. Lu, D. P. Abraham, M. Bettge, J. W. Elam, X. Meng, A. K. Burrell, C. Ban, R. Tenent, J. Nanda and

N. Dudney, Effect of Interface Modifications on Voltage Fade in $0.5Li_2MnO_3 \cdot 0.5LiNi_{0.375}Co_{0.25}Mn_{0.375}O_2$ Cathode Materials, *J. Power Sources*, 2014, **249**, 509-514.

[141] J. Zheng, M. Gu, J. Xiao, B. J. Polzin, P. Yan, X. Chen, C. Wang and J.-G. Zhang, Functioning Mechanism of AlF_3 Coating on the Li- and Mn-Rich Cathode Materials, *Chem. Mater*., 2014, **26**, 6320-6327.

[142] P. Yan, J. Zheng, X. Zhang, R. Xu, K. Amine, J. Xiao, J.-G. Zhang and C.-M. Wang, Atomic to Nanoscale Investigation of Functionalities of an Al_2O_3 Coating Layer on a Cathode for Enhanced Battery Performance, *Chem. Mater*., 2016, **28**, 857-863.

[143] K. Araki, N. Taguchi, H. Sakaebe, K. Tatsumi and Z. Ogumi, Electrochemical Properties of $LiNi_{1/3}Co_{1/3}Mn_{1/3}O_2$ Cathode Material Modified by Coating with Al_2O_3 Nanoparticles, *J. Power Sources*, 2014, **269**, 236-243.

[144] S.-H. Lee, C. S. Yoon, K. Amine and Y.-K. Sun, Improvement of Long-Term Cycling Performance of $Li[Ni_{0.8}Co_{0.15}Al_{0.05}]O_2$ by AlF_3 Coating, *J. Power Sources*, 2013, **234**, 201-207.

[145] Y. Kim, G. M. Veith, J. Nanda, R. R. Unocic, M. Chi and N. J. Dudney, High Voltage Stability of $LiCoO_2$ Particles with a Nano-Scale Lipon Coating, *Electrochim. Acta*, 2011, **56**, 6573-6580.

[146] Y. Yang, X.-Z. Liao, Z.-F. Ma, B.-F. Wang, L. He and Y.-S. He, Superior High-Rate Cycling Performance of $LiFePO_4$/C-PPy Composite at 55°C, *Electrochem. Commun*., 2009, **11**, 1277-1280.

[147] C. Wang, H. Wu, Z. Chen, M. T. McDowell, Y. Cui and Z. Bao, Self-Healing Chemistry Enables the Stable Operation of Silicon Microparticle Anodes for High-Energy Lithium-Ion Batteries, *Nat. Chem*., 2013, **5**, 1042-1048.

[148] X. Li, A. Lushington, J. Liu, R. Li and X. Sun, Superior Stable Sulfur Cathodes of Li-S Batteries Enabled by Molecular Layer Deposition, *Chem. Commun*., 2014, **50**, 9757-9760.

[149] R. Guo, P. Shi, X. Cheng and L. Sun, Effect of ZnO Modification on the Performance of $LiNi_{0.5}Co_{0.25}Mn_{0.25}O_2$ Cathode Material, *Electrochim. Acta*, 2009, **54**, 5796-5803.

[150] Z. Wang, C. Wu, L. Liu, F. Wu, L. Chen and X. Huang, Electrochemical Evaluation and Structural Characterization of Commercial $LiCoO_2$ Surfaces Modified with Mgo for Lithium-Ion Batteries, *J. Electrochem. Soc.*, 2002, **149**, A466.

[151] K. W. Kim, S.-W. Lee, K.-S. Han, H. J. Chung and S. I. Woo, Characterization of Al-Doped Spinel $LiMn_2O_4$ Thin Film Cathode Electrodes Prepared by Liquid Source Misted Chemical Deposition (LSMCD) Technique, *Electrochim. Acta*, 2003, **48**, 4223-4231.

[152] J. S. Kim, C. S. Johnson, J. T. Vaughey, S. A. Hackney, K. A. Walz, W. A. Zeltner, M. A. Anderson and M. M. Thackeray, The Electrochemical Stability of Spinel Electrodes Coated with ZrO_2, Al_2O_3, and SiO_2 from Colloidal Suspensions, *J. Electrochem. Soc.*, 2004, **151**, A1755.

[153] Y. K. Sun, K. J. Hong, J. Prakash and K. Amine, Electrochemical Performance of Nano-Sized ZnO-coated $LiNi_{0.5}Mn_{1.5}O_4$ Spinel as 5 V Materials at Elevated Temperatures, *Electrochem. Commun.*, 2002, **4**, 344-348.

[154] Z. R. Zhang, H. S. Liu, Z. L. Gong and Y. Yang, Electrochemical Performance and Spectroscopic Characterization of TiO_2-Coated $LiNi_{0.8}Co_{0.2}O_2$ Cathode Materials, *J. Power Sources*, 2004, **129**, 101-106.

[155] S. B. Park, H. C. Shin, W.-G. Lee, W. I. Cho and H. Jang, Improvement of Capacity Fading Resistance of $LiMn_2O_4$ by Amphoteric Oxides, *J. Power Sources*, 2008, **180**, 597-601.

[156] Y. K. Sun, S. W. Cho, S. T. Myung, K. Amine and J. Prakash, Effect of AlF_3 Coating Amount on High Voltage Cycling Performance of $LiCoO_2$, *Electrochim. Acta*, 2007, **53**, 1013-1019.

[157] K. Yang, L.-Z. Fan, J. Guo and X. Qu, Significant Improvement of Electrochemical Properties of AlF_3-Coated $LiNi_{0.5}Co_{0.2}Mn_{0.3}O_2$ Cathode Materials, *Electrochim. Acta*, 2012, **63**, 363-368.

[158] Z. Yang, Q. Qiao and W. Yang, Improvement of Structural and Electrochemical Properties of Commercial $LiCoO_2$ by Coating with LaF_3, *Electrochim. Acta*, 2011, **56**, 4791-4796.

[159] K.-S. Lee, S.-T. Myung, D.-W. Kim and Y.-K. Sun, AlF_3-Coated $LiCoO_2$ and $Li[Ni_{1/3}Co_{1/3}Mn_{1/3}]O_2$ Blend Composite Cathode for Lithium Ion Batteries, *J. Power Sources*, 2011, **196**, 6974-6977.

[160] J. M. Zheng, Z. R. Zhang, X. B. Wu, Z. X. Dong, Z. Zhu and Y. Yang, The Effects of AlF3 Coating on the Performance of $Li[Li_{0.2}Mn_{0.54}Ni_{0.13}Co_{0.13}]O_2$ Positive Electrode Material for Lithium-Ion Battery, *J. Electrochem. Soc.*, 2008, **155**, A775.

[161] X. Li, J. Liu, M. N. Banis, A. Lushington, R. Li, M. Cai and X. Sun, Atomic Layer Deposition of Solid-State Electrolyte Coated Cathode Materials with Superior High-Voltage Cycling Behavior for Lithium Ion Battery Application, *Energy Environ. Sci.*, 2014, **7**, 768.

[162] J. Zhou, D. Hong, J. Wang, Y. Hu, X. Xie and H. Fang, Electronic Structure Variation of the Surface and Bulk of a $LiNi_{0.5}Mn_{1.5}O_4$ Cathode as a Function of State of Charge: X-Ray Absorption Spectroscopic Study, *Phys. Chem. Chem. Phys.*, 2014, **16**, 13838-13842.

[163] R. Kurian, K. Kunnus, P. Wernet, S. M. Butorin, P. Glatzel and F. M. de Groot, Intrinsic Deviations in Fluorescence Yield Detected X-Ray Absorption Spectroscopy: The Case of the Transition Metal L(2),(3) Edges, *J Phys: Condens. Matter.*, 2012, **24**, 452201.

[164] Z. Wu, S. Ji, J. Zheng, Z. Hu, S. Xiao, Y. Wei, Z. Zhuo, Y. Lin, W. Yang, K. Xu, K. Amine and F. Pan, Prelithiation Activates $Li(Ni_{0.5}Mn_{0.3}Co_{0.2})O_2$ for High Capacity and Excellent Cycling Stability, *Nano Lett.*, 2015, **15**, 5590-5596.

[165] B. Xiao, J. Liu, Q. Sun, B. Wang, M. N. Banis, D. Zhao, Z. Wang, R. Li, X. Cui, T.-K. Sham and X. Sun, Unravelling the Role of Electrochemically Active $FePO_4$ Coating by

Atomic Layer Deposition for Increased High-Voltage Stability of $LiNi_{0.5}Mn_{1.5}O_4$ Cathode Material, *Adv. Sci*., 2015, **2**, 1500022-1500027.

[166] G. Alva, C. Kim, T. Yi, J. B. Cook, L. Xu, G. M. Nolis and J. Cabana, Surface Chemistry Consequences of Mg-Based Coatings on $LiNi_{0.5}Mn_{1.5}O_4$ electrode Materials Upon Operation at High Voltage, *J. Phys. Chem. C*, 2014, **118**, 10596-10605.

[167] L. Dahéron, R. Dedryvère, H. Martinez, D. Flahaut, M. Ménétrier, C. Delmas and D. Gonbeau, Possible Explanation for the Efficiency of Al-Based Coatings on $LiCoO_2$: Surface Properties of $LiCo_{1-x}Al_xO_2$ Solid Solution, *Chem. Mater*., 2009, **21**, 5607-5616.

[168] A. Eftekhari, $LiMn_2O_4$ Electrode Prepared by Gold–Titanium Co-deposition with Improved Cyclability, *J. Power Sources*, 2004, **130**, 260-265.

[169] J. T. Son, K. S. Park, H. G. Kim and H. T. Chung, Surface-Modification of $LiMn_2O_4$ with a Silver-Metal Coating, *J. Power Sources*, 2004, **126**, 182-185.

[170] C. Liu, J. An, R. Guo, Y. Li and L. Liu, Enhanced Electrochemical Performance of $LiFePO_4/C$ Cathode Material Modified with Highly Conductive Tin, *J. Alloy. Compd*., 2013, **563**, 33-38.

[171] Y. S. Hu, Y. G. Guo, R. Dominko, M. Gaberscek, J. Jamnik and J. Maier, Improved Electrode Performance of Porous $LiFePO_4$ Using RuO_2 as an Oxidic Nanoscale Interconnect, *Adv. Mater.*, 2007, **19**, 1963-1966.

[172] Y. Q. Wang, L. Gu, Y. G. Guo, H. Li, X. Q. He, S. Tsukimoto, Y. Ikuhara and L. J. Wan, Rutile-TiO_2 Nanocoating for a High-Rate $Li_4Ti_5O_{12}$ Anode of a Lithium-Ion Battery, *J. Am. Chem. Soc*., 2012, **134**, 7874-7879.

[173] Y.-H. Huang, K.-S. Park and J. B. Goodenough, Improving Lithium Batteries by Tethering Carbon-Coated $LiFePO_4$ to Polypyrrole, *J. Electrochem. Soc*., 2006, **153**, A2282.

[174] Y.-H. Huang and J. B. Goodenough, High-Rate LiFePO$_4$ lithium Rechargeable Battery Promoted by Electrochemically Active Polymers, *Chem. Mater*., 2008, **20**, 7237-7241.

[175] A. Vadivel Murugan, T. Muraliganth and A. Manthiram, Rapid Microwave-Solvothermal Synthesis of Phospho-Olivine Nanorods and Their Coating with a Mixed Conducting Polymer for Lithium Ion Batteries, *Electrochem. Commun*., 2008, **10**, 903-906.

[176] M. C. Kim, S. H. Kim, V. Aravindan, W. S. Kim, S. Y. Lee and Y. S. Lee, Ultrathin Polyimide Coating for a Spinel LiNi$_{0.5}$Mn$_{1.5}$O$_4$ Cathode and Its Superior Lithium Storage Properties under Elevated Temperature Conditions, *J. Electrochem. Soc*., 2013, **160**, A1003-A1008.

[177] Y.-m. Bai, P. Qiu, Z.-l. Wen and S.-c. Han, Improvement of Electrochemical Performances of LiFePO$_4$ Cathode Materials by Coating of Polythiophene, *J. Alloy. Compd*., 2010, **508**, 1-4.

[178] J. Yang, J. Wang, Y. Tang, D. Wang, X. Li, Y. Hu, R. Li, G. Liang, T.-K. Sham and X. Sun, LiFePO$_4$–Graphene as a Superior Cathode Material for Rechargeable Lithium Batteries: Impact of Stacked Graphene and Unfolded Graphene, *Energy Environ. Sci*., 2013, **6**, 1521.

[179] J. Yang, J. Wang, D. Wang, X. Li, D. Geng, G. Liang, M. Gauthier, R. Li and X. Sun, 3D Porous LiFePO$_4$/Graphene Hybrid Cathodes with Enhanced Performance for Li-Ion Batteries, *J. Power Sources*, 2012, **208**, 340-344.

[180] J. Yang, J. Wang, X. Li, D. Wang, J. Liu, G. Liang, M. Gauthier, Y. Li, D. Geng, R. Li and X. Sun, Hierarchically Porous LiFePO$_4$/Nitrogen-Doped Carbon Nanotubes Composite as a Cathode for Lithium Ion Batteries, *J. Mater. Chem*., 2012, **22**, 7537.

[181] J. Yang, J. Wang, Y. Tang, D. Wang, B. Xiao, X. Li, R. Li, G. Liang, T.-K. Sham and X. Sun, In Situ Self-Catalyzed Formation of Core–Shell LiFePO$_4$@CNT Nanowires for High Rate Performance Lithium-Ion Batteries, *J. Mater. Chem. A*, 2013, **1**, 7306.

[182] H. K. Noh, H. S. Park, H. Y. Jeong, S. U. Lee and H. K. Song, Doubling the Capacity of Lithium Manganese Oxide Spinel by a Flexible Skinny Graphitic Layer, *Angew. Chem. Int. Ed.*, 2014, **53**, 5059-5063.

[183] H. Liu, C. Chen, C. Du, X. He, G. Yin, B. Song, P. Zuo, X. Cheng, Y. Ma and Y. Gao, Lithium-Rich $Li_{1.2}Ni_{0.13}Co_{0.13}Mn_{0.54}O_2$ oxide Coated by Li_3PO_4 and Carbon Nanocomposite Layers as High Performance Cathode Materials for Lithium Ion Batteries, *J. Mater. Chem. A*, 2015, **3**, 2634-2641.

[184] X. Miao, H. Ni, H. Zhang, C. Wang, J. Fang and G. Yang, Li_2ZrO_3-Coated $0.4Li_2MnO_3 \cdot 0.6LiNi_{1/3}Co_{1/3}Mn_{1/3}O_2$ for High Performance Cathode Material in Lithium-Ion Battery, *J. Power Sources*, 2014, **264**, 147-154.

[185] W. Choi, A. Benayard, J.-H. Park, J. Park, S.-G. Doo and J. Mun, Versatile Coating of Lithium Conductive Li_2TiF_6 on over-Lithiated Layered Oxide in Lithium-Ion Batteries, *Electrochim. Acta*, 2014, **117**, 492-497.

[186] F. Cheng, Y. Xin, Y. Huang, J. Chen, H. Zhou and X. Zhang, Enhanced Electrochemical Performances of 5 V Spinel $LiMn_{1.58}Ni_{0.42}O_4$ Cathode Materials by Coating with $LiAlO_2$, *J. Power Sources*, 2013, **239**, 181-188.

[187] Y. Kim, N. J. Dudney, M. Chi, S. K. Martha, J. Nanda, G. M. Veith and C. Liang, A Perspective on Coatings to Stabilize High-Voltage Cathodes: $LiMn_{1.5}Ni_{0.5}O_4$ with Sub-Nanometer LiPON Cycled with $LiPF_6$ Electrolyte, *J. Electrochem. Soc.*, 2013, **160**, A3113-A3125.

[188] H. G. Song, K.-S. Park and Y. J. Park, The Effects of $LaPO_4$ Coating on the Electrochemical Properties of $Li[Ni_{0.5}Co_{0.2}Mn_{0.3}]O_2$ Cathode Material, *Solid State Ionics*, 2012, **225**, 532-537.

[189] H. G. Song, J. Y. Kim, K. T. Kim and Y. J. Park, Enhanced Electrochemical Properties of $Li(Ni_{0.4}Co_{0.3}Mn_{0.3})O_2$ Cathode by Surface Modification Using Li_3PO_4-Based Materials, *J. Power Sources*, 2011, **196**, 6847-6855.

[190] A. Sakuda, A. Hayashi and M. Tatsumisago, Electrochemical Performance of All-Solid-State Lithium Secondary Batteries Improved by the Coating of Li_2O–TiO_2 Films on $LiCoO_2$ Electrode, *J. Power Sources*, 2010, **195**, 599-603.

[191] J.-M. Chen, Y.-D. Cho, C.-L. Hsiao and G. T.-K. Fey, Electrochemical Studies on $LiCoO_2$ Surface Coated with $Y_3Al_5O_{12}$ for Lithium-Ion Cells, *J. Power Sources*, 2009, **189**, 279-287.

[192] J. Chong, S. Xun, J. Zhang, X. Song, H. Xie, V. Battaglia and R. Wang, Li_3PO_4-Coated $LiMn_{1.5}Ni_{0.5}O_4$: A Stable High-Voltage Cathode Material for Lithium-Ion Batteries, *Chemistry*, 2014, **20**, 7479-7485.

[193] J. Wang and X. Sun, Understanding and Recent Development of Carbon Coating on $LiFePO_4$ Cathode Materials for Lithium-Ion Batteries, *Energy Environ. Sci.*, 2012, **5**, 5163.

[194] Y. Gao, Correlation between the Growth of the 3.3 V Discharge Plateau and Capacity Fading in $Li_{1+x}Mn_{2-x}O_4$ Materials, *Solid State Ionics*, 1996, **84**, 33-40.

[195] G. G. Amatucci, N. Pereira, T. Zheng and J. M. Tarascon, Failure Mechanism and Improvement of the Elevated Temperature Cycling of $LiMn_2O_4$ Compounds through the Use of the $LiAl_xMn_{2-x}O_{4-z}F_z$ Solid Solution, *J. Electrochem. Soc.*, 2001, **148**, A171.

[196] S. J. Shi, J. P. Tu, Y. J. Mai, Y. Q. Zhang, C. D. Gu and X. L. Wang, Effect of Carbon Coating on Electrochemical Performance of $Li_{1.048}Mn_{0.381}Ni_{0.286}Co_{0.286}O_2$ Cathode Material for Lithium-Ion Batteries, *Electrochim. Acta*, 2012, **63**, 112-117.

[197] S. Lee, Y. Cho, H. K. Song, K. T. Lee and J. Cho, Carbon-Coated Single-Crystal $LiMn_2O_4$ Nanoparticle Clusters as Cathode Material for High-Energy and High-Power Lithium-Ion Batteries, *Angew. Chem. Int. Ed.*, 2012, **51**, 8748-8752.

[198] J. Liu, Q. Wang, B. Reeja-Jayan and A. Manthiram, Carbon-Coated High Capacity Layered $Li[Li_{0.2}Mn_{0.54}Ni_{0.13}Co_{0.13}]O_2$ Cathodes, *Electrochem. Commun.*, 2010, **12**, 750-753.

[199] J. Liu and A. Manthiram, Understanding the Improvement in the Electrochemical Properties of Surface Modified 5 V LiMn$_{1.42}$Ni$_{0.42}$Co$_{0.16}$O$_4$ Spinel Cathodes in Lithium-Ion Cells, *Chem. Mater.*, 2009, **21**, 1695-1707.

[200] Y. Huang, J. Chen, J. Ni, H. Zhou and X. Zhang, A Modified ZrO$_2$-Coating Process to Improve Electrochemical Performance of Li(Ni$_{1/3}$Co$_{1/3}$Mn$_{1/3}$)O$_2$, *J. Power Sources*, 2009, **188**, 538-545.

[201] A. T. Appapillai, A. N. Mansour, J. Cho and Y. Shao-Horn, Microstructure of LiCoO$_2$ with and without "AlPO$_4$" Nanoparticle Coating: Combined Stem and XPS Studies, *Chem. Mater.*, 2007, 19, 5748-5757.

[202] H. X. Dang, Y.-M. Lin, K. C. Klavetter, T. H. Cell, A. Heller and C. B. Mullins, Lithium Insertion/Deinsertion Characteristics of Nanostructured Amorphous Tantalum Oxide Thin Films, *Chem. Electro. Chem.*, 2014, **1**, 158-164.

[203] M. Wilkening, V. Epp, A. Feldhoff and P. Heitjans, Tuning the Li Diffusivity of Poor Ionic Conductors by Mechanical Treatment: High Li Conductivity of Strongly Defective LiTaO$_3$ Nanoparticles, *J. Phys. Chem. C*, 2008, **112**, 9291-9300.

[204] J. Janek, M. Martin and K. D. Becker, The Electronic Structure and Ionic Diffusion of Nanoscale LiTiO$_2$ Anatase, *Phys. Chem. Chem. Phys.*, 2009, **11**, 3010.

[205] M. Aykol, S. Kirklin and C. Wolverton, Thermodynamic Aspects of Cathode Coatings for Lithium-Ion Batteries, *Adv. Energy Mater.*, 2014, **4**, 1400690.

[206] M. D. Groner, J. W. Elam, F. H. Fabreguette and S. M. George, Electrical Characterization of Thin Al$_2$O$_3$ Films Grown by Atomic Layer Deposition on Silicon and Various Metal Substrates, *Thin Solid Films*, 2002, **413**, 186-197.

[207] J. W. Elam, M. D. Groner and S. M. George, Viscous Flow Reactor with Quartz Crystal Microbalance for Thin Film Growth by Atomic Layer Deposition, *Rev. Sci. Instrum.*, 2002, **73**, 2981.

[208] A. W. Ott, J. W. Klaus, J. M. Johnson and S. M. George, Al_2O_3 Thin Film Growth on Si(100) Using Binary Reaction Sequence Chemistry, *Thin Solid Films*, 1997, **292**, 135-144.

[209] A. C. Dillon, A. W. Ott, J. D. Way and S. M. George, Surface Chemistry of Al_2O_3 Deposition Using $Al(CH_3)_3$ and H_2O in a Binary Reaction Sequence, *Surf. Sci.*, 1995, **322**, 230-242.

[210] J.-F. Fan, K. Sugioka and K. Toyoda, Low-Temperature Growth of Thin Films of Al_2O_3 by Sequential Surface Chemical Reaction of Trimethylaluminum and H_2O_2, *Jpn. J. Appl. Phys.*, 1991, **30**, L1139-L1141.

[211] B. H. Lee, B. Yoon, A. I. Abdulagatov, R. A. Hall and S. M. George, Growth and Properties of Hybrid Organic-Inorganic Metalcone Films Using Molecular Layer Deposition Techniques, *Adv. Funct. Mater.*, 2013, **23**, 532-546.

[212] B. H. Lee, B. Yoon, V. R. Anderson and S. M. George, Alucone Alloys with Tunable Properties Using Alucone Molecular Layer Deposition and Al_2O_3 Atomic Layer Deposition, *J. Phys. Chem. C*, 2012, **116**, 3250-3257.

[213] B. Yoon, B. H. Lee and S. M. George, Highly Conductive and Transparent Hybrid Organic–Inorganic Zincone Thin Films Using Atomic and Molecular Layer Deposition, *J. Phys. Chem. C*, 2012, **116**, 24784-24791.

[214] S. E. Atanasov, M. D. Losego, B. Gong, E. Sachet, J. P. Maria, P. S. Williams and G. N. Parsons, Highly Conductive and Conformal Poly(3,4-Ethylenedioxythiophene) (PEDOT) Thin Films Via Oxidative Molecular Layer Deposition, *Chem. Mater.*, 2014, **26**, 3471-3478.

[215] A. I. Abdulagatov, K. E. Terauds, J. J. Travis, A. S. Cavanagh, R. Raj and S. M. George, Pyrolysis of Titanicone Molecular Layer Deposition Films as Precursors for Conducting TiO_2/Carbon Composite Films, *J. Phys. Chem. C*, 2013, **117**, 17442-17450.

[216] K. Chang, D. Geng, X. Li, J. Yang, Y. Tang, M. Cai, R. Li and X. Sun, Ultrathin MoS$_2$/Nitrogen-Doped Graphene Nanosheets with Highly Reversible Lithium Storage, *Adv. Engery Mater.*, 2013, **3**, 839-844.

[217] J. Yang, J. Wang, Y. Tang, D. Wang, X. Li, Y. Hu, R. Li, G. Liang, T.-K. Sham and X. Sun, LiFePO$_4$/Graphene as a Superior Cathode Material for Rechargeable Lithium Batteries: Impact of Stacked Graphene and Unfolded Graphene, *Energy Environ. Sci.*, 2013, **6**, 1521-1528.

[218] D. Wang, J. Yang, X. Li, D. Geng, R. Li, M. Cai, T.-K. Sham and X. Sun, Layer by Layer Assembly of Sandwiched Graphene/SnO$_2$ Nanowire/Carbon Nanostructures with Ultrahigh Lithium Ion Storage Properties, *Energy Environ. Sci.*, 2013, **6**, 2900-2906.

[219] Y. Hu, X. Li, J. Wang, R. Li and X. Sun, Free Standing Graphene-Carbon Nanotube Hybrid Papers Used as Current Collector and Binder Free Anodes for Lithium Ion Batteries, *J. Power Sources*, 2013, **237**, 41-46.

[220] X. Li, Y. Hu, J. Liu, A. Lushington, R. Li and X. Sun, Structurally Tailored Graphene Nanosheets as Lithium Ion Battery Anodes: An Insight to Yield Exceptionally High Lithium Storage Performance, *Nanoscale*, 2013, **5**, 12607-12615.

[221] C. Uthaisar, V. Barone and J. E. Peralta, Lithium Adsorption on Zigzag Graphene Nanoribbons, *J. Appl. Phys.*, 2009, **106**, 113715-113720.

[222] C. Uthaisar and V. Barone, Edge Effects on the Characteristics of Li Diffusion in Graphene, *Nano Lett.*, 2010, **10**, 2838-2842.

[223] C. K. Chan, H. Peng, G. Liu, K. McIlwrath, X. F. Zhang, R. A. Huggins and Y. Cui, High-Performance Lithium Battery Anodes Using Silicon Nanowires, *Nat. Nanotechnol.*, 2008, **3**, 31-35.

[224] Y. Liu, H. Zheng, X. H. Liu, S. Huang, T. Zhu, J. Wang, A. Kushima, N. S. Hudak, X. Huang, S. Zhang, S. X. Mao, X. Qian, J. Li and J. Y. Huang, Lithiation-Induced Embrittlement of Multiwalled Carbon Nanotubes, *ACS Nano*, 2011, **5**, 7245-7253.

[225] X. H. Liu, J. W. Wang, Y. Liu, H. Zheng, A. Kushima, S. Huang, T. Zhu, S. X. Mao, J. Li, S. Zhang, W. Lu, J. M. Tour and J. Y. Huang, In Situ Transmission Electron Microscopy of Electrochemical Lithiation, Delithiation and Deformation of Individual Graphene Nanoribbons, *Carbon*, 2012, **50**, 3836-3844.

[226] T. Bhardwaj, A. Antic, B. Pavan, V. Barone and B. D. Fahlman, Enhanced Electrochemical Lithium Storage by Graphene Nanoribbons, *J. Am. Chem. Soc.*, 2010, **132**, 36, 12556-12558.

Chapter 2

2 Experimental Methods and Characterization Techniques

2.1 Experimental methods

2.1.1 Synthesis of LiNi$_{0.5}$Mn$_{1.5}$O$_4$ Nanoparticles via Hydrothermal Route

LiNi$_{0.5}$Mn$_{1.5}$O$_4$ was synthesized via a two-step hydrothermal-assisted carbonate precipitation method followed by thermal treatment. The oven for hydrothermal process is shown in Figure 2.1. Ni(NO$_3$)$_2$ ·6H$_2$O (99%, Aldrich, 0.005 mol) and Mn(NO$_3$)$_2$ ·4H$_2$O (99%, Aldrich, 0.015 mol) were dissolved in de-ionized water (5 mL). Na$_2$CO$_3$ (99%, Aldrich, 1mol/ L, 20 mL) solution was subsequently added to the above mixture of nickel nitrate and manganese nitrate under vigorous stirring at a rate of 0.25 mL/min, then the green precipitation was transferred to a 40 mL Teflon-lined autoclave and kept at 140 ^{o}C for 10 h. After cooling down to room temperature (RT), the precipitation was filtered and washed with water several times and dried at 80 ^{o}C overnight. The carbonate powders were annealed at 450 ^{o}C for 4 h in air so as to obtain corresponding oxides. Thereafter, the oxide powders were mixed with Li$_2$CO$_3$ (99%, Sigma-Aldrich, 0.00503 mol) in 1:1 water and ethanol mixture (10 mL) and left to dry under stirring at 60 ^{o}C. The mixed precursor was subsequently sintered in O$_2$ at 800 ^{o}C for 6 h and then cooled to 600 ^{o}C in 3 h. After keeping at 600 ^{o}C for another 6 h, the furnace was cooled to RT at a cooling rate of 1 ^{o}C min^{-1} to obtain the final LNMO.

Figure 2.1 (a) Oven used for hydrothermal synthesis; (b) Teflon-lined autoclaves for hydrothermal synthesis

2.1.2 Atomic Layer Deposition of Amorphous FePO₄ onto LiNi₀.₅Mn₁.₅O₄ Nanoparticles

Amorphous $FePO_4$ was deposited at 300 ºC by using ferrocene ($FeCp_2$, $FeC_{10}H_{10}$, 98% Sigma Aldrich), ozone (O_3, 9.8 wt.%), trimethyl phosphate (TMPO, $(CH_3)_3PO_4$, 97% STREM Chemicals) and distilled water (H_2O) as precursors in a Savannah 100 ALD system (Cambridge Nanotech, USA) shown in Figure 2.2. The source temperature for $FeCp_2$ and TMPO was 130 and 75 °C respectively. O_3 and H_2O were fed into the reactor chamber at RT. The deposition of $FePO_4$ was achieved by following a sequence of $FeCp_2$ pulse (1 s) – purge (10 s) – O_3 pulse (1 s) – purge (10 s) – TMPO pulse (2 s) – purge (10 s) – purge (10 s) – H_2O pulse (1 s) – purge (10 s). Nitrogen gas (99.999 %) was used as a carrying and purging gas at a flow rate of 20 sccm. The above processes were repeated for several (n) times to grow n cycles of $FePO_4$ onto LNMO powders, denoted as LNMO-n (bare LNMO when n=0).

Figure 2.2 Savannah 100 ALD system (Cambridge Nanotech, USA)

2.1.3   Atomic Layer Deposition of TiO_2 onto $LiNi_{0.5}Mn_{1.5}O_4$ Followed by Heat-treatment

The LNMO powders were purchased from Daejung Energy Materials Co. Ltd., South Korea. Atomic layer deposition (ALD) of TiO_2 was performed at 150 °C in a Savannah 100 ALD system (Ultratech/Cambridge Nanotech) by using titanium(IV) isopropoxide (TTIP, $Ti[OCH(CH_3)_2]_4$, Sigma Aldrich, 97%), and distilled water (H_2O) as precursors. The source temperature for TTIP was 85 °C, while H_2O was kept at room temperature (RT). N_2 gas was used as the carrying and purging gas, at a flow rate of 20 sccm. Each ALD cycle of TiO_2 was executed with the following steps: (1) 1s pulse of TTIP; (2) 3s extended exposure of TTIP in the reaction chamber; (3) 20s purge of residual TTIP and any by-products; (4) 1s pulse of H_2O; (5) 3s extended exposure of H_2O in the reaction chamber; (6) 20s purge of residual H_2O and any by-products. LNMO powders were dispersed on a stainless steel tray, and then put at the center of the ALD reaction chamber. TiO_2 was deposited on LNMO powders by repeating the above ALD cycles, the corresponding samples are denoted as $LNMO/nTiO_2$ where n stands for the ALD cycle

number. 5, 25 and 50 cycle numbers were chosen as the performance study parameter. In order to better characterize the consequence of the TiO_2 reaction with LNMO upon post-treatment, 250 ALD cycle number was used for Ti related structural studies. In the post-treatment process, the $LNMO/nTiO_2$ samples were annealed in air under 810 ^{o}C for 6h followed by slow cooling to RT within 10h. The treated samples were named as $LNMO/nTiO_2A$. All of the bare LNMO samples studied were treated under the same conditions as well to make the results comparable.

2.1.4 Synthesis of $Li_{1.2}Mn_{0.54}Co_{0.13}Ni_{0.13}O_2$ Nano-particles via A Modified Pechini Method

HENMC was synthesized using a modified Pechini's method. CH_3COOLi, $Mn(CH_3COO)_2$, $Ni(CH_3COO)_2$ and $Co(CH_3COO)_2$ (Sigma Aldrich, 99%) were mixed with a stoichiometric ratio of 1.25:0.54:0.13:0.13 in 50 mL deionized water under strong stirring. 5.72 g citric acid was dissolved in 25 mL ethanol (Sigma Aldrich, 99.99%). 2.5 g polyethylene glycol (PEG) (Alfa Aesar, 25,000, 99%) was dissolved in 25 mL ethanol separately. The citric acid solution was initially added into the metal acetates solution slowly under stirring for 10 min. Then, the mixture was subsequently added into the PEG solution slowly, pink precipitations were observed during the reaction. Subsequently, 2 mL ethylene glycol (Sigma Aldrich, 99%) and 2 mL HNO_3 (Sigma Aldrich, 70%) were added dropwise until the pink precipitate is dissolved. The final clear solution was dried at 120 ^{o}C to obtain a colloidal gel. This gel was pre-calcined at 400°C for 4 h in air to remove the organic components. After cooling down, the final product was collected and ground to obtain fine particles. The final HENMC was obtained by calcining the fine particles under 850 ^{o}C for 20 h in air.

Figure 2.3 Process of the modified Pechini's method synthesis of $Li_{1.2}Mn_{0.54}Co_{0.13}Ni_{0.13}O_2$

2.1.5 Atomic Layer Deposition of $AlPO_4$ onto $Li_{1.2}Mn_{0.54}Co_{0.13}Ni_{0.13}O_2$ Nano-particles

$AlPO_4$ was deposited on HENMC powders at 250 °C in a Savannah 100 ALD system (Ultratech/Cambridge Nanotech, USA) using trimethylaluminum (TMA, $(CH_3)_3Al$, 98% STREM Chemicals), trimethyl phosphate (TMPO, $(CH_3)_3PO_4$, 97% STREM Chemicals), and distilled water (H_2O) as precursors. The source temperature for TMPO was 75 °C, while TMA and H_2O was kept at RT. $AlPO_y$ was deposited in an exposure model by the sequence of TMA pulse (0.5 s) – exposure (1 s) - purge (10 s) – H_2O pulse (1 s) – exposure (1 s) – purge (15 s) – TMPO pulse (2 s) – exposure (1 s) – purge (10 s) – H_2O pulse (1 s) – exposure (1s) – purge (10 s). Nitrogen gas (99.999 %) was used as a carrying gas at a

flow rate of 20 sccm. AlPO$_4$ films were directly deposited on HENMC powders by repeating the above ALD cycles. In this study, 5, 10 and 20 ALD cycles were selected to control the coating thickness, each of the sample was denoted as HENMC-n AP, where n stands for the ALD cycle number and AP stands for AlPO$_4$. Al$_2$O$_3$ coating with 20 ALD cycles on the HENMC was carried out under 150 °C with TMA and water as the precursors in the same ALD system.

2.1.6 Synthesis of Graphene Nanoribbons via the Chemical Unzipping of Carbon Nanotubes

In a typical unzipping process, 100mg of MWCNTs (Shenzhen Nanotech., China) were dispersed in 3.4mL of sulfuric acid (H$_2$SO$_4$)(98%, Aldrich) via strong ultrasonic agitation for 30min. The viscous solution was then placed in an ice bath under vigorous stirring and 75mg sodium nitrate (NaNO$_3$) (99.9%, Aldrich) was subsequently added. After dissolving, 450mg potassium permanganate (KMnO$_4$) (99.9%, Aldrich) was slowly and carefully added into the viscous mixture. After a desired reaction time(specifically 5min, 30min, 1h, 2.5h, 5h, 10h and 20h), 20mL of 5% sulfuric acid solution was poured into the liquid and left to cool down. Next, 2mL hydrogen peroxide (H$_2$O$_2$) (30%, Aldrich) was added into the solution in a drop-wide manner until no more bubbles were released. After half an hour, the dark solution was centrifuged and thoroughly washed with 5% nitric acid three times and de-ionized water five times, then filtered and dried in an oven at 90 °C for 12h under vacuum. The as prepared GNRs contained high amounts of oxygen-containing functional groups (denoted as GONRs-oxidizing time) and are therefore annealed at 900°C in Ar for reduction (denoted as GNRs-oxidizing time). To make the results more reliable, a reference was created with pristine CNTs which were treated in 30% nitric acid solution for 6 hours to remove the catalysts.

2.2 Characterization Techniques

2.2.1 Physical Characterization Methods

The structure, chemical environment, functional groups and morphology information of the materials are characterized using a variety of methods including SEM, EDX,

(HR)TEM, STEM-HAADF, EELS, XAS, RAMAN, FTIR, BET, XPS and XRD. This section briefly reviews these techniques.

The morphology of the materials was observed using SEM (Hitachi S-4800) shown in Figure 2.4. The SEM was operated at 5 kV in order to observe morphologies of samples. The SEM was coupled with an EDX which gives important information of elemental distribution.

Figure 2.4 Field emission scanning electron microscope (Hitachi S-4800)

TEM is another important tool to study the detailed morphological information, in comparison with SEM, TEM obtains much higher magnifications through the transmission of electrons. A JEOL 2010F high-resolution TEM located at the Canadian Centre for Electron Microscopy (CCEM) at McMaster University was used to observe the fine structures of the samples. The study of atomic level structure of materials by HAADF-STEM was conducted on an aberration-corrcted FEI Titan Cubed 80-300 kV microscope equipped with a Gatan Image Filter Quantum-965 spectrometer operated at 200 kV. The

photos of these equipment are shown in Figure 2.5. The sample particles were cut into slices using a Zeiss NVision 40 dual beam focused ion beam. EELS spectra were recorded with a 0.25 eV/channel dispersion of the spectrometer in order to understand the chemical environment of the elements.
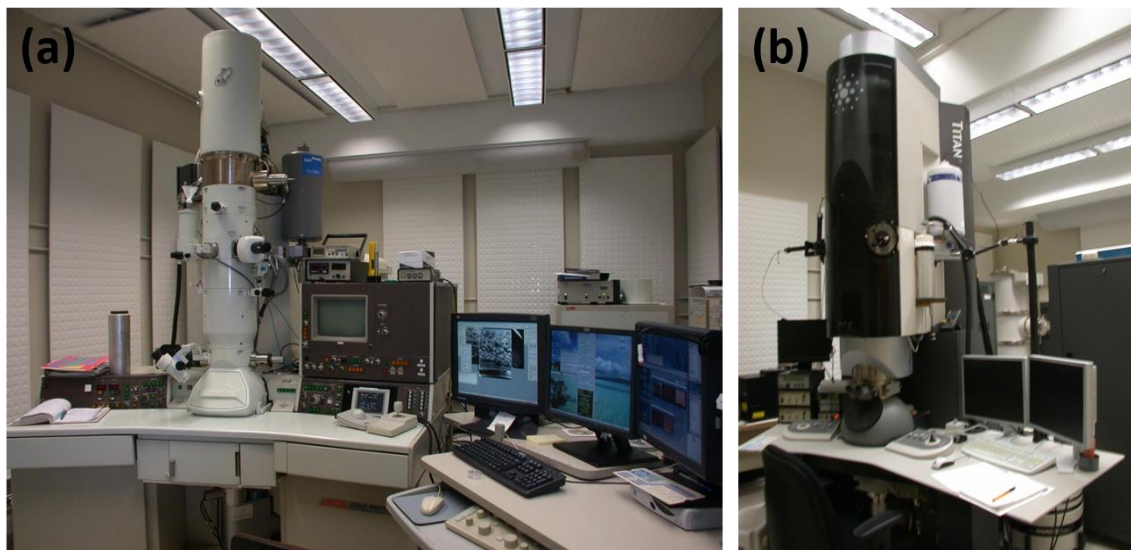
Figure 2.5 (a) JEOL 2010F high-resolution TEM and (b) FEI Titan Cubed 80-300 kV microscope equipped with a Gatan Image Filter Quantum-965 spectrometer

XRD is an exceptionally important tool in studying the structure of materials, especially crystalline ones. The XRD pattern of the samples were collected on a Bruker D8 Advance Diffractometer using Cu Kα radiation at 40 kV and 40 mA. The photo of the XRD is shown in Figure 2.6.

XPS is a tool to understand the chemical information of elements through detecting the number of escaped electrons from the surface of samples at certain binding energies. In this thesis, a PHI Quantera XPS Scanning Microprobe (Physical Electronics, Chanhassen, MN) with a monochromated Al K_a (1486.6 eV) source located at the Global R&D Center of General Motors was used for the XPS analysis. The device is shown in Figure 2.7.

Figure 2.6 Bruker D8 Advance Diffractometer XRD

Figure 2.7 A PHI Quantera XPS Scanning Microprobe

Surface area of the graphene-based studies was collected on a Micromeritics Brunaner-Emmett-Teller (BET) surface area analyzer (Figure 2.8). The BET surface area is analyzed based on the adsorption and de-sorption of gas molecules onto the specimen, in this study, helium gas was used.

Figure 2.8 A Micromeritics Brunauer-Emmett-Teller surface area analyzer

The thermal properties of the materials were determined by a Thermo Instruments SDT Q600 Thermogravimetric (TGA)/Differential Scanning Calorimetry (DSC) analyzer as shown in Figure 2.9.

Figure 2.9 A Thermo Instruments SDT Q600 Thermogravimetric/Differential Scanning Calorimetry analyzer

Raman spectroscopy is a technique to understand the vibration of chemical bonds through detecting the inelastic scattering of incident monochromatic light. The interaction of the light and the molecular vibrations results in light energy shift and provides fingerprint information of the molecules. In this thesis, a HORIBA Scientific LabRAM HR Raman spectrometer system with a 532.4 nm laser and optical microscope at room temperature was used for the Raman analysis, it is shown in Figure 2.10.
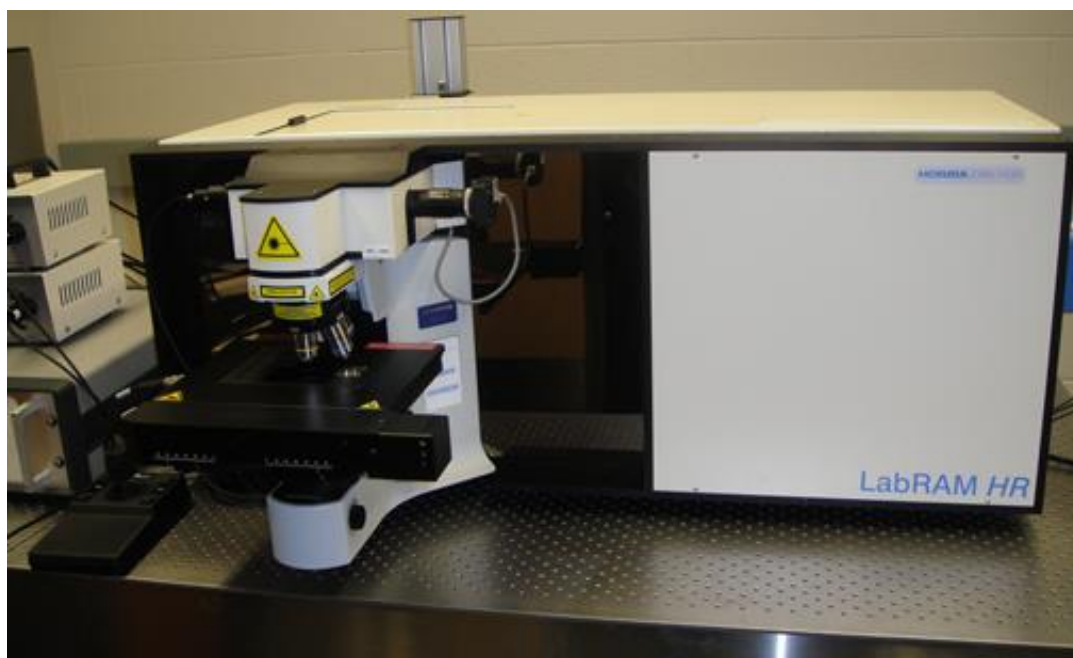
Figure 2.10 HORIBA Scientific LabRAM HR Raman spectrometer system

Another essential characterization technique used in this thesis is the synchrotron radiation technique. Synchrotron radiation is highly collimated X-ray, owing to the broad spectrum, high flux, high brilliance and high stability, it has been widely used in the analysis of material structural properties. The main method involving synchrotron technique in this thesis is the X-ray absorption spectroscopy (XAS). The XAS is a technique used to study the local structure of materials through the absorption of X-ray by atoms, where the core-level electrons are ejected and a core-hole was left. The energy of this absorption is determined by the electronic structures of atoms in the samples studied, therefore it

provides very detailed information of the local structures of materials. Figure 2.11 shows the beamlines available at the Canadian Light Source and a photo of it.
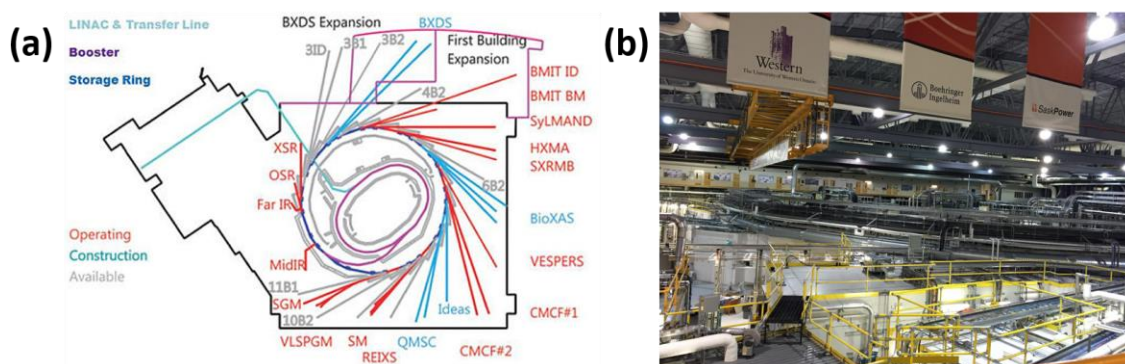
Figure 2.11 (a) Beamlines at the Canadian Light Source; (b) a photo of the Canadian Light Source

2.2.2   Electrochemical Measurements

The electrochemical performance of the electrode materials are tested using CR2032 coin cells. The cathode materials are mixed with acetylene black and polyvinylidene fluoride (PVDF) in a ratio of 80:10:10 using N-methyl-2-pyrrolidone (NMP) as the solvent. The as-prepared slurry was casted on Al foil and dried overnight. For graphene nanoribbons study, the material was mixed with PVDF only with a mass ratio of 90:10, the slurry was casted on Cu foil. The electrodes were thereafter cut into round shapes with a diameter of 13 mm. The electrolyte used in this thesis depends on the materials studied. For high-voltage $LiNi_{0.5}Mn_{1.5}O_4$, the electrolyte used was 1M $LiPF_6$ dissolved in ethylene carbonate (EC) and dimethyl carbonate (DMC) with a volume ratio of 1:1 and a polyethylene Celgard K2045 as the separator. For other materials, the electrolyte used was 1M LiPF6 dissolved in ethylene carbonate (EC) and diethyl carbonate (DEC) a volume ratio of 1:1 and a polypropylene Celgard 2400 as the separator. Lithium metal chips are used as the counter electrode in the coin cells. The coin cells are assembled in a highly pure argon-filled glove box with the oxygen and water level being controlled below 1 ppm. The photo of the glove box is shown in Figure 2.12. The coin cells are electrochemically cycled on an Arbin BT2000 Battery Testing Station according to required protocols. A photo of the Arbin BT2000 is shown in Figure 2.13.

Figure 2.12 Photo of the glovebox used for cell assembly
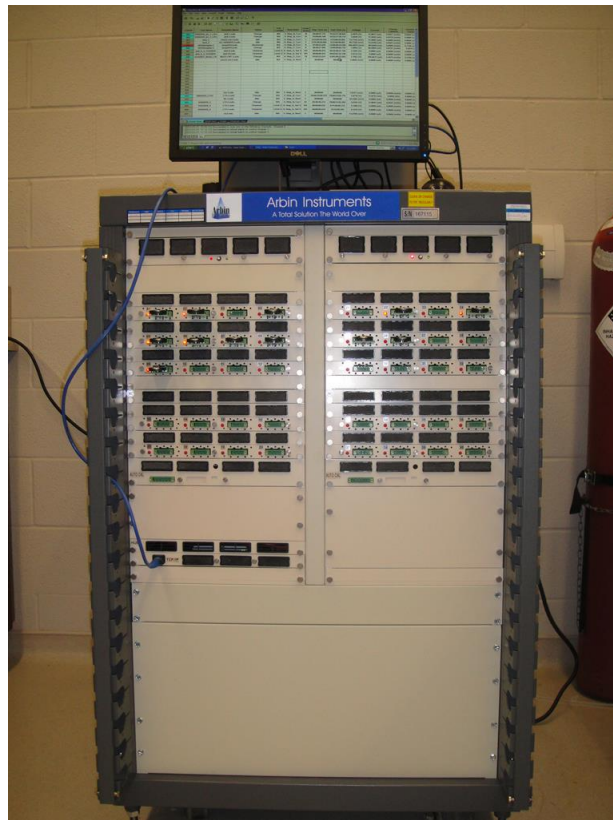
Figure 2.13 Arbin BT2000 battery testing station

Cyclic voltammetry (CV) is an important method to study the electrochemical properties of batteries. The CV curves reflect the potentials where certain reactions such as the lithium insertion/desertion or the redox reactions take place. AC electrochemical impedance spectroscopy (EIS) is another important tool to understand the impedance within a cell. Figure 2.14 shows a multichannel potentiostat 3/Z (VMP3), on which both the CV and EIS measurements are conducted. The CV tests are conducted at a scan rate of 0.1 mVs^{-1} over a voltage range of 0.1 V-3.0 V for graphene nanoribbons studies, 3.5 V-5.0 V for LiNi$_{0.5}$Mn$_{1.5}$O$_4$ studies and 2.0 V-4.6 V for high energy NMC studies.
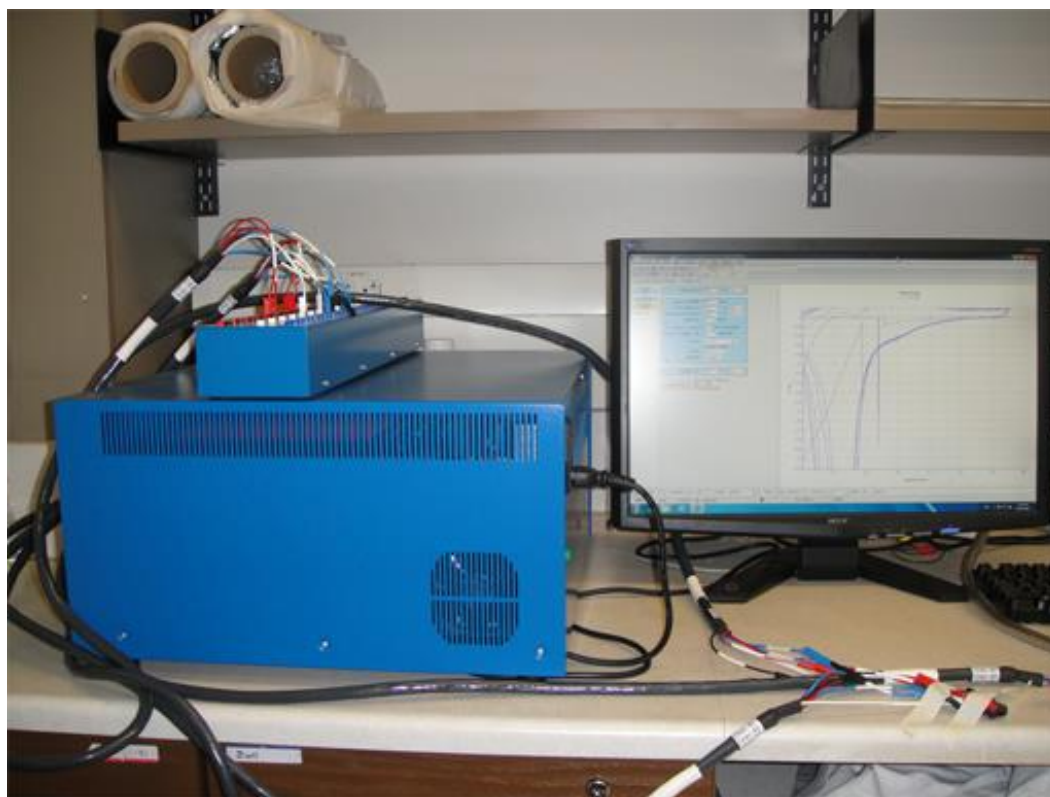
Figure 2.14 A multichannel potentiostat 3/Z (VMP3)

Chapter 3

3 Unravelling the Role of Electrochemically Active FePO$_4$ Coating by Atomic Layer Deposition for Increased High-voltage Stability of LiNi$_{0.5}$Mn$_{1.5}$O$_4$ Cathode Material

Coating is an essential technique to increase the performance of high voltage cathode materials. Atomic layer deposition (ALD) is an emerging technique which allows for ultra-thin and conformal coating. The seamless coating help combat the electrolyte attack to the cathode materials, but prohibits the electrons and lithium ions from fast transportation. Electrochemically active coating is a possible solution to this problem, since the transportation of lithium ions within electrochemically active material matrix can be significantly increased due to abundant diffusion sites.

For the first time, we have adopted ultra-thin layer of electrochemically active FePO$_4$ synthesized by atomic layer deposition (ALD) to coat the surface of LNMO. The precisely controlled growth and uniformity contributed to over 20% higher capacity retention. This advancement can be applied to other electrode materials for LIBs and broadens the application of ALD in energy storage devices.

3.1 Introduction

$LiNi_{0.5}Mn_{1.5}O_4$ (LNMO) is a derivative of the commercialized spinel $LiMn_2O_4$ with Ni^{2+} and Mn^{4+} occupying two octahedral sites of 4a and 16d respectively, aimed at suppressing the intrinsic deficiencies such as the Jahn-Teller distortion of Mn^{3+} with the same theoretical capacity as $LiMn_2O_4$ (148 mAh/g).[1] In addition, since the working mechanism of $LiNi_{0.5}Mn_{1.5}O_4$ is mainly the redox couple of Ni^{2+}/Ni^{4+}, the theoretical operating voltage reaches 4.7 V (vs Li/Li^+) compared with 4.0 V for $LiMn_2O_4$ (vs Li/Li^+).[1, 2] Such a high voltage inevitably involves the aggressive oxidation of the electrolyte and the dissolution of transition metals, which cause the capacity fading.[3-5] In order to overcome these drawbacks, various strategies such as surface modifications using metal oxides and phosphates like Al_2O_3,[6] ZnO,[7] MgO,[8] ZrO_2,[9] Li_3PO_4[10] and $AlPO_4$[11, 12] et al. have been studied. Most of these coatings are, however, still restricted to the poor conductivity and/or non-uniformity, the former deficiency results in poor kinetics during charging/discharging, while the latter does not provide full protection of electrode from HF attacking.[13] Atomic layer deposition (ALD) is a novel coating technique capable of depositing highly conformal and uniform layers with well controlled thickness onto substrates.[14, 15] ALD derived ultrathin Al_2O_3 and $LiAlO_2$ coatings have been used as protection layers on LNMO recently,[16-18] it was found that the coating layer containing lithium favours faster lithium ion diffusion. Most of the non-lithium-containing coating materials, however, increase the cycling stability at the expense of sacrificing capacity.[19, 20] For example, in their attempt to protect the surface of LNMO by ALD derived Al_2O_3, Jung et al.[17] used only 2 ALD cycles of Al_2O_3 growth on LNMO powders, the capacity dropped by 10 mAhg^{-1} immediately, when the ALD cycle number was increased to 10, almost no capacity was delivered. In regard of this, the majority of previous studies deposited ALD layer onto the surface of electrode sheet instead of material powders so as to avoid the insulation between binder, conductive carbon and cathode materials since the coating did not break the contact between them.[21-23] This will certainly restrict the application of ALD because some ALD materials require high deposition temperature, under which the binder may be unstable. Therefore, searching for a coating material with good electron and lithium diffusion, whilst protecting the cathode material uniformly under high voltage is exceptionally important. Despite the versatile design of ALD, coating

materials that are electrochemically active, i.e. capable of accommodating Li^+ within the voltage range of cathode materials are scarcely reported. With the electrochemically active advantage, direct coating onto powders becomes realistic.

Amorphous $FePO_4$ has been widely studied as cathode materials for both lithium-ion batteries (LIBs) and sodium ion batteries (SIBs).[24-26] Its highly amorphous structure does not generate any lattice stress and therefore provides continuous lithium insertion channels and considerable electronic conductivity.[27-29] In our recent work, we successfully synthesized $FePO_4$ via ALD process,[30],[31] which has also been demonstrated by Fjellvåg et al. to deliver a discharge capacity of above 140 mAh/g.[32]

In this study, we propose the novel ALD derived ultrathin amorphous $FePO_4$ coating as a lithium ions reservoir during cycling, which may act as both a lithium diffusion facilitator and an electrochemical buffer layer between the electrolyte and LNMO by keeping the interface electrochemical potential above the electrolyte's highest occupied molecular orbital (HOMO), at which the electrolyte starts to get oxidized.[33, 34] Further, we provide detailed discussion about the role of electrochemically active $FePO_4$ coating based on X-ray absorption spectroscopy analysis.

3.2   Experimental

3.2.1   Materials Synthesis

$LiNi_{0.5}Mn_{1.5}O_4$ was synthesized via a two-step hydrothermal-assisted carbonate precipitation method followed by thermal treatment. $Ni(NO_3)_2 \cdot 6H_2O$ (99%, Aldrich, 0.005 mol) and $Mn(NO_3)_2 \cdot 4H_2O$ (99%, Aldrich, 0.015 mol) were dissolved in de-ionized water (5 mL). Na_2CO_3 (99%, Aldrich, 1mol/ L, 20 mL) solution was subsequently added to the above mixture of nickel nitrate and manganese nitrate under vigorous stirring at a rate of 0.25 mL/min, then the green precipitation was transferred to a 40 mL Teflon-lined autoclave and kept at 140 ^oC for 10 h. After cooling down to room temperature (RT), the precipitation was filtered and washed with water several times and dried at 80 oC overnight. The carbonate powders were annealed at 450 ^oC for 4 h in air so as to obtain corresponding oxides. Thereafter, the oxide powders were mixed with Li_2CO_3 (99%, Sigma-Aldrich, 0.00503 mol) in 1:1 water and ethanol mixture (10 mL) and left to dry

under stirring at 60 ºC. The mixed precursor was subsequently sintered in O_2 at 800 ºC for 6 h and then cooled to 600 ºC in 3 h. After keeping at 600 ºC for another 6 h, the furnace was cooled to RT at a cooling rate of 1 ºC min^{-1} to obtain the final LNMO.

3.2.2   Atomic Layer Deposition of Amorphous FePO₄

Amorphous $FePO_4$ was deposited at 300 ºC by using ferrocene ($FeCp_2$, $FeC_{10}H_{10}$, 98% Sigma Aldrich), ozone (O_3, 9.8 wt.%), trimethyl phosphate (TMPO, $(CH_3)_3PO_4$, 97% STREM Chemicals) and distilled water (H_2O) as precursors in a Savannah 100 ALD system (Cambridge Nanotech, USA). The source temperature for $FeCp_2$ and TMPO was 130 and 75 °C respectively. O_3 and H_2O were fed into the reactor chamber at RT. The deposition of $FePO_4$ was achieved by following a sequence of $FeCp_2$ pulse (1 s) – purge (10 s) – O_3 pulse (1 s) – purge (10 s) – TMPO pulse (2 s) – purge (10 s) – purge (10 s) – H2O pulse (1 s) – purge (10 s). Nitrogen gas (99.999 %) was used as a carrying and purging gas at a flow rate of 20 sccm. The above processes were repeated for several (n) times to grow n cycles of $FePO_4$ onto LNMO powders, denoted as LNMO-n (bare LNMO when n=0).

3.2.3   Characterization Methods

The morphology of LNMO-n was characterized by a Hitachi S-4800 field emission scanning electronic microscopy (FESEM) equipped with an energy dispersive X-ray spectroscope (EDS), Hitachi H-7000 transmission electron microscope (TEM), and a high-resolution transmission electron microscope (HRTEM, JEOL 2010F). Raman scattering (RS) spectra was collected from a HORIBA Scientific LabRAM HR Raman spectrometer system with a 532.4 nm laser and optical microscope at RT. X-ray diffraction (XRD) patterns were collected on a Bruker D8 Advance Diffractometer using Cu $K_α$ radiation at 40 kV and 40 mA. The X-ray absorption near edge structure (XANES) measurements at total electron yield (TEY) and fluorescence yield (FYI) modes of Mn $L_{2,3}$-edge and Fe L_3-edge were performed at the Canadian Light Source (CLS) on the high resolution Spherical Grating Monochromter (SGM) beamline using a 45 mm planar undulator and three gratings with a photon energy range of 250 to 2000 eV, LNMO-20 was chosen as the target sample. The P 2p X-ray photoemission spectroscopy (XPS) was performed at the variable

line spacing plane grating monochromator (VLS PGM) beamline at 200 eV photon energy with a total resolution of 100 meV.

3.2.4   Electrochemical Measurements

The LNMO-n powders were mixed with poly(vinylidene fluoride) binder and acetylene black in a ratio of 8:1:1 in N-methyl-pyrrolidione (NMP) solvent to form slurries. The slurries were subsequently casted onto aluminum foils as the current collector and dried at 80 °C under vacuum overnight. The electrode was assembled in an Ar-filled glovebox with moisture and oxygen concentrations below 1 ppm. A CR-2032 type coin cell using a lithium metal as the counter electrode and Celgard K2045 as the separator was utilized. The electrolyte was composed of 1 M $LiPF_6$ salt dissolved in ethylene carbonate (EC) and dimethyl carbonate (DMC) in a 1:1 volume ratio (BASF Corp.). Cyclic voltammetry (CV) was performed on a multichannel potentiostat 3/Z (VMP3), with a scanning rate of 0.1 mVS^{-1} and a potential range of 3.5−5.0 V (vs Li/Li^+) at RT. Electrochemical impedance spectroscopy (EIS) was also performed on the versatile multichannel potentiostat 3/Z (VMP3) by holding the cells at 5.0 V. Galvanostatical charge/discharge was performed on Arbin BT2000 at various current densities between 3.5 V and 5.0 V (vs Li/Li^+), the stability performance test was done under 0.5 C, which is 73.5 mA/g.

3.3   Results and Discussion

3.3.1   Morphology and Structural Characterization

The preparation process of LNMO powders is described in the supporting information. The phases of LNMO were identified via XRD as shown in Figure SI 3.1. The peaks can be well indexed to the cubic spinel phase of LNMO (JCPDS No. 35-0782). ALD processes did not change the structures of the spinel LNMO. Due to the ultrathin and amorphous nature of the $FePO_4$, no peaks of $FePO_4$ can be observed in the XRD pattern. Figure 3.1a shows the Raman spectra of the samples, the sharp peak at 160 cm^{-1} indicates that the LNMO is ordered $P4_332$ phase, with subtle oxygen deficiencies. The peaks at 400 and 490 cm^{-1} are related to the Ni^{2+}-O stretching and the peak at 630 cm^{-1} corresponds to the Mn-O stretching of MnO_6 octahedra.[35] It can be seen that with higher ALD $FePO_4$ cycles, both the Ni-O and Mn-O vibrations show blue shifts, this is due to the strains induced by

the surface coating, which was also observed in TiO_2 coating.[36] In order to observe the P content evolution with ALD cycles, the P 2p spectra were collected based on synchrotron XPS technique. It can be observed that these P atoms on the LNMO surface show increasing concentration when the ALD cycle increases, indicating that the amount of surface coating layer correlates to the number of ALD cycles. It is worthwhile to note that the P 2p XPS spectra of LNMO-40 did not show linear intensity increase, this is probably due to the surface saturation in synchrotron XPS.
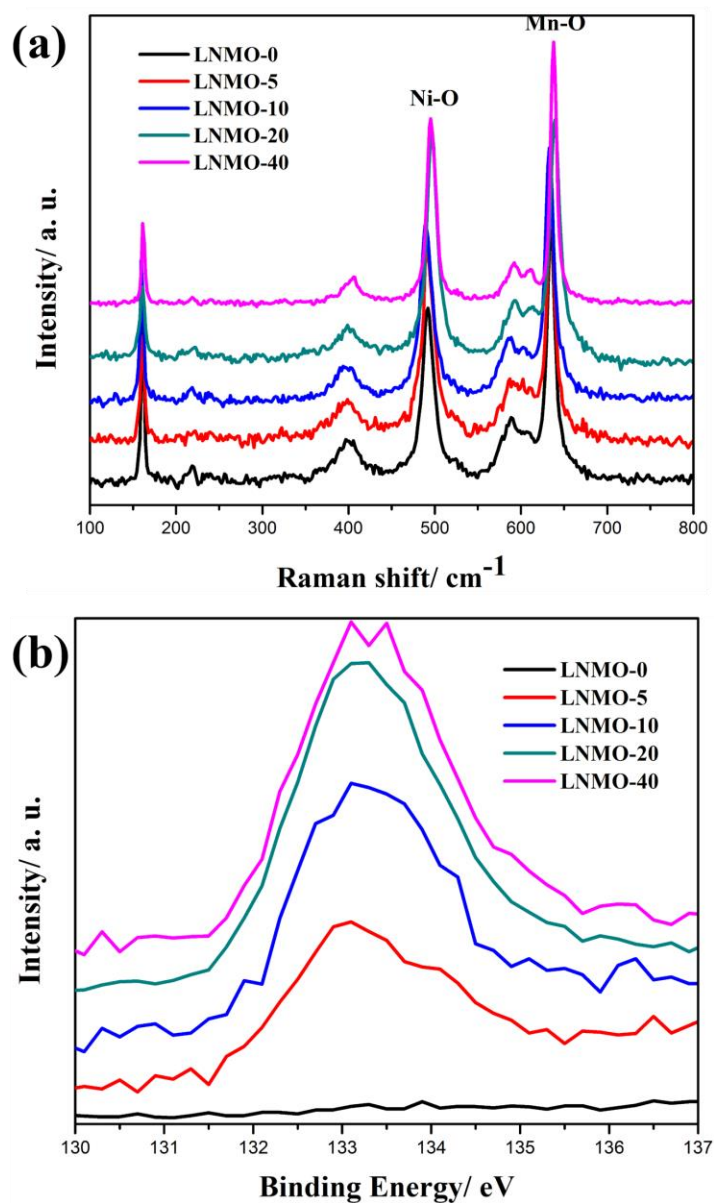
Figure 3.1 (a) Raman spectra and (b) P 2p XPS spectra of LNMO-n

The morphologies of the LNMO-n samples were characterized by FESEM (Figure 3.2a and b show LNMO-0 and LNMO-20 the rest are shown in Figure SI 3.3) and HRTEM (Figure 3.2c). It can be seen that the pristine LNMO shows sharp crystallized edges, the surface becomes rougher when the ALD cycle number increases, Fig. SI 3.2 shows the EDX mapping of Fe, P, Mn, Ni, O, it can be seen that the Fe and P are uniformly coated onto the surface of LNMO. The HRTEM images in Fig. 3.2c reveal that the ultrathin surface coating is about 2 nm in thickness, the growth rate is consistent with our previous findings when depositing $FePO_4$ onto Si wafer.[31] The lattice fringe with basal distance of 0.24 nm is consistent with the (222) spacing of cubic phase LNMO. The inset electron diffraction pattern of LNMO-20 indexes a typical spinel lattice structure.
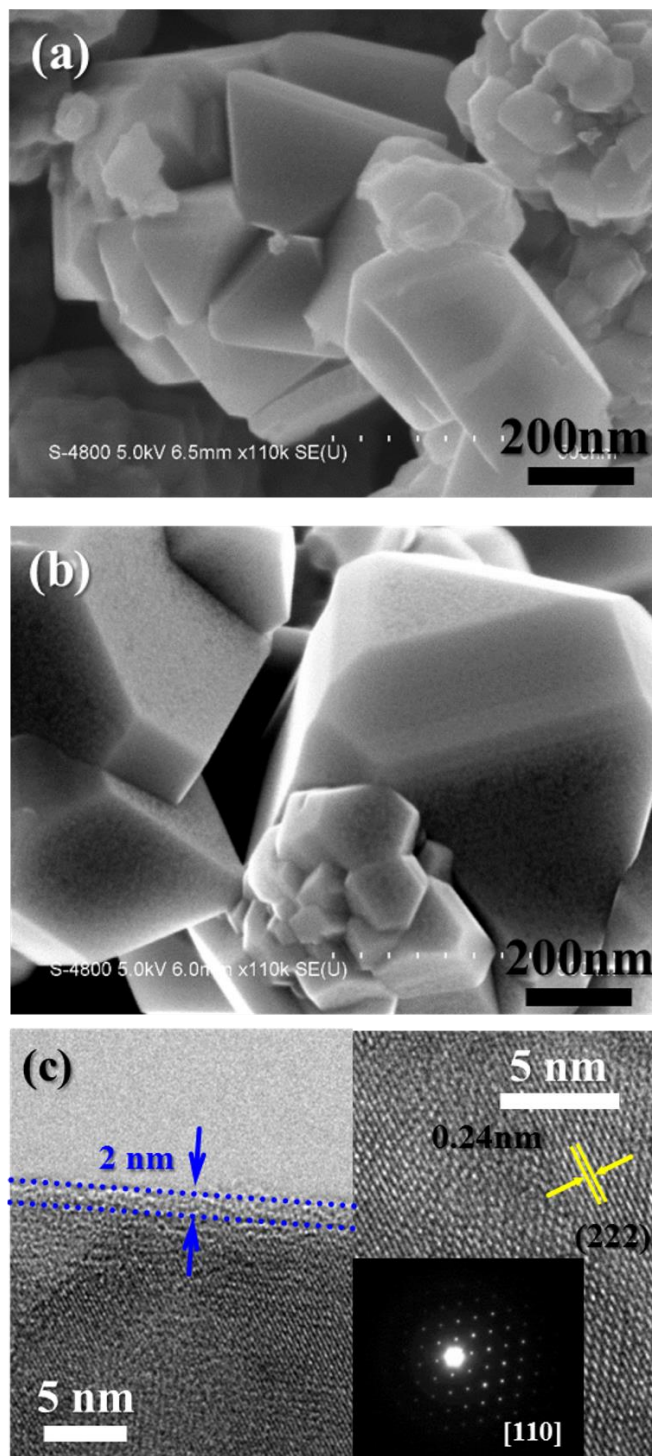
Figure 3.2 FESEM images of (a) LNMO-0 and (b) LNMO-20; (c) HRTEM images of LNMO-20 (inset: Electron diffraction patterns of the LNMO-20 along the [110] zone axis)

3.3.2   Electrochemical Characterization

Figure 3.3a shows the first charge/discharge curves of LNMO-n samples, the plateaus at around 4.7 V correspond to the reduction of Ni^{4+} to Ni^{3+} and N^{i2+}, another small plateau at around 4.0 V corresponds to the reduction of Mn^{4+} to Mn^{3+}. The bare LNMO delivers highest first discharge capacity of 113 $mAhg^{-1}$ among all the samples. Nevertheless, the LNMO-0 sample decays rapidly during cycling, and the capacity retention of LNMO-0 is only 79.89% after 100 cycles, as shown in Figure SI 3.5, Figure 3.3b and Table 1. In contrast, the ALD $FePO_4$ coated samples display increasing capacity retention with more ALD cycle numbers, indicating the protective nature of the $FePO_4$ layer.[37] It is worthwhile to mention that despite the LNMO-40 sample shows greatly enhanced stability, the capacity is lower, possibly due to the relatively lower electrical conductivity of $FePO_4$. Rate capability test (Fig. 3.3c) also reveals that LNMO-10 presents the highest capacity under high current densities, e.g. more than 80 $mAhg^{-1}$ at 5C, while the LNMO-0 sample drops to approximately 0 $mAhg^{-1}$. The Coulombic efficiencies of the samples are shown in Figure SI 3.5, it can be seen that the Coulombic efficiency increases with the ALD cycle number, reavealing that the presence of $FePO_4$ has helped to suppress the electrolyte decomposition.

Cyclic voltammetry (CV) measurements were carried out on the LNMO-n samples with normalized active material loading and electrolyte amount (Fig. 3.3d). Three redox couples can be observed in the CV profiles. The weak and broad pair at around 4.0 V corresponds to the Mn^{3+}/ Mn^{4+}, indicating that the LNMO is mostly in the phase of $P4_332$,[35] in accordance with the Raman spectra. Two pairs of intense redox couples at 4.6-4.9 V are related to the $Ni^{2+}/ Ni^{3+}/ Ni^{4+}$, which are the main sources of capacity. CV curves enlarged at 4.9 V- 5.0 V (Fig. SI 3.7) show that the bare LNMO has much higher resident current value at the cutting voltage of 5.0 V than other samples, implying that the electrolyte oxidation in bare sample is more severe than coated samples. The lower area of the LNMO/40 $FePO_4$ sample is also in accordance with the lower capacity. Table 1 summarizes the potential positions of the redox peaks. The redox peak potentials varied from 0.140 and 0.143 V for LNMO-0 to 0.082 and 0.084 V for LNMO-40 $FePO_4$, suggesting that $FePO_4$ coatings alleviates the polarization of the LNMO materials.

Table 3.1 Potentials of the oxidation/reduction peaks of the first CV scan, the capacity retentions and R$_s$ after 100 charge/discharge cycles

LNMO-n	Ni^{2+}/Ni^{3+} (V)	Ni^{3+}/Ni^{2+} (V)	ΔV (V)	Ni^{3+}/Ni^{4+} (V)	Ni^{4+}/Ni^{3+} (V)	ΔV (V)	Capacity retention (%)	R$_s$ (Ω)
n = 0	4.777	4.637	0.140	4.825	4.682	0.143	79.89	173.1
n = 5	4.776	4.663	0.113	4.808	4.704	0.104	88.94	102.1
n = 10	4.760	4.651	0.109	4.805	4.693	0.112	91.96	91.7
n = 20	4.765	4.654	0.111	4.808	4.698	0.110	93.98	62.6
n = 40	4.750	4.668	0.082	4.794	4.710	0.084	100.00	57.9
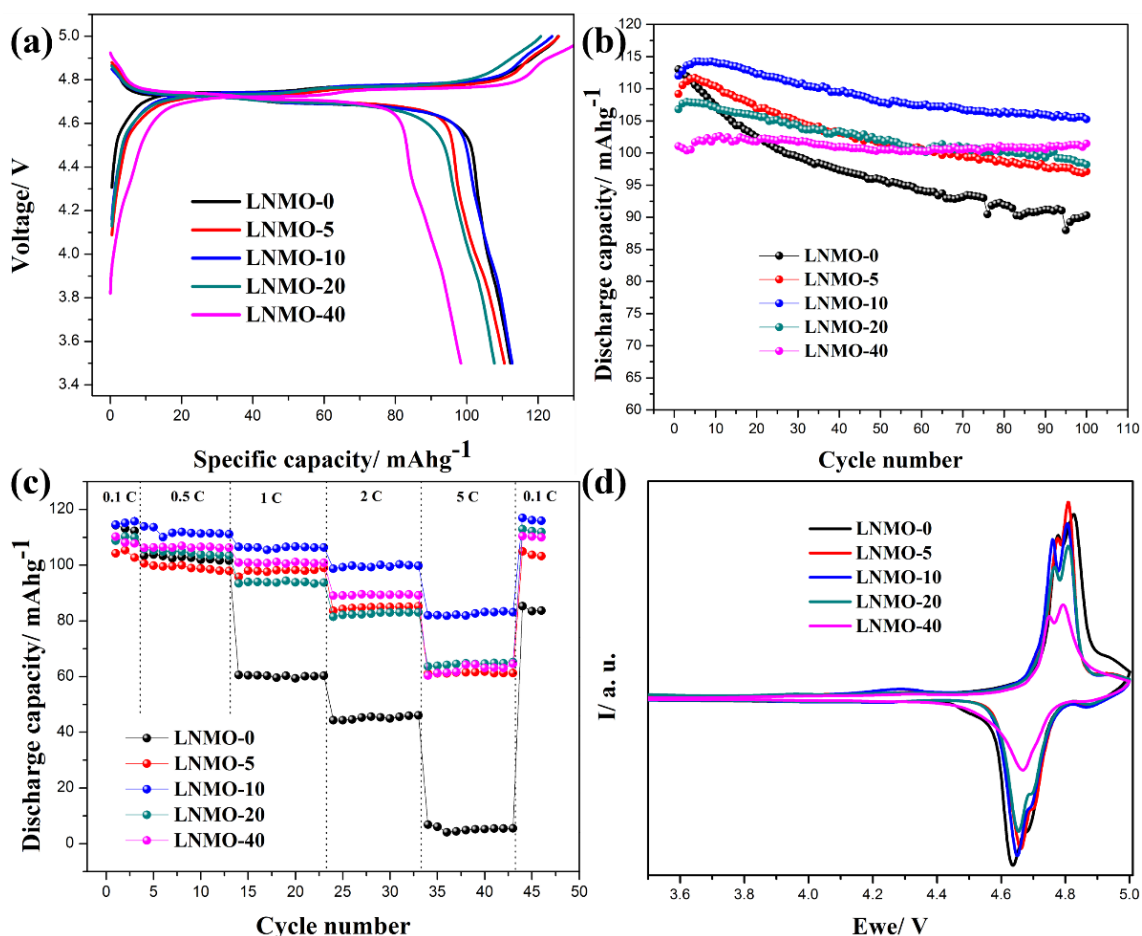
Figure 3.3 (a) First charge/discharge curves; (b) Cycling stability under 0.5C; (c) Rate capabilities; (d) Cyclic voltammetry of the LNMO-n samples

In the effort to understand the formation of solid electrolyte interphase (SEI) on the surface of the electrodes, AC electrochemical impedance spectra (EIS) were conducted on each LNMO-n sample after cycling for 100 times and subsequently charged to 5.0 V as shown in Fig. 3.4a. It can be seen that the LNMO-0 sample shows only one semi-circle whereas those with $FePO_4$ coatings show two semi-circles in the range of high and medium frequencies. A possible equivalent circuit is proposed to illustrate the impedance behaviours on the surface as shown in Fig. 3.4b. R_Ω stands for the Ohmic electrolyte resistance. The semicircle at high frequency is suggested to be a resistor Rs and a constant phase element CPEs, which are related to the migration of Li^+ through the surface film, in this case, it reflects the resistance of SEI. Another semicircle at medium frequency is

related to the charge transfer reaction composed of R_{ct} and another CPE, together with the finite length Warburg impedance.[38] The values of the R_s are presented in Table 3.1, it can be found that without any $FePO_4$ coating, the R_s for LNMO-0 is 173.1 Ω, however, the existence of $FePO_4$ coating layer helped to decrease the R_s values dramatically, which vary monotonically with the number of ALD cycles, to only 57.9 Ω for the LNMO-40 sample. The drop of R_s clearly reveals the less formation of insulating SEI, which is a result of electrolyte decomposition, therefore $FePO_4$ is effective towards suppressing the electrolyte decomposition.
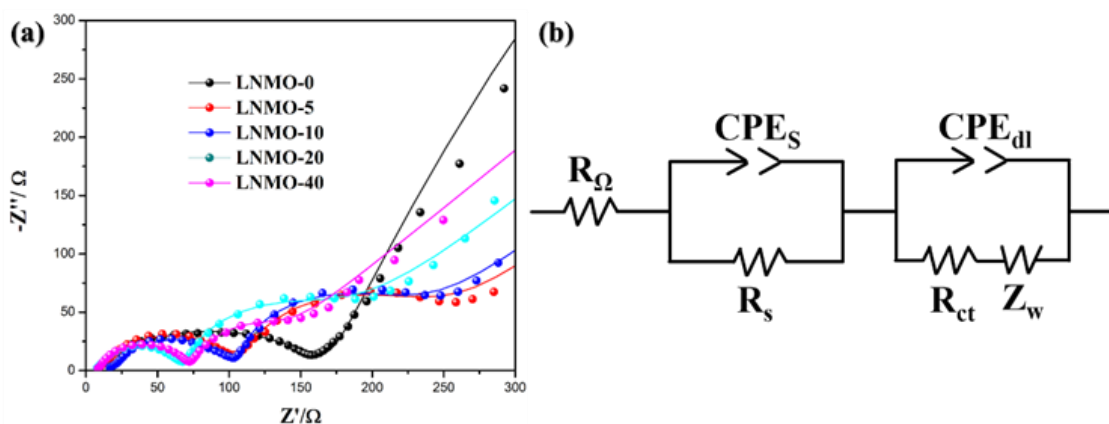
Figure 3.4 (a) Electrochemical impedance spectra (EIS) of the LNMO-n samples (Solid lines: Fitted spectra); (b) A possible equivalent circuit.

3.3.3   XANES Studies

To investigate the change of Mn valence state in the LNMO-n samples, XANES was collected on the Mn $L_{3,2}$-edges. Mn $L_{3,2}$-edges illustrate the electronic transition from Mn $2p_{3/2}$ and $2p_{1/2}$ to an unoccupied 3d state.[39-41] Fig. 5a depicts the total electron yields (TEY) of LNMO-0 and LNMO-20, which is surface sensitive with a probing depth of 5-10 nm. The L_2-edge often appears to be broader due to the core hole lifetime as explained by Coster-Kronig Auger decay.[42] It can be seen that both the LNMO-0 and the LNMO-20 show predominantly Mn^{4+} features that fit well with standard MnO_2, the small peak at 646 eV corresponds to Mn^{3+}, and this is also consistent with the Raman spectra, the unchanged spectra reveal that the coating process did not generate changes to the surface phase of LNMO. However, after charge/discharge cycling, Mn^{4+} at the surface was

partially reduced to Mn^{2+}, and the LNMO-0 shows much higher intensity ratio of Mn^{2+}/Mn^{4+} than the coated LNMO sample. The bulk-sensitive fluorescence yield (FYI) spectra of LNMO-20, LNMO-20 after battery cycling and LNMO-0 after battery cycling are shown in Fig. SI 3.8. It can be seen that the bulk Mn exhibits subtle changes after cycling. The less reduced Mn valence on coated LNMO surface also reveals weaker reduction by the electrolyte, which can be attributed by the inhibitive role of $FePO_4$ against the electrolyte oxidation.[43] It is also generally accepted that the presence of Mn^{3+} triggers the Jahn-Teller distortion because of its $(t_{2g}^3 e_g^1)$ configuration, resulting in its charge disproportionation into non Jahn-Teller active Mn^{2+} and Mn^{4+}, described as $2Mn^{3+} \rightarrow Mn^{2+} + Mn^{4+}$.[3, 44] In the presence of HF from the $LiPF_6$ salt, Mn^{2+} ions dissolve in the electrolyte and migrate through the separator followed by depositing on the anode as Mn metal, with a secondary phase formed on the surface of cathode materials.[45, 46] The suppression of Jahn-Teller distortion by $FePO_4$ coating prevents the formation of Mn^{2+}, thereby decreases the chance of Mn^{2+} dissolution in HF, hence improves the stability.[47]
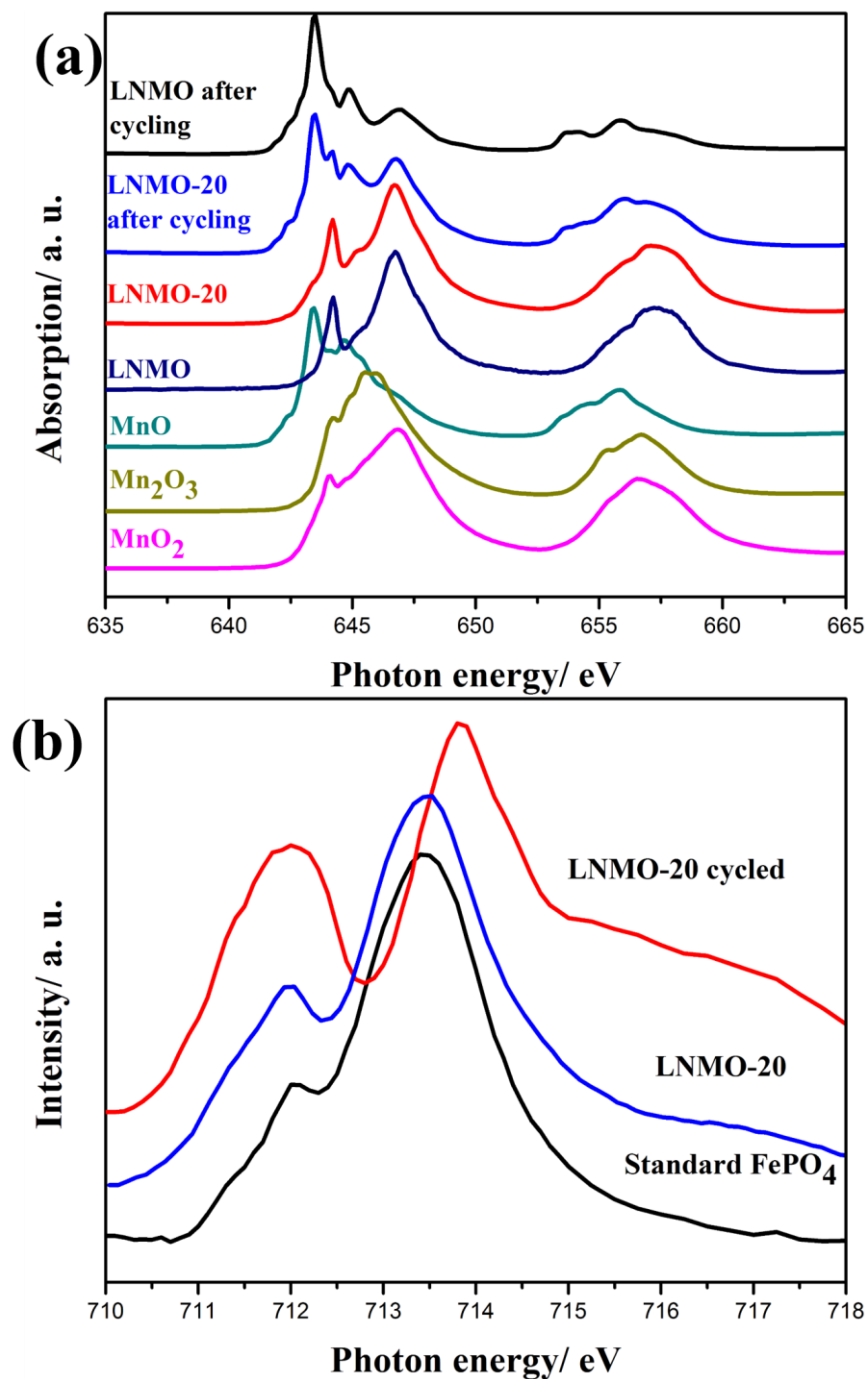
Figure 3.5 (a) XANES Mn L$_{3,2}$-edges of LNMO-20, LNMO-20 cycled, LNMO-0, LNMO-0 cycled, and standard MnO, Mn$_2$O$_3$, MnO$_2$; (b) Fe L$_3$-edges of standard FePO$_4$, LNMO-20 and LNMO-20 after 100 battery cycles collected in TEY mode

Fe L$_3$-edges XANES of standard FePO$_4$, LNMO-20 and LNMO-20 after battery cycling were performed to determine the chemical states of the FePO$_4$ coatings before and after

charge/discharge cycling. As shown in Fig. 3.5b, the spectrum of LNMO-20 fits well with the standard $FePO_4$ spectrum, the intense peak at 713.5 eV (can be ascribed to the dominant spectral feature of Fe^{3+}) and the weaker peak at 712.2 eV are related to the spin-orbit, interplay of crystal-filed and electronic interactions. Their intensity ratio reveals the Fe^{3+}/Fe^{2+} ratio.[37] Nevertheless, upon battery cycling, there is an obvious drop in the Fe^{3+}/Fe^{2+} ratio, indicating that part of the Fe^{3+} has been reduced, and the position of the right peak is, interestingly, shifting to higher energy value close to the peak feature in standard $LiFePO_4$. Such shift was also observed in our previous study on the soft XANES spectroscopies of $LiFePO_4$-related various phases.[48] In this regard, we believe that the insertion of lithium ions into the matrix of amorphous $FePO_4$ has resulted in the partially lithiated $FePO_4$ domains, which acts as a lithium ion reservoir and exhibited improved performance at high current densities by providing abundant Li^+ diffusion pathways.

Based on the aforementioned results, the schematic illustration of the protecting role of $FePO_4$ is presented in Fig. 3.6. The LNMO-0 exposed to electrolyte suffers from fierce transitional metal dissolution and continuous electrolyte decomposition. On the contrary, LNMO with $FePO_4$ coating is resistant to the metal dissolution. This is because it was found that the non-coated sample displayed Mn at reduced state on the surface after cycling, which is much more prone to dissolution compared to Mn^{3+} and/or Mn^{4+}. Additionally, the amorphous $FePO_4$ layer accommodates lithium ions rapidly during cycling, thus provides fast lithium diffusion coefficient. More specific role of $FePO_4$ is shown in Fig. 6b with the electrolyte highest occupied molecular orbital (HOMO) and work functions of $FePO_4$ and $LiNi_{0.5}Mn_{1.5}O_4$. The electrolyte gets readily oxidized when the electrochemical potentials of cathode materials are below the HOMO of it.[33, 34] Unlike other conventional insulating ALD coating materials such as Al_2O_3 or ZrO_2, $FePO_4$ is electrochemically active with an open circuit voltage of $\sim$ 3V,[24] the $FePO_4$ ultrathin layer on the surface prevents the direct contact of LNMO with the electrolyte, helping to avoid the oxidation of electrolyte that results in the reduction and dissolution of Mn ions.
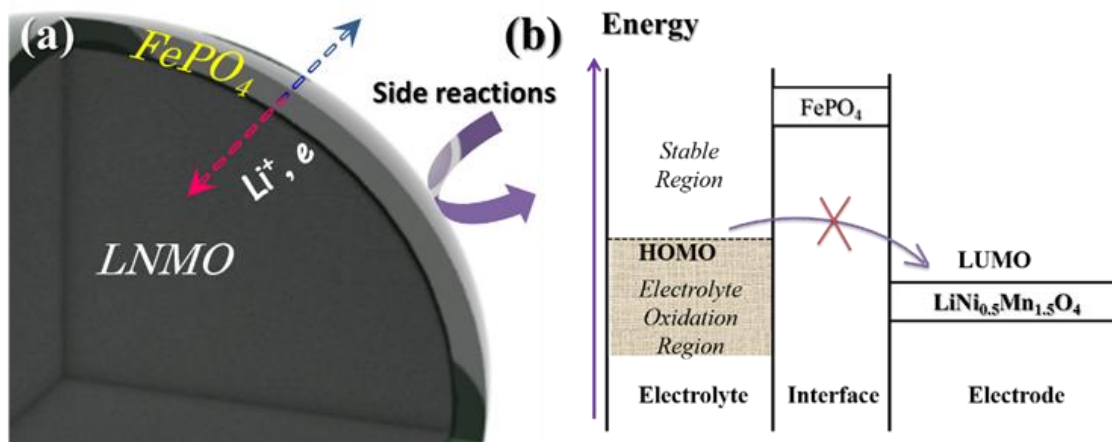
Figure 3.6 Schematic illustrations of (a) LNMO; (b) bare LNMO upon cycling; (c) LNMO-n; (d) LNMO-n upon cycling; (e) illustration of the electrolyte highest occupied molecular orbital (HOMO) and work functions of $FePO_4$ and $LiNi_{0.5}Mn_{1.5}O_4$

3.4 Conclusion

We have proposed a new $FePO_4$ coating on high voltage LNMO cathode material enabled by ALD. Different thicknesses of $FePO_4$ have been deposited onto LNMO powders with 5, 10, 20 and 40 ALD cycles. The LNMO coated with 10 ALD cycles of $FePO_4$ showed the best performance including the highest capacity and stabilized capacity retention under all the current rates. When the LNMO was coated with 40 ALD cycles of $FePO_4$, the capacity retention increased up to 100%. XANES study showed that the ultrathin $FePO_4$ suppressed the surface Mn^{4+} from being heavily reduced to Mn^{2+} by the reduction from the electrolyte and the Jahn-Teller distortion, less amount of Mn^{2+} helped to retain the surface consistency without dissolution into the electrolyte. The $FePO_4$ coating layer was slightly reduced due to remaining Li^+ in the structure after charge/discharge cycling. Compared with the most widely used insulating Al_2O_3, amorphous $FePO_4$ presents many advantages on the electron/ion diffusion on the surface. Our work provides an alternative option of depositing materials onto powders instead of electrode sheets directly using ALD, which expands the deposition temperature, owing to the electrochemically active nature of $FePO_4$.

Acknowledgement

References

[1] A. Kraytsberg and Y. Ein-Eli, Higher, Stronger, Better…A Review of 5 Volt Cathode Materials for Advanced Lithium-Ion Batteries, *Adv. Energy Mater.,* 2012, **2**, 922-939.

[2] A. Manthiram, K. Chemelewski and E.-S. Lee, A Perspective on the High-Voltage $LiMn_{1.5}Ni_{0.5}O_4$ Spinel Cathode for Lithium-Ion Batteries, *Energy Environ. Sci.,* 2014, **7**, 1339.

[3] K. Y. Chung, C.-W. Ryu and K.-B. Kim, Onset Mechanism of Jahn-Teller Distortion in 4 V $LiMn_2O_4$ and Its Suppression by $LiM_{0.05}Mn_{1.95}O_4$ (M = Co, Ni) Coating, *J. Electrochem. Soc.,* 2005, **152**, A791.

[4] P. Arora, R. E. White and M. Doyle, Capacity Fade Mechanisms and Side Reactions in Lithium-Ion Batteries, *J. Electrochem. Soc.,* 1998, **145**, 3647-3667.

[5] N. S. Norberg, S. F. Lux and R. Kostecki, Interfacial Side-Reactions at a $LiNi_{0.5}Mn_{1.5}O_4$ Electrode in Organic Carbonate-Based Electrolytes, *Electrochem. Commun.,* 2013, **34**, 29-32.

[6] J. Xiang, C. Chang, L. Yuan and J. Sun, A Simple and Effective Strategy to Synthesize Al_2O_3-Coated $LiNi_{0.8}Co_{0.2}O_2$ Cathode Materials for Lithium Ion Battery, *Electrochem. Commun.,* 2008, **10**, 1360-1363.

[7] R. Guo, P. Shi, X. Cheng and L. Sun, Effect of ZnO Modification on the Performance of LiNi$_{0.5}$Co$_{0.25}$Mn$_{0.25}$O$_2$ Cathode Material, *Electrochim. Acta,* 2009, **54**, 5796-5803.

[8] G. Alva, C. Kim, T. Yi, J. B. Cook, L. Xu, G. M. Nolis and J. Cabana, Surface Chemistry Consequences of Mg-Based Coatings on LiNi$_{0.5}$Mn$_{1.5}$O$_4$ electrode Materials Upon Operation at High Voltage, *J. Phys. Chem. C,* 2014, **118**, 10596-10605.

[9] S. M. Lee, S. H. Oh, J. P. Ahn, W. I. Cho and H. Jang, Electrochemical Properties of ZrO$_2$-Coated LiNi$_{0.8}$Co$_{0.2}$O$_2$ Cathode Materials, *J. Power Sources, 2006,* **159**, 1334-1339.

[10] J. Chong, S. Xun, J. Zhang, X. Song, H. Xie, V. Battaglia and R. Wang, Li$_3$PO$_4$-Coated LiNi$_{0.5}$Mn$_{1.5}$O$_4$: A Stable High-Voltage Cathode Material for Lithium-Ion Batteries*, Chemistry,* 2014, **20**, 7479-7485.

[11] J. Kim, M. Noh, J. Cho, H. Kim and K.-B. Kim, Controlled Nanoparticle Metal Phosphates (Metal=Al, Fe, Ce, and Sr) Coatings on LiCoO$_2$ Cathode Materials, *J Electrochem. Soc.,* 2005, **152**, A1142.

[12] J. Cho, Correlation between AlPO$_4$ Nanoparticle Coating Thickness on LiCoO$_2$ Cathode and Thermal Stability, *Electrochim. Acta,* 2003, **48**, 2807-2811.

[13] Z. H. Chen, Y. Qin, K. Amine and Y. K. Sun, Role of Surface Coating on Cathode Materials for Lithium-Ion Batteries, *J. Mater. Chem.,* 2010, **20**, 7606-7612.

[14] X. Meng, X. Q. Yang and X. Sun, Emerging Applications of Atomic Layer Deposition for Lithium-Ion Battery Studies, *Adv. Mater.,* 2012, **24**, 3589-3615.

[15] C. Marichy, M. Bechelany and N. Pinna, Atomic Layer Deposition of Nanostructured Materials for Energy and Environmental Applications, *Adv. Mater.,* 2012, **24**, 1017-1032.

[16] J. S. Park, X. Meng, J. W. Elam, S. Hao, C. Wolverton, C. Kim and J. Cabana, Ultrathin Lithium-Ion Conducting Coatings for Increased Interfacial Stability in High Voltage Lithium-Ion Batteries, *Chem. Mater.,* 2014, **26**, 3128-3134.

[17] J. W. Kim, D. H. Kim, D. Y. Oh, H. Lee, J. H. Kim, J. H. Lee and Y. S. Jung, Surface Chemistry of $LiNi_{0.5}Mn_{1.5}O_4$ Particles Coated by Al_2O_3 Using Atomic Layer Deposition for Lithium-Ion Batteries, *J. Power Sources,* 2015, **274**, 1254-1262.

[18] X. Fang, M. Y. Ge, J. P. Rong, Y. C. Che, N. Aroonyadet, X. L. Wang, Y. H. Liu, A. Y. Zhang and C. W. Zhou, Ultrathin Surface Modification by Atomic Layer Deposition on High Voltage Cathode $LiNi_{0.5}Mn_{1.5}O_4$ for Lithium Ion Batteries, *Energy Technol.,* 2014, **2**, 159-165.

[19] Z. Yang, S. Li, S.-A. Xia, Y. Jiang, W.-X. Zhang and Y.-H. Huang, Significant Improved Electrochemical Performance of Spinel $LiMn_2O_4$ Promoted by $FePO_4$ Incorporation, *Electrochem. Solid St.,* 2011, **14**, A109.

[20] D. Liu, Y. Bai, S. Zhao and W. Zhang, Improved Cycling Performance of 5 V Spinel $LiNi_{0.5}Mn_{1.5}O_4$ by Amorphous $FePO_4$ Coating, *J. Power Sources,* 2012, **219**, 333-338.

[21] Y. S. Jung, A. S. Cavanagh, L. A. Riley, S. H. Kang, A. C. Dillon, M. D. Groner, S. M. George and S. H. Lee, Ultrathin Direct Atomic Layer Deposition on Composite Electrodes for Highly Durable and Safe Li-Ion Batteries, *Adv. Mater.,* 2010, **22**, 2172-2176.

[22] X. Li, J. Liu, M. N. Banis, A. Lushington, R. Li, M. Cai and X. Sun, Atomic Layer Deposition of Solid-State Electrolyte Coated Cathode Materials with Superior High-Voltage Cycling Behavior for Lithium Ion Battery Application, *Energy Environ. Sci.,* 2014, **7**, 768.

[23] X. Li, J. Liu, X. Meng, Y. Tang, M. N. Banis, J. Yang, Y. Hu, R. Li, M. Cai and X. Sun, Significant Impact on Cathode Performance of Lithium-Ion Batteries by Precisely Controlled Metal Oxide Nanocoatings Via Atomic Layer Deposition, *J. Power Sources,* 2014, **247**, 57-69.

[24] Q. Fan, L. Lei, G. Yin, Y. Chen and Y. Sun, Direct Growth of $FePO_4$/Graphene Hybrids for Li-Ion and Na-Ion Storage, *Electrochem. Commun.,* 2014, **38**, 120-123.

[25] Y. Fang, L. Xiao, J. Qian, X. Ai, H. Yang and Y. Cao, Mesoporous Amorphous $FePO_4$ Nanospheres as High-Performance Cathode Material for Sodium-Ion Batteries, *Nano Lett.,* 2014, **14**, 3539-3543.

[26] S. Xu, S. Zhang, J. Zhang, T. Tan and Y. Liu, A Maize-Like $FePO_4$@MCNT Nanowire Composite for Sodium-Ion Batteries via a Microemulsion Technique, *J. Mater. Chem.* A, 2014, **2**, 7221.

[27] S. M. Zhang, J. X. Zhang, S. J. Xu, X. J. Yuan and B. C. He, Li Ion Diffusivity and Electrochemical Properties of $FePO_4$ Nanoparticles Acted Directly as Cathode Materials in Lithium Ion Rechargeable Batteries, *Electrochim. Acta,* 2013, **88**, 287-293.

[28] M. Wang, W. Zhang, Y. H. Liu, Y. Yang, C. S. Wang and Y. Wang, Electrochemical Performance of Patterned $LiFePO_4$ Nano-Electrode with a Pristine Amorphous Layer, *Appl. Phys. Lett.,* 2014, **104**, 171604-171607

[29] T. Maxisch, F. Zhou and G. Ceder, Ab Initio Study of the Migration of Small Polarons in Olivine Li_xFePO_4 and Their Association with Lithium Ions and Vacancies, *Phys. Rev. B*, 2006, **73**, 10, 104301-104306

[30] J. Liu, M. N. Banis, Q. Sun, A. Lushington, R. Li, T. K. Sham and X. Sun, Rational Design of Atomic-Layer-Deposited $LiFePO_4$ as a High-Performance Cathode for Lithium-Ion Batteries, *Adv. Mater.,* 2014, **26**, 6472-6477

[31] J. Liu, B. Xiao, M. N. Banis, R. Li, T.-K. Sham and X. Sun, Atomic Layer Deposition of Amorphous Iron Phosphates on Carbon Nanotubes as Cathode Materials for Lithium-Ion Batteries, *Electrochim. Acta,* 2014, **162**, 275-281

[32] K. B. Gandrud, A. Pettersen, O. Nilsen and H. Fjellvåg, High-Performing Iron Phosphate for Enhanced Lithium Ion Solid State Batteries as Grown by Atomic Layer Deposition, *J. Mater. Chem. A,* 2013, **1**, 9054.

[33] J. B. Goodenough and Y. Kim, Challenges for Rechargeable Li Batteries, *Chem. Mater.,* 2010, **22**, 587-603.

[34] J. B. Goodenough and K. S. Park, The Li-Ion Rechargeable Battery: A Perspective, *J. Am. Chem. Soc.,* 2013, **135**, 1167-1176.

[35] J. Zheng, J. Xiao, X. Yu, L. Kovarik, M. Gu, F. Omenya, X. Chen, X. Q. Yang, J. Liu, G. L. Graff, M. S. Whittingham and J. G. Zhang, Enhanced Li^+ Ion Transport in $LiNi_{0.5}Mn_{1.5}O_4$ through Control of Site Disorder, *Phys. Chem. Chem. Phys.,* 2012, **14**, 13515-13521.

[36] C. Y. Xu, P. X. Zhang and L. Yan, Blue Shift of Raman Peak from Coated TiO_2 Nanoparticles, *J. Raman Spectrosc.,* 2001, **32**, 862-865.

[37] K. Edström, T. Gustafsson and J. O. Thomas, The Cathode–Electrolyte Interface in the Li-Ion Battery, *Electrochim. Acta,* 2004, **50**, 397-403.

[38] J. Liu and A. Manthiram, Kinetics Study of the 5 V Spinel Cathode $LiNi_{0.5}Mn_{1.5}O_4$ before and after Surface Modifications, *J. Electrochem. Soc.,* 2009, **156**, A833.

[39] J. Zhou, D. Hong, J. Wang, Y. Hu, X. Xie and H. Fang, Electronic Structure Variation of the Surface and Bulk of a $LiNi_{0.5}Mn_{1.5}O_4$ Cathode as a Function of State of Charge: X-Ray Absorption Spectroscopic Study, *Phys. Chem. Chem. Phys.,* 2014, **16**, 13838-13842.

[40] T. Okumura, M. Shikano and H. Kobayashi, Contribution of Oxygen Partial Density of State on Lithium Intercalation/De-Intercalation Process in $Li_xNi_{0.5}Mn_{1.5}O_4$ Spinel Oxides, *J. Power Sources,* 2013, **244**, 544-547.

[41] T. Okumura, T. Fukutsuka, K. Matsumoto, Y. Orikasa, H. Arai, Z. Ogumi and Y. Uchimoto, Role of Local and Electronic Structural Changes with Partially Anion Substitution Lithium Manganese Spinel Oxides on Their Electrochemical Properties: X-Ray Absorption Spectroscopy Study, *Dalton Trans.,* 2011, **40**, 9752-9764.

[42] F. M. de Groot, J. C. Fuggle, B. T. Thole and G. A. Sawatzky, 2p X-Ray Absorption of 3d Transition-Metal Compounds: An Atomic Multiplet Description Including the Crystal Field, *Phys. Rev. B Condens. Matter.,* 1990, **42**, 5459-5468.

[43] C. Y. Ouyang, X. M. Zeng, Z. Sljivancanin and A. Baldereschi, Oxidation States of Mn Atoms at Clean and Al_2O_3-Covered $LiMn_2O_4$ (001) Surfaces, *J. Phys. Chem. C,* 2010, **114**, 4756-4759.

[44] A. Yamada and M. Tanaka, Jahn-Teller Structural Phase-Transition around 280K in $LiMn_2O_4$, *Mater. Res. Bull.,* 1995, **30**, 715-721.

[45] C. Zhan, J. Lu, A. Jeremy Kropf, T. Wu, A. N. Jansen, Y. K. Sun, X. Qiu and K. Amine, Mn(II) Deposition on Anodes and Its Effects on Capacity Fade in Spinel Lithium Manganate-Carbon Systems, *Nat. Commun.,* 2013, **4**, 2437.

[46] K. T. Lee, S. Jeong and J. Cho, Roles of Surface Chemistry on Safety and Electrochemistry in Lithium Ion Batteries, *Acc. Chem. Res.,* 2013, 46, 1161-1170.

[47] K. Y. Chung, C.-W. Ryu and K.-B. Kim, Onset Mechanism of Jahn-Teller Distortion in 4 V $LiMn_2O_4$ and Its Suppression by $LiM_{0.5}Mn_{1.5}O_4$ (M=Co, Ni) Coating, *J. Electrochem. Soc.,* 2005, **152**, A791.

[48] S. Yang, D. Wang, G. Liang, Y. M. Yiu, J. Wang, L. Liu, X. Sun and T.-K. Sham, Soft X-Ray Xanes Studies of Various Phases Related to $LiFePO_4$ Based Cathode Materials, *Energy Environ. Sci.,* 2012, **5**, 7007.

Supporting Information
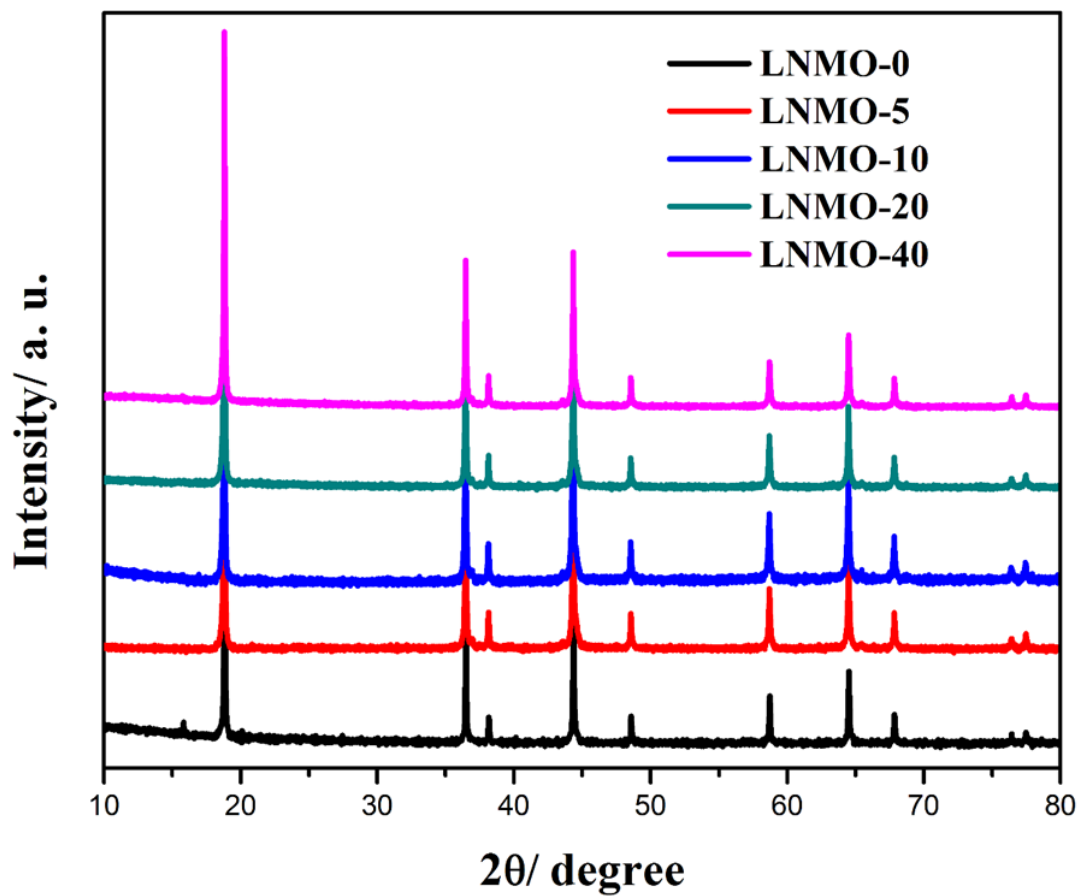
Figure SI 3.1 X-ray diffraction patterns of LNMO/ n FePO$_4$
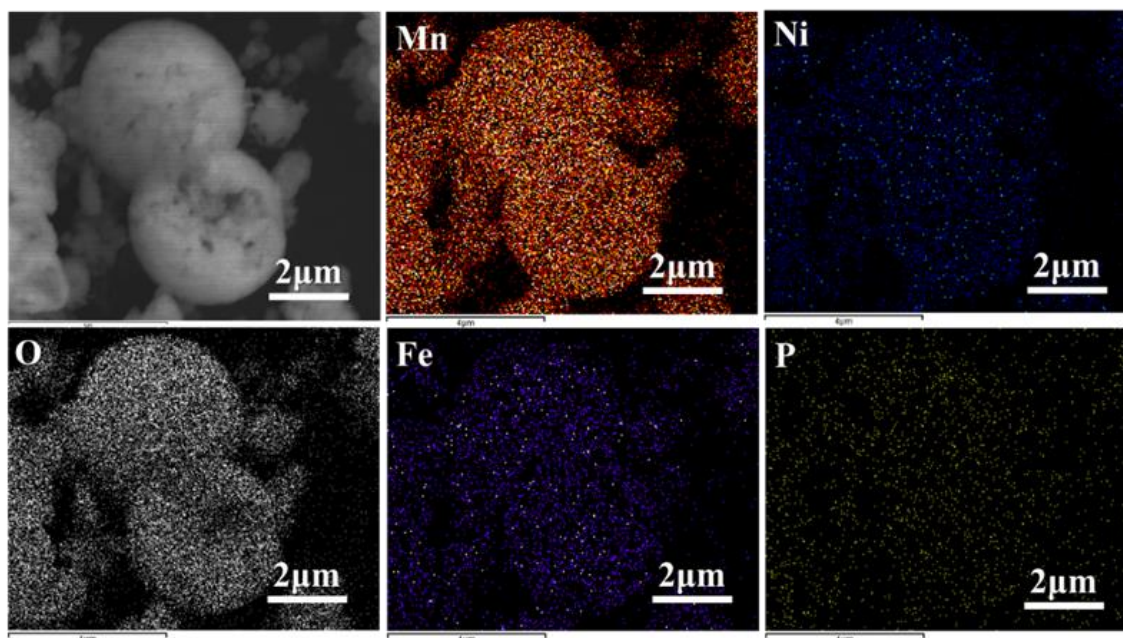
Figure SI 3.2 Energy-dispersive x-ray (EDX) mapping of LNMO-20
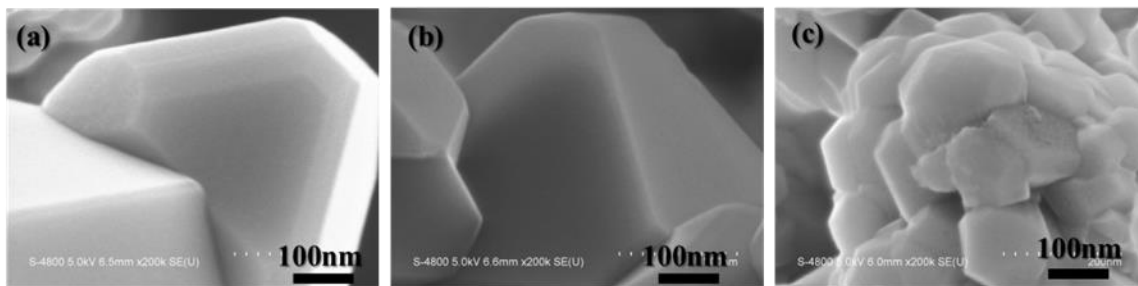
Figure SI 3.3 SEM images of (a) LNMO/5 FePO₄; (b) LNMO/10 FePO₄; (c) LNMO/40 FePO₄
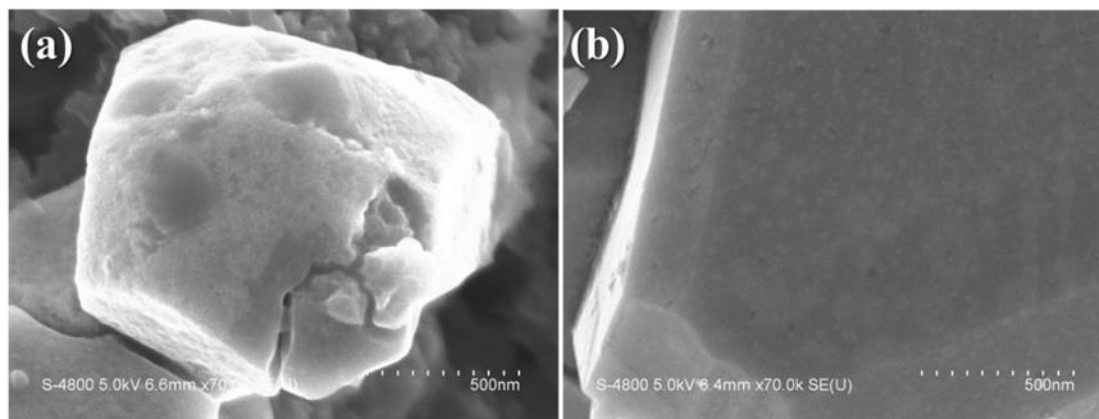
Figure SI 3.4 SEM images of (a) bare LNMO and (b) LNMO-20 after 100 times battery cycling

The surface of bare LNMO is obviously covered by another layer of SEI, also, cracking can be observed due to the lattice volume expansion. Instead, the LNMO-20 $FePO_4$ sample does not show other depositions, indicating the less SEI formation.
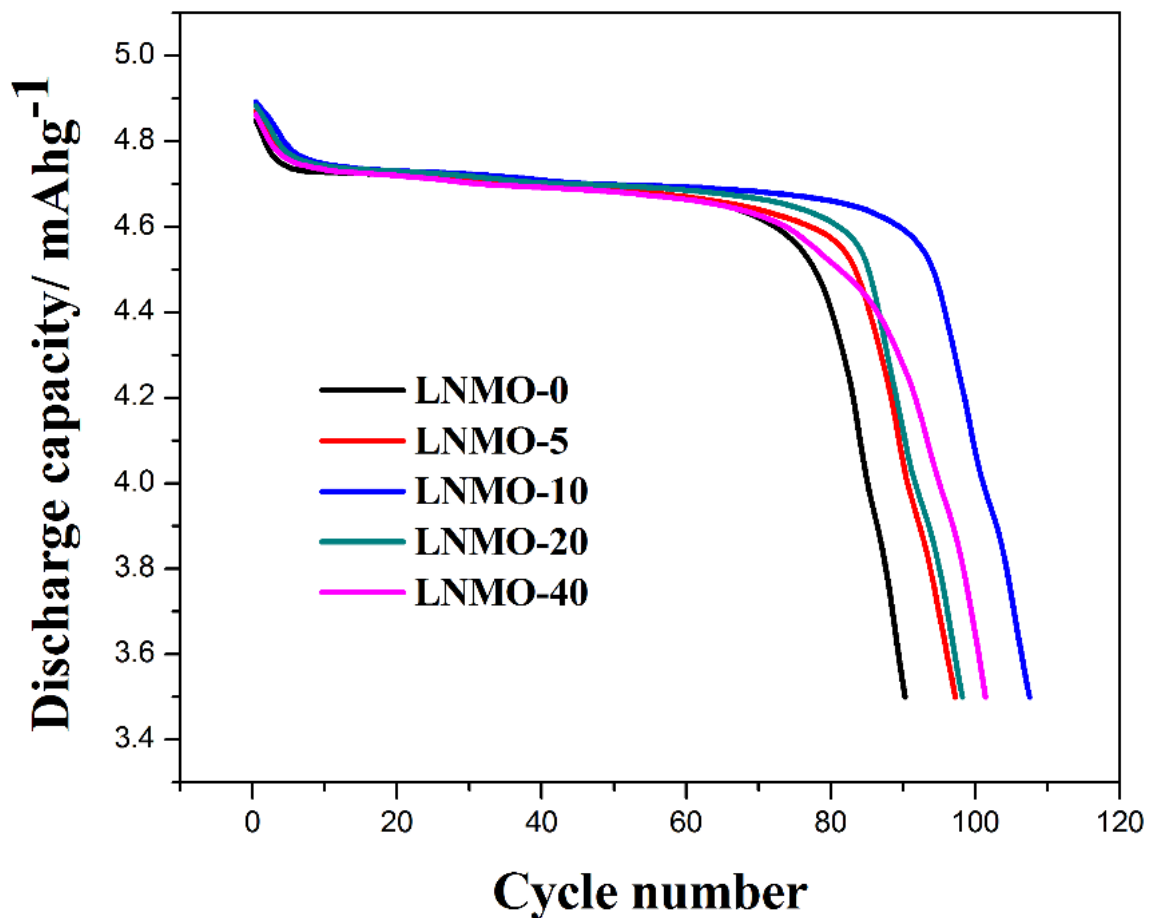
Figure SI 3.5 Discharge curves of the 100th electrochemical cycle of the LNMO-n samples

The 100th discharge curves of the samples show the same trend with the stability test, in which LNMO-10 shows the highest capacity, the voltage plateau is also higher than the others, indicating its superior performance.
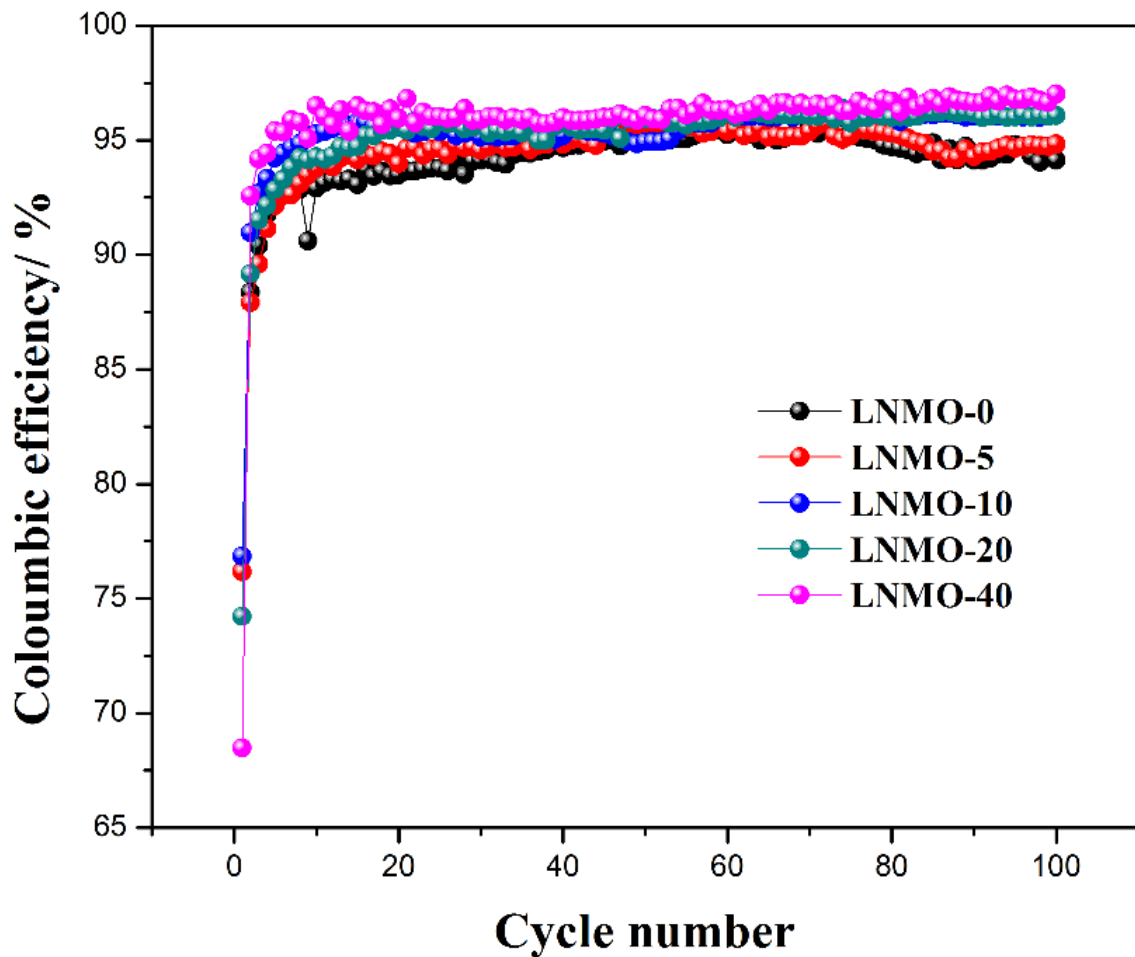
Figure SI 3.6 Coulombic efficiency of the samples

It can be observed that the initial Coulombic efficiency (ICE) decreases with the increase of ALD cycles, this is because some of the lithium were trapped in the matrix of $FePO_4$ during the first charge from an open circuit voltage (OCV) of about 3.0 V. They were not reversible because the discharge cutoff voltage was 3.5 V, which is at the end of the $FePO_4$ electrochemically active window. This loss of lithium was responsible for the decreased ICE.
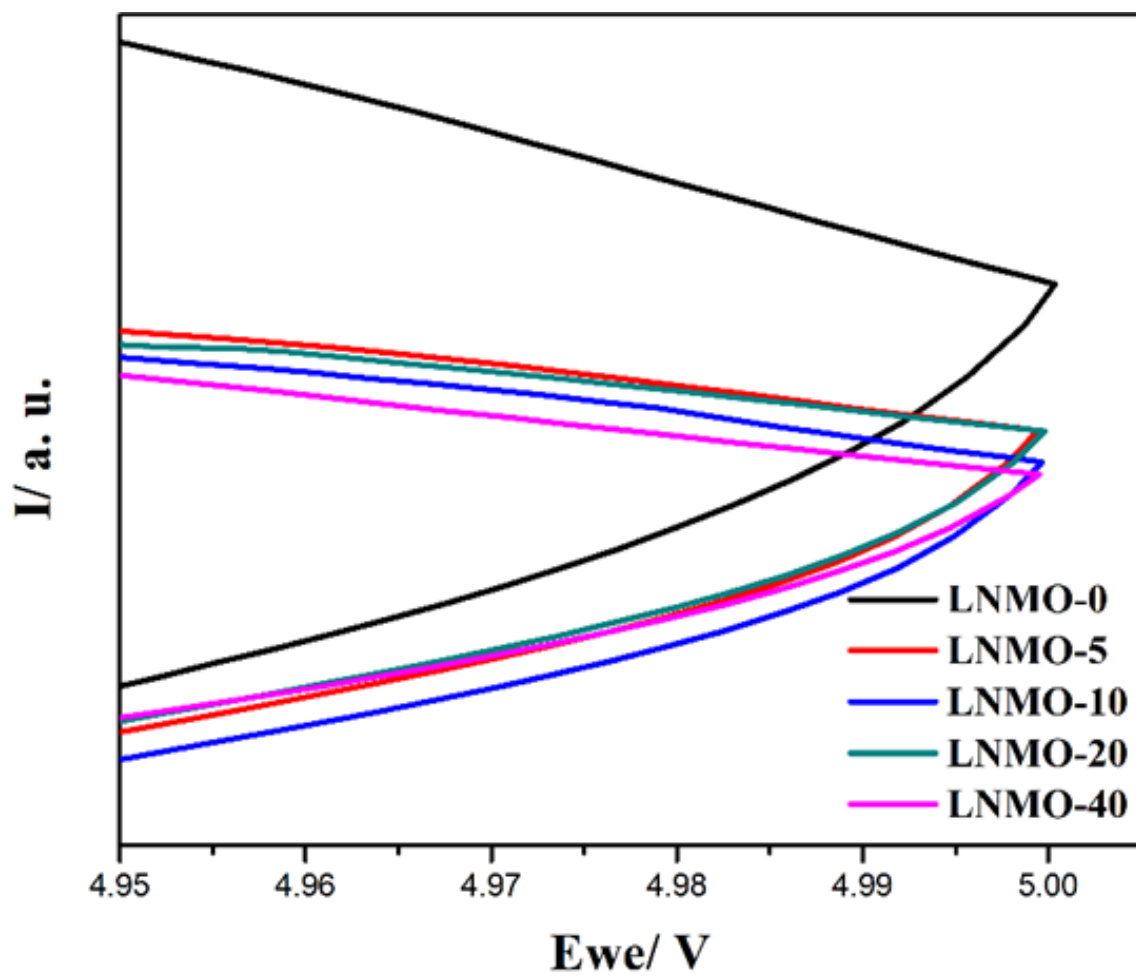
Figure SI 3.7 Enlarged CV curves within 4.9 to 5.0 V
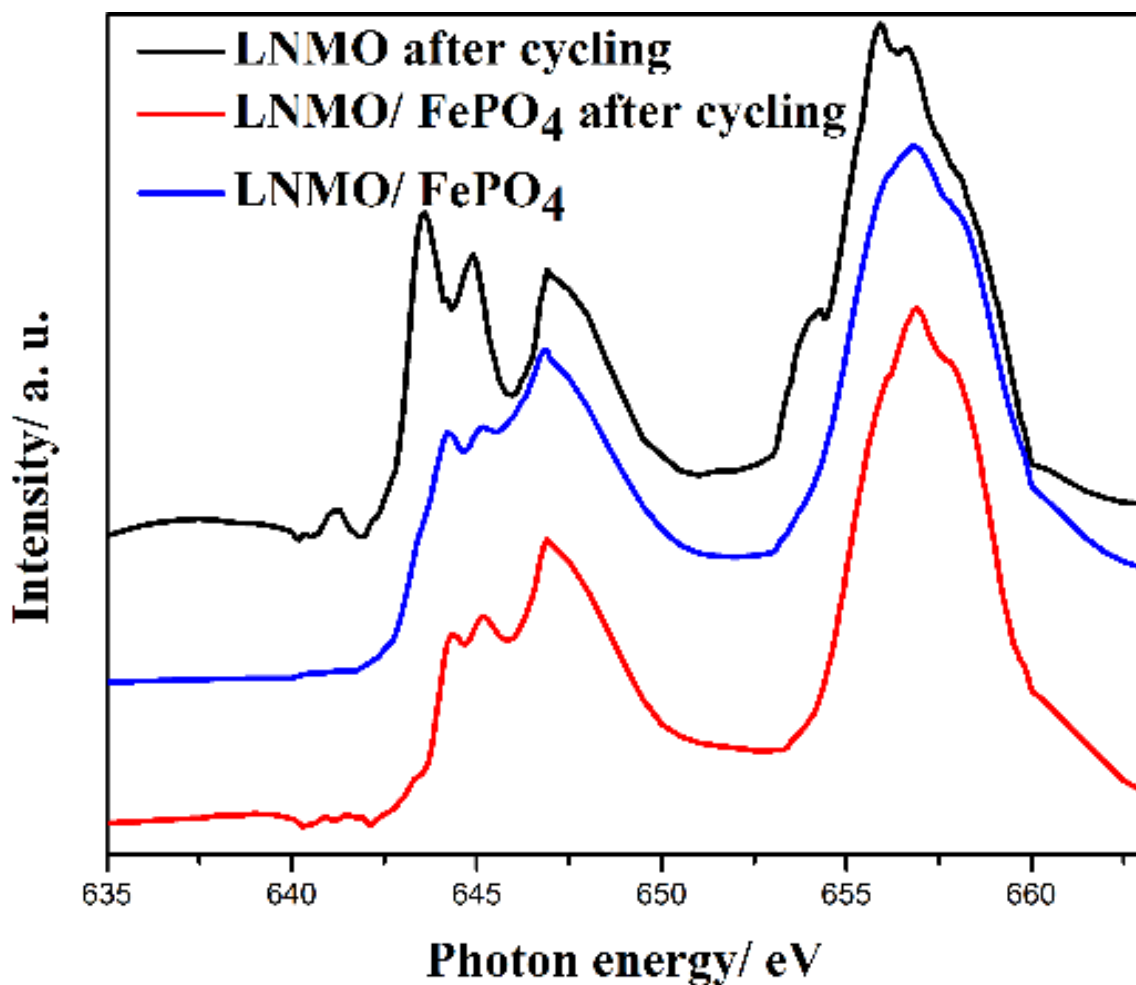
Figure SI 3.8 Mn L$_{3,2}$-edge fluorescence yield (FYI) spectra of LNMO-20, LNMO-20 after battery cycling and bare LNMO after battery cycling

FYI is a bulk-sensitive technique, Fig. SI3.8 indicates that the bulk Mn will be slightly reduced to lower valence without coating. Similar with the surface Mn, coating helps to retain Mn at higher oxidation level in the bulk, thus preventing the vigorous Mn^{3+} Jahn-Teller distortion and Mn^{2+} dissolution. The FYI reveals that the reduction of Mn in LNMO mainly takes place at the outer surface, where the cathode material is exposed to either the coated FePO$_4$ or the liquid electrolyte.

Chapter 4

4 Atomic-scale Manipulation of Spinel Lithium Nickel Manganese Oxide Surface by Tetrahedrally-coordinated Ti as High Performance Cathode Material

The modification of the cathode materials surfaces has been reported by many researchers, it has been speculated that the surface of the material may undergo certain changes depending on the modification method. One of the possible route is to anneal coated cathode materials to allow for transition metal or oxygen substitution by the elements in the coating material. The stress generated by the incorporation of hetero-elements into the lattice may help increase the structural stability against cation migration upon cycling.

In the previous chapter, we have mentioned the importance of sufficient lithium diffusion sites. A novel two-step surface modification method that includes atomic layer deposition (ALD) of TiO_2 followed by post-annealing treatment on spinel $LiNi_{0.5}Mn_{1.5}O_4$ (LNMO) cathode material was developed to optimize the cathode material performance. The post-annealing treatment significantly improves the electrochemical performance of the LNMO, which can be attributed to the formation of a $TiMn_2O_4$ (TMO) – like inverse spinel phase resulting from the reaction of TiO_2 and the LNMO at surface region. The Ti incorporation into the tetrahedral sites helps combatting the impedance growth upon initial charge process that stems from continuous irreversible structural transition and strengthening the Ni-O bond. The TMO–like phase also alleviates the electrolyte oxidation decomposition during electrochemical cycling and could possibly assist Li diffusion through the vacancies existed at the cation sites.

B. Xiao,* H. Liu,* J. Liu, Q. Sun, B. Wang, K. Kaliyappan, Y. Liu, R. Li, T.-K Sham G. Botton, M. Cai and X. Sun, *submitted*

B. Xiao and H. Liu contributed equally to this work.

4.1 Introduction

The growing demand for renewable energy has stimulated the development of lithium-ion batteries (LIBs), which are deemed as the key component for the next generation electric and hybrid electric vehicles. LIBs with high energy density are therefore extremely desirable in these high power devices.[1] Cathode materials that operate over 4.5 V (vs Li/Li$^+$) with high energy density are considered as the superlative candidates to replace the currently commercialized LiCoO$_2$, which is restricted to portable devices such as cell phones and laptops. Among these high-voltage cathode materials, LiNi$_{0.5}$Mn$_{1.5}$O$_4$ (LNMO) with a spinel structure holds great potential in terms of natural elemental abundance, high operating voltage (4.7 V) and theoretical capacity (147 mAhg^{-1}).[2, 3] Nevertheless, such high operating voltage of LNMO involves surface chemistry issues such as irreversible surface phase transition, transition metal dissolution, Jahn-Teller distortion of Mn^{3+} and electrolyte oxidation etc.[4-10] Considerable efforts have been devoted to alleviating these deficiencies by coating the LNMO surface using metal oxides, [11-13] phosphates,[14-17] fluorides[18, 19] and so forth. These coating materials can tackle the metal dissolution, electrolyte decomposition and Mn^{3+} Jahn-Teller distortion problems by simply shielding the cathode material from direct exposure to the electrolyte. Bulk doping during materials preparation is another strategy aimed at suppressing the phase transition in LNMO,[20-26] but the excessive and uncontrollable doping will block the Li ions transportation channels in its bulk structure, leading to active capacity loss.[27-29]

Considering the fact that side reactions predominantly happen on the surface of LNMO due to the unbalanced Li ions mobility on the boundary especially at high current densities,[30] restricting the controllable doping modification within the surface turns out to be a feasible and promising approach. In previous studies, metal oxides or phosphates were often deposited onto the surface of cathode materials by a sol-gel method followed by annealing. During the post-annealing process, the metal ions (Mg^{2+}, Al^{3+} etc.) diffuse into the surface lattices and help improve the performance of the electrode materials by: (1) eliminating the onset of Jahn-Teller distortion of transition metals such as Mn^{3+}; (2) suppressing the transition metals dissolution; (3) preventing severe electrolyte oxidative decomposition; (4) combating second phase formation; (5) strengthening the metal-oxygen

bonds on the surface; and (6) changing the surface bascity.[30-36] However, manipulating the doping amount and uniformity by these methods has yet remained to be unresolved due to the difficulty in realizing uniform and thin coating by conventional methods, also, there is a lack of solid evidence on the doping mechanisms and the structure change upon such treatment. ALD is an emerging technique that is capable of depositing conformal and uniform thin films, and has been extensively used to coat the surface of cathode materials with ultrathin layers for the purpose of improving their electrochemical performance in LIBs.[37-39] Therefore, ALD provides a feasible approach to tailoring the uniformity and amount of surface doping on the cathode materials by easily controlling the thickness of the uniform coating layers. However, the adoption of the combination of ALD and post-treatment to design the surface composition of cathode materials is scarcely reported.

In this work, we successfully modified the surface structures of LNMO particles by post-annealing ALD derived TiO_2 with different thicknesses. Part of the Ti was found to diffuse into the 8a tetrahedral sites which were previously occupied by lithium atoms, creating a uniform layer of $TiMn_2O_4$ (TMO) – like cation deficient inverse spinel phase. Besides, more Ti atoms were found to have diffused into the bulk of the LNMO and resulted in octahedral site doping. The Ti incorporation suppresses the surface phase transformation that could result in impedance build-up as observed during the first charge process, thereby benefiting the discharge capacity from the initial cycle. These synergetic effects help build a surface layer with desired thickness comprising both moderate electrical and ionic conductivity and contributing to increased capacity and stability. Moreover, it was also found that the thickness of the TiO_2 coating layer should be carefully adjusted in order to minimize the formation of impurities such as the $Li_xNi_{1-x}O$ in the rock salt phase, which could jeopardize the battery performance. It was found that TiO_2 coating deposited with 25 ALD cycles (~ 2 nm in thickness) was optimal, whereas thinner or thicker TiO_2 coatings were either inadequate to make desirable difference or excessive that leads to noticeable drop in performance. The comparison between the pure TiO_2 coated LNMO and annealed TiO_2 coated LNMO samples revealed that the post-annealing process is crucial for achieving an optimal battery performance.

4.2 Experimental

4.2.1 Materials Preparation

The LNMO powders were purchased from Daejung Energy Materials Co. Ltd., South Korea. Atomic layer deposition (ALD) of TiO_2 was performed at 150 °C in a Savannah 100 ALD system (Ultratech/Cambridge Nanotech) by using titanium(IV) isopropoxide (TTIP, $Ti[OCH(CH_3)_2]_4$, Sigma Aldrich, 97%), and distilled water (H_2O) as precursors. The source temperature for TTIP was 85 °C, while H_2O was kept at room temperature (RT). N_2 gas was used as the carrying and purging gas, at a flow rate of 20 sccm. Each ALD cycle of TiO_2 was executed with the following steps: (1) 1s pulse of TTIP; (2) 3s extended exposure of TTIP in the reaction chamber; (3) 20s purge of residual TTIP and any by-products; (4) 1s pulse of H_2O; (5) 3s extended exposure of H_2O in the reaction chamber; (6) 20s purge of residual H_2O and any by-products. LNMO powders were dispersed on a stainless steel tray, and then put at the center of the ALD reaction chamber. TiO_2 was deposited on LNMO powders by repeating the above ALD cycles, the corresponding samples are denoted as $LNMO/nTiO_2$ where n stands for the ALD cycle number. 5, 25 and 50 cycle numbers were chosen as the performance study parameter. In order to better characterize the consequence of the TiO_2 reaction with LNMO upon post-treatment, 250 ALD cycle number was used for Ti related structural studies.

In the post-treatment process, the $LNMO/nTiO_2$ samples were annealed in air under 810 °C for 6h followed by slow cooling to RT within 10h. The treated samples were named as $LNMO/nTiO_2A$. All of the bare LNMO samples studied were treated under the same conditions as well to make the results comparable.

4.2.2 Characterization Methods

The morphology of the samples was characterized by a Hitachi S-4800 field emission scanning electronic microscopy (FESEM) and a JEOL 2010F field emission transmission electron microscope (TEM). The X-ray diffraction (XRD) patterns were collected on a Bruker D8 Advance Diffractometer using Cu Kα radiation at 40 kV and 40 mA. The soft X-ray absorption near-edge structure (XANES) measurements with both total electron yield (TEY) and fluorescence yield (FYI) modes at the Mn $L_{3,2}$-edges, Ni $L_{3,2}$-edges and

O K-edge were collected at the Spherical Grating Monochromer (SGM) beamline with a photon energy of 250-2000 eV at the Canadian Light Source. The Ti K-edge XANES was collected at the Soft X-ray Microcharacterization Beamline (SXRMB) beamline at the Canadian Light Source.

For the electron microscope (EM) specimen preparation, the pristine and LNMO/250TiO$_2$ powder samples were suspended on the copper grids for EM characterization. The LNMO/250TiO$_2$A specimen was prepared using a Zeiss NVision 40 dual beam focused ion beam/scanning electron microscope (FIB/SEM) for a detailed structural analysis. Electron energy-loss spectroscopy (EELS) and the scanning transmission electron microscopy (STEM) characterization were carried out on an aberration-corrected (probe and image-forming lenses) FEI Titan Cubed 80-300 kV microscope equipped with a Gatan Image Filter Quantum-965 spectrometer operated at 200 kV. EELS spectra were recorded with a 0.25 eV/channel dispersion of the spectrometer. The high-angle annular dark field (HAADF)-STEM image acquired with a HAADF detector is also called a "Z-contrast" image, whereby the image intensity is proportional to the atomic number ($\propto Z^{1.7}$) of the elements present in the material.

4.2.3   Electrochemical Measurements

The LNMO powders were uniformly mixed with acetylene black (AB) and poly(vinylidene fluoride) in a ratio of 8:1:1 in N-methyl-pyrrolidione (NMP) as solvent. The slurry was then pasted onto aluminum foils and dried at 80 °C overnight under vacuum. The electrode was subsequently cut into round shape with a diameter of 12 cm and assembled into a CR-2032 coin cell in a glove box with moisture and oxygen being controlled below 1.0 ppm. Lithium metal was used as the counter electrode in the coin cells. The electrolyte was composed of 1M LiPF$_6$ dissolved into ethylene carbonate (EC) and dimethyl carbonate (DMC) in a 1:1 volume ratio (BASF corp.). Celgard K2045 was used as the separator. Cyclic voltammetry (CV) was performed on a Bio-Logic multichannel potentiostat 3/Z (VMP3) with a scanning rate of 0.1 mV s^{-1} and a potential range of 3.5-5.0 V (vs Li/Li$^+$) at RT. Galvanostatic charge/discharge test was carried out on an Arbin BT 2000 at various current densities between 3.5 and 5.0 V (vs Li/Li$^+$). The cyclic stability test was done at a current density of 0.5 C (1C = 147 mAg^{-1}) under both room temperature (RT) and 55 °C.

The tested cells were dissembled in the glove box and the cathode sheets were collected and thoroughly washed with DMC for several times and kept in a hermetic box for XANES study.

4.3   Results and Discussions

4.3.1   Structure Investigation
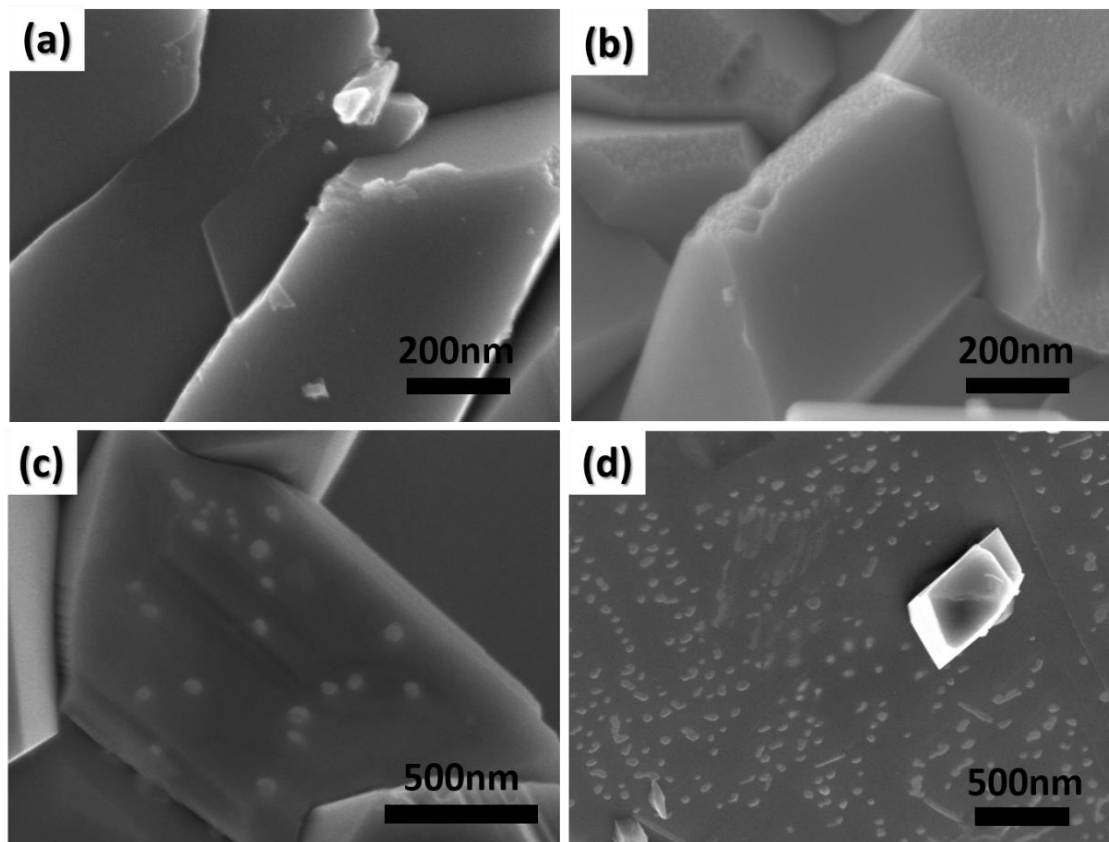
Figure 4.1 SEM images of (a) bare LNMO; (b) LNMO/25TiO₂; (c) LNMO/25TiO₂A; (d) LNMO/250TiO₂A

The morphologies of the LNMO/nTiO$_2$ samples were characterized using SEM and the typical images are shown in Figure1. The bare LNMO particles show very smooth surfaces with well-defined edges (Figure 4.1a). Each primary LNMO particle has a spherical shape with a diameter of around 10-20 μm and is composed of many secondary particles of around 500 nm (Figure SI4.1). Comparing with the bare LNMO, the LNMO/25TiO$_2$ particles shown in Figure 1b present slightly rougher surfaces, due to the presence of TiO$_2$

layer. The TiO₂ coated particles show a noticeable morphology change after post-annealing treatment. Smaller particles (around 50 nm) appear on the surface, and their density is very high on the LNMO/250TiO₂A sample. The occurrence of such particles suggests that the TiO₂ layer underwent some changes during post-annealing process, which will be discussed in following sections.
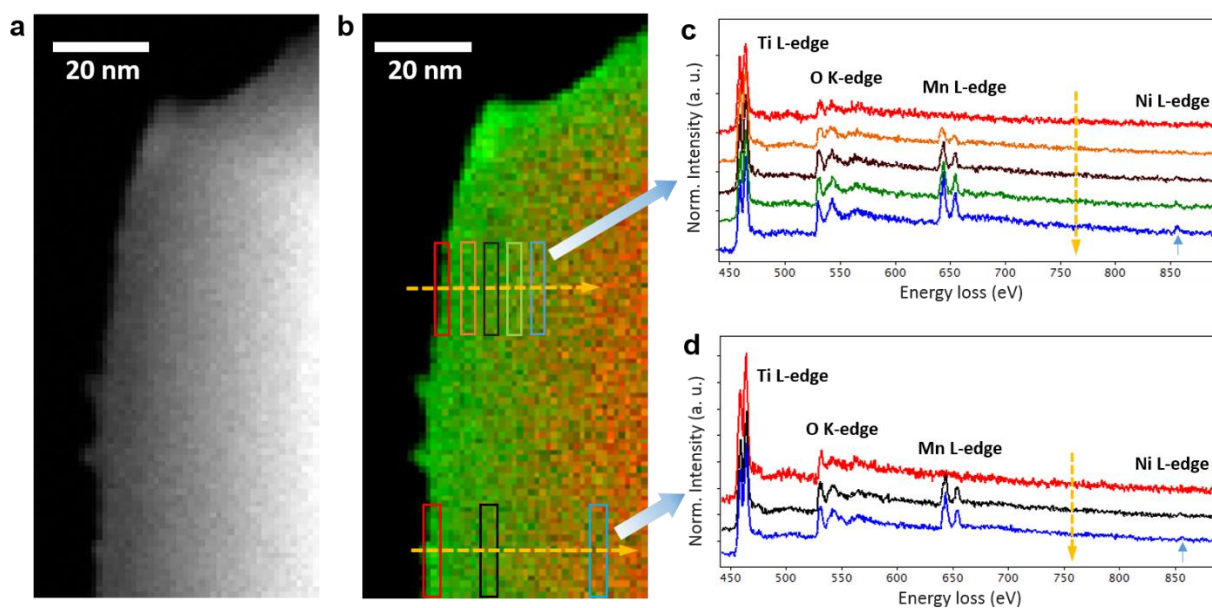
Figure 4.2 EELS map taken from a LNMO/250TiO₂ particle. (a) HAADF-STEM image of the LNMO/250TiO₂ particle. (b) EELS map for the LNMO/250TiO₂ particle (Ti: green; Mn: red). (c, d) EELS spectra integrated from the corresponding areas shown in (b).

The TiO₂ deposition via ALD has been characterized by EELS mapping of the LNMO/250TiO₂ sample. As can be seen from the EELS spectra in Figure 4.2b, only Ti and O are observed at the outermost layer suggesting that a TiO₂ layer has been deposited onto the LNMO particle. The Ti L-edge is still visible when approaching into the bulk of the particle, where Mn and Ni L-edges show up. Since the data collected from each region of interest (ROI) is a 3D projection of that region from the sphere (particle), the EELS spectrum acquired from those bulk ROI windows (shown in Figure 4.2b) is actually a projection of the whole particle, therefore, the observation of Ti from the bulk ROIs indicates that the whole LNMO surface is well covered by the TiO₂ coating. This is further

confirmed by looking into different particles, as shown in Figure S2. The sample with 250 ALD cycles shows a surface TiO_2 layer with the thickness of about 5-10 nm among different particles. In addition, the O K-edge in the metal oxide mainly corresponds to the transition of the O *1s* state to the O *2p* state which is hybridized with the transition metal *3d* and *4sp* orbitals.[40] The peak shape does not show significant change from the surface to the bulk, indicating that the O atoms are simply present in the forms of TM-O octahedra in TiO_2 and LNMO.
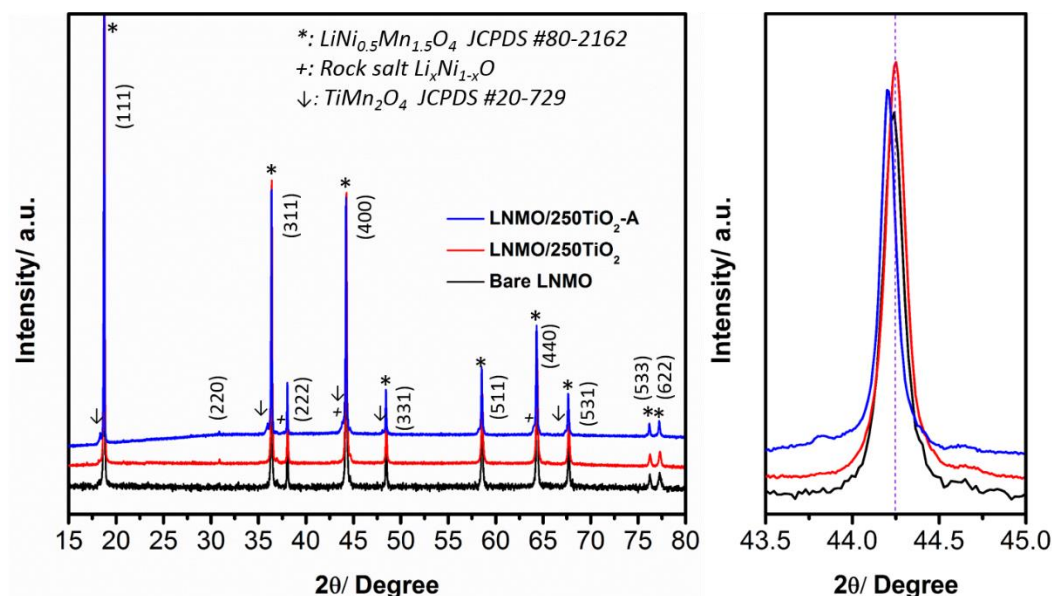
Figure 4.3 XRD patterns of (a) bare LNMO, LNMO/250TiO₂ and LNMO/250TiO₂A

The structures of the samples were investigated by XRD, as shown in Figure 4.3. The bare LNMO can be well indexed to the cubic spinel structure with an $Fd\bar{3}m$ space group, in which Mn and Ni randomly occupy the octahedral 16d sites, O occupies the 32e sites and Li occupies the tetrahedral 8a sites.[2] The presence of oxygen vacancies leads to the existence of Jahn-Teller active Mn^{3+}.[41] No TiO_2 peaks can be found in the LNMO/250TiO₂ sample, most likely due to the thin and amorphous nature of the TiO_2 layer. However, significant difference can be observed on the LNMO/250TiO₂A sample. Some new peaks emerged in the XRD pattern of LNMO/250TiO₂A. Impurity rock salt phase $Li_xNi_{1-x}O$ peaks at $2\theta \approx 37°$, $43°$ and $64°$ marked with "+" symbol appeared on the XRD patterns.[42, 43] Peaks marked with "↓" are indexed to the TMO − like inverse spinel

phase, more details regarding this phase will be discussed below. The figure on the right shows an enlarged degree range between 43.5 and 45°, in which the LNMO/250TiO$_2$A sample clearly shows a shift to lower angles. This shift suggests that part of the Ti has doped into the LNMO lattice and resulted in slight lattice parameter change.
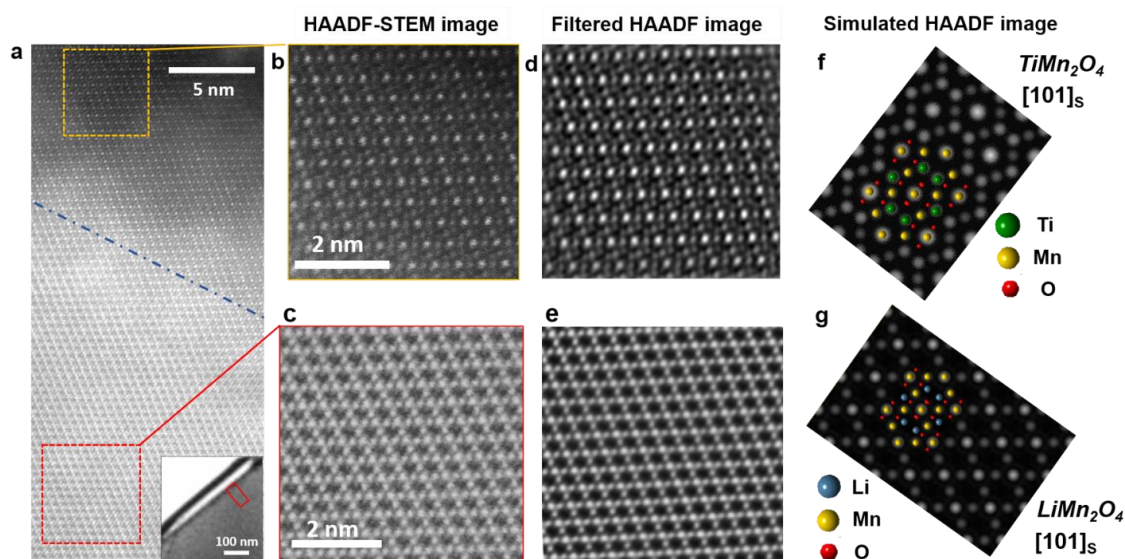
Figure 4.4 (a) HAADF-STEM image of LNMO/250TiO$_2$A particle acquired near the surface, the corresponding region is shown in the inset image. (b, c) Atomic-resolution HAADF-STEM images showing the lattice structure of the outermost layer and the inner region of the particle, respectively. (d, e) Processed images corresponding to the HAADF-STEM images shown in (b, c) with a band-pass filter applied. (f, g) Simulated HAADF images of LiMn$_2$O$_4$ and TiMn$_2$O$_4$.

A structural change is observed near the surface of the TiO$_2$ coated LNMO particle after post heat-treatment. Figure 4.4a shows the HADDF-STEM image of a LNMO/250TiO$_2$A particle from the surface to the bulk. The bulk of the particle maintains the LiM$_2$O$_4$ type $Fd\bar{3}m$ spinel structure (M = Mn and Ni), as shown in the corresponding HAADF-STEM image (Figure 4c) viewing along the [010] zone axis, with Li occupying the 8a tetrahedral sites and transition metal atoms occupying the 16d octahedral sites. Note that the bright atomic columns seen in the HAADF image are the transition metal atom, while the light elements are not visible from the image. Figure 4.4g shows a simulated HADDF image in the [101] zone projection of the LiMn$_2$O$_4$ phase which is consistent with the experimental

data. Interestingly, a noticeable change in the intensity of Li sites is observed near the particle surface from Figure 4.4g, which becomes brighter and visible, indicating that the Li tetrahedral sites are occupied by heavier transition metal atoms. A high-resolution HAADF-STEM image representing the surface structure is shown in Figure 4.4b with the corresponding filtered image shown in Figure 4.4d that enables a clearer view of the transition metal atoms. This near-surface lattice can be indexed to the [010] zone axis of a TMO-like inverse spinel phase with transition metal occupying both the octahedral and tetrahedral sites. The simulated HAADF image of the TMO phase is in good agreement with the experimental data, as shown in Figure 4.4f.
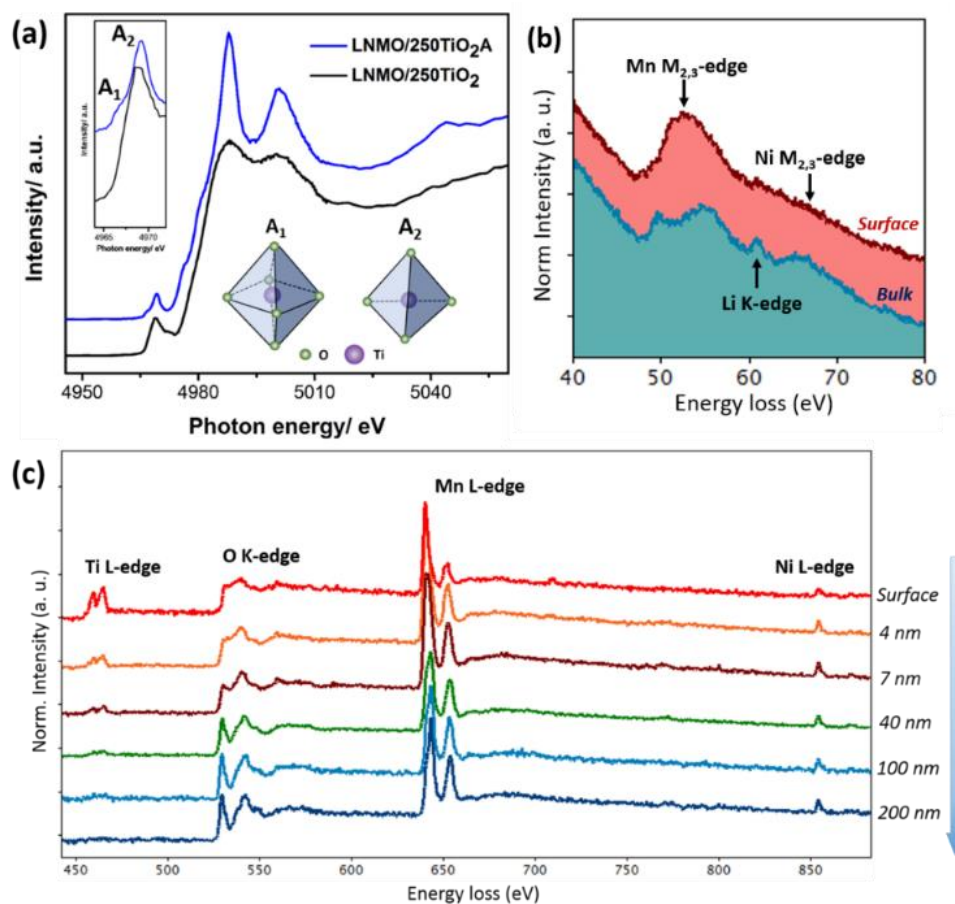
Figure 4.5 (a) XANES spectra of Ti K edges of LNMO/250TiO$_2$ and LNMO/250TiO$_2$A collected at FLY mode (inset: enlarged pre-edge regions; schematics showing tetrahedral and octahedral Ti); (b) EELS spectra of the Mn M-edge and Li K-edge

on the surface and bulk; (c) EELS depth profile of the LNMO/250TiO$_2$A particle from the surface to the bulk.

The coordination environment of Ti before and after annealing is further evaluated by the Ti K-edge XANES collected from LNMO/250TiO$_2$ and LNMO/250TiO$_2$A samples. Figure 4.5a shows the XANES collected at fluorescence yield (FLY) mode, which has a detection depth of up to 100 nm, so that one can obtain the information from the sub-surfaces of the material.[44, 45] The as-deposited LNMO/250TiO$_2$ shows a typical amorphous TiO$_2$ spectra with a broad feature.[46] However, upon post-annealing, the main edge became well-resolved and two clearly identifiable peaks, namely A$_1$ and A$_2$ arose in the pre-edge region. Pre-edge features in Ti K-edge XANES are always employed as an indication of the Ti coordination numbers since these 1s-3d quadruple transitions are very sensitive to the local environment in terms of symmetry and coordination number.[46] A$_1$ is normally assigned to the octahedral Ti^{4+}, which has a dipole-forbidden 1s-3d t$_{2g}$ transition, while peak A$_2$ is generally attributed to the transition of the 1s electron into hybridized Ti 3d/4p states, which has an e$_g$ symmetry. As has been suggested by Miller et al., the intensity of the A$_2$ peak is correlated to the coordination number since it originates from the Ti 3d/4p coordination.[47] A higher A$_2$ peak gives lower coordination number, i.e. more tetrahedral Ti^{4+}.[46] A scrutiny of the spectra features also reveals that the Ti K-edge XANES in the LNMO/250TiO$_2$A sample differs from the Ti K-edge XANES of either rutile or anatase TiO$_2$ as shown in Figure S9a. The extra pre-edge peak appearing at higher energy than the A$_2$ peak in TiO$_2$ XANES is attributed to the transition of 1s electron into 3d states of adjacent Ti^{4+} cations and its intensity is proportional to the coordination number.[47] The disappearance of this peak in the Ti K-edge XANES of LNMO/250TiO$_2$A indicates that some of the Ti^{4+} occupy the tetrahedral sites where Li ions resided previously. Generally, Ti^{4+} is hardly found to occupy the tetrahedral sites, but exceptions have been observed when there is Ni^{2+} in the spinel, since Ni^{2+} has high octahedral site preference because it has high crystal field stabilization energy whereas Ti^{4+} has no preference because it has an empty 3d orbital (see Figure SI4.5 for details).[48] The presence of Ni^{2+} in LiNi$_{0.5}$Mn$_{1.5}$O$_4$ might also explain why only octahedrally coordinated Ti was found in the case of surface doping of LiMn$_2$O$_4$ by Ti as reported by Amine et al.[49] Besides, a small portion of the Ti^{4+} are octahedrally coordinated, indicating that the Ti has replaced part of the bulk Mn/Ni

and formed a $LiTi_xNi_{0.5}Mn_{1.5-x}O_4$ phase, this complies well with the XRD results, where peak shift was observed. Partial occupation of Ti in octahedral sites of TMO-like phase is also a possible explanation to the A_1 peak.

In addition, the new phase is further confirmed by the EELS spectrum acquired from the surface region of the LNMO/250TiO$_2$A particle, as shown in Figure 4.5c. Both Ti and Mn are observed from the surface region with a small amount of co-existing Ni, which is consistent with the surface structural indexation of the TMO-like inverse spinel phase with Ti substituting into the 8a tetrahedral sites. Furthermore, a significant change in the Li K-edge is observed from the bulk to the surface of the annealed particle. The intensive Li K-edge presents in the bulk is not detected in the surface layer, as shown in Figure 4.5b, indicating that the surface TMO-like inverse spinel phase formed after annealing does not contain Li. According to the EELS quantification, the ratio between Mn:Ni:Ti:O is 28:5:6:61, we may conclude that the tetrahedral sites are cation deficient. The Ti concentration decreases dramatically when approaching from the outermost surface to the bulk, whereas a weak Ti L-edge signal is still observed beyond 40nm depth, suggesting that the diffusion of Ti is rather vigorous under such post-annealing conditions. Besides, the Mn L-edge acquired from the bulk to the surface exhibits a clear chemical shift of ~3 eV towards lower energy and the L_3/L_2 ratio of the Mn L-edge decreases dramatically. It is generally accepted that the energy shift and the relative intensity of the two peaks in Mn L-edge are correlated with the oxidation level of the Mn ions.[50, 51] Therefore, it can be concluded from the spectra that the oxidation level of the Mn from the bulk to the surface varies, with predominantly Mn^{2+} near the surface and Mn^{3+}/Mn^{4+} in the bulk. The reduction of Mn ions can be ascribed to the charge balance with the incorporation of Ti^{4+}. It was reported from a previous study that the end member of Ti doping into $LiMn_2O_4$ was $LiMn_{0.5}Ti_{1.5}O_4$, in which Mn was reduced to divalent state.[50] The O K-edge EELS spectra is also shown in Figure 4.5c. It is noticed that the peak features of the O K-edge vary greatly when approaching the surface. It has been reported that the reduction of transition metals will result in an intensity decrease of the O pre-edge since the O *2p* state is highly hybridized with the transition metal *3d* states,[40] thus the significant drop of the O pre-peak is consistent with the Mn reduction observed from the Mn L-edge. The O K-

edge feature resembles a TiM_2O_4 (M = metals) O K-edge as has been reported by Fleet et al.[52]

The above observations clearly indicate that TiO_2 was deposited onto the surface of LNMO particle with controlled thickness and that upon post-annealing treatment, part of the Ti substituted the surface Li in the 8a tetrahedral sites and formed a layer with TMO – like inverse spinel structure. The Li, together with part of the Ni, formed a rock salt $Li_xNi_{1-x}O$ phase. Some Ti atoms were found to have diffused into deeper regions of the LNMO particle and occupied the 16d octahedral sites, leading to a slight lattice distortion. An EDX map of the surface tiny particle has been presented in Figure SI4.6, the particle was rich in Ti and Mn, indicating that with longer treatment time, the surface TMO-like phase tend to agglomerate into tiny particles. A schematic illustration of the process is demonstrated in Figure SI4.7.

4.3.2   Electrochemical Performance Study
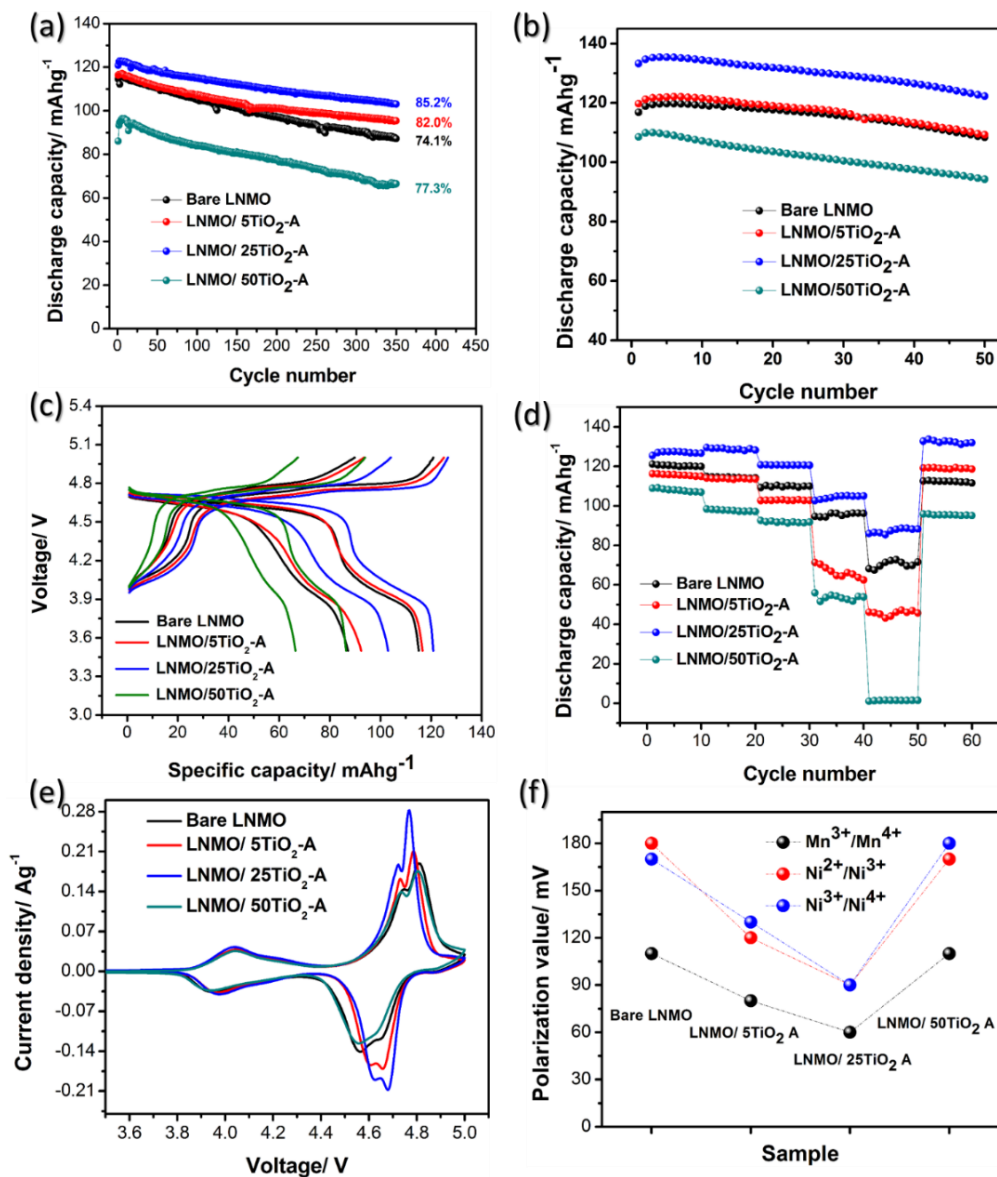
Figure 4.6 (a) Stability test at 0.5C under room temperature; (b) Stability test at 0.5C under 55°C; (c) 1st and 350th charge/discharge curves under RT; (d) Rate capability test at 0.1, 0.5, 1, 2, 5 and 0.1C under RT; (e) CV curves of the first cycle normalized by active materials weight; (f) Plots of the polarization potentials of the Mn³⁺/Mn⁴⁺, Ni²⁺/Ni³⁺ and Ni³⁺/Ni⁴⁺ redox couples calculated based on the CV curves; All of the spectra are based on sample: Bare LNMO, LNMO/5TiO₂A, LNMO/25TiO₂A and LNMO/50TiO₂A;

To reveal the impact of the TMO–like phase and surface Ti doping on the electrochemical performance of LNMO samples, charge/discharge measurements were carried out at both RT and 55°C. Figure 4.6a shows the cyclic stability of the samples at a current density of 0.5C under RT. Bare LNMO shows an initial discharge capacity of 116 mAhg^{-1}. The plateau at 4.0 V corresponds to the redox couple of Mn^{3+}/Mn^{4+} and it provides approximately 25% of the capacity, indicating that there exists a large amount of oxygen deficiencies in the lattice and the LNMO is in the phase of nonstoichiometric $Fd\bar{3}m$ crystallographic structure, which will lead to severe Jahn-Teller distortion that has an onset voltage of 4 V. However, after 350 charge/discharge cycles, its capacity retention was only 74.1%. Besides, the performance of LNMO/25TiO$_2$ without post-annealing treatment has been studied and shown in Figure SI4.8. An initial discharge of only 80 mAhg^{-1} was observed in the LNMO/25TiO$_2$ sample even though the stability also reached 85.2 %. The inferior performance of LNMO/25TiO$_2$ is probably due the insulating nature of TiO$_2$, which could hamper the Li ions and electron transportation, as schematically shown in Figure SI4.8d.[53] In contrast, the LNMO/25TiO$_2$A sample shows apparent improvement. The sample demonstrates increased discharge capacity as well as good stability with 85.2% capacity retention after 350 cycles, 10% higher than that of the bare LNMO. The improved capacity of LNMO/25TiO$_2$A compared with LNMO/25TiO$_2$ also suggests that the new surface formed after annealing has a better conductivity than amorphous TiO$_2$. Such improved kinetics can be presumably ascribed to the 8a tetrahedral vacancies in the TMO-like inverse spinel phase, which can significantly improve the Li ion diffusion rate compared to pure amorphous TiO$_2$ coating.[54, 55] Coulombic efficiencies shown in Figure SI4.10 also reveal that the electrolyte decomposition of the LNMO/25TiO$_2$A is much less severe than the bare LNMO. These results indicate that surface modification helps to suppress the side reactions between the LNMO particles and the electrolyte. Despite that the TMO–like phase is also possibly dissolvable in the electrolyte, the stronger Ti-O bond should enable much higher resistivity against the electrolyte than bare LNMO.[56, 57] The LNMO/5TiO$_2$A sample shows slightly improved capacity, but higher capacity retention than the bare LNMO after 350 cycles. In contrast, when the TiO$_2$ cycle number was increased to 50, the capacity in the LNMO/50TiO$_2$A sample dropped immediately with only 87 mAhg^{-1} initial discharge capacity, the stability is lower than the

bare LNMO or the samples with 5 and 25 ALD cycles either. This capacity drop reveals that the surface structure of the excessive TiO_2 coating on LNMO followed by annealing does not benefit the performance at all and could be ascribed to (1) the lattice distortion caused by overwhelming Ti substitution, as has been observed in bulk doping studies;[28] (2) increasing amount of the impurity $Li_xNi_{1-x}O_y$ rock salt phase; (3) overwhelming number of Ti^{4+} that replace Li^+ on 8a sites.[56] and (4) too much soluble Mn^{2+}. Moreover, the same test carried out under 55 ^{o}C is shown in Figure 4.6b, it can be seen that all of the capacity fading rates are rather close, this may be due to the fierce side reactions under such high operating temperature. Nevertheless, the discharge capacity follows the same trend as the test under RT, the LNMO/25TiO_2A sample shows even more remarkable improvement with an initial discharge capacity of over 130 mAhg^{-1}. The reason for this capacity improvement will be discussed below. It is reasonable that the overall capacity obtained under 55 ^{o}C is higher than that of the room temperature because the kinetics of the lithium ions is much more vigorous. The 1st and 350th charge/discharge curves displayed in Figure 6e reveal that the capacity mainly originates from three redox couples, Mn^{3+}/Mn^{4+} at 4V, Ni^{2+}/Ni^{3+} at 4.6V and Ni^{3+}/Ni^{4+} at 4.7V. Rate capability of the samples are shown in Figure 4.6d, it can be seen that the LNMO/25TiO_2A sample shows the best performance as well. More than 90 mAhg^{-1} discharge capacity can still be maintained under 5 C, whereas LNMO/50TiO_2A shows no capacity at all under this current density. In addition, LNMO/25TiO_2 shows a worse rate capability compared with the LNMO/25TiO_2A sample as shown in Figure SI4.8.

In order to further elucidate the redox couples, CV tests were also conducted under RT on these samples. The CV redox peaks support the charge/discharge curves observed in Figure 4.6c, redox couples of Mn^{3+}/Mn^{4+} at 4V, Ni^{2+}/Ni^{3+} at 4.6V and Ni^{3+}/Ni^{4+} at 4.7V are clearly shown. Also, the normalized intensity of the redox peaks fits well with the trend of the discharge capacities in Figure 4.6a. The potential polarizations of the redox couples are plotted in Figure 6f, the LNMO/25TiO_2A sample shows the lowest polarization in all of the three redox couples, revealing the optimized kinetics of the surface. The abovementioned electrochemical studies reveal that the controlled growth of the TMO – like phase is essential to the performance of LNMO, 25 ALD cycle number has demonstrated the most promising performance.
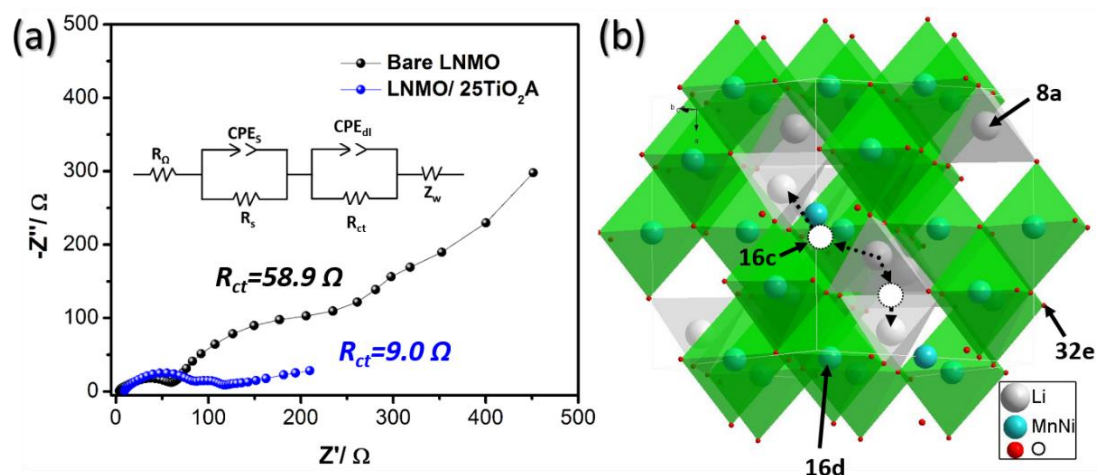
Figure 4.7 (a) EIS of bare LNMO and LNMO/25TiO₂A after initial charge to 5V; inset: an equivalent-circuit simulation model; (b) Structure of LNMO showing the lithium ions diffusion path

In an effort to understand the improved discharge capacity of the LNMO/25TiO$_2$A sample, electrochemical impedance spectra (EIS) were collected on both the bare LNMO and the LNMO/25TiO$_2$A samples after charging to 5V and holding for 3h. The EIS of the two charged cells of bare LNMO/Li and LNMO/25TiO$_2$A/Li samples are shown in Figure 4.7a, two semicircles from high to medium frequency and one inclined line at low frequency can be observed. The simulated equivalent circuit is presented as an inset. The R$_\Omega$ stands for the Ohmic resistance arose from the electrolyte, separator and other components. The semi-circle in the high frequency range represents the lithium diffusion across the surface film, simulated as a resistor R$_s$ and a constant phase element (CPE), the semi-circle in the medium frequency range shows the charge transfer reaction composed of a resistor R$_{ct}$ and another CPE, the inclined line is interpreted as the finite length Warburg impedance. In this case, the value of R$_s$ stands for the SEI resistance and R$_{ct}$ epitomizes the likely phase transformation on the surface of LNMO after initial charging. It can be seen that the bare LNMO shows a R$_{ct}$ value of 58.9 Ω, whereas the LNMO/25TiO$_2$A sample shows only 9.0 Ω. Lithium diffusion paths in the spinel structured LNMO is illustrated in Figure 4.7b, the lithium ions hop into adjacent empty 16c octahedral sites and then migrate into the next 8a tetrahedral site. Huang et al. reported that the surface of LNMO will transform into a

Mn_3O_4-like structure during the first charge due to cation (Ni/Mn) migration to the 8a tetrahedral sites, subsequent cation migration from 16d sites into the empty 16c octahedral sites leads to the formation of rocksalt-like structure that extends to the interior part of the particles, therefore the occupation of the empty 16c sites by transition metals will result in severe impedance buildup. They also suggested that pre-occupation of the lithium tetrahedral sites with a small amount of insoluble ions can stabilize the structure,[58] in this study, we have validated this assumption by using Ti to occupy the tetrahedral sites. Therefore, the formation of the TMO-like phase at the surface region after annealing with Ti substituting into the 8a tetrahedral site should play a key role in inhibiting the structural evolution of the LNMO cathode material during cycling.

The significant impedance difference between the abovementioned samples reveals that the presence of Ti in tetrahedral sites helps to prevent the LNMO cathode material from the surface structural transformation into a Mn_3O_4-like phase and subsequent formation of a rocksalt structure, such modification mitigates the impedance build-up that happens at the initial charge process, this explains why the LNMO/25TiO$_2$A sample shows higher capacity than bare LNMO under both RT and 55 ℃.
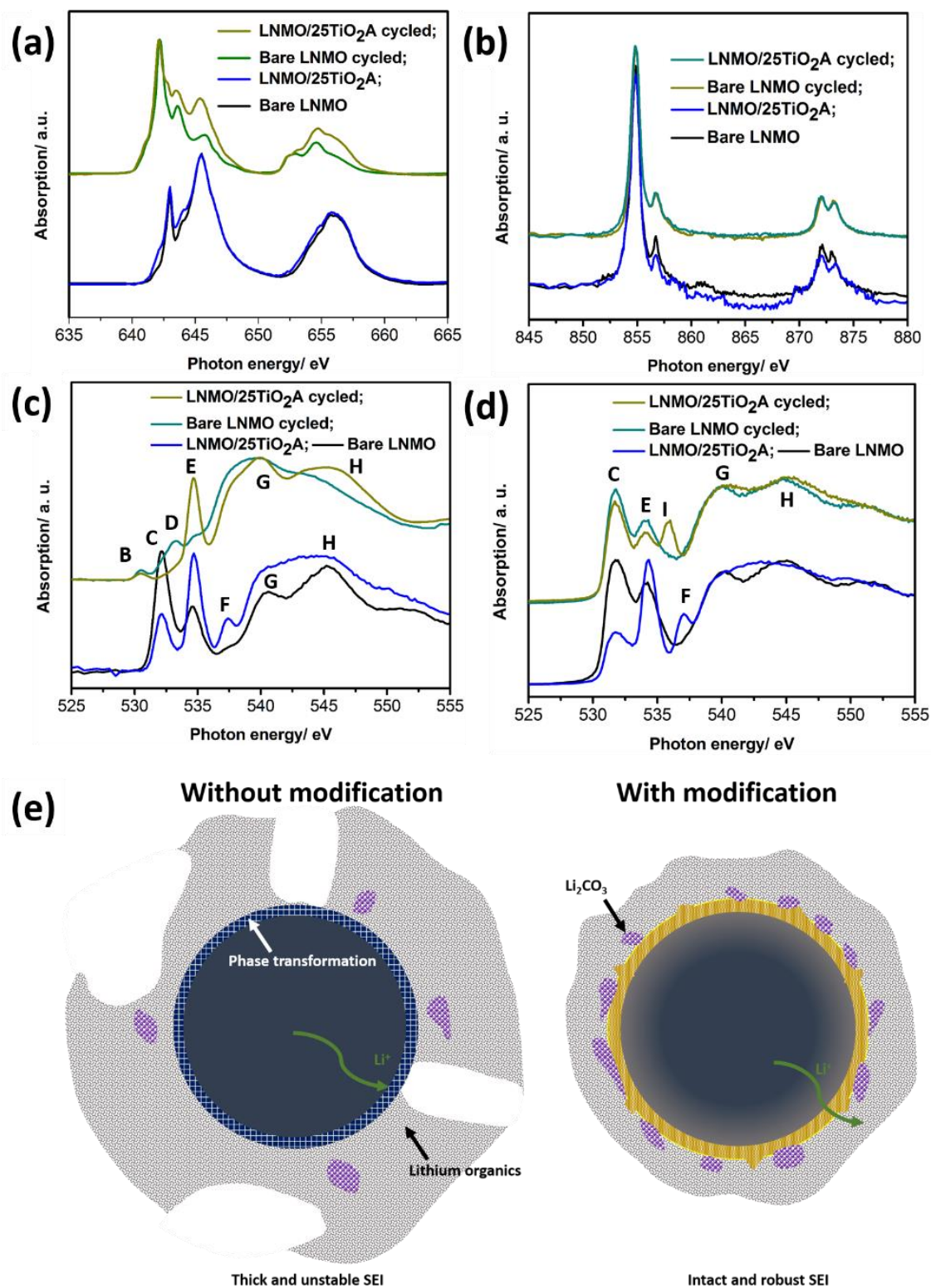
Figure 4.8 XANES spectra of the bare LNMO, LNMO/25TiO₂A, bare LNMO after 350 charge/discharge cycles and LNMO/25TiO₂A after 350 charge/discharge cycles

in (a) Mn L$_{3,2}$-edges collected at TEY mode; (b) Ni L$_{3,2}$-edges collected at TEY mode; (c) O K-edges collected at TEY mode; (d) O K-edges collected at FLY mode; (e) Schematic illustration of the bare LNMO and LNMO/25TiO$_2$A after 350 charge/discharge cycles.

In order to further unveil the phase transformation mechanism and the change of surface chemical states upon charging/discharging, the bare LNMO and LNMO-25TiO$_2$A samples were characterized using soft XANES and the results are shown in Figure 4.8a-d. Mn, Ni L$_{3,2}$-edges and O K-edges of the bare LNMO, LNMO/25TiO$_2$A, and electrochemically cycled bare LNMO and LNMO/25TiO$_2$A were recorded. Standard MnO, Mn$_2$O$_3$ and MnO$_2$ were also studied and their Mn L$_{3,2}$ XANES spectra are shown in Figure S9b, it can be seen that the relative intensity of the peaks correlates well with the oxidation state of the corresponding Mn oxides, which is in accordance with the EELS results shown above. Figure 4.8a shows the Mn L$_{3,2}$ edge XANES spectra of the referred samples. It can be seen that the samples before electrochemical cycling, whether bare or modified, show predominantly Mn^{4+} feature, with the presence of a small amount of Mn^{3+}, this is in correspondence with the electrochemically tests, where extra plateau at around 4.0 V was observed. A closer scrutiny reveals that the LNMO/25TiO$_2$A sample has extra shoulders at lower photon energy, this also proves the presence of Mn^{2+} and this is in agreement with the EELS results. Since this sample has a thin layer of TiO$_2$ with only 25 ALD cycles, the change in the peak feature is not as obvious as what was observed in the EELS results. Nevertheless, the Mn L$_{3,2}$ edge XANES shows a significant change after electrochemical cycling, the majority of the Mn ions are in the state of 2+ and, strikingly, the LNMO/25TiO$_2$A sample shows much more Mn^{4+} feature than the bare LNMO. A similar phenomenon has also been found in our previous work using FePO$_4$ as coating material to protect the LNMO surface.[59] We can therefore conclude that the presence of the TMO–like phase prevents the Mn in the LNMO from being heavily reduced so that more stable performance can be retained after the electrochemical cycling process.[60, 61] Mn L$_{3,2}$ edge XANES spectra collected at FLY mode shown in Figure S9c indicate that such reduction does not occur in the bulk. The Ni L$_{3,2}$ edge XANES spectra are shown in Figure 8b, it is apparent that the Ni does not show any changes in any of the samples, this is because Ni^{2+} is already in low valence state.[62] The F K edges of the cycled bare LNMO

and cycled LNMO/25TiO$_2$-A have also been shown in Figure SI4.9d, peaks other than the PVdF have emerged in the cycled bare LNMO. In addition, the sharp peaks at around 710-730 eV assigned to the L$_{3,2}$ edges of Fe in the cycled bare LNMO indicate that the HF amount was very high that even the coin cell cans were corroded. As has been mentioned before, TEY mode has a detection depth of ~5 nm, and this range falls into the thickness of the SEI, so the Mn, Ni L$_{3,2}$ edge XANES spectra of the cycled samples obtained in TEY mode also contain information from the solid electrolyte interphase (SEI).

Kostecki et al. proved that the transition metals mainly exist as fluorides and/or organic salts such as oxalate in the SEI layer,[63] indicating the absence of Me-O (Me = Mn, Ni) bonds. Therefore, the O K-edge XANES was collected to understand the composition of the SEI, as shown in Figure 4.8c where O K edge XANES spectra before electrochemical cycling show 5 features, labelled C, E, F, G and H. Features C and E in the pre-edge regions represent the excitation of O 1s electron to the hybridization of the O 2p with the transition metals 3d orbitals, and are believed to be related to t$_{2g}$ and e$_g$ symmetry respectively. The broader peaks G and H are due to the hybridization of the O 2p with the transition metals 4sp orbitals.[64, 65] It is noticed that feature F appears only in the LNMO/25TiO$_2$A sample. Actually the O K-edge threshold of Ti-O bonds appears at higher photon energy than Mn-O as has been discussed by F. de Groot,[64] therefore, the feature F corresponds to the e$_g$ symmetry of Ti-O and its t$_{2g}$ symmetry overlaps with the Mn-O and Ni-O e$_g$ symmetry, that is the reason why the intensity of feature E appears to be much higher than feature C after post annealing. The feature F can be seen in the FLY spectra as well, implying that the Ti-O hybridization exists in rather high depth, which is consistent with the EELS result discussed above. The samples were electrochemically cycled and dissembled so as to understand the oxygen species in the SEI layer.

The TEY spectra of the electrode samples show drastic difference after electrochemical cycling. The bare LNMO shows mostly weak peaks like B and D, they are assigned to the organic compounds in the SEI, whereas in the LNMO/25TiO$_2$A sample, features E, G and H still exist. These features are assigned to the hybridization of O 2p and Ni 3d orbitals, the 3d electron configuration of Ni^{2+} is $t_{2g}^6 e_g^2$, where the 3 t$_{2g}$ orbitals have been fully filled by electrons, therefore, no t$_{2g}$ peak is expected in Ni^{2+}, that is why only peak E is observed

in the pre-edge regions. Ni-O bonds are extremely weak when the LNMO is charged to high voltage since Ni^{4+} is highly electron-depleted, its catalytic effect facilitates the electrolyte decomposition.[35] We can therefore conclude that the transition metal dissolution in the electrochemically cycled bare LNMO sample is so intense that none of the surface Mn or Ni were in the form of oxides any more, whereas Ni-O bonds still exist in the LNMO/25TiO$_2$A sample since the incorporation of Ti^{4+} can possibly strengthen the Ni-O bond, as has been observed in Cabana's work of incorporating Mg^{2+} into the surface of LNMO.[35] Another possibility is that the rock salt $Li_xNi_{1-x}O$ phase remains on the surface, it acted as a protection agent against HF attack. Taking a look at the FLY spectra, one can find that the features C, E, F, G and H still exist, indicating that the loss of Me-O bonds mainly happens on the superficial surface. The area of peaks C and E is lower in the cycled LNMO/25TiO$_2$A than the cycled bare LNMO, indicating the presence of less oxygen 2p hybridization with TM 3d orbitals in the bulk, which complies with the reduction of Mn. A new peak "I" appears in the electrochemically cycled LNMO/25TiO$_2$A sample. This intensive peak has also been reported in many references where electrolyte additives were studied. It can be assigned to the π^* orbital of the C=O bond in Li_2CO_3.[66] Li_2CO_3 is a well-known favorable SEI component since it helps create a more robust and dense SEI layer, this can be another reason of the improved stability.[67-69] The Li_2CO_3 signal can be observed in FLY spectra but not TEY spectra, indicating that it mainly locates at the "inner" layer of the SEI which is closer to the surface of the electrode materials, probably because that Li_2CO_3 forms at the beginning of the electrochemical cycling.

To summarize the results above, we depict a schematic illustration in Figure 4.8e. The presence of spinel TMO–like phase and Ti occupation of octahedral sites in LNMO help create an SEI with more Li_2CO_3, strengthen the Ni-O bonds and prevent severe Mn reduction and dissolution during electrochemical cycling. The Li_2CO_3 helps build more robust SEI. The suppression of the reduction of Mn and the stronger Ni-O interaction help retain better surface consistency upon electrochemical cycling.

4.4 Conclusions

We have carried out a systematic study of the post-annealing effect on the performance of ALD-TiO$_2$ coated LNMO. It is found that the surface of the LNMO undergoes several

changes during the process: (1) partial Ti substitution of 8a Li tetrahedral sites, forming a TMO–like phase; (2) Li and Ni extrusion, forming rock salt $Li_xNi_{1-x}O$ phase; (3) Octahedrally coordinated Mn/Ni replacement by Ti in deeper region, resulting in slight doping of LNMO; (4) Aggregation of the TMO–like phase into tiny particles. Electrochemical studies reveal that the formation of the TMO-like inverse spinel phase on the surface through the substitution of Ti in the 8a tetrahedral sites will help undermine the impedance buildup resulting from the continuous phase change of the LNMO to rocksalt structure during electrochemical cycling. In addition, the presence of the substituted Ti strengthens the Ni-O bond. The TMO–like phase helps form an SEI with more desirable Li_2CO_3 and hampers the reduction of Mn after electrochemical cycling. More importantly, the effect of Ti substitution highly depends on the ALD cycle number, 25 ALD cycle appears to produce the optimal thickness that yields improved stability, Coulombic efficiency, discharge capacity and rate capability. Nevertheless, other factors such as annealing time and temperature are worthwhile to be further studied. This work has paved the path to controlled manipulation of surface structures on cathode materials, provided a novel explanation to the role of surface modification and extended the practice of ALD technique in LIBs and related research.

Acknowledgement

References

[1] J. B. Goodenough and K. S. Park, The Li-Ion Rechargeable Battery: A Perspective, *J. Am. Chem. Soc*., 2013, **135**, 1167-1176.

[2] A. Manthiram, K. Chemelewski and E. S. Lee, A Perspective on the High-Voltage $LiMn_{1.5}Ni_{0.5}O_4$ Spinel Cathode for Lithium-Ion Batteries, *Energy Environ. Sci*., 2014, **7**, 1339-1350.

[3] A. Kraytsberg and Y. Ein-Eli, Higher, Stronger, Better… a Review of 5 Volt Cathode Materials for Advanced Lithium-Ion Batteries, *Adv. Energy Mater.*, 2012, **2**, 922-939.

[4] Y. Shao-Horn, S. A. Hackney, A. J. Kahaian, K. D. Kepler, E. Skinner, J. T. Vaughey and M. M. Thackeray, Structural Fatigue in Spinel Electrodes in $Li/Li_x[Mn_2]O_4$ Cells, *J. Power Sources*, 1999, **81-82**, 496-499.

[5] T. Eriksson, T. Gustafsson and J. O. Thomas, Surface Structure of $LiMn_2O_4$ Electrodes, *Electrochem. Solid St*., 2002, **5**, A35.

[6] K. Y. Chung and K.-B. Kim, Investigations into Capacity Fading as a Result of a Jahn–Teller Distortion in 4V $LiMn_2O_4$ Thin Film Electrodes, *Electrochim. Acta*, 2004, **49**, 3327-3337.

[7] P. Arora, Capacity Fade Mechanisms and Side Reactions in Lithium-Ion Batteries, *J. Electrochem. Soc*., 1998, 145, 3647.

[8] K. Xu, Nonaqueous Liquid Electrolytes for Lithium-Based Rechargeable Batteries, *Chem. Rev.*, 2004, **104**, 4303-4418.

[9] D. H. Jang, Dissolution of Spinel Oxides and Capacity Losses in 4 V Li / LixMn$_2$O$_4$ Cells, *J. Electrochem. Soc*., 1996, **143**, 2204.

[10] F. Lin, I. M. Markus, D. Nordlund, T. C. Weng, M. D. Asta, H. L. Xin and M. M. Doeff, Surface Reconstruction and Chemical Evolution of Stoichiometric Layered Cathode Materials for Lithium-Ion Batteries, *Nat. Commun*., 2014, **5**, 3529.

[11] J. Cho, Y. J. Kim and B. Park, Novel LiCoO$_2$ Cathode Material with Al$_2$O$_3$ Coating for a Li Ion Cell, *Chem. Mater*., 2000, **12**, 3788-3791.

[12] J. S. Kim, C. S. Johnson, J. T. Vaughey, S. A. Hackney, K. A. Walz, W. A. Zeltner, M. A. Anderson and M. M. Thackeray, The Electrochemical Stability of Spinel Electrodes Coated with ZrO$_2$, Al$_2$O$_3$, and SiO$_2$ from Colloidal Suspensions, *J. Electrochem. Soc*., 2004, **151**, A1755.

[13] S.-T. Myung, K. Izumi, S. Komaba, Y.-K. Sun, H. Yashiro and N. Kumagai, Role of Alumina Coating on Li−Ni−Co−Mn−O Particles as Positive Electrode Material for Lithium-Ion Batteries, *Chem. Mater*., 2005, **17**, 3695-3704.

[14] Z. Wang, E. Liu, C. He, C. Shi, J. Li and N. Zhao, Effect of Amorphous FePO$_4$ Coating on Structure and Electrochemical Performance of Li$_{1.2}$Ni$_{0.13}$Co$_{0.13}$Mn$_{0.54}$O$_2$ as Cathode Material for Li-Ion Batteries, *J. Power Sources*, 2013, **236**, 25-32.

[15] Y. Kim, N. J. Dudney, M. Chi, S. K. Martha, J. Nanda, G. M. Veith and C. Liang, A Perspective on Coatings to Stabilize High-Voltage Cathodes: LiMn$_{1.5}$Ni$_{0.5}$O$_4$ with Sub-Nanometer LiPON Cycled with LiPF$_6$ Electrolyte, *J. Electrochem. Soc*., 2013, **160**, A3113-A3125.

[16] H. G. Song, K.-S. Park and Y. J. Park, The Effects of $LaPO_4$ Coating on the Electrochemical Properties of $Li[Ni_{0.5}Co_{0.2}Mn_{0.3}]O_2$ Cathode Material, *Solid State Ionics*, 2012, **225**, 532-537.

[17] J. Chong, S. Xun, J. Zhang, X. Song, H. Xie, V. Battaglia and R. Wang, Li_3PO_4-Coated $LiNi_{0.5}Mn_{1.5}O_4$: A Stable High-Voltage Cathode Material for Lithium-Ion Batteries, *Chemistry*, 2014, **20**, 7479-7485.

[18] J. Zheng, M. Gu, J. Xiao, B. J. Polzin, P. Yan, X. Chen, C. Wang and J.-G. Zhang, Functioning Mechanism of AlF_3 Coating on the Li- and Mn-Rich Cathode Materials, *Chem. Mater.*, 2014, **26**, 6320-6327.

[19] H. J. Lee and Y. J. Park, Interface Characterization of MgF_2-Coated $LiCoO_2$ Thin Films, *Solid State Ionics*, 2013, **230**, 86-91.

[20] S.-T. Myung, S. Komaba and N. Kumagai, Enhanced Structural Stability and Cyclability of Al-Doped $LiMn_2O_4$ Spinel Synthesized by the Emulsion Drying Method, *J. Electrochem. Soc.*, 2001, **148**, A482.

[21] M.-H. Liu, H.-T. Huang, C.-M. Lin, J.-M. Chen and S.-C. Liao, Mg Gradient-Doped $LiNi_{0.5}Mn_{1.5}O_4$ as the Cathode Material for Li-Ion Batteries, *Electrochim. Acta*, 2014, **120**, 133-139.

[22] K. R. Chemelewski, W. Li, A. Gutierrez and A. Manthiram, High-Voltage Spinel Cathodes for Lithium-Ion Batteries: Controlling the Growth of Preferred Crystallographic Planes through Cation Doping, *J. Mater. Chem. A*, 2013, **1**, 15334.

[23] S. J. R. Prabakar, S. C. Han, S. P. Singh, D. K. Lee, K.-S. Sohn and M. Pyo, W-Doped LiW$_x$Ni$_{0.5}$Mn$_{1.5-x}$O$_4$ Cathodes for the Improvement of High Rate Performances in Li Ion Batteries, *J. Power Sources*, 2012, 209, 57-64.

[24] H. Wang, T. A. Tan, P. Yang, M. O. Lai and L. Lu, High-Rate Performances of the Ru-Doped Spinel LiNi$_{0.5}$Mn$_{1.5}$O$_4$: Effects of Doping and Particle Size, *J. Phys. Chem. C*, 2011, **115**, 6102-6110.

[25] J. Liu and A. Manthiram, Understanding the Improved Electrochemical Performances of Fe-Substituted 5 V Spinel Cathode LiMn$_{1.5}$Ni$_{0.5}$O$_4$, *J. Phys. Chem. C*, 2009, **113**, 15073-15079.

[26] M. Lin, S. H. Wang, Z. L. Gong, X. K. Huang and Y. Yang, A Strategy to Improve Cyclic Performance of LiNi$_{0.5}$Mn$_{1.5}$O$_4$ in a Wide Voltage Region by Ti-Doping, *J. Electrochem. Soc.*, 2013, **160**, A3036-A3040.

[27] A. Höweling, S. Glatthaar, D. Nötzel and J. R. Binder, Evidence of Loss of Active Lithium in Titanium-Doped LiNi$_{0.5}$Mn$_{1.5}$O$_4$/Graphite Cells, *J. Power Sources*, 2015, **274**, 1267-1275.

[28] R. Alcántara, M. Jaraba, P. Lavela, J. L. Tirado, P. Biensan, A. de Guibert, C. Jordy and J. P. Peres, Structural and Electrochemical Study of New LiNi$_{0.5}$Ti$_x$Mn$_{1.5-x}$O$_4$ Spinel Oxides for 5-V Cathode Materials, *Chem. Mater.*, 2003, **15**, 2376-2382.

[29] J. H. Kim, S. T. Myung, C. S. Yoon, I. H. Oh and Y. K. Sun, Effect of Ti Substitution for Mn on the Structure of LiNi$_{0.5}$Mn$_{1.5-x}$Ti$_x$O$_4$ and Their Electrochemical Properties as Lithium Insertion Material, *J. Electrochem. Soc.*, 2004, **151**, A1911.

[30] K. Y. Chung, W.-S. Yoon, H. S. Lee, X.-Q. Yang, J. McBreen, B. H. Deng, X. Q. Wang, M. Yoshio, R. Wang, J. Gui and M. Okada, Comparative Studies between Oxygen-Deficient $LiMn_2O_4$ and Al-Doped $LiMn_2O_4$, *J. Power Sources*, 2005, **146**, 226-231.

[31] J. Cho, Y. J. Kim and B. Park, $LiCoO_2$ Cathode Material That Does Not Show a Phase Transition from Hexagonal to Monoclinic Phase, *J. Electrochem. Soc*., 2001, **148**, A1110.

[32] J. Cho, T.-J. Kim and B. Park, The Effect of a Metal-Oxide Coating on the Cycling Behavior at 55°C in Orthorhombic $LiMnO_2$ Cathode Materials, *J. Electrochem. Soc*., 2002, **149**, A288.

[33] S. Verdier, L. El Ouatani, R. Dedryvère, F. Bonhomme, P. Biensan and D. Gonbeau, XPS Study on Al_2O_3- and $AlPO_4$-Coated $LiCoO_2$ Cathode Material for High-Capacity Li Ion Batteries, *J. Electrochem. Soc*., 2007, **154**, A1088.

[34] L. Dahéron, R. Dedryvère, H. Martinez, D. Flahaut, M. Ménétrier, C. Delmas and D. Gonbeau, Possible Explanation for the Efficiency of Al-Based Coatings on $LiCoO_2$: Surface Properties of $LiCo_{1-x}Al_xO_2$solid Solution, *Chem. Mater*., 2009, **21**, 5607-5616.

[35] G. Alva, C. Kim, T. Yi, J. B. Cook, L. Xu, G. M. Nolis and J. Cabana, Surface Chemistry Consequences of Mg-Based Coatings on $LiNi_{0.5}Mn_{1.5}O_4$ Electrode Materials Upon Operation at High Voltage, *J. Phys. Chem. C*, 2014, **118**, 10596-10605.

[36] J.-H. Shim, S. Lee and S. S. Park, Effects of MgO Coating on the Structural and Electrochemical Characteristics of $LiCoO_2$ as Cathode Materials for Lithium Ion Battery, *Chem. Mater*., 2014, **26**, 2537-2543.

[37] X. Li, J. Liu, M. N. Banis, A. Lushington, R. Li, M. Cai and X. Sun, Atomic Layer Deposition of Solid-State Electrolyte Coated Cathode Materials with Superior High-Voltage Cycling Behavior for Lithium Ion Battery Application, *Energy Environ. Sci*., 2014, **7**, 768.

[38] X. Li, J. Liu, X. Meng, Y. Tang, M. N. Banis, J. Yang, Y. Hu, R. Li, M. Cai and X. Sun, Significant Impact on Cathode Performance of Lithium-Ion Batteries by Precisely Controlled Metal Oxide Nanocoatings Via Atomic Layer Deposition, *J. Power Sources*, 2014, **247**, 57-69.

[39] C. Marichy, M. Bechelany and N. Pinna, Atomic Layer Deposition of Nanostructured Materials for Energy and Environmental Applications, *Adv. Mater*., 2012, **24**, 1017-1032.

[40] D. Qian, B. Xu, M. Chi and Y. S. Meng, Uncovering the Roles of Oxygen Vacancies in Cation Migration in Lithium Excess Layered Oxides, *Phys. Chem. Chem. Phys*., 2014, **16**, 14665-14668.

[41] M. Arroyo y de Dompablo, C. Marianetti, A. Van der Ven and G. Ceder, Jahn-Teller Mediated Ordering in Layered Li_xMO_2 Compounds, *Phys. Rev. B*, 2001, **63**.

[42] J.-H. Kim, N. P. W. Pieczonka, Y.-K. Sun and B. R. Powell, Improved Lithium-Ion Battery Performance of $LiNi_{0.5}Mn_{1.5-x}Ti_xO_4$ High Voltage Spinel in Full-Cells Paired with Graphite and $Li4Ti5O_{12}$ Negative Electrodes, *J. Power Sources*, 2014, **262**, 62-71.

[43] M.-L.-P. Le, P. Strobel, F. Alloin and T. Pagnier, Influence of the Tetravalent Cation on the High-Voltage Electrochemical Activity of $LiNi_{0.5}Mn_{1.5}O_4$ Spinel Cathode Materials, *Electrochim. Acta*, 2010, **56**, 592-599.

[44] A. Erbil, I. G. Cargill, R. Frahm and R. F. Boehme, Total-Electron-Yield Current Measurements for near-Surface Extended X-Ray-Absorption Fine Structure, *Phys. Rev. B*, 1988, **37**, 2450-2464.

[45] J. Jaklevic, J. A. Kirby, M. P. Klein, A. S. Robertson, G. S. Brown and P. Eisenberger, Fluorescence Detection of Exafs: Sensitivity Enhancement for Dilute Species and Thin Films, *Solid State Commun*., 1977, **23**, 679-682.

[46] T. Hiratoko, A. Yoshiasa, T. Nakatani, M. Okube, A. Nakatsuka and K. Sugiyama, Temperature Dependence of Pre-Edge Features in Ti K-Edge Xanes Spectra for $ATiO_3$ (a = Ca and Sr), A_2TiO_4 (a = Mg and Fe), TiO_2 Rutile and TiO_2 Anatase, *J. Synchrotron. Radiat*, 2013, **20**, 641-643.

[47] D. T. Murphy, S. Schmid, J. R. Hester, P. E. Blanchard and W. Miiller, Coordination Site Disorder in Spinel-Type $LiMnTiO_4$, *Inorg. Chem*., 2015, **54**, 4636-4643.

[48] G. A. Lager, T. Armbruster, F. K. Ross, F. J. Rotella and J. D. Jorgensen, Neutron Powder Diffraction Study of Defect Spinel Structures: Tetrahedrally Coordinated Ti^{4+} in $Ni_{2.62}Ti_{0.69}O_4$ and $Ni_{2.42}Ti_{0.74}Si_{0.05}O_4$, *J. Appl. Crystallogr*., 1981, **14**, 261-264.

[49] J. Lu, C. Zhan, T. Wu, J. Wen, Y. Lei, A. Kropf, H. Wu, D. Miller, J. Elam, Y. Sun, X. Qiu and K. Amine, Effectively Suppressing Dissolution of Manganese from Spinel Lithium Manganate via A Nanoscale Surface-doping Approach, *Nat. Commun*., 2014, **5**, 5693-5700

[50] K. Petrov, R. M. Rojas, P. J. Alonso, J. M. Amarilla, M. G. Lazarraga and J. M. Rojo, Cation Distribution and Phase Transformations in $LiMn_{2-y}Ti_yO_4$ Solid Solutions, *Solid State Sci.*, 2005, **7**, 277-286.

[51] J. H. Paterson and O. L. Krivanek, ELNES of 3d Transition-Metal Oxides, *Ultramicroscopy*, 1990, **32**, 319-325.

[52] G. S. Henderson, X. Liu and M. E. Fleet, Titanium Coordination in Silicate Glasses Investigated Using O K-Edge X-Ray Absorption Spectroscopy, *Mineral. Mag.*, 2003, **67**, 597-607.

[53] Y. S. Jung, A. S. Cavanagh, L. A. Riley, S. H. Kang, A. C. Dillon, M. D. Groner, S. M. George and S. H. Lee, Ultrathin Direct Atomic Layer Deposition on Composite Electrodes for Highly Durable and Safe Li-Ion Batteries, *Adv. Mater.*, 2010, **22**, 2172-2176.

[54] Z. Moorhead-Rosenberg, A. Huq, J. B. Goodenough and A. Manthiram, Electronic and Electrochemical Properties of $Li_{1-x}Mn_{1.5}Ni_{0.5}O_4$spinel Cathodes as a Function of Lithium Content and Cation Ordering, *Chem. Mater.*, 2015, **27**, 6934-6945.

[55] K. Hoang, Understanding the Electronic and Ionic Conduction and Lithium over-Stoichiometry in $LiMn_2O_4$ Spinel, *J. Mater. Chem. A*, 2014, **2**, 18271-18280.

[56] S. Wang, J. Yang, X. Wu, Y. Li, Z. Gong, W. Wen, M. Lin, J. Yang and Y. Yang, Toward High Capacity and Stable Manganese-Spinel Electrode Materials: A Case Study of Ti-Substituted System, *J. Power Sources*, 2014, **245**, 570-578.

[57] R. Chen, M. Knapp, M. Yavuz, R. Heinzmann, D. Wang, S. Ren, V. Trouillet, S. Lebedkin, S. Doyle, H. Hahn, H. Ehrenberg and S. Indris, Reversible Li^+ Storage in a $LiMnTiO_4$ Spinel and Its Structural Transition Mechanisms, *J. Phys. Chem. C*, 2014, **118**, 12608-12616.

[58] M. Lin, L. Ben, Y. Sun, H. Wang, Z. Yang, L. Gu, X. Yu, X.-Q. Yang, H. Zhao, R. Yu, M. Armand and X. Huang, Insight into the Atomic Structure of High-Voltage Spinel $LiNi_{0.5}Mn_{1.5}O_4$ Cathode Material in the First Cycle, *Chem. Mater.*, 2015, **27**, 292-303.

[59] B. Xiao, J. Liu, Q. Sun, B. Wang, M. N. Banis, D. Zhao, Z. Wang, R. Li, X. Cui, T.-K. Sham and X. Sun, Unravelling the Role of Electrochemically Active Fepo4coating by Atomic Layer Deposition for Increased High-Voltage Stability of $LiNi_{0.5}Mn_{1.5}O_4$ Cathode Material, *Adv. Sci.*, 2015, **2**, 1500022-1500027.

[60] N. P. W. Pieczonka, Z. Y. Liu, P. Lu, K. L. Olson, J. Moote, B. R. Powell and J. H. Kim, Understanding Transition-Metal Dissolution Behavior in $LiNi_{0.5}Mn_{1.5}O_4$ High-Voltage Spinel for Lithium Ion Batteries, *J. Phys. Chem. C*, 2013, **117**, 15947-15957.

[61] C. Zhan, J. Lu, A. Jeremy Kropf, T. Wu, A. N. Jansen, Y. K. Sun, X. Qiu and K. Amine, Mn(II) Deposition on Anodes and Its Effects on Capacity Fade in Spinel Lithium Manganate-Carbon Systems, *Nat. Commun.*, 2013, **4**, 2437.

[62] R. Qiao, Y. Wang, P. Olalde-Velasco, H. Li, Y.-S. Hu and W. Yang, Direct Evidence of Gradient Mn(II) Evolution at Charged States in $LiNi_{0.5}Mn_{1.5}O_4$ Electrodes with Capacity Fading, *J. Power Sources*, 2015, **273**, 1120-1126.

[63] A. Jarry, S. Gottis, Y. S. Yu, J. Roque-Rosell, C. Kim, J. Cabana, J. Kerr and R. Kostecki, The Formation Mechanism of Fluorescent Metal Complexes at the $Li_xNi_{0.5}Mn_{1.5}O_{4-delta}$/Carbonate Ester Electrolyte Interface, *J. Am. Chem. Soc.*, 2015, **137**, 3533-3539.

[64] F. de Groot, M. Grioni, J. Fuggle, J. Ghijsen, G. Sawatzky and H. Petersen, Oxygen 1s X-Ray-Absorption Edges of Transition-Metal Oxides, *Phys. Rev. B*, 1989, **40**, 5715-5723.

[65] J. Zhou, D. Hong, J. Wang, Y. Hu, X. Xie and H. Fang, Electronic Structure Variation of the Surface and Bulk of a $LiNi_{0.5}Mn_{1.5}O_4$ Cathode as a Function of State of Charge: X-Ray Absorption Spectroscopic Study, *Phys. Chem. Chem. Phys.*, 2014, **16**, 13838-13842.

[66] C. Yogi, D. Takamatsu, K. Yamanaka, H. Arai, Y. Uchimoto, K. Kojima, I. Watanabe, T. Ohta and Z. Ogumi, Soft X-Ray Absorption Spectroscopic Studies with Different Probing Depths: Effect of an Electrolyte Additive on Electrode Surfaces, *J. Power Sources*, 2014, **248**, 994-999.

[67] S. Shi, P. Lu, Z. Liu, Y. Qi, L. G. Hector, Jr., H. Li and S. J. Harris, Direct Calculation of Li-Ion Transport in the Solid Electrolyte Interphase, *J. Am. Chem. Soc.*, 2012, **134**, 15476-15487.

[68] B. R. Wu, Y. H. Ren, D. B. Mu, X. J. Liu, G. C. Yang and F. Wu, Effect of Lithium Carbonate Precipitates on the Electrochemical Cycling Stability of $LiCoO_2$ Cathodes at a High Voltage, *RSC Adv.*, 2014, **4**, 10196-10203.

[69] L. Yang, B. Ravdel and B. L. Lucht, Electrolyte Reactions with the Surface of High Voltage $LiNi_{0.5}Mn_{1.5}O_4$ Cathodes for Lithium-Ion Batteries, *Electrochem. Solid St*, 2010, **13**, A95-A97.

Supporting Information
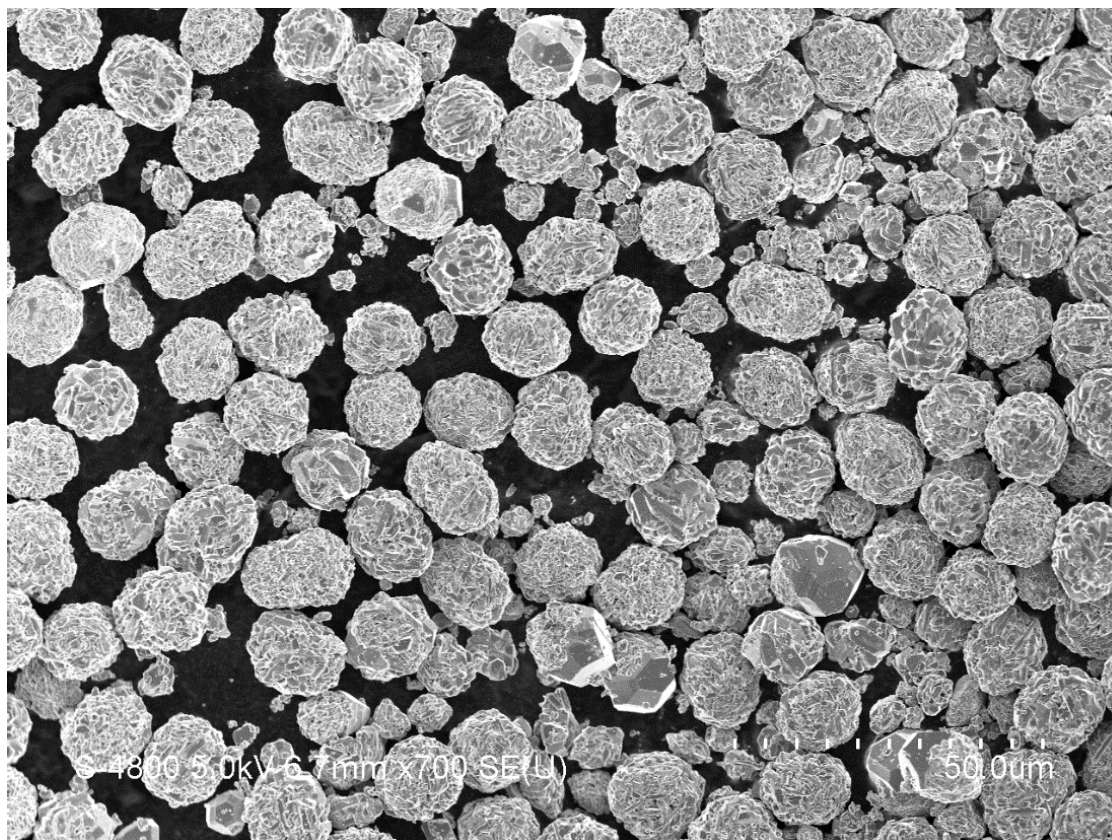
Figure SI 4.1 SEM image of bare LNMO under low magnification
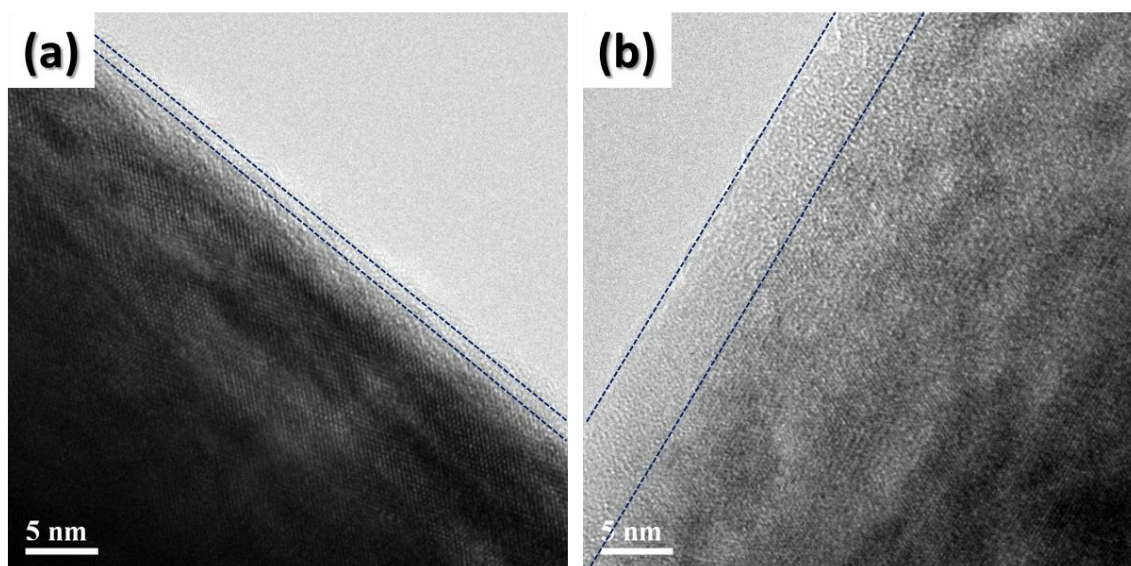
Figure SI 4.2 HRTEM images of (a) LNMO/25TiO$_2$ and (b) LNMO/250TiO$_2$
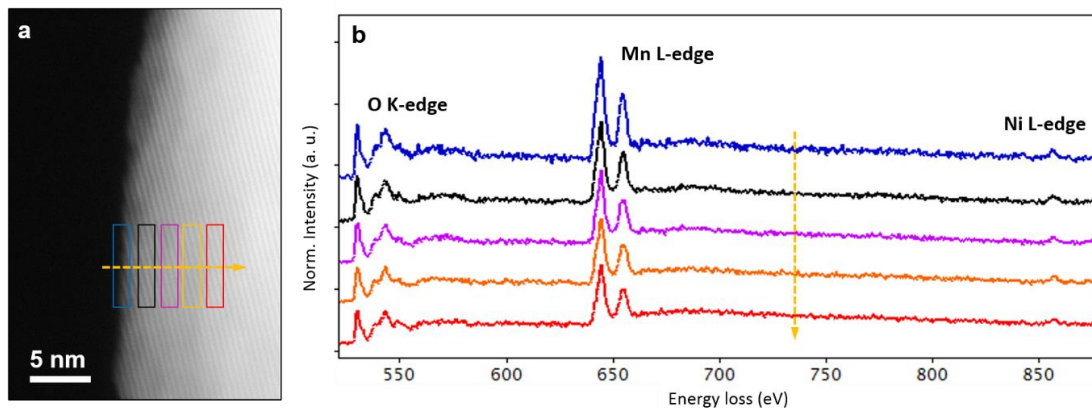
Figure SI 4.3 EELS spectra integrated from different location of a pristine LNMO particle.
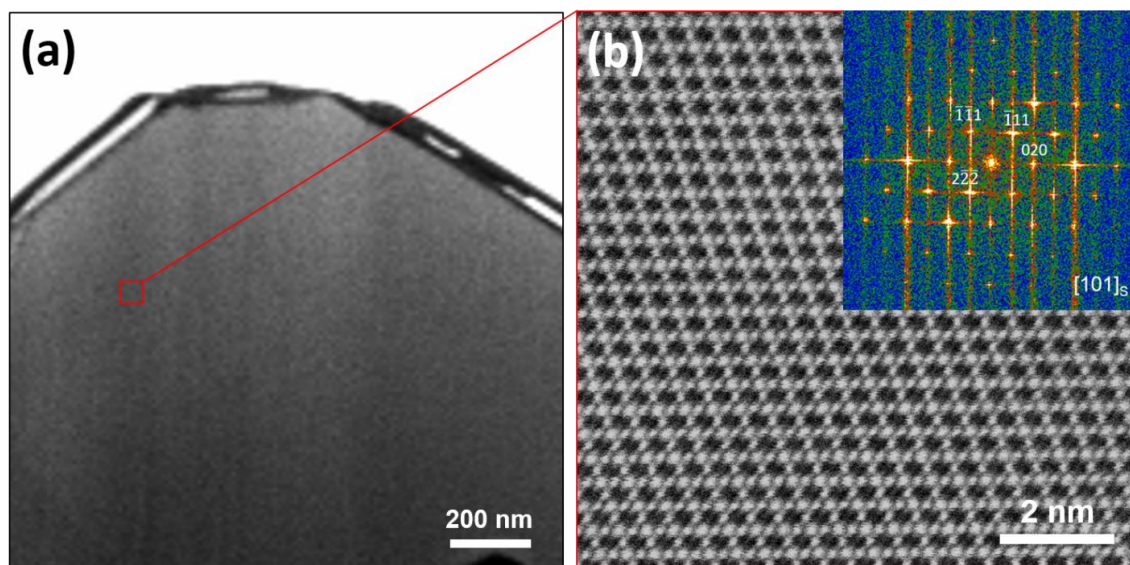
Figure SI 4.4 (a) HAADF-STEM images of a LNMO/250TiO₂A particle, the top white region is the W protection layer. (b) Atomic-resolution HAADF-STEM image taken from the bulk of the LNMO/250TiO₂A particle shown in (a). The corresponding Fourier transform diffractogram is displayed in the top inset.
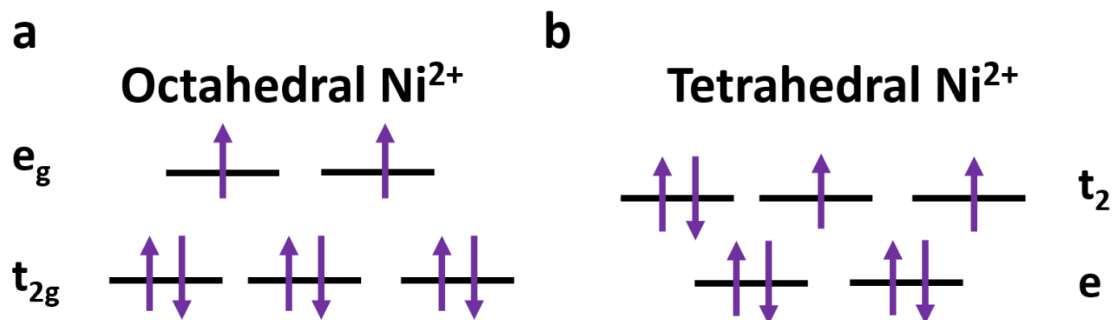
Figure SI 4.5 Crystal field splitting of Ni^{2+} with (a) octahedral coordination and (b) tetrahedral coordination

For octahedrally coordinated Ni^{2+}, the ligand field stabilization energy (LFSE) is:

$$LFSE = 0.4\Delta_o \times 6 - 0.6\Delta_o \times 2 = 1.2\Delta_o$$

For tetrahedrally coordinated Ni^{2+}, the ligand field stabilization energy (LFSE) is:

$$LFSE = 0.6\Delta_t \times 4 - 0.4\Delta_t \times 4 = 0.8\Delta_t$$

Since Δ_t is approximately 4/9 Δ_o, the LFSE for tetrahedrally coordinated Ni^{2+} is 0.356 Δ_o, which is much lower than the LFSE for octahedral coordination, therefore, tetrahedrally coordinated Ni^{2+} is hardly seen in solid materials.

The electron configuration of Ti^{4+} is $[Ar]4s^03d^0$, it has no 3d electrons, so it does not have any preference on octahedral or tetrahedral coordination.
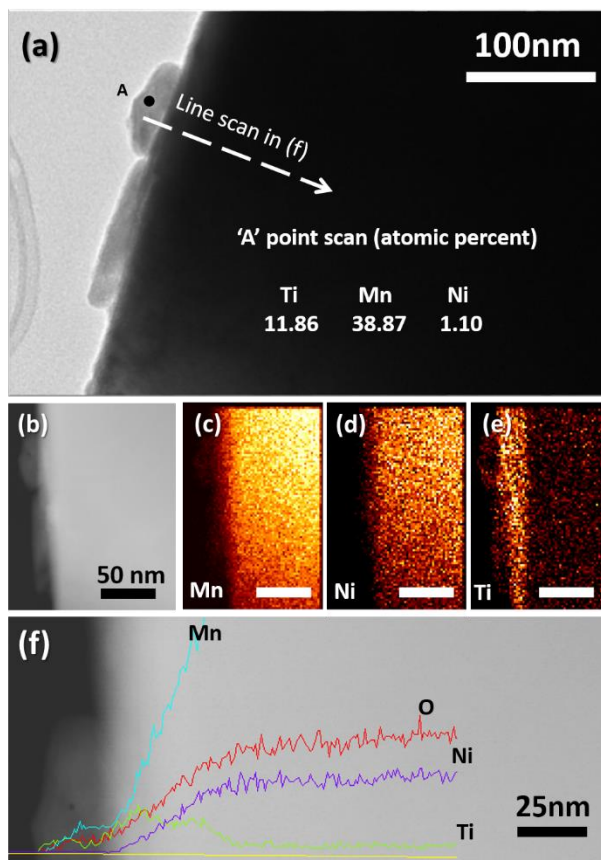
Figure SI 4.6 (a) TEM image of the tiny particle attached to the LNMO surface after annealing. (b-e) EDX mapping of Mn, Ni and Ti and corresponding STEM image. (f) EDX line scan across the surface
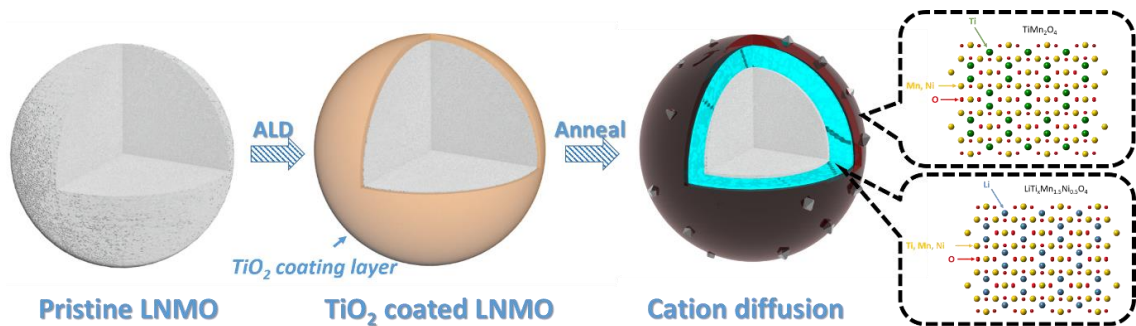
Figure SI 4.7 Schematic illustration of the process of post annealing treatment on LNMO/250TiO₂
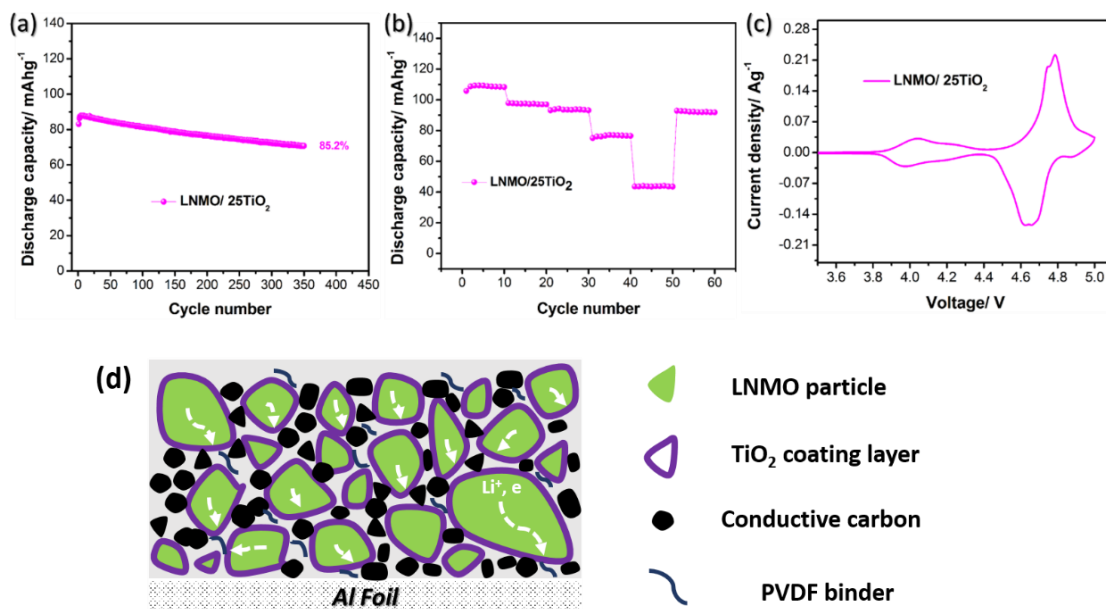
Figure SI 4.8 (a) Cycling performance; (b) Rate capability; (c) CV curves of LNMO/25TiO₂; and (d) Schematic illustration of the reason for the poor performance of amorphous TiO₂ coated LNMO powder *via* ALD.
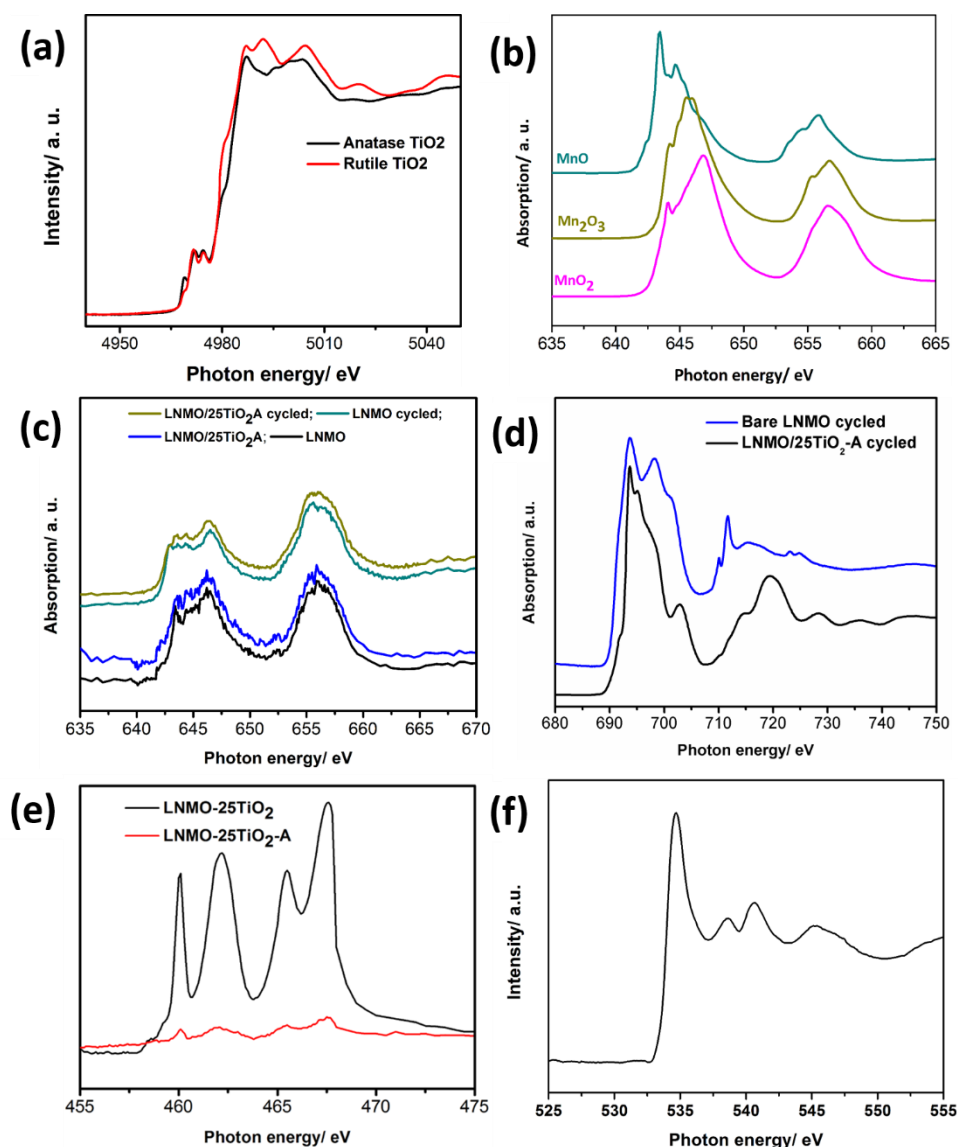
Figure SI 4.9 (a) XANES spectra of anatase and rutile TiO$_2$; (b) Standard XANES spectra of MnO, Mn$_2$O$_3$ and MnO$_2$; (c) Mn L$_{3,2}$ edges XANES of bare LNMO, LNMO/25TiO$_2$A, cycled bare LNMO and cycled LNMO/25TiO$_2$-A collected at FLY mode; (d) F K edge of cycled bare LNMO and cycled LNMO/25TiO$_2$-A; (e) Ti L$_{3,2}$ edges of LNMO/25TiO$_2$ and LNMO/25TiO$_2$A; (f) O K-edge XANES of Li$_2$CO$_3$;

Figure SI4.9e reveals that the concentration of the Ti in LNMO/25TiO$_2$A sample is much lower than the LNMO/25TiO$_2$ sample, indicating that the distribution of Ti has been diluted, which confirms the diffusion of Ti.
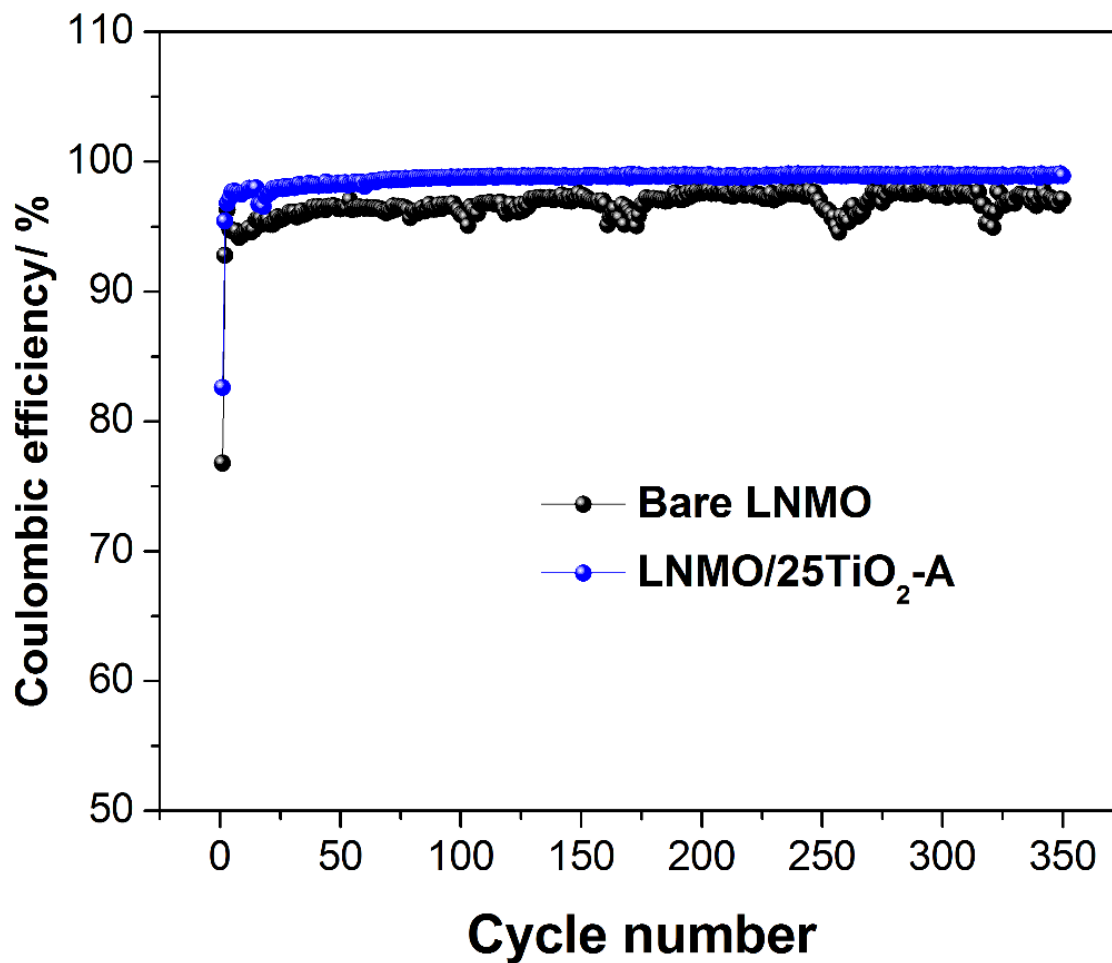
Figure SI 4.10 Coulombic efficiencies of bare LNMO and LNMO/25TiO₂A

The LNMO/25TiO₂A sample shows constantly higher Coulombic efficiency than the bare LNMO, indicating that the surface layer is helpful in preventing the electrolyte decomposition. The initial Coulombic efficiency explains the suppression of phase transformation as described in Figure 4.7.

Chapter 5

5 Highly Stable $Li_{1.2}Mn_{0.54}Co_{0.13}Ni_{0.13}O_2$ Enabled by Novel Atomic Layer Deposited $AlPO_4$ Coating

Lithium-rich layered material is one of the most promising candidates of cathode materials for next-generation electric vehicles. However, one of the major issues that pertains to this material is the oxygen release during initial charge, which results in low initial coulombic efficiency (ICE), intense electrolyte oxidation and thermal instability. In order to improve the safety of this cathode material, metal phosphates deposition using regular chemical method has been reported, but there is a lack of using ALD to create such coatings. In addition, the change of this material under ALD process remains unvisited.

In this study, we have conducted aluminum phosphate ($AlPO_4$) coating via atomic layer deposition (ALD) approach to protect the surface of this cathode material powders. It was found that part of the $C2/m$ Li_2MnO_3 phase turned into a spinel-like phase during the ALD process. The oxygen release has been effectively suppressed by such transformation, the initial CE increased from 75.2 % for the bare electrode to 86.2 % for the electrode with only 5 ALD cycles of $AlPO_4$ coating. Furthermore, $AlPO_4$ was also found to be more effective in improving the thermal stability of the cathode material comparing to bare or Al_2O_3 coated samples. Our study has provided a new possible solution towards cathode materials with high thermal resistance via conformal coating.

B. Xiao, B. Wang, J. Liu, K. Kaliyappan, Q. Sun, M. Banis, G. Dadheech, M. Balogh, M. Cai, T.-K Sham R. Li and X. Sun, *submitted*

5.1 Introduction

Lithium-rich layered oxides x Li$_2$MnO$_3$ • (1-x) LiMO$_2$ (M = Mn, Ni, Co), or otherwise termed as high energy NMC (HENMC) are a class of cathode materials that deliver a discharge capacity higher than 250 mAh/g within the voltage window of 2.0-4.8 V (vs. Li/Li$^+$), making it a very promising cathode material for the next-generation high energy lithium-ion batteries (LIBs) used in electric vehicles (EV).[1, 2] The crystalline structure of HENMC is composed of a phase of Li$_2$MnO$_3$ with a space group of C2/m and a phase of conventional layered LiMO$_2$ (M = Ni, Mn, Co) with a space group of R$\bar{3}$m. Li$_2$MnO$_3$ is electrochemically inert since Mn^{4+} cannot be oxidized any more under the normal operating voltage range of conventional LIBs. It can, however, be activated from the initial charging process by the simultaneous leaching of Li$^+$ from the transition metal layer and O$_2$ from the lattice, with an irreversible net loss of Li$_2$O.[3, 4] The initial activation process of HENMC results in its significantly increased capacity compared to other layered structure cathode materials, but also leads to several disadvantages. Firstly, the transition metal ions move into the Li layer vacancies and cause subsequent cation disordering, forming a spinel phase continuously to the interior of the material that will lead to sluggish lithium ions transportation and severe voltage fade.[5, 6] Secondly, O$_2$ release results in low initial CE and internal pressure increase in the cell, furthermore, O$_2$ facilitates the oxidation of the electrolyte under high voltage, forming a thick and insulating solid electrolyte interphase (SEI) on the surface.[7] Thirdly, O$_2$ release always gives rise to the safety harassment of thermal instability of the cathode materials.[8, 9] Fourthly, severe transition metal dissolution into the electrolyte also leads to capacity fade. To address these problems, surface modification of HENMC has been studied widely. Surface coating with metal oxides, phosphates and fluorides from chemical methods have been widely reported aimed at solving the abovementioned problems.[10-12] The coating layer can shield the direct contact between the cathode material and the electrolyte and thus preventing the transition metals from dissolving and electrolyte decomposition.[13] But these coating methods lack of full protection of the cathode materials since the coating layer tends to form isolated islands.[12, 14, 15] Atomic layer deposition (ALD) is a powerful technique to create a uniform and conformal coating layer on the surface of substrates.[16] This

advantage makes ALD outperform other chemical methods in terms of full protection on electrodes against the attack from the electrolytes, and it has been vastly used in the surface modification of battery materials.[17-19] Aluminum phosphate (AP) is widely known for its higher capability of enhancing the high temperature stability of cathode materials than metal oxides when used as a coating material,[20] but its controlled coating via ALD has not been reported as far.

Herein, for the first time, we have demonstrated the use of ALD to coat cathode materials with different thicknesses of $AlPO_4$. Benefiting from the uniform coating layer and the partial transformation of Li_2MnO_3 to a spinel-like phase, the oxygen release from the HENMC has been successfully controlled and the electrolyte decomposition was suppressed. The CE of the HENMC coated by $AlPO_4$ was significantly improved. More surprisingly, the $AlPO_y$ coated HENMC has demonstrated much higher thermal resistivity than samples coated by Al_2O_3, which is a most common ALD coating material. These results have demonstrated that atomic layer deposited $AlPO_4$ is a promising coating material on HENMC in order to achieve better performance and that ALD process can exert non-negligible effect on the structure of cathode materials.

5.2   Experimental

5.2.1   Materials Synthesis

HENMC was synthesized using a modified Pechini's method. CH_3COOLi, $Mn(CH_3COO)_2$, $Ni(CH_3COO)_2$ and $Co(CH_3COO)_2$ (Sigma Aldrich, 99%) were mixed with a stoichiometric ratio of 1.25:0.54:0.13:0.13 in 50 mL deionized water under strong stirring. 5.72 g citric acid was dissolved in 25 mL ethanol (Sigma Aldrich, 99.99%). 2.5 g polyethylene glycol (PEG) (Alfa Aesar, 25,000, 99%) was dissolved in 25 mL ethanol separately. The citric acid solution was initially added into the metal acetates solution slowly under stirring for 10 min. Then, the mixture was subsequently added into the PEG solution slowly, pink precipitations were observed during the reaction. Subsequently, 2 mL ethylene glycol (Sigma Aldrich, 99%) and 2 mL HNO_3 (Sigma Aldrich, 70%) were added dropwise until the pink precipitate is dissolved. The final clear solution was dried at 120 ºC to obtain a colloidal gel. This gel was pre-calcined at 400 ºC for 4 h in air to remove the

organic components. After cooling down, the final product was collected and ground to obtain fine particles. The final HENMC was obtained by calcining the fine particles under 850 $^{\circ}$C for 20 h in air.

$AlPO_4$ was deposited on HENMC powders at 250 °C in a Savannah 100 ALD system (Ultratech/Cambridge Nanotech, USA) using trimethylaluminum (TMA, $(CH_3)_3Al$, 98% STREM Chemicals), trimethyl phosphate (TMPO, $(CH_3)_3PO_4$, 97% STREM Chemicals), and distilled water (H_2O) as precursors. The source temperature for TMPO was 75 °C, while TMA and H_2O was kept at RT. $AlPO_4$ was deposited in an exposure model by the sequence of TMA pulse (0.5 s) – exposure (1 s) - purge (10 s) – H_2O pulse (1 s) – exposure (1 s) – purge (15 s) – TMPO pulse (2 s) – exposure (1 s) – purge (10 s) – H_2O pulse (1 s) – exposure (1s) – purge (10 s). Nitrogen gas (99.999 %) was used as a carrying gas at a flow rate of 20 sccm. $AlPO_4$ films were directly deposited on HENMC powders by repeating the above ALD cycles. In this study, 5, 10 and 20 ALD cycles were selected to control the coating thickness, each of the sample was denoted as HENMC-n AP, where n stands for the ALD cycle number and AP stands for $AlPO_4$. Al_2O_3 coating with 20 ALD cycles on the HENMC was carried out under 150 $^{\circ}$C with TMA and water as the precursors in the same ALD system.

5.2.2   Characterization Methods

The morphology of the samples was characterized by a Hitachi S-4800 field emission scanning electron microscopy (FESEM) and a JEOL 2010F high-resolution transmission electron microscope (HRTEM). The X-ray diffraction (XRD) patterns were collected on a Bruker D8 Advance Diffractometer using Cu Kα radiation at 40 kV and 40 mA. The soft X-ray absorption spectroscopy (XAS) measurements of P $L_{3,2}$ edges were collected at the Variable Line Spacing Plane Grating Monochromator (VLS PGM) beamline with a photon energy of 5.5 - 250 eV at the Canadian Light Source. The soft X-ray absorption spectroscopy (XAS) measurements at both total electron yield (TEY) and fluorescence yield (FYI) modes of Mn $L_{3,2}$ edges, Ni $L_{3,2}$ edges, Co $L_{3,2}$ edges and O K edge were collected at the Spherical Grating Monochrometer (SGM) beamline with a photon energy of 250-2000 eV at the Canadian Light Source. A PHI Quantera XPS Scanning Microprobe (Physical Electronics, Chanhassen, MN) with a monochromated Al K_a (1486.6 eV) source

was used for the XPS analysis. Differential scanning calorimetry (DSC) measurements were carried out on a TA Instrument SDT Q600. The cells were cycled for 5 times and stopped at fully charged state and opened in the glovebox to collect the fully de-lithiated cathode powders. The powders were then soaked in certain amount of electrolyte as mentioned below and heated to 400ºC under N_2 atmosphere at a ramp rate of 1 ºC/min.

5.2.3   Electrochemical Measurements

To prepare the electrodes for coin cell fabrication, the HENMC powders were uniformly mixed with acetylene black (AB) and poly(vinylidene fluoride) (PVDF) in a ratio of 70:20:10 in an N-methyl-pyrrolidione (NMP) solvent. Then, the slurry was pasted on aluminum foils and dried at 80 ºC under vacuum overnight. The electrode was subsequently cut into round shape and assembled into a CR-2032 coin cell in an argon-filled glove box with the moisture and oxygen being controlled below 0.1 ppm. Lithium metal was used as the counter electrode in the coin cells. 1M $LiPF_6$ dissolved into ethylene carbonate (EC) and diethyl carbonate (DEC) in a 1:1 volume ratio (BASF corp., US) was used as the electrolyte. Celgard 2400 was used as the separator. Cyclic voltammetry (CV) was performed on a Bio-Logic multichannel potentiostat 3/Z (VMP3) with a scanning rate of 0.1 mV s^{-1} and a potential range of 2.0 – 4.6 V (vs Li/Li^+). Galvanostatical charge/discharge test was carried out on Maccor 4000 between 2.0 V and 4.6 V (vs Li/Li^+), the initial cycle was conducted under 1/20 C (12.5 mAg^{-1}) for activation, and the following cycles were tested under 1/10 C (25 mAg^{-1}). The tested cells were dissembled in a glove box and the cathode sheets were collected and thoroughly washed with DMC several times for XPS study.

5.3   Results and Discussions

The SEM image of the HENMC particles is shown in Figure 1a, the uniform nanoparticles have sizes of around 300 nm. The smooth face and sharp edges indicate that the HENMC was well-crystalline and highly interconnect, which is essential for faster ionic transportation. The XRD pattern of the HENMC (Figure 5.1b) was well indexed to the hexagonal α-$NaFeO_2$ phase with a space group of R$\bar{3}$m. The weak peaks located between

20-25° are assigned to the diffraction of the monoclinic Li_2MnO_3 phase with a space group of C2/m.
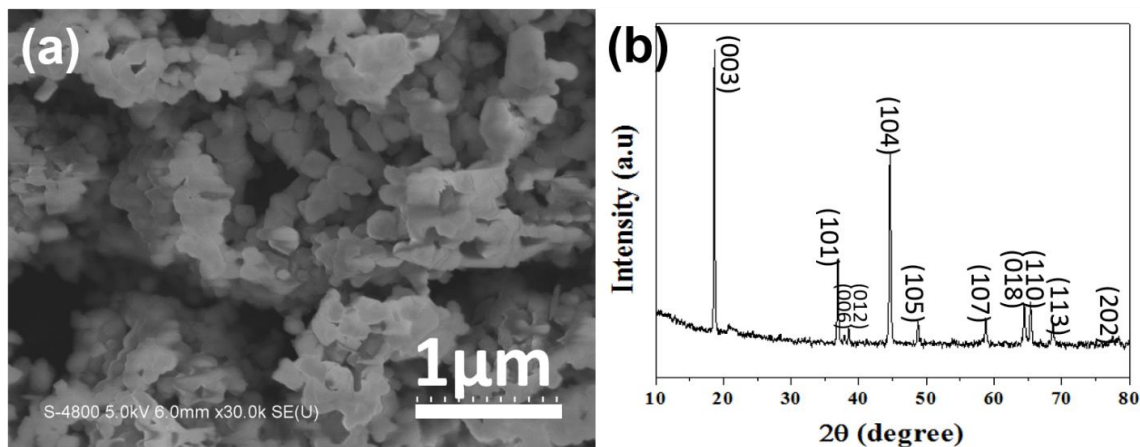
Figure 5.1 (a) SEM image and (b) XRD pattern of the pristine $Li_{1.2}Mn_{0.54}Co_{0.13}Ni_{0.13}O_2$ particles prepared using the modified Pechini's method

The elemental distribution of the HENMC-20AP sample was studied using EDS under the STEM mode. Figure 5.2a-f present the distribution of Co, Mn, Ni, Al, P elements and the overlapping mapping of Al and P. It can be seen that the Al and P are uniformly distributed on the surface of the HENMC particles. The inset P $L_{3,2}$ edges X-ray absorption spectroscopy (XAS) in Figure 5.2g reveals that the ALD derived $AlPO_4$ has very close chemical environment with standard $AlPO_4$. The HRTEM image reveals that the thickness of the 20 AP sample is around 4 nm and the $AlPO_4$ is structurally amorphous and uniformly distributed on the surface of the powders.
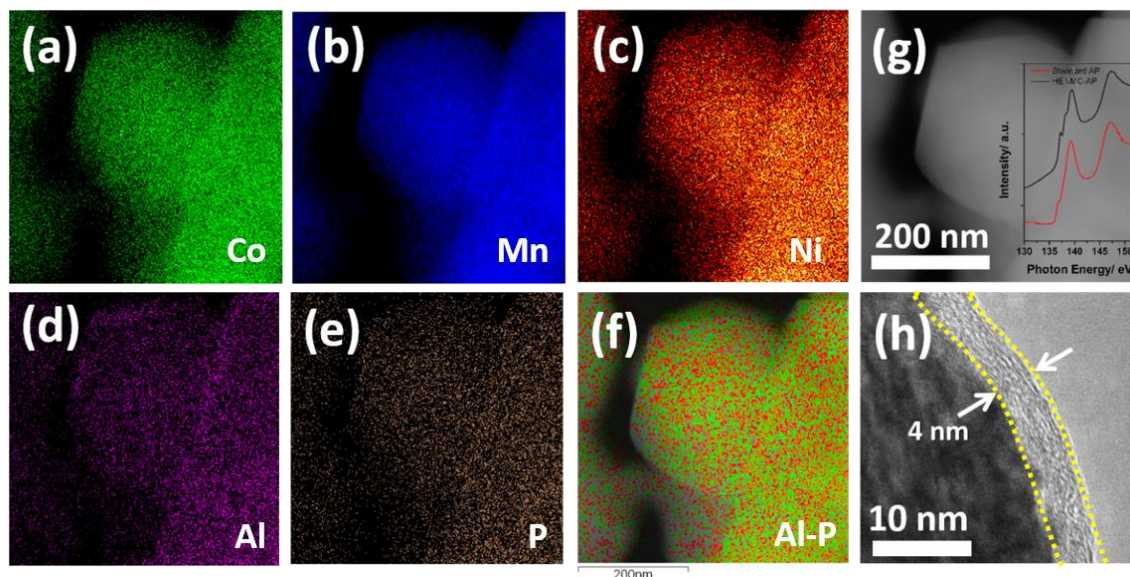
Figure 5.2 (a-f) EDS mapping of Co, Mn, Ni, Al, P and Al-P overlapping of HENMC-20AP (g) STEM image of the EDS mapping region (inset: XAS spectra of P $L_{3,2}$ edges of HENMC-AP (Black) and standard $AlPO_4$ (Red)) and (h) HRTEM image of the HENMC-20AP showing the coating layer

The Ni, Mn and Co $L_{3,2}$ edges and O K edge XAS data of the pristine HENMC and 20AP coated HENMC was collected in order to study the local material compositional change upon ALD process. Figure 5.3a-e illustrate the total electron yield (TEY) mode results, which have a detection depth of 5-10 nm. Transition meal $L_{3,2}$ edges reveal the electron transition of *$2p_{3/2}$* and *$2p_{1/2}$* states to an unoccupied *3d* state, and thus can provide information of spin configuration, ligand field and metal valence.[21] The Co $L_{3,2}$ edges of these two samples were fitted using a linear fitting method with standard CoO (divalent Co) and $LiCoO_2$ (trivalent Co) respectively in order to understand the Co valence states. Figure 4.3a shows the fitted result of the pristine HENMC, it can be seen that the Co ions in the pristine HENMC are composed of 15.4% divalent Co and 85.6% trivalent Co. After ALD treatment, however, an increase in the ratio of Co^{2+} occurred, with the trivalent Co dropped to only 62%. The decrease of Co^{3+} amount in the HENMC-20AP sample reveals that the surface of the HENMC was reduced upon ALD treatment. The reduction was also observed in the Mn $L_{3,2}$ edges. Since Mn $L_{3,2}$ edges of the HENMC sample were very hard to fit using MnO_2, Mn_2O_3 and MnO, we used the Mn $L_{3,2}$ edges of the HENMC directly as

standards to fit the HENMC-20AP sample. The results clearly show that the surface of the HENMC-20AP sample had 17.8% Mn existing in divalent state and only 82.2% in the original form of Mn in HENMC. In contrast to the Mn and Co, Ni did not show any change in the coated sample. O K edge show several identical peaks, the peaks in yellow and purple regions are due to electron transition from the O *1s* core level to the hybridization of the O *2p* with the transition metal *3d* and *4sp* orbitals, respectively.[22] An intensity drop happened on the sample after ALD process in the yellow region, this complies with the finding of transition metal reduction.[22] On the other hand, the new peak marked with "*" indicates that a TM-O ligand with different environment has evolved, which also supports that a different phase formed on the surface. Results measured under fluorescence yield (FYI) mode with a depth of up to 100 nm [23] are shown in Figure SI5.1, the two samples don't show any difference, indicating that the effect of ALD process only happens on the surface. In fact, the surface reduction of Li-rich material when exposed to hydrazine and carbon has been reported by other groups, they found that a spinel phase formed as a result of this reduction. Such spinel phase differs from the spinel-like phase formed after oxygen removal, where Li vacancy was the reason and it caused continuous growth to the interior particle.[24, 25] Cho et al. investigated the formation of a $Fd\bar{3}m$ $Li_{1+x}[CoNiMn_{2-x}]_2O_4$ spinel phase on a *R3-m* $Li[Ni_{0.54}Co_{0.12}Mn_{0.34}]$ layered phase and found that such transition was accompanied with oxygen loss, which is reflected as transition metal reduction in order to keep charge balance.[26] To better understand the possible phase change in our samples, HRTEM images on the surface region of a HENMC-20AP sample particle were collected. As shown in Figure 5.3g, two distinctive phases are observed. The one in the deeper region has a spacing of 0.238 nm, and can be indexed to the (113) crystalline plane of a typical layered $R\bar{3}m$ phase. Interestingly, a spinel phase with a spacing of 0.284 nm on the surface can be observed. Combined with the XAS data, we conclude that the surface spinel phase formed upon ALD treatment. In this case, it is believed that the HENMC particles reacted with the ALD precursors and formed such spinel structure, in the meantime, $AlPO_4$ was deposited. This transformation was also observed in AlF_3 coating reported by Scrosati et. al, it was attributed to the Li^+ leaching from the Li_2MnO_3 phase.[27] In previous ALD-related surface modification studies, none of them provide any insight into the structural change upon the ALD process. In fact, ALD process happens in vacuum with gaseous

precursors that are highly reactive, the cathode materials, especially those in nanometer size, are prone to experiencing structural change. Therefore, the effect of ALD coating on the performance of cathode materials is worthwhile to be revisited, though the coating layer also plays a pivotal role.
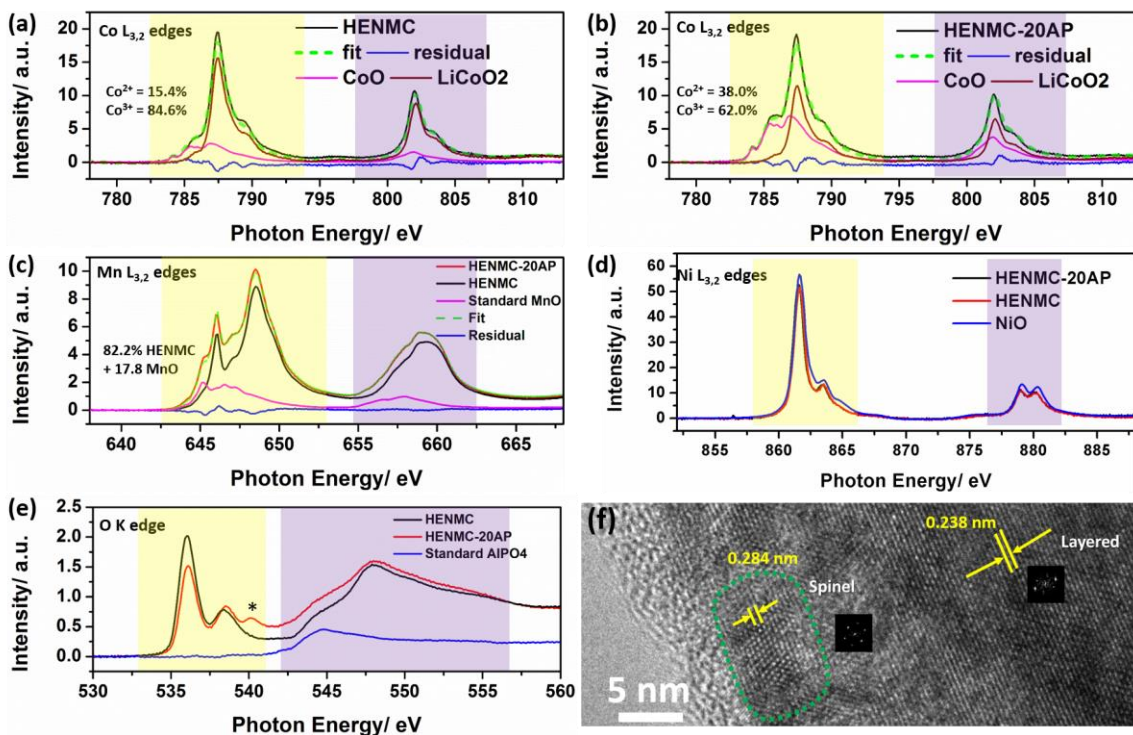
Figure 5.3 Soft XAS data of (a) HENMC Co L$_{3,2}$ edges and (b) HENMC-20AP Co L$_{3,2}$ edges fitted to standard CoO and LiCoO$_2$ (c) Mn L$_{3,2}$ edges (the HENMC-20AP sample is fitted to the HENMC sample and standard MnO) (d) Ni L$_{3,2}$ edges (L$_3$ edges are marked with yellow color and L$_2$ edges are marked with purple color) (e) O K edge (all of the XAS results in this figure are collected at total electron yield (TEY) mode) and (f) HRTEM image showing the different phases in the HENMC-20AP sample (inset: Fast Fourier Transform patterns)

Initially, the CV curves of the pristine HENMC and the HENMC coated with various ALD cycles of AP were recorded at 0.1 mVs^{-1} scan rate within 2.0-4.6 V and the results are illustrated in Figure 5.4. In a typical HENMC CV profile, the anodic peak at around 4.1 V corresponds to the oxidation of Ni^{2+} to Ni^{4+}. Another sharp anodic peak at 4.5 V is attributed to the leaching of oxygen from the crystal structure and formation of O$_2$$^{2-}$ or O$_2$,

which are distinctive resultants of the activation of the Li_2MnO_3 phase.[4] In the following cathodic process, the peak at around 3.8 V corresponds to the reduction of Ni^{4+} to Ni^{2+}.[5, 28] In general, it is believed that the Li_2MnO_3, after the Li_2O net leaching, turns into layer-structured MnO_2,[5] which is capable of accommodating lithium ions at the potential of ~ 3.5 V. This is consistent with what was observed from the pristine HENMC CV curve, that a peak increases gradually at ~ 3.25 V with continuous cycle numbers. Interestingly, the AP coated samples show significant difference compared to the pristine sample. The oxygen formation peak intensity has dropped gradually with more ALD cycles, indicating that the amount of the Li_2MnO_3 phase has dropped with ALD treatment and, interestingly, the coating thickness of AP correlates with the degree of oxygen removal from the HENMC. This observation complies with the XAS study, that the surface Li_2MnO_3 phase has been changed upon ALD process. The decreasing cathodic current peak of lithium insertion into layered MnO_2 also confirms the controlled oxygen removal since they form simultaneously.

Figure 5.4 Cyclic voltammetry of (a) pristine HENMC (b) HENMC-5AP (c) HENMC-10AP (d) HENMC-20AP

In order to evaluate the electrochemical performance of the samples, charge/discharge measurements were conducted with one activation cycle at 1/20 C and another 39 cycles at 1/10 C rate, the result is shown in Figure 5.5a. The initial charge capacity, discharge capacity and CE are listed in Table 5.1. The pristine HENMC delivers an initial charge capacity of 327 mAh/g, which decreases with thicker coating. The initial discharge capacity of the pristine HENMC is only 249 mAh/g, which is lower than those of the coated samples. Interestingly, the capacity of the HENMC drops rapidly after 40 cycles, whereas those of the coated samples remain rather stable, and an increase of capacity can even be observed in the first several cycles.

The CE is plotted in Figure 5.5b. The pristine HENMC has an initial CE of only 76.1%, whereas the coated HENMC samples demonstrate initial CEs of 85.2 %, 84.1 % and 83.2 % for 5 AP, 10 AP and 20 AP, respectively. Due to the lower electrical conductivity of the

AP coating layer, the discharge capacities of the HENMC-10AP and HENMC-20AP samples are lower than that of the HENMC-5AP sample. This explains why the initial CE drops with increasing coating thickness and 5 ALD cycles demonstrates the highest CE. The CE of the HENMC-20AP sample even exceeds 100 % in the 3rd and 4th cycle, which is also an evidence of extra discharge capacity. Furthermore, the low initial CE normally results from the electrolyte decomposition and the oxygen release in the class of lithium-rich cathode materials.[2] As observed and discussed in the CV curves (Figure 5.4), the suppression of oxygen release has been well controlled by process of ALD treatment. This would account for the increase of initial CE as well. On the other hand, the release of oxygen will certainly facilitate the decomposition of the electrolyte under high voltage, it inevitably brings another consideration, that the solid electrolyte interphase (SEI) on the HENMC surface becomes very thick and results in the build-up of impedance, which explains why the pristine HENMC shows decreasing stability within following several cycles.

Table 5.1 Initial charge/discharge capacity and the Coulombic efficiencies of the samples

Sample name	Initial charge capacity (mAhg^{-1})	Initial discharge capacity (mAhg^{-1})	Initial CE (%)
HENMC	327.4	249.4	76.2
5 AP	307.3	261.9	85.2
10 AP	304.0	255.8	84.1
20 AP	300.3	249.9	83.2

As has been introduced, the voltage fade issue is an important concern in lithium-rich cathodes since it causes energy density drop, and the reason for the voltage fade is still under debate. One possible explanation is that the removal of Li$^+$ from the transition metal layer will lead to Ni migration into these Li vacancies, resulting in the formation of a spinel phase on the surface. The average voltage for this spinel phase is lower than that of the

layered NMC, therefore the overall voltage drops.[6, 29, 30] In order to analyze the effect of AP coating on the voltage fade of HENMC materials, the charge/discharge curves of the first and 40th cycles are plotted and illustrated in Figure 5.4c-d. Another figure showing the 1st to 15th charge/discharge curves of all the samples are plotted in Figure SI5.4. In a typical HENMC charge curve, the slope in the voltage range of 3.7 V to 4.5 V corresponds to the lithium de-lithiation from the NMC phase, and the long plateau at 4.5 V to 4.6 V can be assigned to the oxygen release from the lattice. The charge capacity of the pristine HENMC, however, still shows much more oxygen release. For a pristine HENMC, the discharge capacity, in theory, mostly originates from the voltage above 3.0 V, considering the voltage window of Ni^{4+} to Ni^{2+} (4.0 V) and lithium insertion into MnO_2 (3.5 V). Therefore, in the pristine HENMC, very limited discharge capacity is expected to originate from the voltage below 3.0 V, as shown in Figure 5.4c. However, we can also observe that the higher initial discharge capacities of coated samples mainly come from the voltage below 3.0 V. The 20AP sample shows highest capacity below 3.0 V but obviously dropped capacity in the voltage range of 3.0 V-3.5 V. This phenomenon is in consistent with the CV curves, and indicates that the formation of MnO_2 has been suppressed and there was much less Li insertion into MnO_2. This difference becomes more apparent in the charge/discharge curves of the 40th cycle. Voltage drop can be observed in all of the samples, and it is likely that such treatment is not effective towards the voltage drop suppression. Nevertheless, the discharge capacities of 5 AP and 10 AP below 3.0 V are much higher than that of the pristine HENMC. The above observations indicate that the presence of AP coating can help exploit the electrochemical reactions that take place below 3.0 V. In theory, capacities below 3.0 V in HENMC system stem from several sources: 1) polarization of the electrochemical processes that are supposed to take place above 3.0 V; 2) lithium insertion into the spinel phase on the surface [29] and 3) oxygen reduction reaction.[31, 32] A tiny plateau at ~2.7 V can be observed in coated samples, this agrees well with previous findings that a new spinel phase has formed upon ALD treatment. Aside from this plateau, extra capacity has been obtained below 3.0 V. Oxygen reduction reaction in HENMC normally happens as the O_2 gas that was released during initial charging process is reduced to lower valence during discharge.[4, 31, 32] The final product of the

oxygen reduction reaction is Li_2CO_3, which is electrochemically inert and enables stable SEI.[33-35]

Figure 5.5 (a) Cyclic stability performance; (b) Coulombic efficiencies; (c) First cycle charge/discharge curves; (d) 40th cycle charge/discharge curves of the samples

In order to evaluate the effect of the oxygen release on the formation of the SEI layer, EIS measurements were conducted on the pristine HENMC and coated HENMC samples after initial charge and 6th charge. The simulated equivalent circuit is presented as an inset. The R_Ω stands for the Ohmic resistance arose from the electrolyte, separator and other components. The semi-circle in the high frequency range represents the lithium diffusion across the surface film, simulated as a resistor R_s and a constant phase element (CPE), the semi-circle in the medium frequency range shows the charge transfer reaction composed of a resistor R_{ct} and another CPE, the inclined line is interpreted as the finite length Warburg impedance. In this case, the value of R_s stands for the SEI resistance and the R_{ct} stands for the charge transfer resistance across the material surface. The R_s for each of the

sample after initial charge and 6th charge has been listed in Table SI5.1. It can be seen that the pristine HENMC has an R_s of 432.9 Ω, whereas AP coating has demonstrated effectiveness in decreasing this resistivity. The drop of SEI impedance reveals that the electrolyte decomposition is much less intense in coated samples. This can be explained as that the AlPO$_4$ shields the HENMC particles from direct contact with the electrolyte. On the other hand, it could be due to the suppressed oxygen release, since oxygen will facilitate the electrolyte decomposition and hydrolysis under very high voltage. The R_s values of these samples after the 6th charge show an apparent drop, as can be seen from the right column of Table SI5.1. For pristine HENMC, the R_s has a slight decrease of about 20 Ω. However, this drop becomes much more obvious in the coated samples, in the 20 AP sample, the R_s value has dropped by 85%. The reason for the impedance drop in these samples can be presumably ascribed to a more stable and thin SEI and/or the transformation of AP into lithium conductive Li$_3$PO$_4$ and LiAlO$_2$.[12, 37] The 20 AP sample shows the lowest R_s, but its capacity is lower than the 5 AP and 10 AP sample. Furthermore, voltage fade was not effectively alleviated even though the charge transfer impedance was much lower. This has also been observed in the work of Wang et al.,[37] where they reported the suppression of layered to spinel change through ALD-derived Al$_2$O$_3$ coating, but voltage decay was still observed. These phenomena can be tentatively ascribed to the lack of MnO$_2$ phase due to the missing of the Li$_2$MnO$_3$ phase. The lithiation voltage window of layered MnO$_2$ falls into the window where voltage fade happens.

Figure 5.6 EIS profiles of the samples (a) after initial charge and (b) after 6th charge (inset: A simulated equivalent circuit)

Figure 5.7 XPS results of F 1s of (a) Pristine HENMC electrode (b) HENMC-20AP electrode (c) Cycled pristine HENMC electrode (d) Cycled HENMC-20AP electrode and XPS results of C 1s of (e) Pristine HENMC electrode (f) HENMC-20AP electrode (g) Cycled pristine HENMC electrode (h) Cycled HENMC-20AP electrode

The surface compositions of the pristine HENMC, HENMC-20AP, cycled pristine HENMC and cycled HENMC-20AP electrodes are analyzed using XPS. Figure 5.7a-d illustrate the F 1s XPS spectra. It can be seen that in fresh samples, two types of fluorine, PVdF at 687.1 eV and metal fluorides (LiF and transition metal fluorides) at 684 eV are observed. In general, LiF is not expected in fresh samples, but due to the dehydrofluorination of PVdF according to reaction [1], HF is produced.

$$-CH_2 - CF_2- \rightarrow -CH = CF- + HF \tag{1}$$
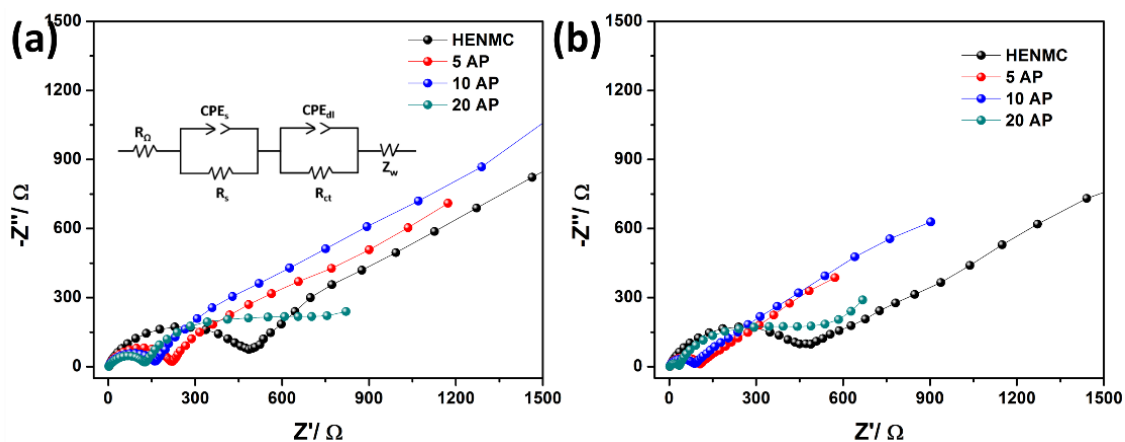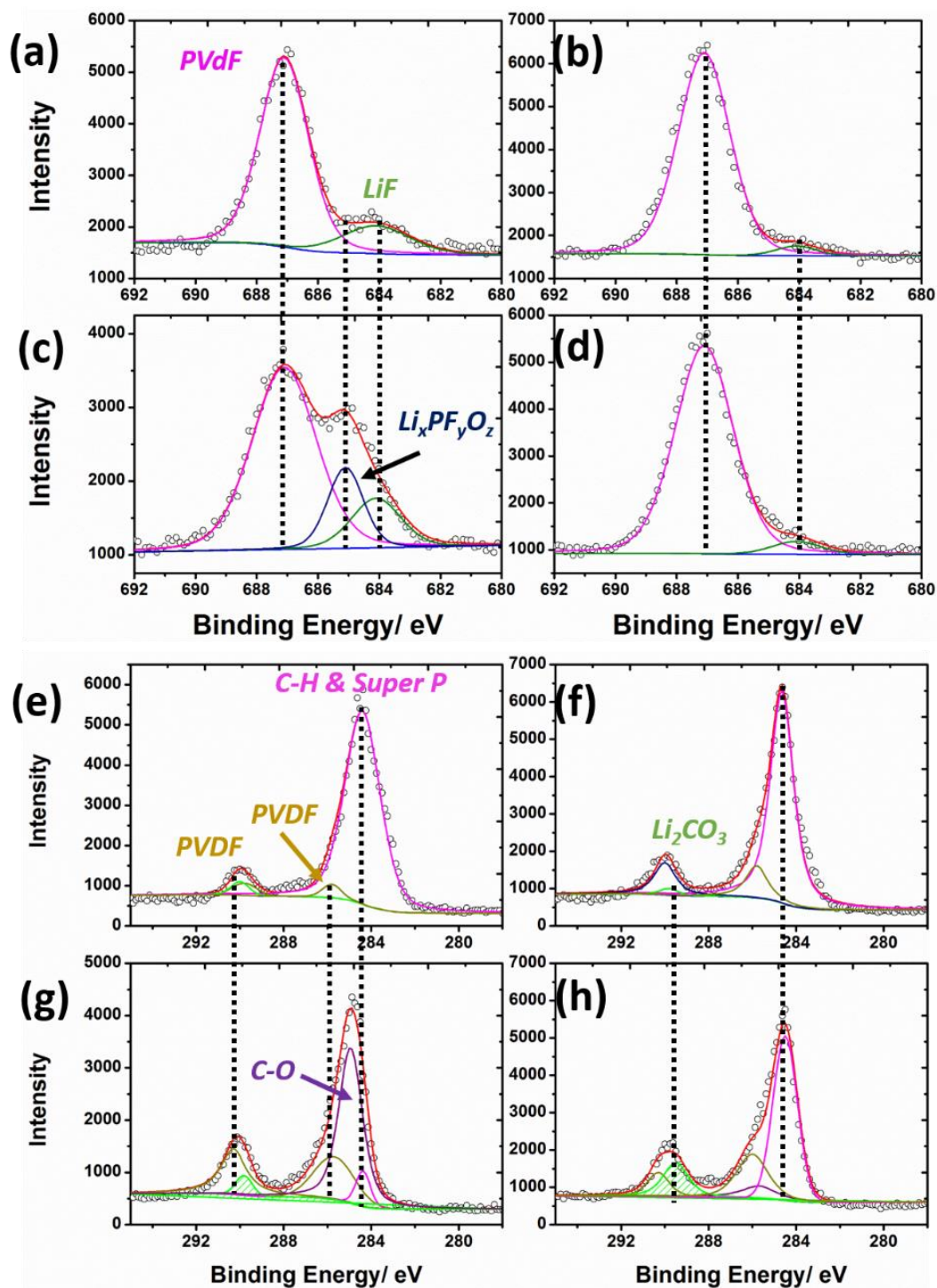
The surface of HENMC, after exposure to HF, generates LiF.[38] Apparently, the coated sample shows much less LiF even in fresh samples, indicating that the presence of $AlPO_y$ is capable of protecting the material surface. Furthermore, after intensive cycling, the surface F 1s XPS spectrum of pristine HENMC can be deconvoluted into three components, with an extra peak at 685.1 eV, this peak is generally assigned to $Li_xPF_y/Li_xPF_yO_z$, which are the main products of the hydrolysis of $LiPF_6$ when exposed to O_2 and water.[39, 40] The $Li_xPF_y/Li_xPF_yO_z$ peak cannot be observed in the coated cycled sample and the LiF in cycled pristine HENMC is also much more than that of the coated HENMC, indicating that the coating can effectively prevent the decomposition of the electrolyte upon cycling, especially when there is excessive oxygen generated in HENMC material.

The C 1s XPS spectra of the same samples were also studied. In the C 1s XPS, several peaks corresponding to the C-F and C-H bonds in PVdF, the C-C bonds in super P conductive agent and a small amount of Li_2CO_3 can be observed in the fresh electrodes.[41] However, after cycling, the pristine HENMC electrode shows a sharp peak of C-O single bond at the binding energy of 285.1 eV. In addition, the contribution from the super P conductive agent has dropped significantly in this sample, indicating that the surface has been covered by a very thick layer of electrolyte decomposition compounds. Since C-O bonds are normally assigned to species such as ether that are unfavorable SEI components due to their instability and insulating nature,[42, 43] we can conclude that the capacity fade of pristine HENMC is also closely related to the build-up of surface impedance. On the other hand, the coated HENMC, after cycling, shows much less C-O single bond, but the

Li_2CO_3 peak turns out to be much higher than that of the pristine HENMC, this observation confirms our previous assumption that the decreasing impedance upon cycling in coated samples is because of that Li_2CO_3 helps create a more stable and robust SEI.[36]

As has been reported by our previous work, $AlPO_4$ coating is capable of enhancing the thermal resistivity of carbon nanotubes,[44] therefore the DSC of overcharged pristine HENMC and AP coated HENMC was also conducted. Since Al_2O_3 is the most widely used ALD derived coating, a sample with Al_2O_3 coating was studied as a reference. It can be seen from Figure 5.8, the pristine HENMC shows two exothermal peaks, indicating that the dissociation of the HENMC was a two-step process. The first peak is normally assigned to the solvent decomposition and the second peak is supposed to originate from the cathode material phase change and the electrolyte oxidation.[45] The onset decomposing temperature was about 219 °C, whereas the Al_2O_3 coated sample shows a slightly higher onset temperature was 223 °C. However, AP coated sample shows significant improvement and the onset temperature was 237 °C, which is much higher than those of the pristine HENMC and Al_2O_3 coated HENMC. The thermal stability improvement of $AlPO_4$ coating can be ascribed to the high thermal stability of phosphate, thus proving that ALD-derived $AlPO_4$ is also a superior coating material in retaining the thermal stability of overcharged HENMC, especially when there is excessive oxygen release.
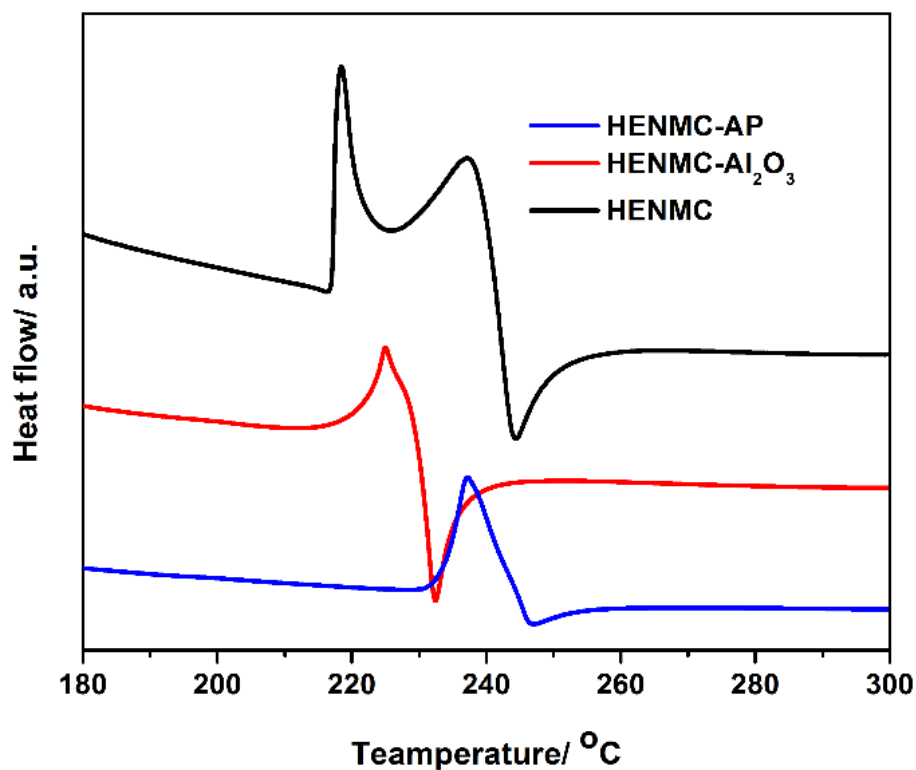
Figure 5.8 DSC curves of pristine HENMC, HENMC-Al2O3 and HENMC-AP

To better clarify the mechanism of the performance improvement by AP coating, we have shown a schematic diagram in Figure 5.9. ALD process generates a spinel phase on the outer part of the material that enables fast Li^+ ion transportation, this differs from the cation migration caused phase which is due to lithium vacancies. The AP coating protects the surface of HENMC from metal dissolution by shielding the particles from direct contact with the electrolyte. More importantly, the continuous oxygen release was suppressed so that the oxidation decomposition of the electrolyte under high voltage can be suppressed. By limiting the oxygen release, the surface cation migration has been restrained and thus the charge transfer impedance has significantly dropped. Furthermore, the oxygen reduction reaction that happens below 3.0 V has helped create a robust SEI with more Li_2CO_3, it also demonstrates increasing performance and over 100 % CE within the first several cycles.

Figure 5.9 Schematic illustration of the mechanisms of performance improvement by AP coating

5.4 Conclusions

We have successfully used ALD to coat the HENMC cathode material with aluminum phosphate. This coating layer has demonstrated effective protection of the cathode material against the attack from the electrolyte. ALD process can slightly reduce the material surface and convert the Li_2MnO_3 to a spinel-like phase, and the oxygen release during initial charge can be effectively controlled. The initial coulombic efficiency can be significantly improved with the presence of the coating. Oxygen reduction reaction was more intense in the coated samples, it helped create a more robust SEI layer, so that the performance of the coated samples show significant improvement. Besides, AP coated HENMC has demonstrated much better thermal stability than Al_2O_3 coated HENMC and pristine HENMC, making it an outstanding candidate for the surface coating modification of HENMC since oxygen release may lead to severe thermal instability issues.

Acknowledgement

References

[1] P. Yan, J. Zheng, J. Xiao, C.-M. Wang and J.-G. Zhang, Recent Advances on the Understanding of Structural and Composition Evolution of LMR Cathodes for Li-Ion Batteries, *Front. Energy Res.*, 2015, **3**.

[2] H. Yu and H. Zhou, High-Energy Cathode Materials (Li_2MnO_3-$LiMO_2$) for Lithium-Ion Batteries, *J. Phys. Chem. Lett.*, 2013, **4**, 1268-1280.

[3] J. Rana, M. Stan, R. Kloepsch, J. Li, G. Schumacher, E. Welter, I. Zizak, J. Banhart and M. Winter, Structural Changes in Li_2MnO_3 Cathode Material for Li-Ion Batteries, *Adv. Energy Mater.*, 2014, **4**, 1300998

[4] N. Yabuuchi, K. Yoshii, S. T. Myung, I. Nakai and S. Komaba, Detailed Studies of a High-Capacity Electrode Material for Rechargeable Batteries, $Li2MnO_3$-$LiCo_{(1/3)}Ni_{(1/3)}Mn_{(1/3)}O_2$, *J. Am. Chem. Soc.*, 2011, **133**, 4404-4419.

[5] P. Yan, L. Xiao, J. Zheng, Y. Zhou, Y. He, X. Zu, S. X. Mao, J. Xiao, F. Gao, J.-G. Zhang and C.-M. Wang, Probing the Degradation Mechanism of Li_2MnO_3 Cathode for Li-Ion Batteries, *Chem. Mater.*, 2015, **27**, 975-982.

[6] Y. Wu, C. Ma, J. Yang, Z. Li, L. F. Allard, C. Liang and M. Chi, Probing the Initiation of Voltage Decay in Li-Rich Layered Cathode Materials at the Atomic Scale, *J. Mater. Chem. A*, 2015, **3**, 5385-5391.

[7] N. Dupre, M. Cuisinier, E. Legall, D. War and D. Guyomard, Contribution of the Oxygen Extracted from Overlithiated Layered Oxides at High Potential to the Formation of the Interphase, *J. Power Sources*, 2015, **299**, 231-240.

[8] K.-W. Nam, S.-M. Bak, E. Hu, X. Yu, Y. Zhou, X. Wang, L. Wu, Y. Zhu, K.-Y. Chung and X.-Q. Yang, Combining in Situ Synchrotron X-Ray Diffraction and Absorption Techniques with Transmission Electron Microscopy to Study the Origin of Thermal Instability in Overcharged Cathode Materials for Lithium-Ion Batteries, *Adv. Funct. Mater.*, 2013, **23**, 1047-1063.

[9] S.-M. Bak, K.-W. Nam, W. Chang, X. Yu, E. Hu, S. Hwang, E. A. Stach, K.-B. Kim, K. Y. Chung and X.-Q. Yang, Correlating Structural Changes and Gas Evolution During the Thermal Decomposition of Charged $Li_xNi_{0.8}Co_{0.15}Al_{0.05}O_2$ Cathode Materials, *Chem. Mater.*, 2013, **25**, 337-351.

[10] J. Zheng, M. Gu, J. Xiao, B. J. Polzin, P. Yan, X. Chen, C. Wang and J.-G. Zhang, Functioning Mechanism of AlF_3 Coating on the Li- and Mn-Rich Cathode Materials, *Chem. Mater.*, 2014, **26**, 6320-6327.

[11] Z. Wang, E. Liu, C. He, C. Shi, J. Li and N. Zhao, Effect of Amorphous $FePO_4$ Coating on Structure and Electrochemical Performance of $Li_{1.2}Ni_{0.13}Co_{0.13}Mn_{0.54}O_2$ as Cathode Material for Li-Ion Batteries, *J. Power Sources*, 2013, **236**, 25-32.

[12] Y. Wu, A. Vadivel Murugan and A. Manthiram, Surface Modification of High Capacity Layered $Li_{1.2}Ni_{0.13}Co_{0.13}Mn_{0.54}O_2$ Cathodes by $AlPO_4$, *J. Electrochem. Soc.*, 2008, **155**, A635.

[13] A. Mauger and C. Julien, Surface Modifications of Electrode Materials for Lithium-Ion Batteries: Status and Trends, *Ionics*, 2014, **20**, 751-787.

[14] H. Liu, C. Chen, C. Du, X. He, G. Yin, B. Song, P. Zuo, X. Cheng, Y. Ma and Y. Gao, Lithium-Rich $Li_{1.2}Ni_{0.13}Co_{0.13}Mn_{0.54}O_2$ Oxide Coated by Li_3PO_4 and Carbon Nanocomposite Layers as High Performance Cathode Materials for Lithium Ion Batteries, *J. Mater. Chem. A*, 2015, **3**, 2634-2641.

[15] Y. S. Jung, A. S. Cavanagh, L. A. Riley, S. H. Kang, A. C. Dillon, M. D. Groner, S. M. George and S. H. Lee, Ultrathin Direct Atomic Layer Deposition on Composite Electrodes for Highly Durable and Safe Li-Ion Batteries, *Adv. Mater.*, 2010, **22**, 2172-2176.

[16] X. Meng, X. Q. Yang and X. Sun, Emerging Applications of Atomic Layer Deposition for Lithium-Ion Battery Studies, *Adv. Mater.*, 2012, **24**, 3589-3615.

[17] J. S. Park, X. Meng, J. W. Elam, S. Hao, C. Wolverton, C. Kim and J. Cabana, Ultrathin Lithium-Ion Conducting Coatings for Increased Interfacial Stability in High Voltage Lithium-Ion Batteries, *Chem. Mater.*, 2014, **26**, 3128-3134.

[18] J. Liu, M. N. Banis, Q. Sun, A. Lushington, R. Li, T. K. Sham and X. Sun, Rational Design of Atomic-Layer-Deposited $LiFePO_4$ as a High-Performance Cathode for Lithium-Ion Batteries, *Adv. Mater.*, 2014, **26**, 6472-6477.

[19] X. Li, J. Liu, M. N. Banis, A. Lushington, R. Li, M. Cai and X. Sun, Atomic Layer Deposition of Solid-State Electrolyte Coated Cathode Materials with Superior High-Voltage Cycling Behavior for Lithium Ion Battery Application, *Energy Environ. Sci.*, 2014, **7**, 768.

[20] J. Cho, T.-G. Kim, C. Kim, J.-G. Lee, Y.-W. Kim and B. Park, Comparison of Al_2O_3- and $AlPO_4$-Coated $LiCoO_2$ Cathode Materials for a Li-Ion Cell, *J. Power Sources*, 2005, **146**, 58-64.

[21] S. P. Cramer, F. M. F. Degroot, Y. Ma, C. T. Chen, F. Sette, C. A. Kipke, D. M. Eichhorn, M. K. Chan, W. H. Armstrong, E. Libby, G. Christou, S. Brooker, V. Mckee, O. C. Mullins and J. C. Fuggle, Ligand-Field Strengths and Oxidation-States from Manganese L-Edge Spectroscopy, *J. Am. Chem. Soc*., 1991, **113**, 7937-7940.

[22] R. M. Qiao, T. Chin, S. J. Harris, S. S. Yan and W. L. Yang, Spectroscopic Fingerprints of Valence and Spin States in Manganese Oxides and Fluorides, *Curr. Appl. Phys.*, 2013, **13**, 544-548.

[23] A. J. Achkar, T. Z. Regier, E. J. Monkman, K. M. Shen and D. G. Hawthorn, Determination of Total X-Ray Absorption Coefficient Using Non-Resonant X-Ray Emission, *Sci. Rep.*, 2011, **1**, 182.

[24] L. Guo, N. Zhao, J. Li, C. He, C. Shi and E. Liu, Surface Double Phase Network Modified Lithium Rich Layered Oxides with Improved Rate Capability for Li-Ion Batteries, *ACS Appl. Mater. Inter.*, 2015, **7**, 391-399.

[25] Q. Xia, X. Zhao, M. Xu, Z. Ding, J. Liu, L. Chen, D. G. Ivey and W. Wei, A Li-Rich Layered@Spinel@Carbon Heterostructured Cathode Material for High Capacity and High Rate Lithium-Ion Batteries Fabricated *via* an in situ Synchronous Carbonization-Reduction Method, *J. Mater. Chem. A*, 2015, **3**, 3995-4003.

[26] Y. Cho, S. Lee, Y. Lee, T. Hong and J. Cho, Spinel-Layered Core-Shell Cathode Materials for Li-Ion Batteries, *Adv. Energy Mater.*, 2011, **1**, 821-828.

[27] Y. K. Sun, M. J. Lee, C. S. Yoon, J. Hassoun, K. Amine and B. Scrosati, The Role of AlF_3 Coatings in Improving Electrochemical Cycling of Li-Enriched Nickel-Manganese Oxide Electrodes for Li-Ion Batteries, *Adv. Mater.*, 2012, **24**, 1192-1196.

[28] J. Zheng, P. Xu, M. Gu, J. Xiao, N. D. Browning, P. Yan, C. Wang and J.-G. Zhang, Structural and Chemical Evolution of Li- and Mn-Rich Layered Cathode Material, *Chem. Mater.*, 2015, **27**, 1381-1390.

[29] P. Yan, A. Nie, J. Zheng, Y. Zhou, D. Lu, X. Zhang, R. Xu, I. Belharouak, X. Zu, J. Xiao, K. Amine, J. Liu, F. Gao, R. Shahbazian-Yassar, J. G. Zhang and C. M. Wang, Evolution of Lattice Structure and Chemical Composition of the Surface Reconstruction Layer in $Li_{1.2}Ni_{0.2}Mn_{0.6}O_2$ Cathode Material for Lithium Ion Batteries, *Nano Lett.*, 2015, **15**, 514-522.

[30] M. Sathiya, A. M. Abakumov, D. Foix, G. Rousse, K. Ramesha, M. Saubanere, M. L. Doublet, H. Vezin, C. P. Laisa, A. S. Prakash, D. Gonbeau, G. VanTendeloo and J. M. Tarascon, Origin of Voltage Decay in High-Capacity Layered Oxide Electrodes, *Nature Mater.*, 2015, **14**, 230-238.

[31] H. Koga, L. Croguennec, M. Menetrier, K. Douhil, S. Belin, L. Bourgeois, E. Suard, F. Weill and C. Delmas, Reversible Oxygen Participation to the Redox Processes Revealed for $Li_{1.20}Mn_{0.54}Co_{0.13}Ni_{0.13}O_2$, *J. Electrochem. Soc.*, 2013, **160**, A786-A792.

[32] H. Koga, L. Croguennec, M. Ménétrier, P. Mannessiez, F. Weill and C. Delmas, Different Oxygen Redox Participation for Bulk and Surface: A Possible Global Explanation for the Cycling Mechanism of $Li_{1.20}Mn_{0.54}Co_{0.13}Ni_{0.13}O_2$, *J. Power Sources*, 2013, **236**, 250-258.

[33] J. S. Shin, C. H. Han, U. H. Jung, S. I. Lee, H. J. Kim and K. Kim, Effect of Li_2CO_3 Additive on Gas Generation in Lithium-Ion Batteries, *J. Power Sources*, 2002, **109**, 47-52.

[34] B. R. Wu, Y. H. Ren, D. B. Mu, X. J. Liu, G. C. Yang and F. Wu, Effect of Lithium Carbonate Precipitates on the Electrochemical Cycling Stability of $LiCoO_2$ Cathodes at a High Voltage, *RSC Adv.*, 2014, **4**, 10196-10203.

[35] C. Yogi, D. Takamatsu, K. Yamanaka, H. Arai, Y. Uchimoto, K. Kojima, I. Watanabe, T. Ohta and Z. Ogumi, Soft X-Ray Absorption Spectroscopic Studies with Different Probing Depths: Effect of an Electrolyte Additive on Electrode Surfaces, *J. Power Sources*, 2014, **248**, 994-999.

[36] P. Verma, P. Maire and P. Novák, A Review of the Features and Analyses of the Solid Electrolyte Interphase in Li-Ion Batteries, *Electrochim. Acta*, 2010, **55**, 6332-6341.

[37] P. Yan, J. Zheng, X. Zhang, R. Xu, K. Amine, J. Xiao, J.-G. Zhang and C.-M. Wang, Atomic to Nanoscale Investigation of Functionalities of an Al_2O_3 Coating Layer on a Cathode for Enhanced Battery Performance, *Chem. Mater.*, 2016, **28**, 857-863.

[38] Y.-C. Lu, A. N. Mansour, N. Yabuuchi and Y. Shao-Horn, Probing the Origin of Enhanced Stability of "$AlPO_4$" Nanoparticle Coated $LiCoO_2$ during Cycling to High Voltages: Combined XRD and XPS Studies, *Chem. Mater.*, 2009, **21**, 4408-4424.

[39] T. Eriksson, A. M. Andersson, C. Gejke, T. Gustafsson and J. O. Thomas, Influence of Temperature on the Interface Chemistry of $Li_xMn_2O_4$ Electrodes, *Langmuir*, 2002, **18**, 3609-3619.

[40] T. Eriksson, A. M. Andersson, A. G. Bishop, C. Gejke, T. r. Gustafsson and J. O. Thomas, Surface Analysis of $LiMn_2O_4$ Electrodes in Carbonate-Based Electrolytes, *J. Electrochem. Soc.*, 2002, **149**, A69.

[41] L. Yang and B. L. Lucht, Inhibition of Electrolyte Oxidation in Lithium Ion Batteries with Electrolyte Additives, *Electrochem. Solid-State Lett.*, 2009, **12**, A229.

[42] H. Bouayad, Z. Wang, N. Dupré, R. Dedryvère, D. Foix, S. Franger, J. F. Martin, L. Boutafa, S. Patoux, D. Gonbeau and D. Guyomard, Improvement of Electrode/Electrolyte Interfaces in High-Voltage Spinel Lithium-Ion Batteries by Using Glutaric Anhydride as Electrolyte Additive, *J. Phys. Chem. C*, 2014, **118**, 4634-4648.

[43] L. Yang, B. Ravdel and B. L. Lucht, Electrolyte Reactions with the Surface of High Voltage $LiNi_{0.5}Mn_{1.5}O_4$ Cathodes for Lithium-Ion Batteries, *Electrochem. Solid-State Lett*, 2010, **13**, A95.

[44] J. Liu, Y. J. Tang, B. W. Xiao, T. K. Sham, R. Y. Li and X. L. Sun, Atomic Layer Deposited Aluminium Phosphate Thin Films on N-Doped Cnts, *RSC Adv.*, 2013, **3**, 4492-4495.

[45] M. S. Park, J. W. Lee, W. Choi, D. Im, S. G. Doo and K. S. Park, On the Surface Modifications of High-Voltage Oxide Cathodes for Lithium-Ion Batteries: New Insight and Significant Safety Improvement, *J. Mater. Chem.*, 2010, **20**, 7208-7213.

Supporting Information

Table SI 5.1 R$_s$ values of the samples after initial charge and 6th charge

	R$_s$ (After initial charge)	**R$_s$ (After 6th charge)**
HENMC	432.9 Ω	412.9 Ω
5 AP	212.9 Ω	97.0 Ω
10 AP	157.2 Ω	79.0 Ω
20 AP	143.1 Ω	32.3 Ω
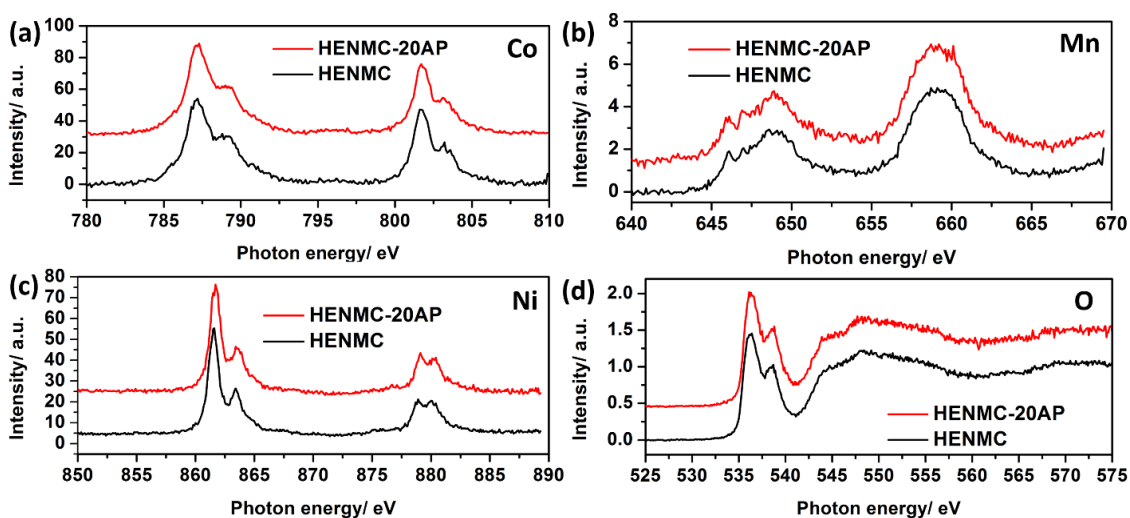
Figure SI 5.1 XAS of (a) Co, (b) Mn, (c) Ni and (d) O collected at fluorescence yield mode (FYI)

The XAS of Co, Mn, Ni and O are the same for the HENMC and HENMC-20AP sample under FYI mode, indicating that the effect of ALD process only happens on the surface, and the bulk of these two materials remain the same.
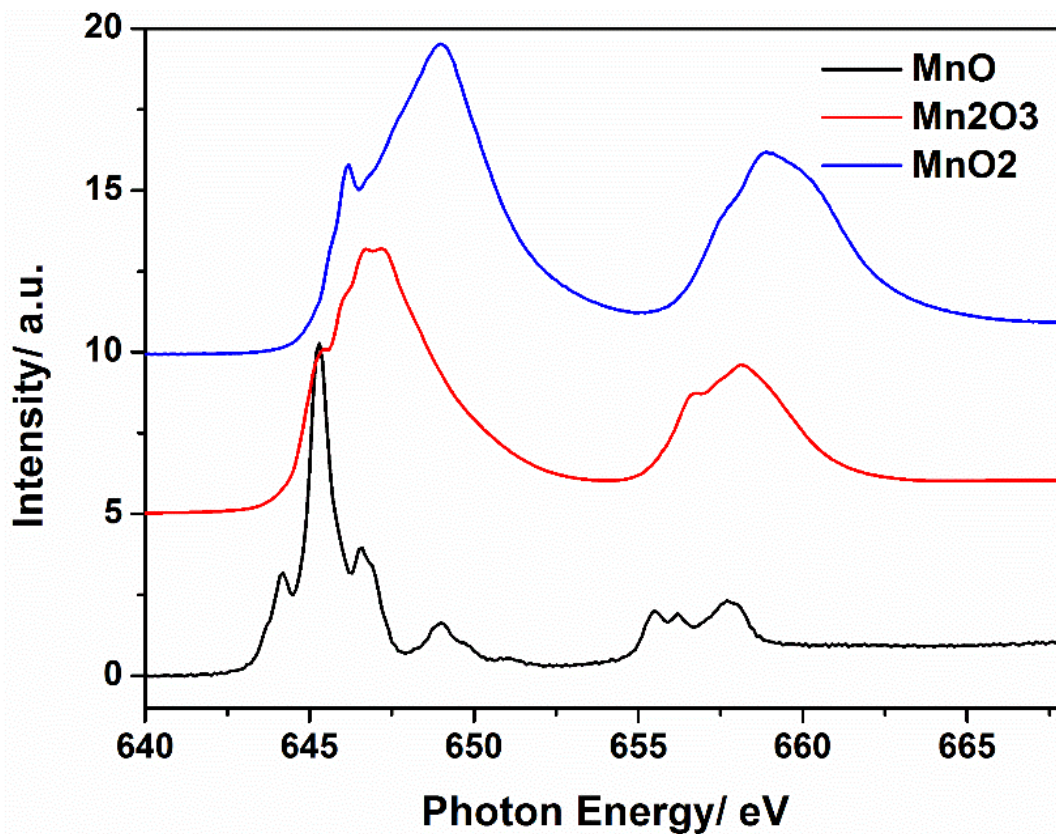
Figure SI 5.2 XAS of standard MnO$_2$, Mn$_2$O$_3$ and MnO
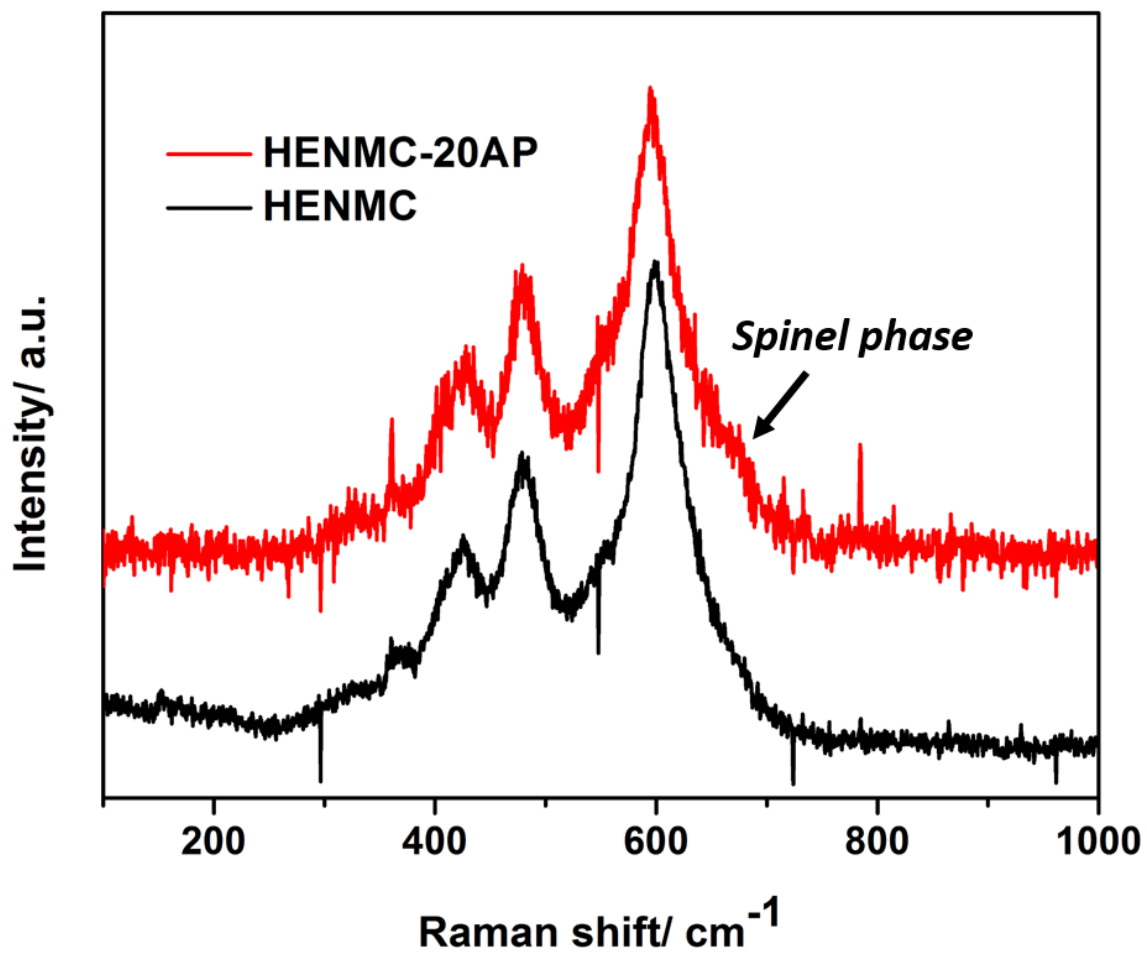
Figure SI 5.3 Raman spectra of HENMC and HENMC-20AP

The extra peak at around 660 cm^{-1} can be assigned to the Raman signal of the extra spinel phase after ALD treatment.
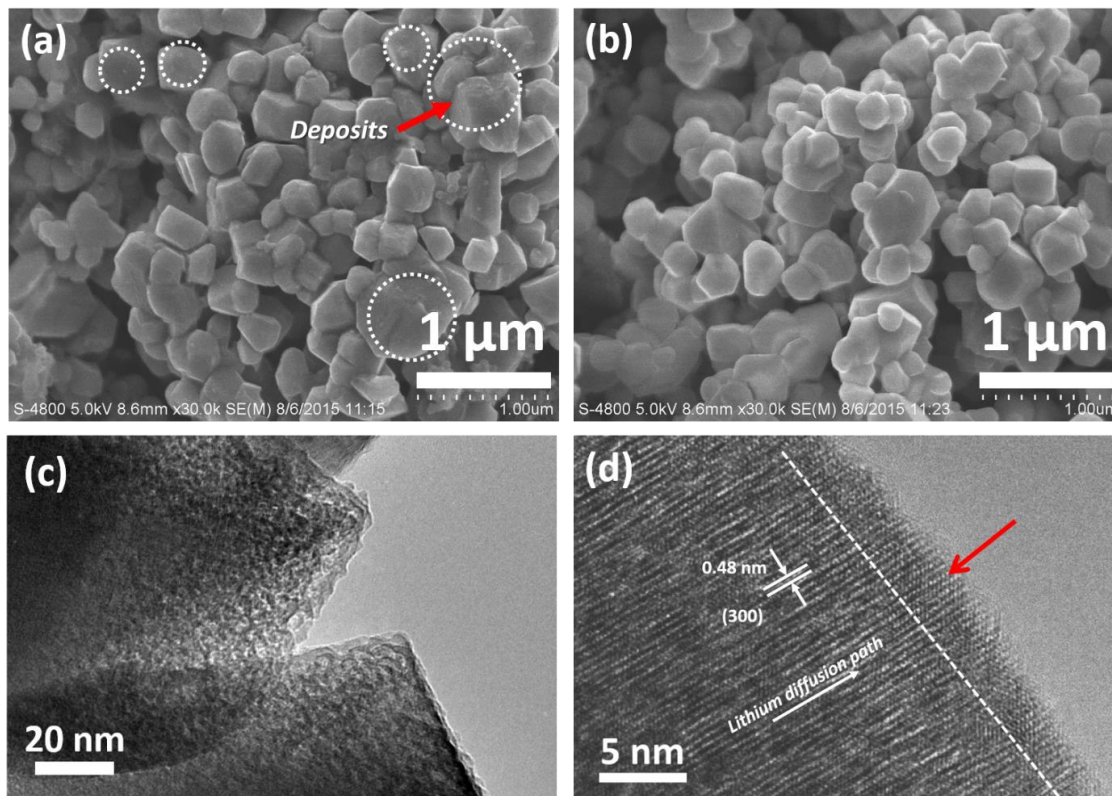
Figure SI 5.4 (a) SEM image of pristine HENMC after first charge; (b) SEM image of HENMC-20AP after initial charge; (c) TEM image of pristine HENMC after 40 cycles; (d) HRTEM image of pristine HENMC after 40 cycles

The surface of the pristine HENMC shows lots of deposits after initial charge, but the 20 AP sample does not show such deposits, indicating that the formation of SEI has been effectively suppressed by the coating layer.

The cycled pristine HENMC shows sponge-like surface, indicating that the attack from the HF has been very intense and resulted in the formation of pits on the surface. Also, HETEM image has clearly revealed that there is a new column of atoms forming on the surface with a depth of about 3 nm. This proves that the spinel phase formation due to cation migration into Li layer has happened during cycling.

Chapter 6

6   Insight into the Structure Evolution of Li-rich NMC via In-situ X-ray Absorption Spectroscopy

The irreversible structural change of lithium-ion battery cathode materials is a major hindrance to the longevity of it. Previous studies have thoroughly investigated the role of surface modification methods in enhancing the cathode materials performance. In this chapter, we focus on unveiling the consequences of the cathode materials phase changes. Such change initiates from the surface where defects exist widely and are close to the electrolyte, therefore, understanding the mechanism will provide strong supports for the design of surface modification methods.

We used in-situ XAS measurement to track the change of the transition metals in Li-rich NMC during the initial cycle and the 450th cycle. The initial cycle was found to involve major redox reactions of Ni and Co, which are the main charge compensation mechanism, Mn was slightly reduced from tetravalent state during discharge. On the contrary, the sample cycled for 450 times showed almost no electrochemical activity in Co and Ni, it was found that Mn was the only transition metal that participated in the charge compensation process. Such discoveries will help understand how Li-rich NMC loses the capacity and achieve high-performance LIBs.

6.1 Introduction

Li-rich transition metal oxides, with a net chemical formula of $xLi_2MnO_3 \cdot (1-x)LiMeO_2$ (Me = Mn, Ni, Co etc.), have been regarded as one of the most promising cathode materials for the next generation high energy density lithium-ion batteries (LIBs).[1] Different from conventional layered $LiMeO_2$, excessive lithium ions reside in the transition metal layers, forming an inter-grown Li_2MnO_3 phase with $LiMn_6$ units in the parent $LiMeO_2$ structure.[2] The combination of the C2/m Li_2MnO_3 and the R3m $LiMeO_2$ phases has allowed this material to deliver a capacity of over 250 mAhg^{-1} within a voltage window of $2.0 - 4.6$ V (vs Li/Li$^+$), thus it is also named high energy NMC (HENMC). The activation of the electrochemically inactive Li_2MnO_3 during initial charge results in simultaneous oxygen release and delithiation, with a net loss of Li_2O. The remaining MnO_2 phase is electrochemically active and therefore can accept excessive lithium ions during discharge.[3] Within current understanding, the benefit of extra capacity is, however, a tradeoff of irreversible structural change, which is a result of cation migration into the lithium vacancies in the lithium layers after oxygen release, forming a spinel structure that continuously grows into the bulk of the material and severely blocks the lithium diffusion pathways, ending up with very poor rate capability.[4, 5] On the other hand, the agglomeration of the spinel phase leads to the decay of average voltage and results in the loss of energy density of the whole cell, as has been proposed by numerous studies.[3, 6-8] The migration of the transition metals has also been studied by many researchers through microscopic devices, most of them found that the Ni tend to segregate from the layered phase, due to the low valence of Ni^{2+} and close radii with Li$^+$.[9, 10] Despite the well-accepted phase transition mechanism, there still remains many unresolved questions in the HENMC. First, are all the three transition metals transforming into spinel phases? Second, are all of them contributing to the capacity throughout the test? Last but not least, is the spinel phase the only charge compensation mechanism after long term cycling process?

X-ray absorption spectroscopy (XAS) that allows for the acquisition of local structures of transition metals has been carried out by many researchers. Transition metals K edges provide abundant information of electronic configuration and the oxidation level, therefore are extensively used for the understanding of structural changes of cathode materials. In

this study, an in-situ XAS measurement was carried out to track the change of transition metals in the first and 450th cycle, which allows for the understanding of charging compensation and structural evolution mechanisms of HENMC. It was found that in the first charge process, Mn does not change its valence, only MnO_6 octahedra distortion was observed, on the other hand, Ni and Co are oxidized. The initial discharge showed slight reduction of Mn and reversible reduction of Ni and Co to the original state. The most striking discovery was that in the 450th cycle, the Ni and Co showed almost no valence change at all throughout the test, which has not been observed before. The loss of electrochemical activity of Ni and Co demonstrates that the phase segregation of Co and Ni into inactive phases is the main reason of capacity loss.

6.2   Experimental

6.2.1   Materials Synthesis

The Li-rich NMC was synthesized via following steps: stoichiometric $MnSO_4 \bullet H_2O$, $NiSO_4 \bullet 6H_2O$ and $CoSO_4 \bullet 7H_2O$ were mixed to form solution A with a concentration of 1 mole/L. Na_2CO_3 and ammonia were mixed to form solution B with $NaCO_3$ concentration of 1 mole/L and ammonia concentration of 0.15 mol/L. Solutions A and B were fed into the reactor by a peristatic pump in a speed of 1 mL/min, the temperature was controlled to be 60 ^oC, the mixed solution was strongly agitated under a speed of 400 rmp, pH was controlled to be 7-8. After 6 hours, the precipitates were washed by de-ionized water and dried in vacuum under 120 ^oC for 12 hours to obtain the Ni-Co-Mn carbonate precursors. Afterwards, the precursor was mixed with certain amount of LiOH thoroughly and sintered under 500 ^oC for 5 hours and 900 ^oC for 20 hours to obtain the final material.

6.2.2   Characterization Methods

The morphology of the samples was characterized by a Hitachi S-4800 field emission scanning electron microscopy (FESEM) and a JEOL 2010F high-resolution transmission electron microscope (HRTEM). The X-ray diffraction (XRD) patterns were collected on a Bruker D8 Advance Diffractometer using Cu K_α radiation at 40 kV and 40 mA. Raman results were collected on a HORIBA Scientific LabRAM HR Raman spectrometer system

with a 532.4 nm laser and optical microscope. In-situ hard X-ray absorption spectroscopy was collected on the HXMA beamline in CLS under fluorescence mode. The energy was calibrated to Co metal so as to collect the K edge XAS of Mn, Co and Ni in a row.

6.2.3   Electrochemical Measurement

To prepare the electrodes for coin cell fabrication, the Li-rich NMC powders were uniformly mixed with acetylene black (AB) and poly(vinylidene fluoride) (PVDF) in a ratio of 80:10:10 in an N-methyl-pyrrolidione (NMP) solvent. Then, the slurry was pasted on aluminum foils and dried at 80 $^{\circ}$C under vacuum overnight. The electrode was subsequently cut into round shape and assembled into a CR-2032 coin cell in an argon-filled glove box with the moisture and oxygen being controlled below 0.1 ppm. Lithium metal was used as the counter electrode in the coin cells. 1M $LiPF_6$ dissolved into ethylene carbonate (EC) and diethyl carbonate (DEC) in a 1:1 volume ratio (BASF corp., US) was used as the electrolyte. Celgard 2400 was used as the separator. Galvanostatical charge/discharge test was carried out on Maccor 4000 between 2.0 V and 4.6 V (vs Li/Li^+), the initial cycle was conducted under 1/20 C (12.5 mA/g) for activation, and the following cycles were tested under 1/2 C (125 mA/g). The tested cells were dissembled in a glove box and assembled into an in-situ cell for in-situ XAS study. The in-situ cells were tested on a portable Neware BTS 3000 battery charging station at the beamline.

6.3 Results and Discussions
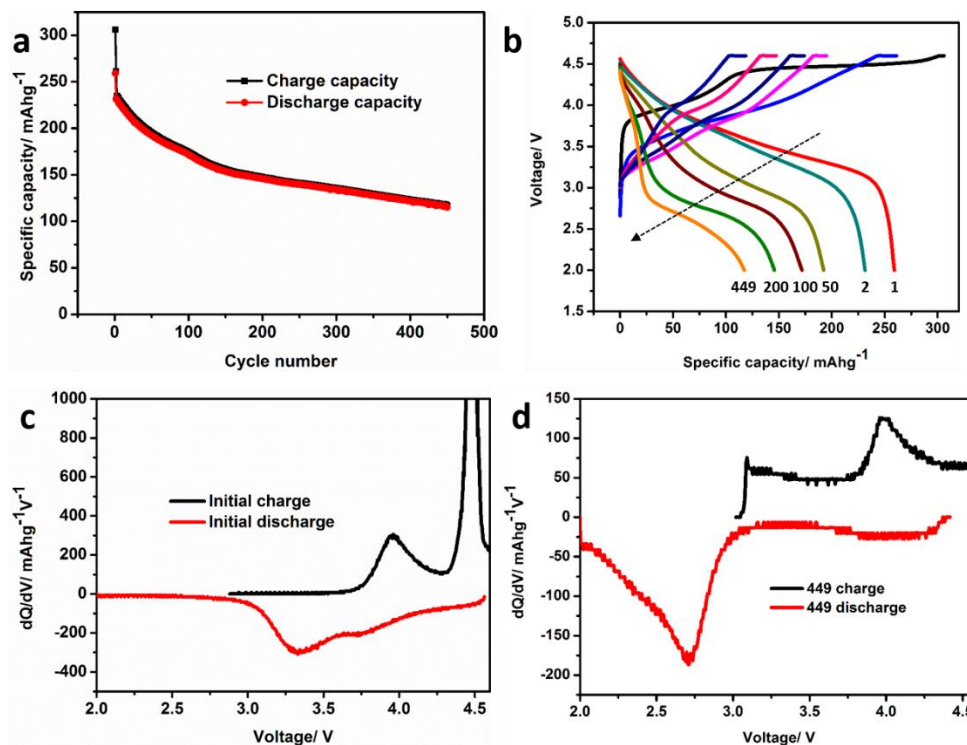
Figure 6.1 Cycling performance of the HENMC; (b) Charge/discharge curves of the 1st, 2nd, 50th, 100th, 200th, and 449th cycle; (c) dQ/dV curves of the initial cycle and (d) dQ/dV curves of the 449th cycle

The HENMC cathode material was cycled under C/2 rate after an initial activation cycle at C/20, the initial charge capacity was 303 mAhg^{-1} and the initial discharge capacity was 253 mAhg^{-1}, as has been shown in Figure 6.1a. The large irreversible capacity in this material leads to the loss of active Li$^+$ and remains one of the most critical problems of it. The capacity shows dramatic decay after long-term cycling, only 123 mAhg^{-1} discharge capacity was obtained in the 449th cycle. Figure 6.1b shows the charge/discharge curves of the 1st, 2nd, 50th, 100th, 200th and 449th cycles, the average voltage has dropped significantly. SEM images of the fresh electrode and the electrode after 449 cycles are presented in Figure SI6.1, the original HENMC particles are around 100 nm. After cycling, the size of the particles remains almost unchanged, the particles are covered by a dense film, which is possibly the solid electrolyte interphase (SEI) that was formed from the oxidation decomposition of the electrolyte. dQ/dV curves show typical redox reactions in the Li-rich

NMC, the peak during discharge shifts from 3.25 V to 2.75 V, indicating obvious voltage drop.
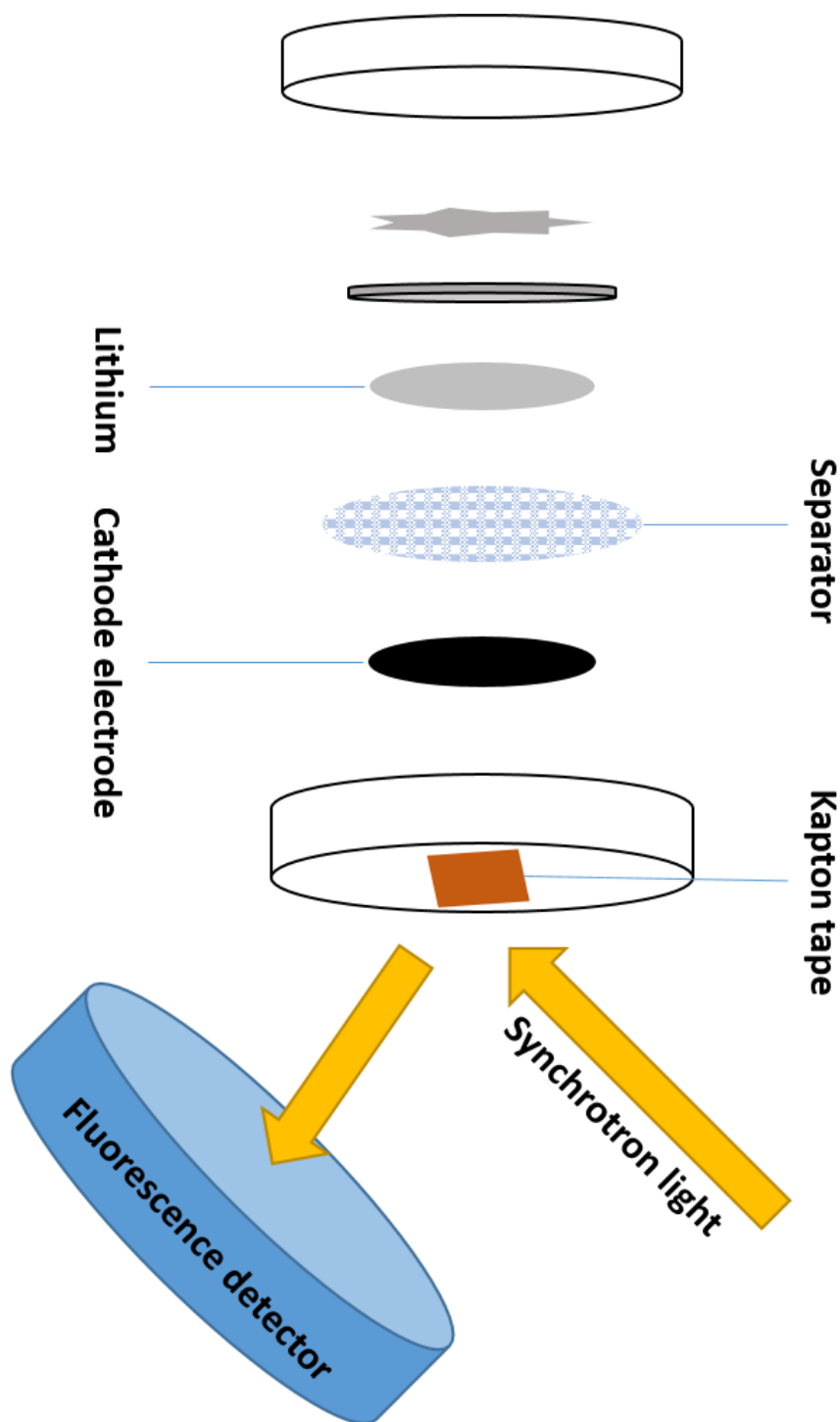
Figure 6.2 Schematic illustration of the in-situ cell
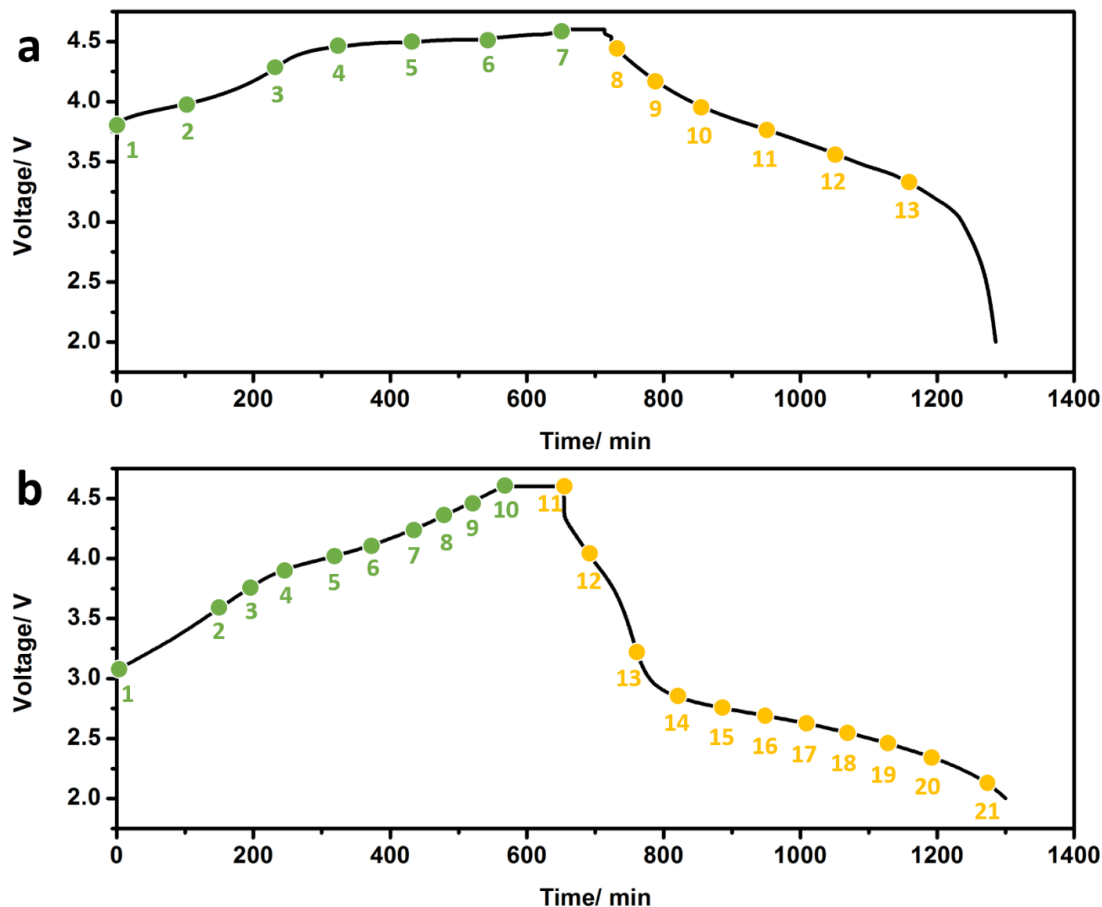
Figure 6.3 Charge/discharge voltage versus time of the in-situ first cycle under 1/10 C and 450th cycle under 1/20 C

The in-situ XAS measurements were taken on a fresh electrode and an electrode that has been previously cycled for 449 times. The configuration of the in-situ cell is shown in Figure 6.2, a hole was drilled on the cathode case and covered by a transparent Kapton tape to allow for the collection of fluorescence signals from the cathode electrode during operation. Since the heavily cycled cell had only about 50% capacity retention, the C-rate for it was decreased to C/20 in order to allow for sufficient data collection time on the beamline. The collected points are shown in Figure 6.3. In the fresh cycle, 7 points were collected during charging and 6 were collected during discharging. In the 450th cycle, 10 points were collected during charging and 11 points were collected during discharging.

6.3.1   In-situ XAS Measurement of the Initial Cycle
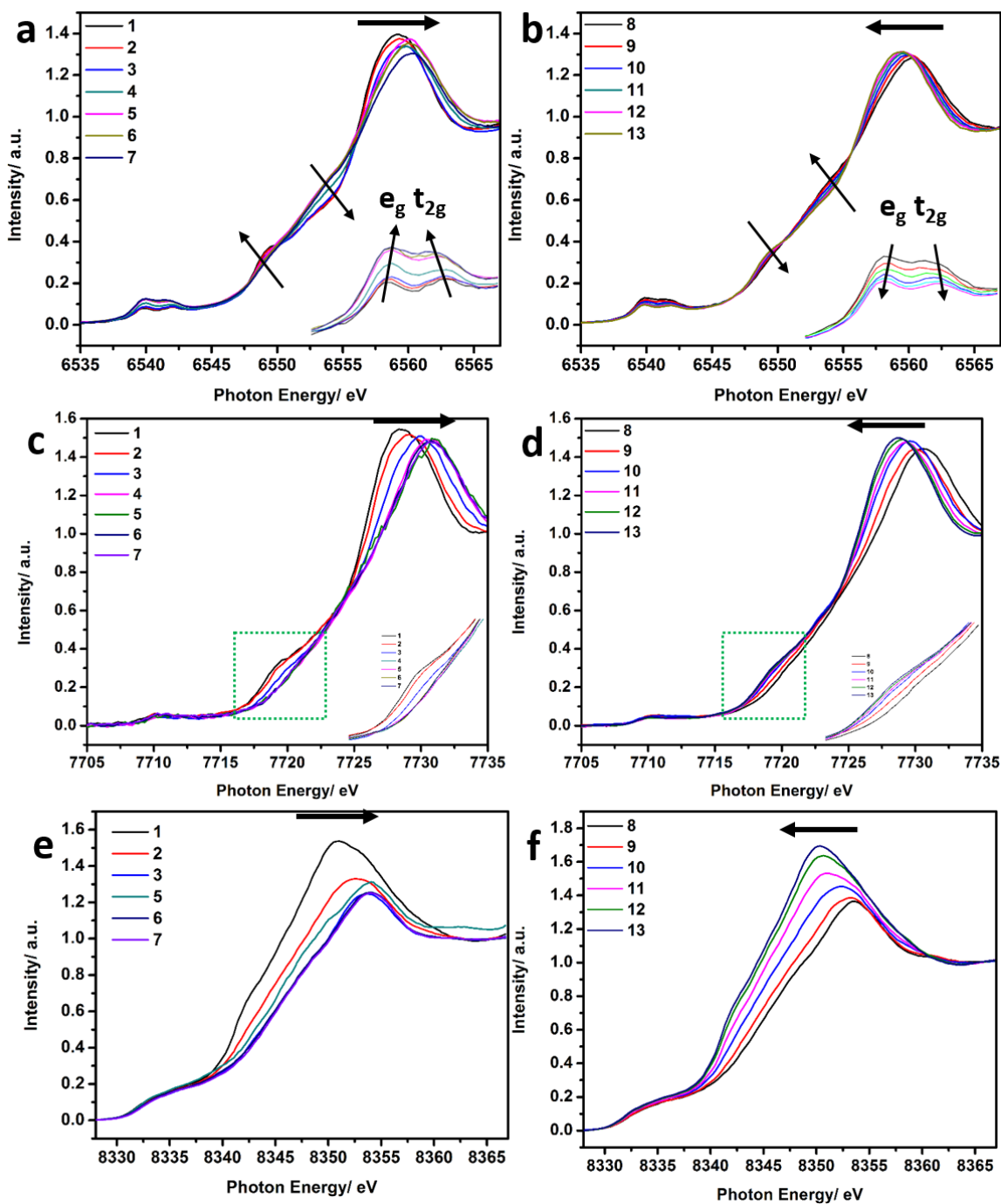
Figure 6.4 In-situ XANES measurement of initial cycle Mn K-edges during (a) charging and (b) discharging; Co K-edges during (c) charging and (d) discharging and Ni K-edges during (e) charging and (f) discharging;

The in-situ XAS measurement of the Mn K-edges of the fresh electrode are shown in Figure 6.4a-b. Each of the spectra shows significant difference throughout the whole process. Figure 6.4a displays the Mn K-edge XANES of the charging process. At the open circuit voltage (OCV) point, the Mn K-edge has a threshold energy (E_0) of 6548.25 eV. A plot of the E_0 values against the formal valences of various manganese oxides is shown in Figure SI6.3, it can be seen that the E_0 values of these manganese compounds are linearly correlated to the valences, the slight deviation of $LiMn_2O_4$ and Mn_2O_4 might be due to the presence of Mn^{3+} in these compounds, which is Jahn-Teller active and may change the shape of the XANES.[11] The OCV Mn K-edge XANES reveals that the Mn in the fresh HENMC sample is at tetravalent state with a 3d configuration of high spin $t_{2g}^3 e_g^0$.[12] The intensity of the Mn pre-edges increases continuously during charging process. Mn pre-edges are assigned to the dipole forbidden transition of 1s to 3d states, it appears to be very weak in octahedral coordination. Due to the mixing of the 4p and 3d state, an electric quadrupole-allowed transition has contributed to the pre-edge peak as well, therefore the pre-edge peaks are discernable and can be found to have splitted into two peaks.[12] The presence of the two pre-edge peaks also confirms that the Mn ions are in tetravalent state since trivalent Mn only show one pre-edge peak due to the Jahn-Teller distortion modification of low spin $t_{2g}^3 e_g^1$.[13] The peak at lower energy can be assigned to the 3d e_g energy level and the one at higher energy can be assigned to the 3d t_{2g} energy level. The continuous growth of these two peaks in the charge process reveals that the MnO_6 octahedral sites are distorted by the removal of Li^+ from the lattice. Figure SI6.5a depicts the first derivative of the XANES of the Mn K-edge, generally the first inflection peak after the pre-edge peaks corresponds to the threshold energy (E_0), which is indicative of the oxidation level. During the charging process, the threshold energy of the Mn appears to be unchanged, such observation confirms that the Mn does not participate in the charge compensation due to the removal of Li^+, which agrees well with other studies.[12, 14] During discharge, the Mn K-edges show reversing trend, the intensities of the pre-edges gradually return to the original level, confirming that part of the insertion of Li^+ is reversible. The main difference of the Mn K-edge during discharge is that slight reduction has been observed in Figure SI6.5b. However, due to the complexity of the Mn K edges affected by the ligand field splitting of Mn-O bonds, it is hard to quantitatively measure

the level of reduction simply by looking at the shift of E_0. The reduction of Mn was also reported by Ito et al., they found that the Mn was reduced to 3.6+ based on the linear calculation of the position of the half height of the pre-edge.[14] It has been reported that the activation of the Li_2MnO_3 during the charging process leads to the formation of layered MnO_2 and O_2 with the extraction of Li^+. The MnO_2 is electrochemically active and thus can accommodate Li^+ and form $LiMnO_2$, this process is accompanied with the reduction of Mn^{4+}.

The Co K-edge XANES were recorded and shown in Figure 6.4c-d. The Co K-edge at the OCV has an E_0 of 7718.21 eV, which is close to that of $LiCoO_2$, indicating that the Co is in 3+ in the HENMC. The charging/discharging process of Co shows essentially different behaviors to that of Mn. Besides the shift of the white line to a higher energy, the E_0 also changes, indicating that the Co has participated in the redox reaction to compensate the Li^+ removal. The inset figure in Figure 6.3c shows that the oxidation of Co started from the very beginning of the charging process and ceased to change at the 4th point, which corresponds to the voltage value of 4.43 V. It has been reported that the reaction of the HENMC below 4.4 V during initial charging is mainly the Li^+ extraction from the $LiMeO_2$ (Me = Mn, Co, Ni). No reactions related to Co are expected above 4.4 V since the long plateau in this voltage range is attributed to the loss of oxygen and Li^+ from the lattice of Li_2MnO_3. The above observation complies with literatures and confirms the effectiveness of in-situ XAS on the study of transition metal valence changes. The E_0 at OCV and fully charged state of Co are plotted in Figure SI6.5c, the E_0 at fully charged state shows an E_0 of 7719.92 eV, which is 1.71 eV higher than that of the OCV. Due to the difficulty of obtaining naturally stable Co^{4+} compounds, we drew an extension line according to the E_0 values of CoO, Co_2O_3 and $LiCoO_2$ against their formal valences as shown in Figure SI6.4. Assuming that the valence of Co is linear with the values of E_0 in these cobalt oxides, it can be found that the fully charged state displays a Co at 4.02+ oxidation level, which also agrees with previous literatures. The reversible change of Co can be observed in the Co K-edges in the discharge process. The E_0 values, as shown in the inset of Figure 6.3d, show continuous decrease from point 8 to point 10 and remain almost unchanged from point 10 to point 13. Point 10 corresponds to the voltage of 3.57 V, indicating that the reduction of Co happens predominantly above 3.57 V, this is consistent with other reports that the

layered $R\bar{3}m$ $LiMeO_2$ phase mainly delivers its capacity above 3.50 V. The fully discharged point shows a Co K-edge E_0 of about 7718.12eV, which can be assigned to trivalent Co according to Figure SI6.4. The results indicate that the redox reaction of Co is between Co^{3+} and Co^{4+}, similar with other layered cathode materials such as $LiCoO_2$ and $LiNi_{1/3}Co_{1/3}Mn_{1/3}O_2$.

The redox reactions of Ni have also been observed. Similar with the Co K-edges, the oxidation of Ni predominately happens before point 6, as can be observed from Figure 6.4e, point 6 and 7 almost overlap. The E_0 position of Ni turns out to change much more significantly compared to Mn and Co, indicating that the valence of Ni underwent more profound change, which agrees with previous reports that Ni was oxidized from 2+ to 4+.[12,14]

Aside from the reduction of Mn, Co and Ni, there are numerous studies reporting that oxygen has participated in the charge compensation process during the initial charge.[15] Ito et al. calculated the capacity based on the valence change of Mn, Ni and Co using Faraday's law and found that the discharge capacity is lower than actual capacity, indicating that the oxygen has participated in the charge compensation.[14] Bruce et al. found that the localized electron holes on O coordinated by Mn^{4+} and Li^+ ions instead of the formation of true O_2^{2-} species was the main source of charge compensation.[16] In both cases, O participation is found to be a profound reason of the high capacity of HENMC.

6.3.2　In-situ XAS Measurement of the 450th Cycle

The capacity fade of cathode materials has been systematically investigated by many researchers. Transition metal dissolution into the electrolyte, electrolyte decomposition and phase segregation have been proposed to be the chief reasons of capacity loss in HENMC.[17] ICP measurements were carried out to estimate the amount of transition metal dissolved into the electrolyte. The ratio of Mn:Co:Ni was found to be 67:16:17 in the fresh sample, which is close to the theoretical ratio of 68:16:16 according to the chemical formula of $Li_{1.2}Mn_{0.54}Co_{0.13}Ni_{0.13}O_2$. However, in the heavily cycled electrode, the ratio changed to 65:17:18. The obvious drop of Mn reveals that the dissolution of Mn is the most intense among the three transition metals, which agrees well with previous reports.[18]

Aside from the transition metal dissolution, intense phase transformation has also been found in the XRD and Raman results shown in Figure SI6.3. Though it is very hard to index the composition of each element simply by looking at these results, we can still find that the original layered structure has turned into multiple phases including rock-salt like phases and spinel phases. Wang et al. studied the distribution of transition metals in fresh sample surfaces and found that, thermodynamically, Ni tends to aggregate on the surface and form a spinel-like structure, whereas the formation of Co-rich rock phase is favorable.[19] The advantage of in-situ XAS is that it can isolate each of the element and study individually, making it an ideal technique to track the behaviors of the transition metals in the cells after prolonged cycling. The in-situ XAS measurements results of the 450th cycle are therefore presented in Figure 6.5.
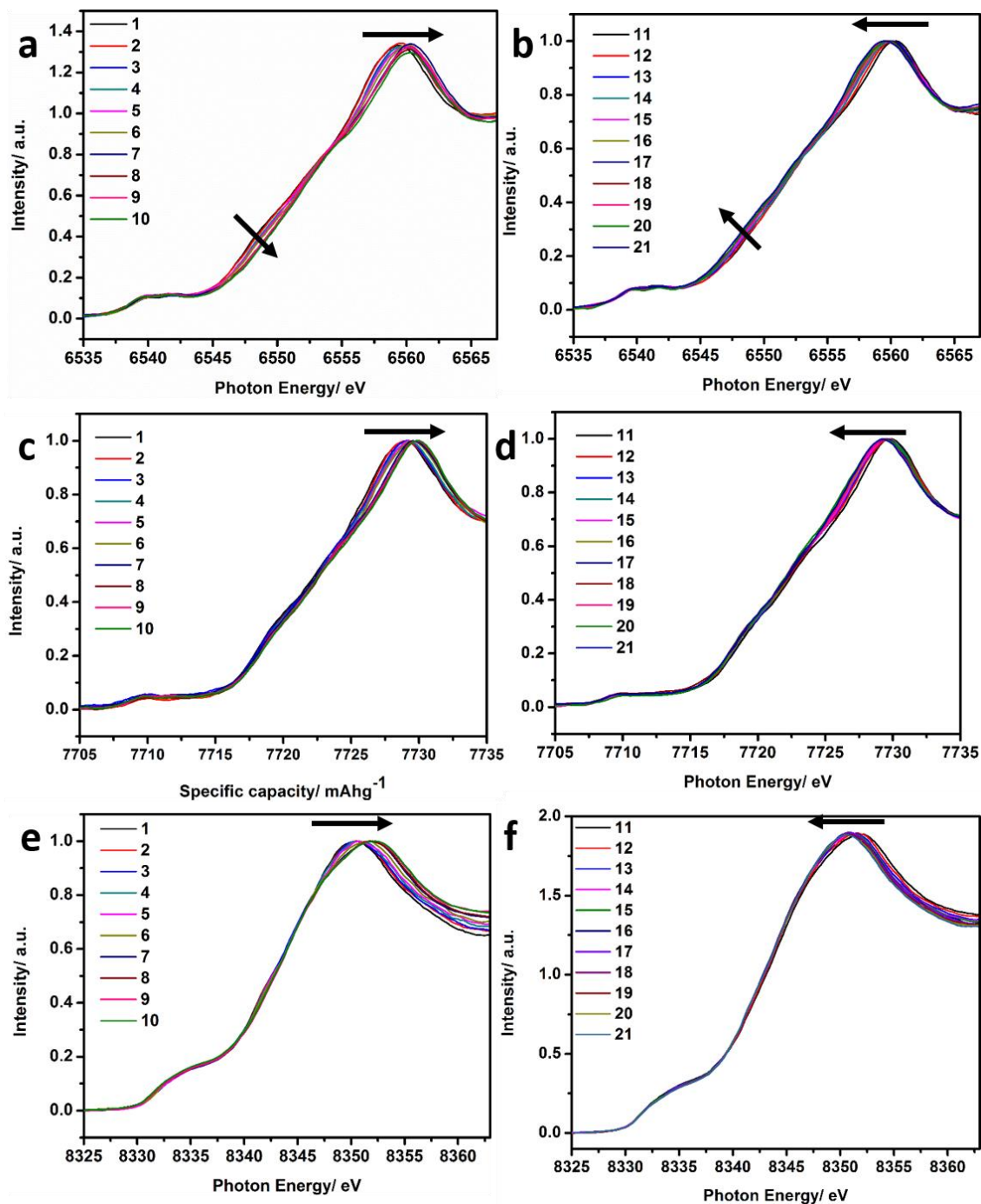
Figure 6.5 In-situ XANES measurement of the 450th cycle Mn K-edges during (a) charging and (b) discharging; Co K-edges during (c) charging and (d) discharging and Ni K-edges during (e) charging and (f) discharging;

In the Mn K-edges, the pre-edge becomes much less discernable, the two peaks observed in the initial cycle have merged into one, as has been mentioned before, it is a result of

Jahn-Teller modifications to the Mn^{3+} with a configuration of low spin $t_{2g}^3 e_g^1$. Therefore, after extensive cycling, the Mn was reduced in the whole material. Compared with the initial cycle, it shows much less intense shape change, though the edges can be found to shift reversibly slightly during charging and discharging. The change of Mn reveals that it still participates in the charge compensation process in the heavily cycled sample. Though it is very hard to quantify the exact change of valence, such change is not as profound, since the pre-edges did not show significant change of intensity or position, as opposed to the initial cycle. The insertion of Li^+ in the surrounding environment of MnO_6 octahedra changes the white-line position.

The evolution of Co differs significantly from the initial cycle, as shown in Figure 6.5c, after long term cycling, the Co shows an E_0 of 7718.36 eV, which corresponds to a valence of about 3.1+, however, the absorption edges of the Co do not show any obvious shift, which is also observed in the first inflection peak in Figure SI6.7c. On the other hand, the shape of the Co XANES results changes continuously, indicating that the CoO_6 octahedra were distorted even though Co did not participate in the charge compensation process. Nevertheless, the change of the shape is still not as profound as the fresh sample. The loss of Co activity should be directly responsible for the capacity loss of HENMC.

Similar results can be found in the Ni K-edge XANES as well. In the initial cycle, the change of Ni is very significant, since the valence changed from 2+ to 4+ during charging. However, in the heavily cycled electrode, the edge positions of the Ni K-edges were almost overlapping without any changes. The unchanged edge positions of Ni indicate that the same as Co, Ni has lost its electrochemical activity.

The simultaneous loss of electrochemical activities of Co and Ni, together with the trivial Mn K-edge change, brings about the speculation that there might remain other charge compensation mechanisms so as to obtain a discharge capacity of as high as 125 mAhg^{-1} in the 450th cycle. It is possible that oxygen participation as observed in the first discharge process might have remained in the heavily cycled sample, which needs to be further confirmed.

6.4   Conclusions

In-situ XAS measurements have been carried out to investigate the behaviors of the transition metals in HENMC during both the initial cycle and the 450th cycle. Through comparison of these two sets of in-situ XAS studies, it was found that the initial cycle involves the structural distortion of Mn-related phases without oxidation of Mn, instead, Ni and Co were oxidized to compensate the charge, together with the oxidization of crystalline O^{2-}. The initial charge involves reduction of all of the three transition metals. In sharp contrast to the initial cycle, Ni and Co were found to be unable to be oxidized/reduced in the 450th cycle, only Mn was slightly oxidized/reduced. The loss of electrochemical activity of both Ni and Co is the main reason of capacity fade after prolonged cycling. The charge compensation simply by the slight change of Mn cannot exclude the possibility of the participation of anionic redox reaction in the heavily cycled samples. The results in this paper will help researchers design high-energy cathode materials through the manipulation of transition metals and the exploitation of oxygen.

Acknowledgement

References

[1] H. Yu and H. Zhou, High-Energy Cathode Materials (Li_2MnO_3-$LiMO_2$) for Lithium-Ion Batteries, *J. Phys. Chem. Lett.*, 2013, **4**, 1268-1280.

[2] H. Yu, H. Kim, Y. Wang, P. He, D. Asakura, Y. Nakamura and H. Zhou, High-Energy 'Composite' Layered Manganese-Rich Cathode Materials Via Controlling Li_2MnO_3 Phase Activation for Lithium-Ion Batteries, *Phys. Chem. Chem. Phys.*, 2012, **14**, 6584-6595.

[3] N. Yabuuchi, K. Yoshii, S. T. Myung, I. Nakai and S. Komaba, Detailed Studies of a High-Capacity Electrode Material for Rechargeable Batteries, Li_2MnO_3-$LiCo_{(1/3)}Ni_{(1/3)}Mn_{(1/3)}O_2$, *J. Am. Chem. Soc.*, 2011, **133**, 4404-4419.

[4] P. Yan, A. Nie, J. Zheng, Y. Zhou, D. Lu, X. Zhang, R. Xu, I. Belharouak, X. Zu, J. Xiao, K. Amine, J. Liu, F. Gao, R. Shahbazian-Yassar, J. G. Zhang and C. M. Wang, Evolution of Lattice Structure and Chemical Composition of the Surface Reconstruction Layer in $Li_{(1.2)}Ni_{(0.2)}Mn_{(0.6)}O_2$ Cathode Material for Lithium Ion Batteries, *Nano Lett.*, 2015, **15**, 514-522.

[5] M. Gu, I. Belharouak, J. Zheng, H. Wu, J. Xiao, A. Genc, K. Amine, S. Thevuthasan, D. R. Baer, J. G. Zhang, N. D. Browning, J. Liu and C. Wang, Formation of the Spinel Phase in the Layered Composite Cathode Used in Li-Ion Batteries, *ACS Nano*, 2013, **7**, 760-767.

[6] L. Xiao, J. Xiao, X. Yu, P. Yan, J. Zheng, M. Engelhard, P. Bhattacharya, C. Wang, X.-Q. Yang and J.-G. Zhang, Effects of Structural Defects on the Electrochemical Activation of Li_2MnO_3, *Nano Energy*, 2015, **16**, 143-151.

[7] X. Xiang, J. C. Knight, W. Li and A. Manthiram, Sensitivity and Intricacy of Cationic Substitutions on the First Charge/Discharge Cycle of Lithium-Rich Layered Oxide Cathodes, *J. Electrochem. Soc.*, 2015, **162**, A1662-A1666.

[8] D. Mohanty, A. S. Sefat, J. Li, R. A. Meisner, A. J. Rondinone, E. A. Payzant, D. P. Abraham, D. L. Wood, C. Daniel, Correlating Cation Ordering and Voltage Fade in a Lithium-Manganese-Rich Lithium-Ion Battery Cathode Oxide: A Joint Magnetic Susceptibility and Tem Study, *Phys. Chem. Chem. Phys.*, 2013, **15**, 19496-19509.

[9] D. Mohanty, J. Li, S. C. Nagpure, D. L. Wood and C. Daniel, Understanding the Structure and Structural Degradation Mechanisms in High-Voltage, Lithium-Manganese–Rich Lithium-Ion Battery Cathode Oxides: A Review of Materials Diagnostics, *MRS Energy & Sustainability*, 2015, **2**.

[10] L. Gu, D. Xiao, Y. S. Hu, H. Li and Y. Ikuhara, Atomic-Scale Structure Evolution in a Quasi-Equilibrated Electrochemical Process of Electrode Materials for Rechargeable Batteries, *Adv. Mater.*, 2015, **27**, 2134-2149.

[11] T. Kim, B. H. Song, A. J. G. Lunt, G. Cibin, A. J. Dent, L. Lu and A. M. Korsunsky, Operando X-Ray Absorption Spectroscopy Study of Atomic Phase Reversibility with Wavelet Transform in the Lithium-Rich Manganese Based Oxide Cathode, *Chem. Mater.*, 2016, **28**, 4191-4203.

[12] H. Koga, L. Croguennec, M. Ménétrier, P. Mannessiez, F. Weill, C. Delmas and S. Belin, Operando X-Ray Absorption Study of the Redox Processes Involved Upon Cycling of the Li-Rich Layered Oxide $Li_{1.20}Mn_{0.54}Co_{0.13}Ni_{0.13}O_2$ in Li Ion Batteries, *J. Phys. Chem. C*, 2014, **118**, 5700-5709.

[13] A. Deb, U. Bergmann, S. P. Cramer and E. J. Cairns, In Situ X-Ray Absorption Spectroscopic Study of the $Li[Ni_{1/3}Co_{1/3}Mn_{1/3}]O_2$ Cathode Material, *J. Appl. Phys.*, 2005, **97**, 113523.

[14] A. Ito, Y. Sato, T. Sanada, M. Hatano, H. Horie and Y. Ohsawa, In Situ X-Ray Absorption Spectroscopic Study of Li-Rich Layered Cathode Material $Li[Ni_{0.17}Li_{0.2}Co_{0.07}Mn_{0.56}]O_2$, *J. Power Sources*, 2011, **196**, 6828-6834.

[15] S. Muhammad, H. Kim, Y. Kim, D. Kim, J. H. Song, J. Yoon, J.-H. Park, S.-J. Ahn, S.-H. Kang, M. M. Thackeray and W.-S. Yoon, Evidence of Reversible Oxygen Participation in Anomalously High Capacity Li- and Mn-Rich Cathodes for Li-Ion Batteries, *Nano Energy*, 2016, **21**, 172-184.

[16] K. Luo, M. R. Roberts, R. Hao, N. Guerrini, D. M. Pickup, Y. S. Liu, K. Edstrom, J. Guo, A. V. Chadwick, L. C. Duda and P. G. Bruce, Charge-Compensation in 3d-

Transition-Metal-Oxide Intercalation Cathodes through the Generation of Localized Electron Holes on Oxygen, *Nat. Chem.*, 2016, **8**, 684-691.

[17] A. Manthiram, J. C. Knight, S.-T. Myung, S.-M. Oh and Y.-K. Sun, Nickel-Rich and Lithium-Rich Layered Oxide Cathodes: Progress and Perspectives, *Adv. Energy Mater.*, 2015, **6**, 1501010-1501032.

[18] X. Li, J. Liu, M. N. Banis, A. Lushington, R. Li, M. Cai and X. Sun, Atomic Layer Deposition of Solid-State Electrolyte Coated Cathode Materials with Superior High-Voltage Cycling Behavior for Lithium Ion Battery Application, *Energy Environ. Sci.*, 2014, **7**, 768.

[19] P. Yan, J. Zheng, J. Zheng, Z. Wang, G. Teng, S. Kuppan, J. Xiao, G. Chen, F. Pan, J.-G. Zhang and C.-M. Wang, Ni and Co Segregations on Selective Surface Facets and Rational Design of Layered Lithium Transition-Metal Oxide Cathodes, *Adv. Energy Mater.*, 2016, **6**, 1502455.

Supporting Information
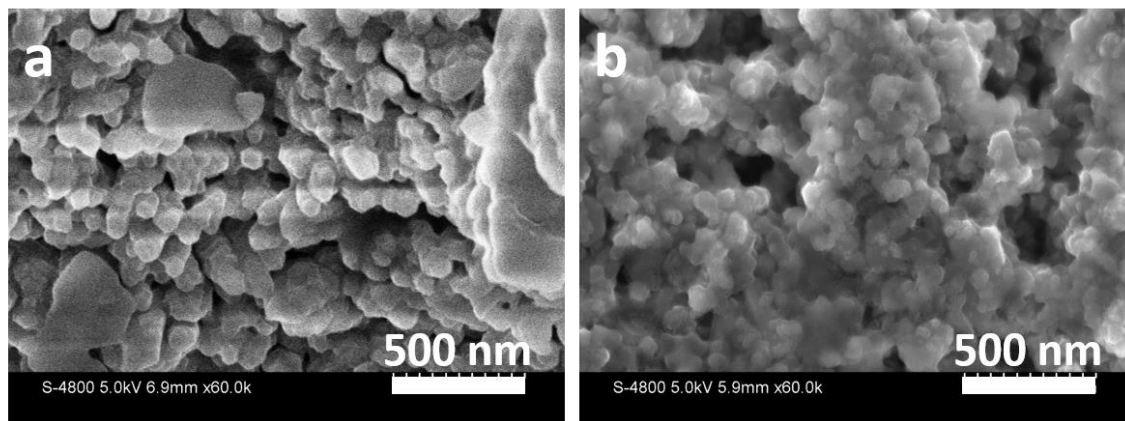
Figure SI 6.1 SEM images of (a) fresh electrode and (b) electrode after 450 cycles
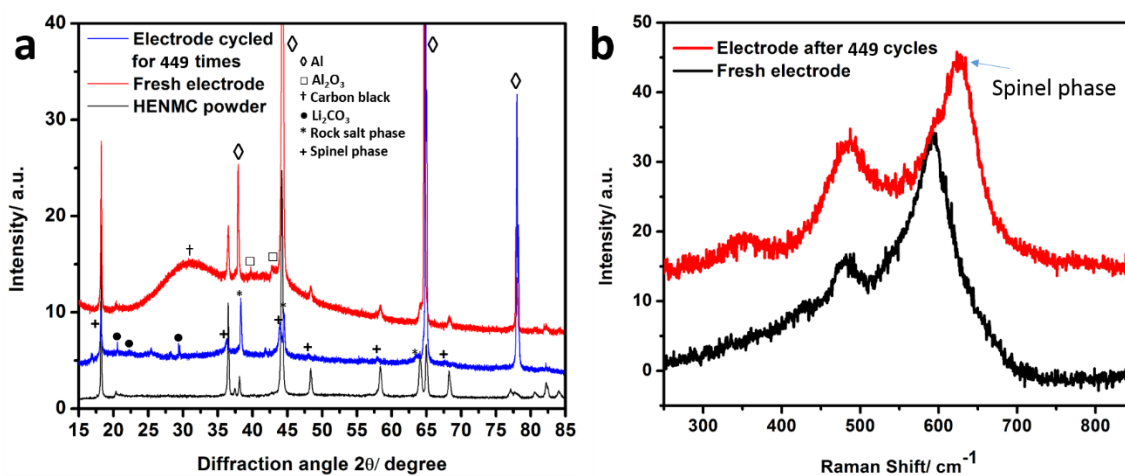
Figure SI 6.2 (a) XRD results of the HENMC particle, fresh electrode and electrode cycled for 450 times; (b) Raman results of the fresh electrode and the electrode cycled for 450 times
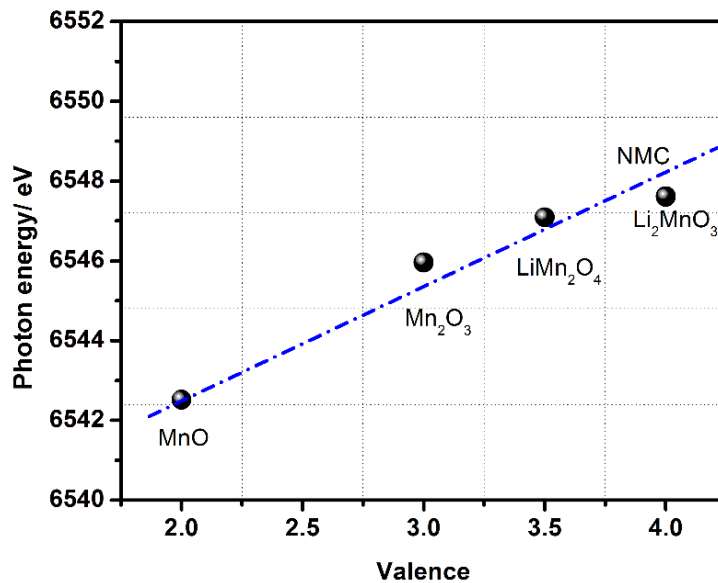
Figure SI 6.3 Plot of the E$_0$ values of various standard manganese oxides vs their formal valence
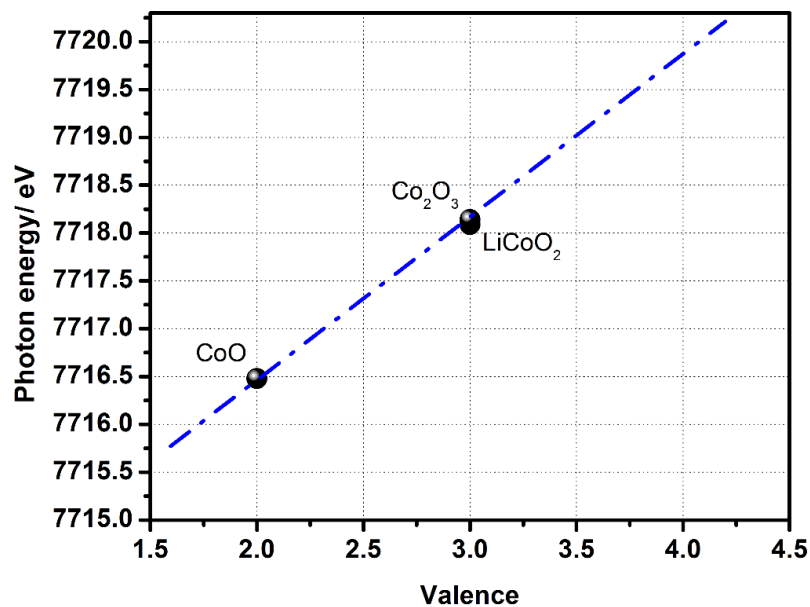
Figure SI 6.4 Plot of the E$_0$ values of various standard manganese oxides vs their formal valence
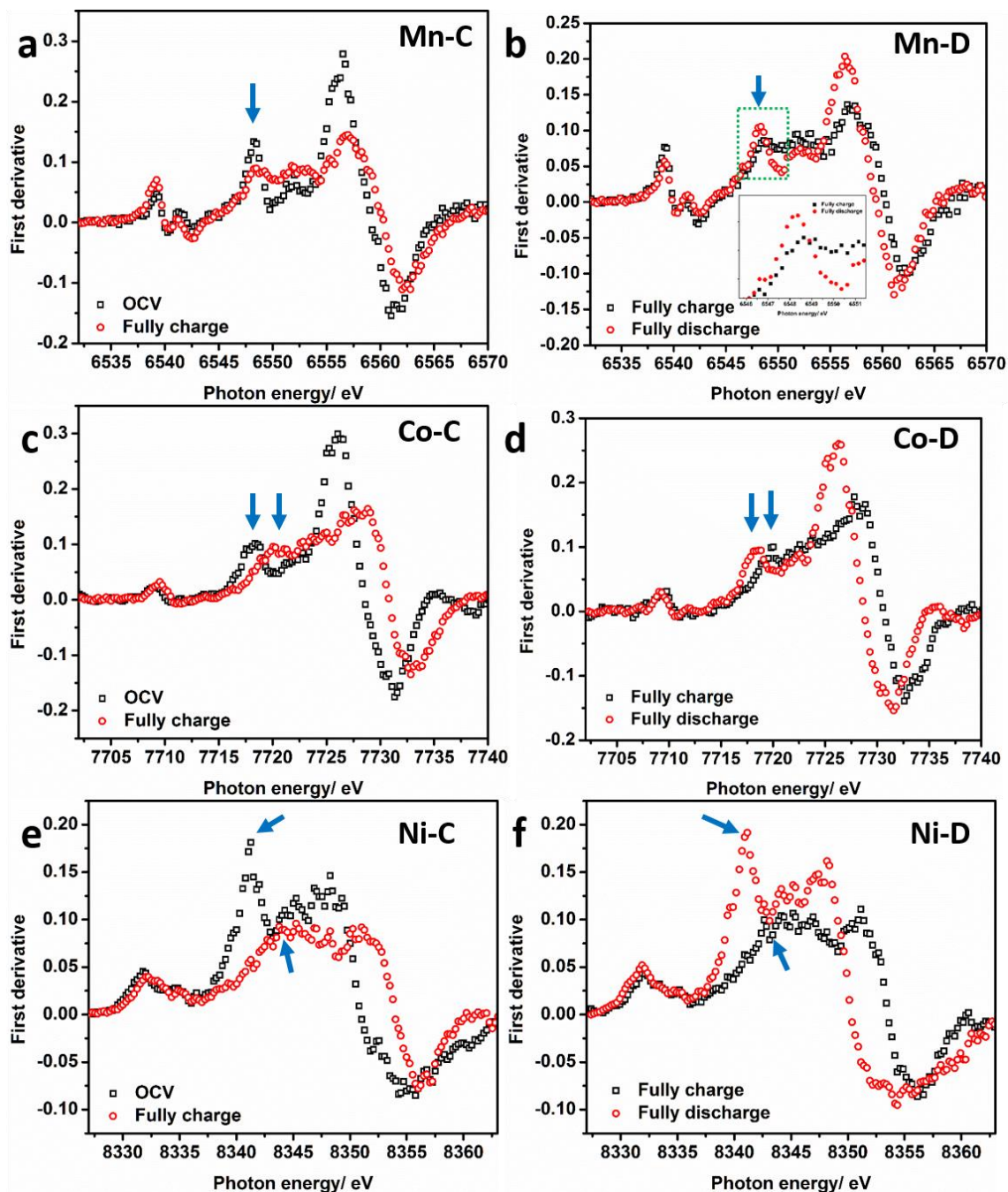
Figure SI 6.5 First derivative plots of the first cycle XANES with Mn (a) open circuit voltage (OCV) and fully charged state; (b) Fully charged state and fully discharged state; Co (c) open circuit voltage (OCV) and fully charged state; (d) Fully charged state and fully discharged state; Ni (e) open circuit voltage (OCV) and fully charged state; (f) Fully charged state and fully discharged state;
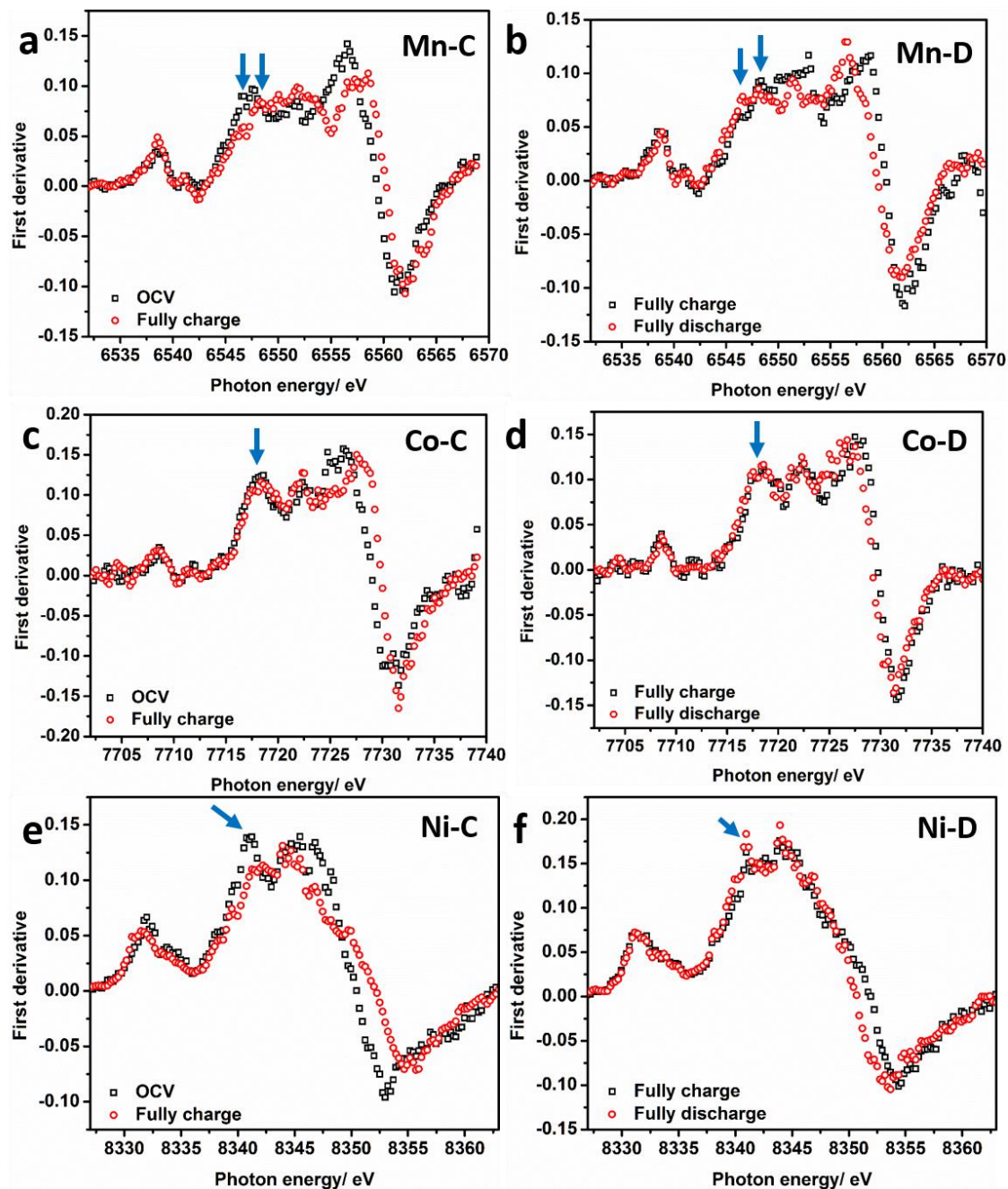
Figure SI 6.6 First derivative plots of the 450th cycle XANES with Mn (a) open circuit voltage (OCV) and fully charged state; (b) Fully charged state and fully discharged state; Co (c) open circuit voltage (OCV) and fully charged state; (d) Fully charged state and fully discharged state; Ni (e) open circuit voltage (OCV) and fully charged state; (f) Fully charged state and fully discharged state;

Chapter 7

7 Graphene Nanoribbons Derived from the Unzipping of Carbon Nanotubes: Controlled Synthesis and Superior Lithium Storage Performance

Graphene nanoribbons (GNRs) from chemical unzipping of carbon nanotubes (CNTs) have been reported to be a suitable candidate for lithium-ion battery materials, but very few of them focused on controlling GNRs with different unzipping levels. Here we present a study of GNRs with controlled unzipping level and the prevailing factors that affect the lithium storage performance at early and final unzipping level, besides, the effect of thermal reduction has been investigated. Based on Raman and BET surface area tests, we found that the unzipping of CNTs starts with surface etching, then proceeds to partial and full unzipping, finally fragmentation and aggregation. Galvanostatic charge-discharge reveals that defect increase is mainly responsible for the capacity enhancement at the early unzipping level, surface area drop is associated with the capacity fade at final unzipping level. Surface functional groups can result in low electrical conductivity, therefore causes capacity drop within several cycles. The GNRs with controlled unzipping level display different electrochemical behaviors, thus can provide rational choices for researchers who are searching for desired functions using GNRs as additives in lithium-ion batteries.

7.1   Introduction

Graphene is a two-dimensional monolayer of sp^2 hybridized carbon atoms with a honeycomb lattice structure. It has attracted extensive investigations due to its unusual mechanical strength, excellent electrical and thermal stability.[1] Carbon nanotubes(CNTs) are layers of graphene rolled up into seamless tubes,[2] as a result, by unzipping carbon nanotubes, it is possible to obtain graphene nanoribbons (GNRs)[3-6]. Pioneered work was reported by Tour et al.,[7, 8] By exposing the multi-walled CNTs in highly oxidizing solutions, they successfully achieved longitudinal cutting and unraveling of MWCNTs. Since then, many other strategies such as plasma etching,[9, 10] insertion and exfoliation,[11] metal nanoparticles-catalyzed cutting[12, 13] and mechanical sonication[14] have been reported. The success of unzipping CNTs to GNRs has thereafter inspired the unzipping of other species of nanotubes such as boron nitride. [15, 16]

In the past few decades, Lithium-ion batteries have become an emerging technology for high performance energy storage systems.[17-19] Graphite is the currently commercialized anode material, but its inherent capacity is relatively low.[20] CNTs and graphene have been recognized as promising anode materials due to their unique high electrical conductivity and mechanical strength.[21] The performance of CNTs and graphene strongly relies on their structural configuration such as surface area[22, 23] and defects.[24-27] Therefore, much effort has been made to modify their pristine structures. Peralta et al.[28] have calculated the lithium storage capability of graphene nanosheet(GNS), fullerenes and GNRs based on density functional theory and revealed that the interaction between lithium and zigzag GNRs is 50% stronger than that of GNS. This advantage contributes to the performance of lithium-ion batteries both as anode materials and additives for electrode material composites. Besides the enhanced lithium storage property, the lithium diffusion coefficient has also been calculated in GNRs and was found to be elevated for up to two orders of magnitude compared with GNS.[29] In addition, the robust mechanical property and enormous surface area of GNRs during lithiation have shown that GNRs can be an outstanding anode of MWCNTs in terms of durability and capacity.[30] Despite this, the lithium storage capability of GNRs based on

the unzipping level has not yet been studied and the key factors that affect the performance are not clear.

In this study, we used modified Hummer's method [31] to synthesize GNRs. By controlling the treatment time, we obtained GNRs with controlled unzipping level with changed surface areas, defect amounts and functionalized surfaces. Moreover, we present a comprehensive study of the prevailing factor that influences the lithium storage capability of GNRs at different unzipping level. To the best of our knowledge, it is the first time systematically studying the morphology evolution of GNRs derived from CNTs and the lithium-ion battery performance based on the GNRs series. It has been demonstrated that number of defects increases right after exposure to oxidants, surface area changes gradually with the aggregation of GNRs under longer time due to the fragmentation of GNRs. The lithium storage capability of unzipped CNTs relies on different factors at different unzipping level. Defects are mainly responsible for the enhanced capacity at the early stage whereas surface area is associated with the capacity at high unzipping levels. Surface functional groups are found to enhance the discharge capacity, however the increased impedance will lead to fading performance.

7.2   Experimental

7.2.1   Materials Synthesis

In a typical unzipping process, 100mg of MWCNTs(Shenzhen Nanotech., China) were dispersed in 3.4mL of sulfuric acid (H_2SO_4)(98%, Aldrich) via strong ultrasonic agitation for 30min. The viscous solution was then placed in an ice bath under vigorous stirring and 75mg sodium nitrate ($NaNO_3$) (99.9%, Aldrich) was subsequently added. After dissolving, 450mg potassium permanganate ($KMnO_4$) (99.9%, Aldrich) was slowly and carefully added into the viscous mixture. After a desired reaction time(specifically 5min, 30min, 1h, 2.5h, 5h, 10h and 20h), 20mL of 5% sulfuric acid solution was poured into the liquid and left to cool down. Next, 2mL hydrogen peroxide (H_2O_2) (30%, Aldrich) was added into the solution in a drop-wide manner until no more bubbles were released. After half an hour, the dark solution was centrifuged and thoroughly washed with 5% nitric acid three times and de-ionized water five times, then filtered and dried in an oven at 90ºC for 12h under

vacuum. The as prepared GNRs contained high amounts of oxygen-containing functional groups (denoted as GONRs-oxidizing time) and are therefore annealed at 900ºC in Ar for reduction (denoted as GNRs-oxidizing time). To make the results more reliable, a reference was created with pristine CNTs which were treated in 30% nitric acid solution for 6 hours to remove the catalysts.

7.2.2   Characterization Methods

The morphologies and structures of CNTs and GNRs were characterized by a Hitachi S-4800 field emission scanning electronic microscopy (FESEM) equipped with energy dispersive X-ray spectroscopy (EDS), a Hitachi H-7000 transmission electron microscopy (TEM) and high-resolution transmission electron microscope (HRTEM, JEOL 2010F). Raman scattering (RS) spectra was obtained by a HORIBA Scientific LabRAM HR Raman spectrometer system with a 532.4 nm laser and optical microscope at room temperature, the intensity ratio of D and G band was calculated by integrating the areas after subtracting the baseline and applying Lorenzian fit. N_2 adsorption/desorption isotherms were obtained by a Folio Micromeritics Tristar II Surface Area Analyser. Fourier transform infrared spectroscopy (FTIR) was obtained by a Nicolet 6700 FTIR spectrometer. Thermogravimetric analysis (TGA) was carried out on a TA SDT Q600 in an air atmosphere from room temperature to 700 ºC at a rate of 10 ºC/min.

7.2.3   Electrochemical Measurements

Pristine CNTs and GNRs were dispersed homogeneously in slurry with 10% polyvinylidene fluoride binder in N-methylpyrrolidione (NMP) solvents. The slurry was subsequently casted onto a Cu foil as current collector and dried at 100 ºC under vacuum overnight. The electrode was assembled in a glove box with moisture and oxygen concentrations below 1ppm. A CR-2325-type coin cell with lithium metal as the counter-electrode and Celgard 2400 as the separator was utilized. The electrolyte was composed of 1M $LiPF_6$ salt dissolved in ethylene carbonate: diethyl carbonate: ethyl methyl carbonate in a 1:1:1 volume ratio.

Both cyclic voltammetry (CV) and electrochemical impedance spectra (EIS) were performed on a multichannel potentiostat 3/Z (VMP3), with a scanning rate of 0.1 mV/s

and a potential range of 0.1 V to 3.0 V (vs. Li/Li$^+$) at room temperature. Galvanostatical charge-discharge was performed on Arbin BT2000 at a current density of 100mA/g between 0.01 and 3.0 V (vs. Li/Li$^+$).

7.3 Results and Discussions

Fig. 7.1a shows the SEM image of pristine CNTs. Pristine CNTs have relatively uniform diameter distribution with an average value of 40 nm. Fig. 7.1b-h show time dependent GNRs. It can be clearly observed that upon oxidizing, the pristine CNTs present remarkable morphology evolution. CNTs have been successfully unzipped into U-shaped curved GNRs longitudinally. With increasing treatment time, the number of remaining CNTs become fewer and fewer. This is because CNTs with lower diameters are generally more stable in oxidizing conditions [7], therefore the ratio of remaining CNTs is a direct indication of the level of oxidizing. After a 1h treatment, about 50% of the CNTs were unzipped. In the case of a 5h treatment, the CNTs have been fully unzipped. Continuous treatments lead to stacking of GNRs in the 10h and 20h samples.
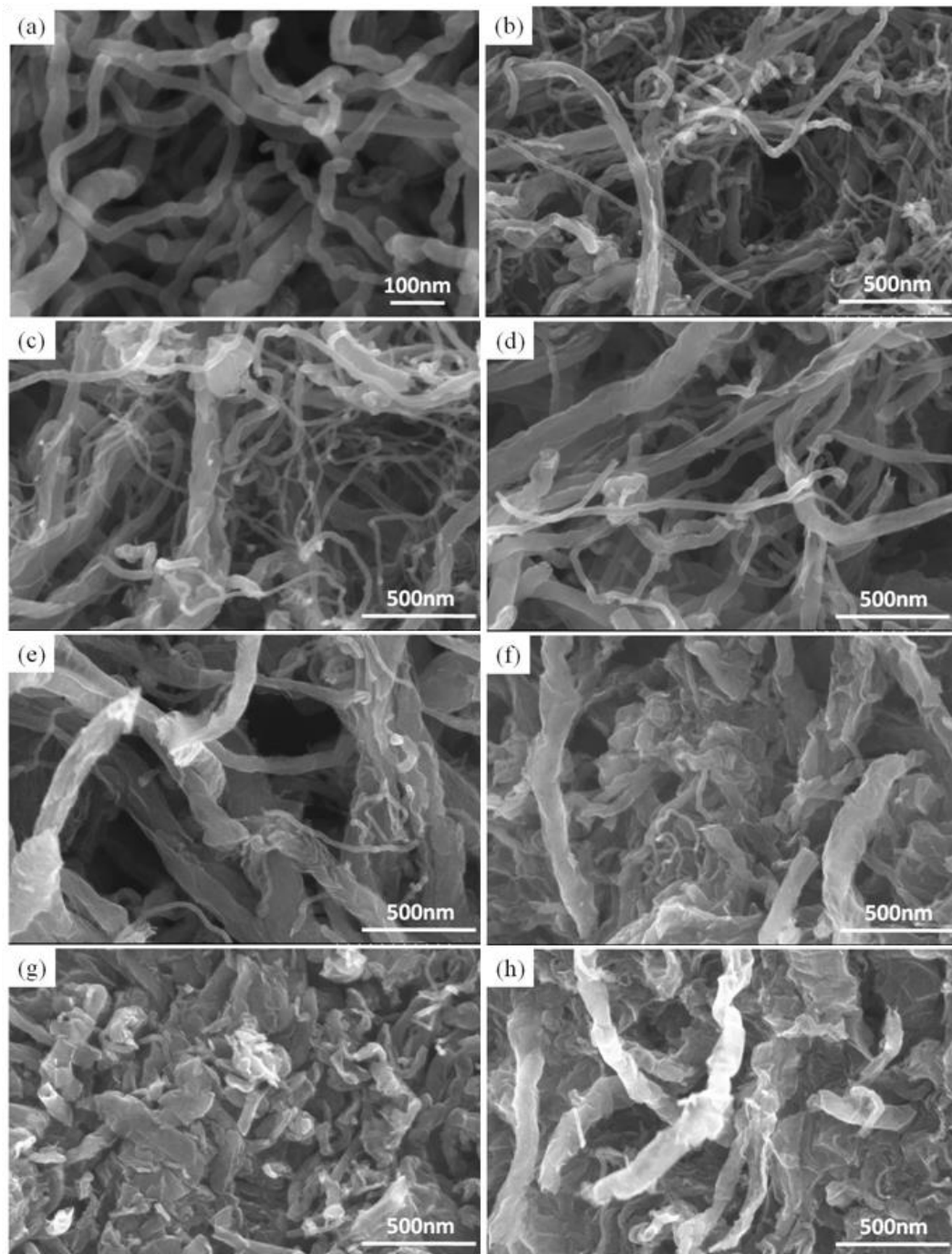
Figure 7.1 FE-SEM images of the pristine CNTs and GNRs series: Pristine CNTs; (b)GNRs-5min; (c)GNRs-30min; (d)GNRs-1h; (e)GNRs-2.5h; (f)GNRs-5h; (g)GNRs-10h; (h)GNRs-20h

TEM and HRTEM were carried out in order to investigate the morphology evolution at higher magnifications as shown in Fig. 7.2(a-e). It can be seen that the unzipping of CNTs

can be divided into four stages, namely surface etching, partially unzipping, fully unzipping and aggregation. To better illustrate the process, we have proposed a schematic diagram of different unzipping levels. Fig. 7.3a shows pristine CNTs. Fig. 7.3b is mostly observed in GNRs-5min, where the CNT has been etched with some cracks on the surface, however, the tubular structure still remains. HRTEM image Fig. 7.2b (inset) clearly displays the etched layer of CNTs. It can be predicted that the cracks are generated on defect sites and the unzipping starts from these structures. Partially unzipped CNTs displayed in Fig. 7.3c reveal that the CNT is unwrapped layer by layer. With increasing time, the CNTs are fully unzipped longitudinally. However, extra treatment would produce fragmentation. As shown in Fig. 7.2(d inset) and Fig. 7.3e, the GNRs have turned into flat structures, but the length decreases a lot in comparison with Fig. 7.2a-c. At this stage, other fragments are also formed besides the ribbon-like structure. Severe aggregations can be observed in Fig. 7.2d. The defects generated by initial unzipping are highly active sites for further attack of potassium permanganate, thus forming fragments. The fragments of GNRs are mainly responsible for the stacking found in Fig. 7.1g-h.
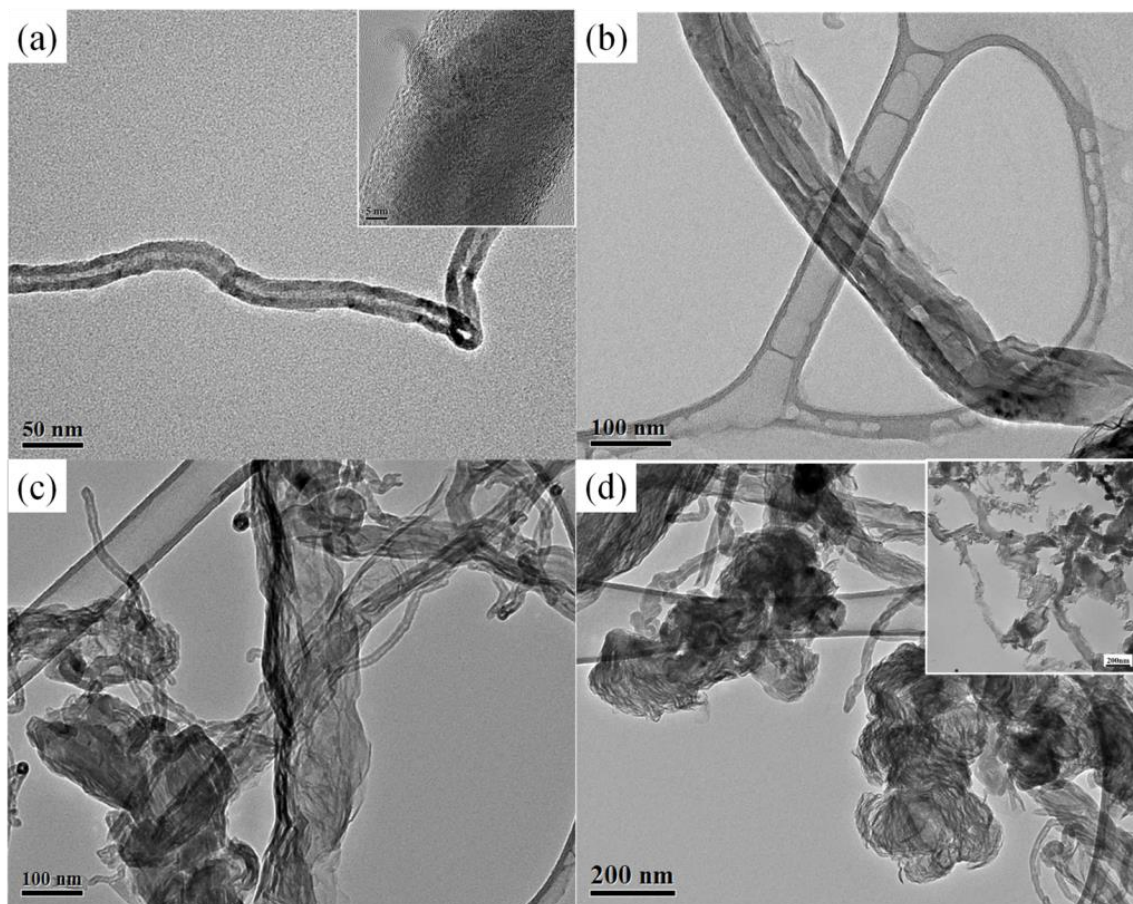
Figure 7.2 TEM images of CNTs during different unzipping stages: (a) Etched CNTs; (b) Partially unzipped CNTs; (c) Fully unzipped CNTs; (d) Stacked GNRs
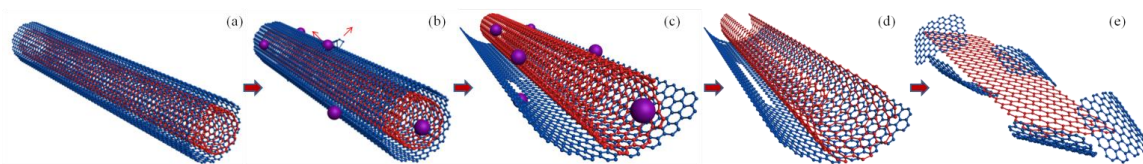
Figure 7.3 Schematic diagrams of (a)Pristine CNTs; (b) Etched CNTs; (c) Partially unzipped CNTs; (d) Fully unzipped CNTs; (e) Stacked GNRs fragments

Fig. 7.4a shows the RAMAN spectra of pristine CNTs and GNRs. It can be observed that the pristine CNTs feature three obvious peaks at 1340.4, 1572.1 and 2683.1 cm^{-1}. The peaks correspond to the D band induced by disordered defect, the G band caused by sp^2 carbon vibration and the 2D band of second-order Raman scattering process respectively.[32] The intensity ratio of the D and G bands of pristine CNTs is 0.56, indicating that the pristine

CNTs are mostly sp^2 hybridized. Besides the small amount of defect, amorphous carbon which is sp^3 hybridized is also responsible for the D band intensity. The unzipping of CNTs creates new peaks both for D and G band at 1461.8 and 1610.4cm^{-1} respectively, this can be ascribed to the vibration of graphite layers exfoliated from the CNTs.[32] The 2D peak becomes much weaker as the unzipping proceeds as its peak intensity strongly relies on the D band intensity because of the defect-induced renormalization of electron and phonon energies.[33, 34] Therefore, the increase of the D band intensity inevitably induces the drop of the 2D band intensity.

Fig. 7.4b displays a plot of the I_D/I_G ratio calculated by the intensity of D and G bands. It can be seen that the defect amount increases significantly after the CNTs are exposed to oxidants. Further, longer treatment time does not cause severe change to the defect amount, and the values oscillate around 2.15 within the next 10h of treatment. This implies that the defects are mostly created by the initial attack of the oxidants. Unzipping of CNTs does not exert strong impact on the formation of defects.

Fig. 7.4b also shows the plot of the Brunauer-Emmett-Teller specific surface area of GNRs as a function of treated time. It can be seen that the surface area of pristine CNTs is 47.3m^2/g. Within 5min of treatment, the surface area is slightly increased to 49.1m^2/g, which is in contrast with the sudden increase of defect. This reveals that the CNTs are likely to be etched on the surface at the early steps without damage of the tubular structures. The surface area is highest when the treatment time is 5h with a value of 321.6m^2/g, however, when the treatment time increased up to 10h, the surface area slightly decreased to 321.1m^2/g. The balance of surface area at GNRs-5h and GNRs-10h implies that within this period of time, unzipping and fragmentation-induced stacking happen simultaneously. When further reaction occurs at 20h, the surface area dramatically drops to 126.6 m^2/g, which indicates that unzipping has been mostly finished. But during this stage, the formation of GNRs fragments exceeds that of unzipping. The surface area change further shows that the fragmentation at 10h and 20h is the reason of the surface area drop.

The thermal stability of the pristine CNTs and GONRs was confirmed by TGA shown in Fig. 7.4c. The initial weight loss below 100 ºC is due to adsorbed moisture. Then, most of

the GONRs display a weight loss from 150-450 °C, which corresponds to the surface functional groups. The oxygen-containing groups are generally released as CO_2. With higher oxidation level, the GONRs become less thermally stable, implying that the surface functional group magnitude increases with longer treatment. The final weight loss from 450 °C to 600 °C is because of the release of CO_2 due to the burning of carbon.

The functional groups of GNRs-5h and GONRs-5h were confirmed via Fourier transform infrared spectroscopy (FTIR) as displayed in Fig. 7.4d. The strong peaks at 3343 cm^{-1} and 1630cm^{-1} correspond to the hydroxyl stretching related to the -OH group and adsorbed water. It can be observed that before reduction, GONRs-5h contains a large amount of adsorbed water due to the hydrophilic nature.[35, 36] After reduction, the vibration of hydroxyl has been decreased a lot. The broad peak at 3343 cm^{-1} can be ascribed to the KBr humidity. [37] The doublet peaks at 2927 and 2872 cm^{-1} are due to the symmetric and antisymmetric stretching vibrations of –CH_2.[38] The existence of –CH_2 indicates that that the carbon basal planes are well maintained. Two intense peaks at 1714 and 1380 cm^{-1} are found at GONRs-5h, corresponding to the C=O and C-O stretching vibrations of COOH groups.[39] Another strong band at 1380 cm^{-1} can be assigned to the O-H deformations of the C-OH groups.[40] FTIR has clearly revealed that the majority of the functional groups in the GONRs-5h sample are oxygen-containing groups such as hydroxyl and carboxyl. Upon thermal reduction, the functional groups have been removed and released in the form of CO_2.

As has been shown in Fig. 7.4a and Fig. 7.4b, the defect of GNRs at 5 min is much higher than that of pristine CNTs while there is no surface area change. Therefore, it is good reference material to compare the performance of GNRs-5min with pristine CNTs to study the effect of defects. On the other hand, as both the defect and surface area keep increasing at GNRs-5min to GNRs-5h, it is difficult to ascribe the performance change to any of these two single factors. Therefore the samples of the GNRs-5h and GNRs-20h provide us to study the surface area effect while there is a drop in surface area whereas an increase in defect amount. Moreover, the comparison of the GONRs-5h and GNRs-5h could help investigate the impact of surface functional groups.
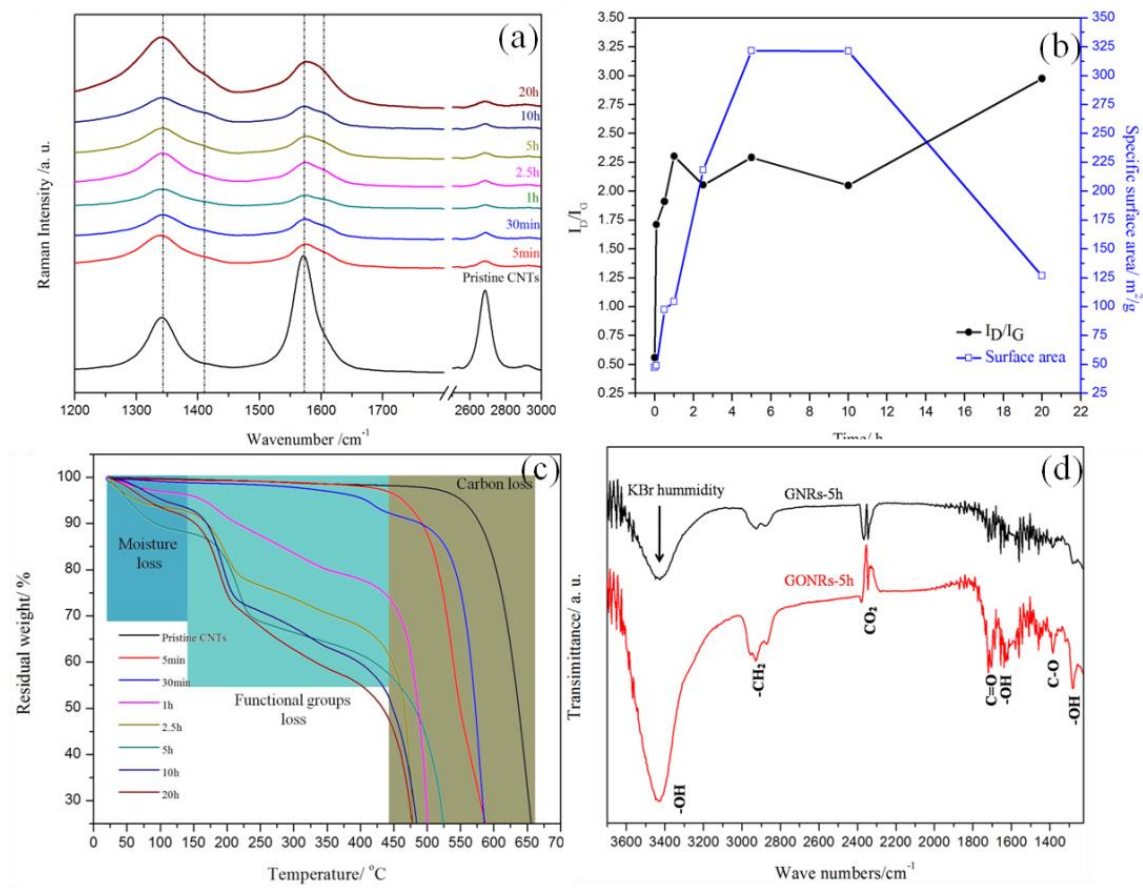
Figure 7.4 (a) Raman spectra of the pristine CNTs and GNRs; (b) Plot of the ID/IG ratio and surface area; (c) TGA curves of pristine CNTs and GONRs; (d)FTIR of GNRs-oxide-5h and GNRs-5h

The electrochemical behavior of pristine CNTs, GNRs-5min, 5h, 20h and GONRs-5h were characterized by cyclic voltammetry(CV) and galvanostatic charge and discharge process. Fig. 7.5, 7.6a-b present the CV and charge/discharge curves of pristine CNTs and GNRs-5min at the first three cycles. It can be observed that both CV curves display two typical peaks at the first cathodic scan. The peak at about 0.75 V corresponds to the irreversible formation of SEI due to the decomposition of electrolyte,[41] which is mainly responsible for the initial irreversible capacity.[42] This peak disappears in the second and third cycle, indicating that the SEI is very stable. Another peak at 0.1V reveals the insertion of Li^+ into the graphite layers. During anodic scan, the sharp peak at 0.24 V for pristine CNTs and 0.30 V for GNRs-5min are related to the de-intercalation if Li^+ from the graphene layers.[43] A weak peak is observed in GNRs-5min at 1.85 V, which is consistent with the

previous results of ball-milled CNTs, chemically etched CNTs and nano-drilled CNTs as anodes[44-46] where small holes are created on the tube walls or the tube caps have been removed. This allows more Li^+ extraction from the interior space of nanotubes. This shows a strong evidence that surface defects on CNTs provides more sites for lithium storage. The peak at 2.34 V is due to the absorption of the Li^+ on remaining functional groups. [45] In the case of GNRs-5min, this peak only exists at the first cycle, implying that there is no consequent capacity contribution. The reversible discharge capacity has been increased from 232.5 mAh/g to 375.8 mAh/g, this significant increase is due to the sudden increase of defect, which allows to accommodate more lithium.[47]

Fig. 7.5, 7.6c-d depict the CV and charge/discharge curves of GNRs-5h and GNRs-20h. Similar with that of GNRs-5min, a reversible peak at 1.85 V has been observed in GNRs-5h whereas there is no such peak in GNRs-20h. This change reveals that the tubular structure has been totally destroyed in GNRs-20h, which is consistent with the SEM and TEM images that the GNRs have been turned into fragments. The oxidation peaks related to the extraction of Li^+ from graphite layers are located at 0.35 V and 0.52 V for GNRs-5h and GNRs-20h respectively. The charge/discharge curves show that GNRs-5h delivers much higher capacity than GNRs-20h. In the case of pristine CNTs and GNRs-5min, defects are mainly responsible for the capacity increase, however, in the case of GNRs-5h and GNRs-20h, the discharge capacity decreases from 515.5 mAh/g to 391.5 mAh/g even if there is an increase of defect amount. Realizing that the defect amount increase can possibly induce lower electrical conductivity for carbon materials, we conducted studies of electrochemical impedance spectroscopy (EIS) on GNRs-5h and GNRs-20h. As shown in Figure 7.4f, GNRs-5h and GNRs-20h at open circuit voltage (inset) display one semicircle and one straight line. The impedance of GNRs-5h is similar to GNRs-20h at open circuit voltage. In contrast to the EIS at open circuit voltage, the EIS at 0.01 V displays to semicircles at high and medium frequency regions. To better illustrate the impedance behavior, we proposed a modified equivalent circuit in the insert of Figure 7.4f. R_e stands for the electrolyte Ohmic resistance. The high-frequency semicircle can be ascribed to the resistance of SEI with the migration of Li^+ and interfacial capacitance (C_{sl}) related to R_{sl}. The semicircle in medium-frequency region can be assigned to the charge-transfer resistance (R_{ct}) and the double-layer capacitance (C_{dl}). W denotes the finite length Warburg

impedance corresponding to the solid-state diffusion. Through the simulated equivalent circuit, we found that the charge transfer resistances of GNRs-5h and GNRs-20h are 21.9 and 22.2 Ω, respectively, indicating that the electrical conductivity of GNRs-20h was not seriously affected by the presence of defects. Given the similar electrical conductivities of GNRs-5h and GNRs-20h, we therefore ascribe the capacity fade to the drop of surface area. High surface area allows for a high contact area between electrode and electrolyte to form SEI film by consuming a considerable amount of Li^+. This leads to a high capacity at the first discharge.[48] Despite the consumption of Li^+, the high surface area provides much more free sites for the storage of Li^+,[49] therefore the reversible capacity of GNRs-5h is much higher than that of GNRs-20h.

Fig. 7.5, 7.6e display the CV and charge/discharge curves of GONRs-5h. By comparing with Fig. 7.5, 7.6c (GNRs-5h) one can find two obvious redox peaks. The cathodic peaks located at the potential of Li^+ extraction from interior space (1.88 V) and functional groups (2.37 V) are reversible during cycling. The redox peaks at 1.88 V and 1.60 V correspond to the extraction of Li^+ from interior space of nanotubes. This peak is reversible and much more intense than GNRs-5h, but this observation remains unclear which possibly results from the self-repair effect during annealing.[50] Another redox peaks at 2.37 V and 2.13 V are assigned to the adsorption and extraction of Li+ onto surface functional groups. It can be clearly seen that the oxidizing peak is very intense at the first cycle and becomes gradually weaker at the second and third cycles. It indicates that the adsorption of Li^+ on functional groups have a big contribution to the irreversible capacity. However, quite similar with the SEI film, the Li^+ are consumed rather than stored. The charge/discharge curves display two extra voltage plateaus, corresponding to the redox peaks of the functional groups. The curves also confirm the high irreversible discharge capacity of GONRs at 1088.0 mAh/g compared with GNR-5h (910.4 mAh/g).

Fig. 7.6f shows the cyclability of the performance and the Coulombic efficiencies of each sample. It is worthwhile to notify that the Coulombic efficiencies of GNRs-5h and GONRs-5h exceed 100%, we believe this is caused by the double-layer capacitance enhanced by the high surface area. It can be seen that the GONRs-5h displays a higher reversible capacity in the first five cycles than other samples, but the stability is very poor, even lower

than pristine CNTs. Fahlman[51] also observed the similar performance of GONR. The high capacity of GONRs is ascribed to the stable Li-rich SEI which prevents the electrolyte from further degradation. However, the poor cyclability of GONRs-5h may result from the decrease of electrical conductivity. To confirm this, electrochemical impedance spectroscopy (EIS) of GNRs-5h and GONRs-5h was conducted. As shown in Fig. 7.5f, through the simulated equivalent circuit, we found that the charge transfer resistances of GNRs-5h and GONRs-5h are 21.9 Ω and 82.0 Ω respectively, revealing that the electrical conductivity of GONRs-5h is much lower than that of GNRs-5h. Therefore, we can conclude that the poor cyclability of GONRs-5h is because of the increased impedance due to the presence of surface functional groups.
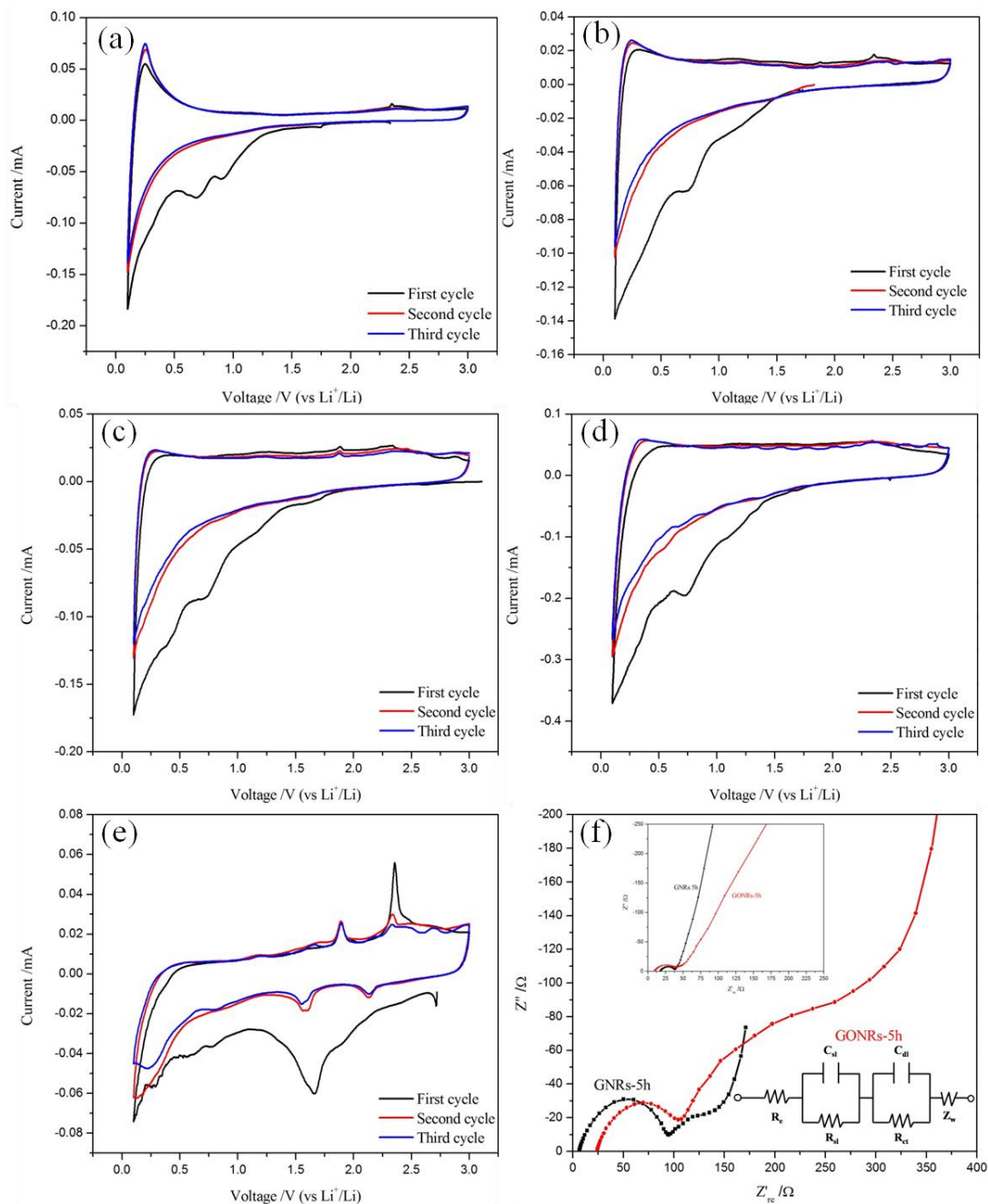
Figure 7.5 Charge/discharge profiles of (a) Pristine CNTs; (b) GNRs-5min; (c) GNRs-5h; (d) GNRs-20h; (e) GONRs-5h with a current density of 100 mA/g; (f) Discharge capacity and coulombic efficiency versus cycle numbers of pristine CNTs and GNRs/GONRs at a current density of 100 mA/g
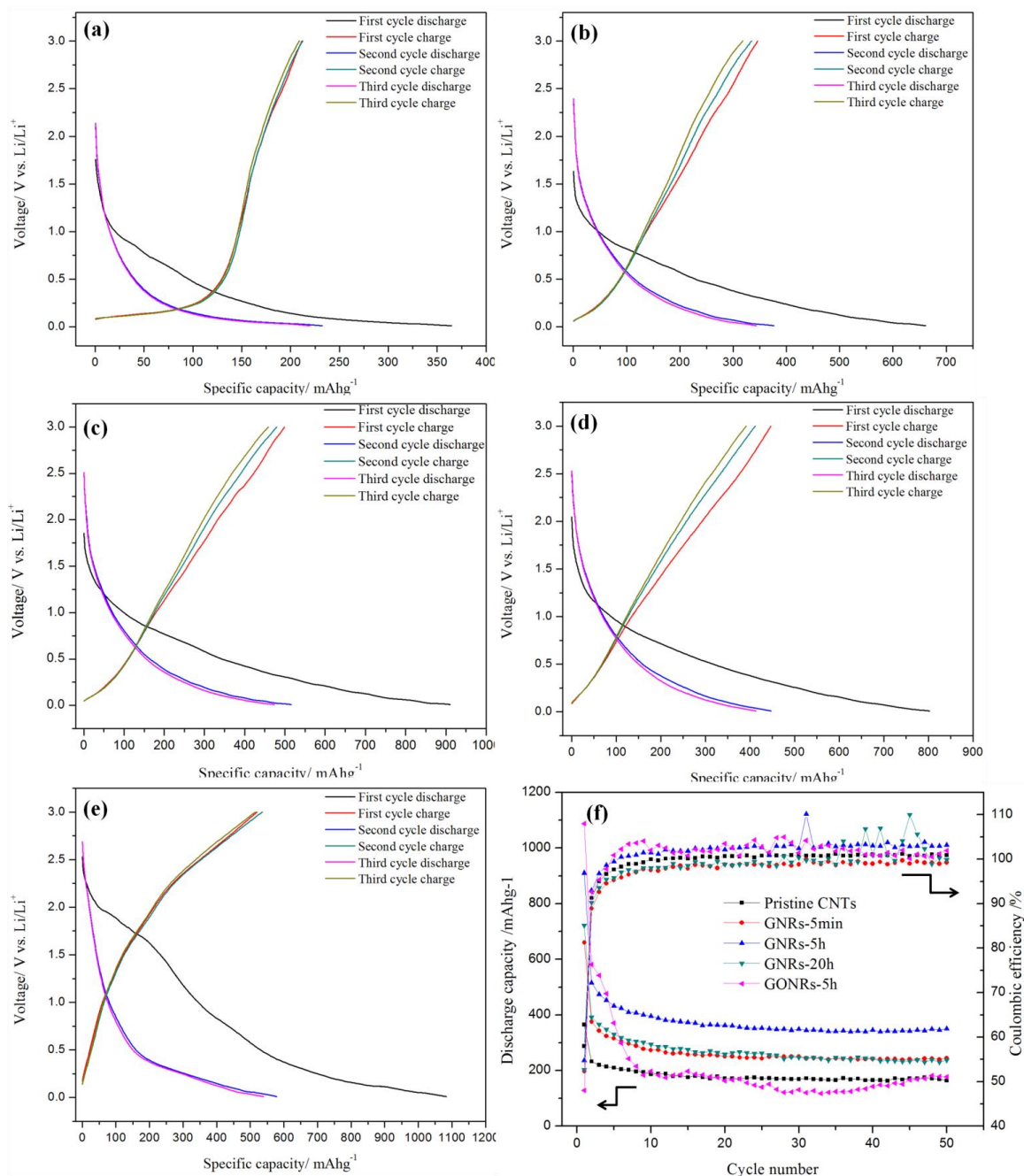
Figure 7.6 Charge/discharge profiles of (a) Pristine CNTs; (b) GNRs-5min; (c) GNRs-5h; (d) GNRs-20h; (e) GONRs-5h with a current density of 100 mA/g; (f) Discharge capacity and coulombic efficiency versus cycle numbers of pristine CNTs and GNRs/GONRs at a current density of 100 mA/g

To sum up, we have proposed the mechanisms of the enhanced capacity of GONRs and GNRs at each stage. Fig. 7.7a depicts the mechanism of Li$^+$ insertion into inter-layers of

MWCNTs at the early stage. Defects are created by oxidizing at the surface, thus allowing Li^+ migrate through the vacancies into the inter-layers. This effect results in more sites for the accommodation of Li^+, as the defect sites are generally highly active and, therefore can absorb Li^+. The mechanism of enhanced lithium storage capability at the later stage is shown in Fig. 7.7b. The noticeably increased surface area exposed to electrolyte provides more free sites to accommodate Li^+ while a thicker SEI film is formed. In the case of GONRs shown in Fig. 7.7c, the functional groups can absorb a remarkable amount of Li^+, and along with the increased surface area, GONRs display very high irreversible capacity. [52]
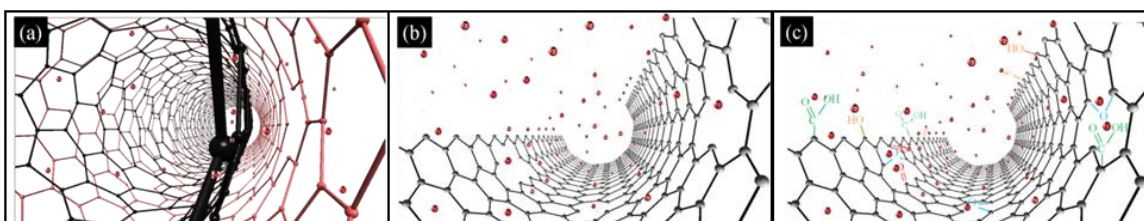
Figure 7.7 Schematic diagrams of insertion of lithium ions into (a) CNTs (b) GNRs (c) GONRs

7.4   Conclusion

In conclusion, the morphological evolution of GNRs derived from chemically unzipped CNTs has been divided into four steps according to the Raman spectra, TEM images, HRTEM images and surface area. Specifically, the unzipping begins with chemical etching at the tube walls without severe damage to the tubular structure. Following etching results in partially and fully unzipped CNTs, however, continuous etching will lead to fragmentation of GNRs which is reflected as a drop of surface area due to aggregation.

We have studied the lithium storage performance of GNRs at different unzipping levels. The enhanced capacity at the early stage is mainly related to the obvious increase of defects. GNRs-5h, which has the highest surface area, delivers a reversible discharge capacity of over 500mAh/g. However, when the unzipping level comes to its final stage, the capacity drops noticeably due to the drop of surface area. Also, we have studied the functional groups effect on cycling performance of anodes, demonstrating that the functional groups

can absorb a considerable amount of Li^+ which is mostly irreversible. The dropped cyclability of GONRs-5h is due to the decreased electrical conductivity. The systematic study on the lithium-ion battery performance of GNRs with controlled unzipping levels can provide a strong reference for future utilization of GNRs and GNR composites.

Acknowledgement

References

[1] A. K. Geim and K. S. Novoselov, The Rise of Graphene, *Nat. Mater.*, 2007, **6**, 183-191.

[2] S. Iijima, Helical Microtubules of Graphitic Carbon, *Nature*, 1991, **354**, 56-58.

[3] N. Al-Aqtash, H. Li, L. Wang, W.-N. Mei and R. F. Sabirianov, Electromechanical Switching in Graphene Nanoribbons, *Carbon*, 2013, **51**, 102-109.

[4] Z. Wang, H. Hu and H. Zeng, The Electronic Properties of Graphene Nanoribbons with Boron/Nitrogen Codoping, *Appl. Phys. Lett.*, 2010, **96**, 243110.

[5] J. Bai and Y. Huang, Fabrication and Electrical Properties of Graphene Nanoribbons, *Mater. Sci. Eng.: R: Rep.*, 2010, **70**, 341-353.

[6] L. Chen, Y. Hernandez, X. Feng and K. Müllen, From Nanographene and Graphene Nanoribbons to Graphene Sheets: Chemical Synthesis, *Angew. Chem. Int. Ed.*, 2012, **51**, 7640-7654.

[7] D. V. Kosynkin, A. L. Higginbotham, A. Sinitskii, J. R. Lomeda, A. Dimiev, B. K. Price and J. M. Tour, Longitudinal Unzipping of Carbon Nanotubes to Form Graphene, *Nature*, 2009, **458**, 872-876.

[8] A. L. Higginbotham, D. V. Kosynkin, A. Sinitskii, Z. Sun and J. M. Tour, Lower-Defect Graphene Oxide Nanoribbons from Multiwalled Carbon Nanotubes, *ACS Nano*, 2010, **4**, 2059-2069.

[9] L. Jiao, L. Zhang, X. Wang, G. Diankov and H. Dai, Narrow Graphene Nanoribbons from Carbon Nanotubes, *Nature*, 2009, **458**, 877-880.

[10] S. Mohammadi, Z. Kolahdouz and S. Mohajerzadeh, Hydrogenation-Assisted Unzipping of Carbon Nanotubes to Realize Graphene Nano-Sheets, *J. Mater. Chem. C*, 2013, **1**, 1309.

[11] A. G. Cano-Marquez, F. J. Rodriguez-Macias, J. Campos-Delgado, C. G. Espinosa-Gonzalez, F. Tristan-Lopez, D. Ramirez-Gonzalez, D. A. Cullen, D. J. Smith, M. Terrones and Y. I. Vega-Cantu, Ex-MWNTs: Graphene Sheets and Ribbons Produced by Lithium Intercalation and Exfoliation of Carbon Nanotubes, *Nano Lett.*, 2009, **9**, 1527-1533.

[12] U. K. Parashar, S. Bhandari, R. K. Srivastava, D. Jariwala and A. Srivastava, Single Step Synthesis of Graphene Nanoribbons by Catalyst Particle Size Dependent Cutting of Multiwalled Carbon Nanotubes, *Nanoscale*, 2011, **3**, 3876-3882.

[13] A. L. Elías, A. R. Botello-Méndez, D. Meneses-Rodríguez, V. J. González, D. Ramírez-González, L. Ci, E. Muñoz-Sandoval, P. M. Ajayan, H. Terrones and M. Terrones, Longitudinal Cutting of Pure and Doped Carbon Nanotubes to Form Graphitic Nanoribbons Using Metal Clusters as Nanoscalpels, *Nano Lett.*, 2010, **10**, 366-372.

[14] L. Jiao, X. Wang, G. Diankov, H. Wang and H. Dai, Facile Synthesis of High-Quality Graphene Nanoribbons, *Nat. Nanotechnol.*, 2010, **5**, 321-325.

[15] K. J. Erickson, A. L. Gibb, A. Sinitskii, M. Rousseas, N. Alem, J. M. Tour and A. K. Zettl, Longitudinal Splitting of Boron Nitride Nanotubes for the Facile Synthesis of High Quality Boron Nitride Nanoribbons, *Nano Lett.*, 2011, **11**, 3221-3226.

[16] H. Zeng, C. Zhi, Z. Zhang, X. Wei, X. Wang, W. Guo, Y. Bando and D. Golberg, "White Graphenes": Boron Nitride Nanoribbons *via* Boron Nitride Nanotube Unwrapping, *Nano Lett*., 2010, **10**, 5049-5055.

[17] A. Yoshino, The Birth of the Lithium-Ion Battery, *Angew. Chem. Int. Ed*., 2012, **51**, 2-5.

[18] J. M. Tarascon, Key Challenges in Future Li-Battery Research, *Philos. T. Roy. Soc. A*, 2010, **368**, 3227-3241.

[19] B. Scrosati, J. Hassoun and Y.-K. Sun, Lithium-Ion Batteries. A Look into the Future, *Energy Environ. Sci*., 2011, **4**, 3287-3295.

[20] B. Simon, S. Flandrois, K. Guerin, A. Fevrier-Bouvier, I. Teulat and P. Biensan, On the Choice of Graphite for Lithium Ion Batteries, *J. Power Sources*, 1999, **81**, 312-316.

[21] C. de las Casas and W. Li, A Review of Application of Carbon Nanotubes for Lithium Ion Battery Anode Material, *J. Power Sources*, 2012, **208**, 74-85.

[22] C. Liu, F. Li, L.-P. Ma and H.-M. Cheng, Advanced Materials for Energy Storage, *Adv. Mater*., 2010, **22**, E28-E62.

[23] Felipe Valencia, Aldo H. Romero, Francesco Acilotto and P. L. Silvestrelli, Lithium Adsorption on Graphite from Density Functional Theory Calculations, *J. Phys. Chem. B*, 2006, **110**, 14832-14841.

[24] X. Li, J. Liu, Y. Zhang, Y. Li, H. Liu, X. Meng, J. Yang, D. Geng, D. Wang, R. Li and X. Sun, High Concentration Nitrogen Doped Carbon Nanotube Anodes with Superior Li^+ Storage Performance for Lithium Rechargeable Battery Application, *J. Power Sources*, 2012, **197**, 238-245.

[25] Liu-Jiang Zhou, Z. F. Hou and L.-M. Wu, First-Principles Study of Lithium Adsorption and Diffusion on Graphene with Point Defects, *J. Phys. Chem.* C, 2012, **116**, 21780-21787.

[26] J. Yang, J. Wang, X. Li, D. Wang, J. Liu, G. Liang, M. Gauthier, Y. Li, D. Geng, R. Li and X. Sun, Hierarchically Porous $LiFePO_4$/Nitrogen-Doped Carbon Nanotubes Composite as a Cathode for Lithium Ion Batteries, *J. Mater. Chem.*, 2012, **22**, 7537-7543.

[27] Z.-S. Wu, W. Ren, L. Xu, F. Li and H.-M. Cheng, Doped Graphene Sheets as Anode Materials with Super High Rate and Large Capacity for Lithium Ion Batteries, *ACS Nano*, 2011, **5**, 5463-5471.

[28] C. Uthaisar, V. Barone and J. E. Peralta, Lithium Adsorption on Zigzag Graphene Nanoribbons, *J. Appl. Phys.*, 2009, **106**, 113715.

[29] C. Uthaisar and V. Barone, Edge Effects on the Characteristics of Li Diffusion in Graphene, *Nano Lett.*, 2010, **10**, 2838-2842.

[30] X. H. Liu, J. W. Wang, Y. Liu, H. Zheng, A. Kushima, S. Huang, T. Zhu, S. X. Mao, J. Li, S. Zhang, W. Lu, J. M. Tour and J. Y. Huang, In Situ Transmission Electron Microscopy of Electrochemical Lithiation, Delithiation and Deformation of Individual Graphene Nanoribbons, *Carbon*, 2012, **50**, 3836-3844.

[31] W. S. Hummers and R. E. Offeman, Preparation of Graphitic Oxide, *J. Am. Chem. Soc.*, 1958, **80**, 1339-1339.

[32] M. S. Dresselhaus, G. Dresselhaus, R. Saito and A. Jorio, Raman Spectroscopy of Carbon Nanotubes, *Phys. Rep.*, 2005, **409**, 47-99.

[33] I. O. Maciel, N. Anderson, M. A. Pimenta, A. Hartshuh, H. Qian, M. Terrones, H. Terrones, J. Campos-Delgado, A. M. Rao, L. Novotny and A. Jorio, Electron and Phonon Renormalization near Charged Defects in Carbon Nanotubes, *Nat. Mater.*, 2008, **7**, 878-883.

[34] M. S. Dresselhaus, A. Jorio, M. Hofmann, G. Dresselhaus and R. Saito, Perspectives on Carbon Nanotubes and Graphene Raman Spectroscopy, *Nano Lett*., 2010, **10**, 751-758.

[35] A. Dimiev, D. V. Kosynkin, L. B. Alemany, P. Chaguine and J. M. Tour, Pristine Graphite Oxide, *J. Am. Chem. Soc*., 2012, **134**, 2815-2822.

[36] S. Pei and H.-M. Cheng, The Reduction of Graphene Oxide, *Carbon*, 2012, **50**, 3210-3228.

[37] A. Kaniyoor, T. T. Baby and S. Ramaprabhu, Graphene Synthesis Via Hydrogen Induced Low Temperature Exfoliation of Graphite Oxide, *J. Mater. Chem*., 2010, **20**, 8467-8469.

[38] X. Sun, Z. Liu, K. Welsher, J. T. Robinson, A. Goodwin, S. Zaric and H. Dai, Nano-Graphene Oxide for Cellular Imaging and Drug Delivery, *Nano Res*., 2008, **1**, 203-212.

[39] H.-K. Jeong, L. Colakerol, M. H. Jin, P.-A. Glans, K. E. Smith and Y. H. Lee, Unoccupied Electronic States in Graphite Oxides, *Chem. Phys. Lett*., 2008, **460**, 499-502

[40] A. B. Bourlinos, D. Gournis, D. Petridis, T. Szabo, A. Szeri and I. Dekany, Graphite Oxide: Chemical Reduction to Graphite and Surface Modification with Primary Aliphatic Amines and Amino Acids, *Langmuir*, 2003, **19**, 6050-6055.

[41] Brian J. Landi, Matthew J. Ganter, Christopher M. Schauerman, Cory D. Cress and R. P. Raffaelle, Lithium Ion Capacity of Single Wall Carbon Nanotube Paper Electrodes, *J. Phys. Chem.* C, 2008, **112**, 19, 7509-7515.

[42] O. Y. Chusid, Y. E. Ely, M. Babai, Y. Carmeli and D. Aurbach, Electrochemical and Spectroscopic Studies of Carbon Electrodes in Lithium Battery Electrolyte Systems, *J. Power Sources*, 1993, **43**, 47-64.

[43] B. J. Landi, M. J. Ganter, C. D. Cress, R. A. DiLeo and R. P. Raffaelle, Carbon Nanotubes for Lithium Ion Batteries, *Energy Environ. Sci*., 2009, **2**, 638-654.

[44] H. Shimoda, B. Gao, X. Tang, A. Kleinhammes, L. Fleming, Y. Wu and O. Zhou, Lithium Intercalation into Opened Single-Wall Carbon Nanotubes: Storage Capacity and Electronic Properties, *Phys. Rev. Lett*., 2001, **88**, 015502-015505.

[45] H. S. Oktaviano, K. Yamada and K. Waki, Nano-Drilled Multiwalled Carbon Nanotubes: Characterizations and Application for LIB Anode Materials, *J. Mater. Chem*., 2012, **22**, 25167.

[46] J. Y. Eom and H. Kwon, Improved Lithium Insertion/Extraction Properties of Single-Walled Carbon Nanotubes by High-Energy Ball Milling, *J. Mater. Res*., 2008, **23**, 2458-2466.

[47] F. Yao, F. Güneş, H. Q. Ta, S. M. Lee, S. J. Chae, K. Y. Sheem, C. S. Cojocaru, S. S. Xie and Y. H. Lee, Diffusion Mechanism of Lithium Ion through Basal Plane of Layered Graphene, *J. Am. Chem. Soc*., 2012, **134**, 8646-8654.

[48] F. Béguin, F. Chevallier, C. Vix-Guterl, S. Saadallah, V. Bertagna, J. N. Rouzaud and E. Frackowiak, Correlation of the Irreversible Lithium Capacity with the Active Surface Area of Modified Carbons, *Carbon*, 2005, **43**, 2160-2167.

[49] H. F. Xiang, Z. D. Li, K. Xie, J. Z. Jiang, J. J. Chen, P. C. Lian, J. S. Wu, Y. Yu and H. H. Wang, Graphene Sheets as Anode Materials for Li-Ion Batteries: Preparation, Structure, Electrochemical Properties and Mechanism for Lithium Storage, *RSC Adv*., 2012, **2**, 6792.

[50] V. Lopez, R. S. Sundaram, C. Gomez-Navarro, D. Olea, M. Burghard, J. Gomez-Herrero, F. Zamora and K. Kern, Chemical Vapor Deposition Repair of Graphene Oxide: A Route to Highly-Conductive Graphene Monolayers, *Adv Mater*., 2009, **21**, 4683-4686

[51] T. Bhardwaj, A. Antic, B. Pavan, V. Barone and B. D. Fahlman, Enhanced Electrochemical Lithium Storage by Graphene Nanoribbons, *J. Am. Chem. Soc.*, 2010, **132**, 12556-12558.

[52] S. W. Lee, N. Yabuuchi, B. M. Gallant, S. Chen, B.-S. Kim, P. T. Hammond and Y. Shao-Horn, High-Power Lithium Batteries from Functionalized Carbon-Nanotube Electrodes, *Nat. Nanotechnol.*, 2010, **5**, 531-537.

Supporting Information
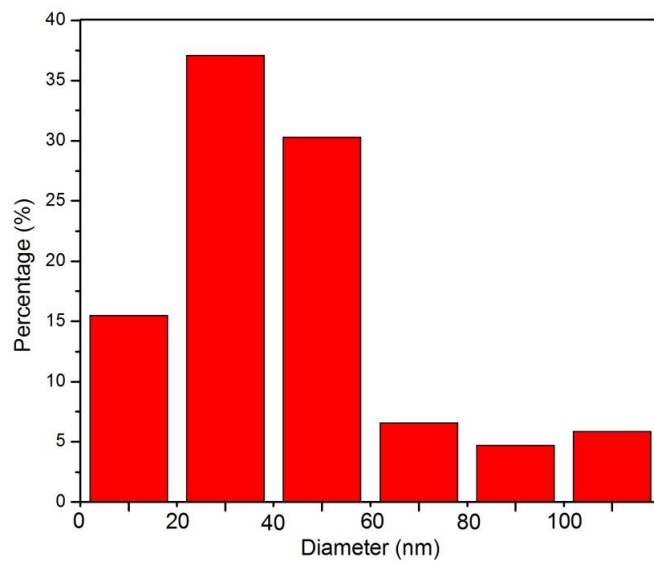
Figure SI 7.1 Diameter distribution of the pristine CNTs
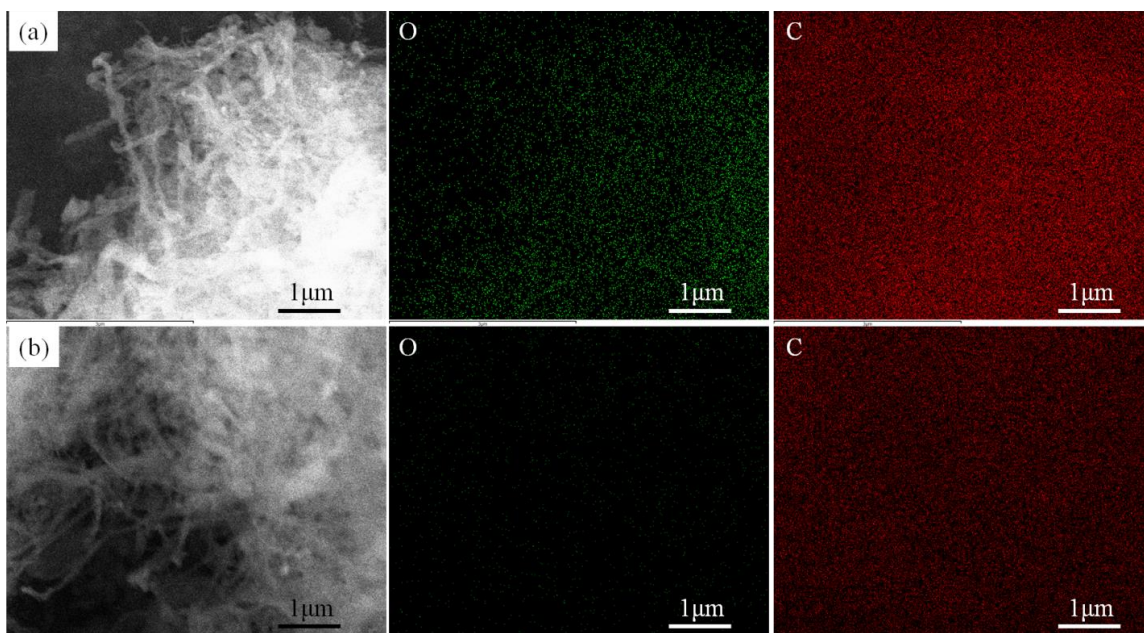
Figure SI 7.2 EDS elemental mapping of (a) GONRs-5h and (b) GNRs-5h

Chapter 8

8 Conclusions and Future Perspective

This chapter summarizes the results and contribution of this thesis and proposes possible suggestions to the future directions in the realm of surface modification of electrode materials for LIBs.

8.1   Conclusions

Lithium-ion batteries are the dominating energy storage device in the market nowadays due to the relatively high energy density, environmental benignity and low cost. However, in contrast to the burgeoning energy output demanded by electronics and electric vehicles (EVs), LIBs performance development has been under stagnation. The challenges that prohibit LIBs from powering enduring electronics and high mileage EVs include the energy density, rate capability, safety and cost.

In order to increase the energy density of the LIBs, cathode materials with either high capacity and/or operating voltage are desired. This thesis focuses on two types of cathode materials, the high voltage spinel $LiNi_{0.5}Mn_{1.5}O_4$ (LNMO) and high capacity layered Li-rich NMC. These materials suffer from harsh side reactions such as transition metal dissolution, electrolyte decomposition and irreversible phase transition initiated from the surface under high voltage. In addition, delithiated cathode materials are highly oxidizing and are always accompanied with oxygen gas release, it can therefore increase the risk of explosion due to the flammability of the non-aqueous electrolyte used.

The main objective of this thesis is to develop various surface modification methods to alleviate the side reactions on the surface of the electrode materials and understand how such modification works towards achieving better performance by combining with synchrotron radiation technique.

First, an electrochemically active $FePO_4$ coating was deposited onto LNMO particles *via* ALD. The thickness of the $FePO_4$ coating was precisely controlled by the ALD cycle numbers, specifically, 5, 10, 20 and 40 ALD cycle numbers were used. The coating thickness of 20 ALD cycles was found to be about 2 nm. Cycling test showed that the stability of the LNMO increased continuously with more ALD cycles. The capacity retention increased from 79.9% to 100.0% from bare LNMO to LNMO with 40 ALD cycles coating. CV results revealed that the sample with 40 ALD cycles showed lowest polarization and electrolyte decomposition. XAS results showed that the presence of the ALD coating can prevent the LNMO surface from heavy Mn reduction, making Mn dissolution less likely to happen since Mn^{2+} is prone to dissolving into the electrolyte.

Investigation on the Fe L edge XAS revealed that the $FePO_4$ derived by ALD is the same with that of the commercial $FePO_4$. After cycling, the Fe was found to be slightly reduced and the features resemble amorphous $LiFePO_4$, such finding demonstrated that the amorphous $FePO_4$ coating was capable of accommodating Li^+ ions to form nano-domains of amorphous $LiFePO_4$. The electrochemically active nature of $FePO_4$ layer allows for fast Li+ ions transportation and protects the LNMO material surface, in the meantime, it prevents the electrolyte from oxidation decomposition. Therefore, $FePO_4$ appears to be a very promising coating material *via* ALD.

The utilization of ALD in cathode materials has been focusing on surface coating in most cases, but the conformal nature of ALD coating layer can always deteriorate the performance significantly since the coating materials do not allow fast electron and Li ions transportation simultaneously. In the second part, we reported a method using post-treatment of TiO_2 coated LNMO to create a surface layer that prohibits surface phase change and allows for moderate electron/Lithium transportation. Different ALD cycles (5, 25, 50) of TiO_2 were deposited onto the surface of LNMO powders followed by annealing. It was found that 25 ALD cycles of TiO_2 coating followed by annealing was able to increase the capacity, stability and rate capability of LNMO significantly compared to the one prior to annealing and the ones with other ALD cycle numbers. By using XAS and STEM-HAADF, we found that the Ti atoms occupy both the tetrahedrally coordinated 8a sites which was previously occupied by Li atoms and the octahedrally coordinated 16d sites previously occupied by Ni and Mn. Such substitution resulted in a surface layer composed of spinel $TiMn_2O_4$ and a $LiTi_xNi_{0.5}Mn_{1.5-x}O_4$ subsurface. The significantly improved performance of the LNMO with 25 ALD cycles of TiO_2 coating followed by annealing can be attributed to several aspects. The $TiMn_2O_4$ can protect the material surface from electrolyte attack. Second, the pre-occupation of Ti on Li sites prevent continuous phase change to rock salt phase on the surface.

Li-rich NMC with a composition of $Li_{1.2}Mn_{0.54}Co_{0.13}Ni_{0.13}O_2$ is another cathode material studied in this thesis. The oxygen release and simultaneous irreversible phase change during the first charge process result in low initial coulombic efficiency, fading capacity and risk of heat runaway. To address these problems, we used ALD to deposit $AlPO_4$

coating onto the surface of the Li-rich NMC powders. HRTEM image revealed that the thickness of 20 ALD cycled of $AlPO_4$ coating was about 4 nm. Soft XAS studies on the transition metals L edges and the oxygen K edge reveal that the surface of the Li-rich NMC has been altered during the ALD process, reduction of Mn and Co has been observed. HRTEM images show that a spinel phase formed on the surface of the ALD coated sample, which is a result of the reduction. The oxygen release peak was retarded by the $AlPO_4$ coating in the CV results, which indicates that the Li_2MnO_3 has changed, likely into the spinel phase. XPS results of the fresh electrode and cycled electrode show the bare sample was covered by thick SEI, whereas the coated sample show a less thick SEI. Also, the presence of $AlPO_4$ coating increased the thermal stability of the bare sample and Al_2O_3 coated Li-rich NMC, making it a promising candidate of coating material to enhance the safety of Li-rich NMC cathode materials.

To understand the structure development of Li-rich NMC, we conducted in-situ XAS study on a fresh electrode of Li-rich NMC and another one after 449 cycles. Transition metals K edges were tracked to investigate the valence and electronic configurations. It was found that the initial charge process involves the oxidation of Ni and Co, whereas Mn only underwent structural distortion, the first discharge process involves simultaneous reduction of Ni, Co and Mn as charge compensation. The most striking discovery was that the heavily cycled sample showed no evidence of redox reactions of Co and Ni, indicating that these two transition metals have lost their electrochemical activity. Mn was found to be able to be slightly oxidized and reduced, but the change is trivial and it is possible that anionic redox reaction remains in the heavily cycled cells.

In order to increase the energy density of a LIB, both cathode and anode materials demand high specific capacity, in this thesis, efforts were also made to investigate the performance of carbon nanotubes as anode materials. Carbon nanotubes can be regarded as rolled-up graphene nanoribbons, therefore, we used a chemical oxidation method to unzip commercial carbon nanotubes so as to control the surface area, defect amount and functional groups on the surface. In the seventh chapter of this thesis, we carried out controlled unzipping of carbon nanotubes by tuning the oxidation time and obtained graphene nanoribbons with different unzipping level. It was found that even only 5 min of

treatment would result in an abrupt increase of the defect amount and longer treatment time does not change the defect amount significantly. On the other hand, the surface area increases continuously until 5 h treatment owing to the unzipping of carbon nanotubes, it starts to drop after 10 h treatment due to the fragmentation of the nanoribbons into small pieces and they tend to agglomerate. The performances of the samples with different unzipping level reveal that the enhancement of capacity in early unzipping stage is driven by the increase of defect which can accommodate more Li^+ ions. In the final unzipping stage, the capacity drops due to less surface area. The different electrochemical behaviors of the unzipped carbon nanotubes demonstrate that the Li^+ insertion into carbon layers can be adjusted by controlling defects, surface area and functional groups.

8.2   Perspectives

The thesis has developed a novel electrochemically active $FePO_4$ coating *via* ALD. Such coating involves lithiation of the coating material during charging, but this mechanism was not fully understood. XAS results only provided information that the Fe was reduced, it would be interesting if one can track the change of the coating material *via* in-situ methods like in-situ XAS. Such measurement is not restricted to $FePO_4$ only, other coating materials that involve lithiation are also great candidates, such as TiO_2, Al_2O_3 and Ta_2O_5. The feasibility of such measurement depends on the energy threshold of the elements detected, which determines whether it should be carried out in soft X-ray beamlines or hard X-ray beamlines. The former one requires vacuum and makes the whole experiment hard to conduct, whereas the latter one can be conducted on ambient table easily.

The thesis also exploited the possibility of surface composition engineering via ALD TiO_2. Simple ALD coating has been widely reported, but using ALD to adjust the surface composition is less seen. The benefit of such modification method, as discussed in chapter 4, is that it involves both coating and doping simultaneously, these two modification methods target at different problems. In this thesis, we only tried to use Ti as the modification element, but such treatment shall not be restricted to Ti only. Numerous doping elements in cathode materials such as Al and Mg can be potentially beneficial to the performance since the lower valence of these elements might allow for easier diffusion than Ti. Furthermore, how surface doping benefits the performance can be further studied.

In chapter 5, we used $AlPO_4$ coating to modify the surface of Li-rich NMC. XAS results showed that the ALD process could alter the surface of the Li-rich NMC, therefore, it is very valuable to conduct studies of the interaction between ALD precursors and Li-rich NMC. In addition, the change was found to happen mainly in Li_2MnO_3 phase in the Li-rich NMC, it is also of great importance to investigate how such reaction took place. Also, it is worthwhile to investigate the reactions between ALD precursors with other cathode materials so as to better understand ALD coating roles in LIBs.

Chapter 6 describes our attempts of understanding the structural and valence change of Li-rich NMC material in the first cycle and 450th cycle. The in-situ XAS measurements showed important information about the transition metal changes especially in the heavily cycled sample. We found that the Mn was the only element that shows redox reaction in the heavily cycled sample, therefore it is very interesting if we can track the change of Mn through either in-situ or ex-situ method to identify the voltage where redox reactions take place. Furthermore, XAS of the oxygen K edge should provide critical information of whether anionic reactions remain or not. HRTEM studies on how and why the Co and Ni lose their electrochemical activity is also very important.

Carbon nanotubes derived graphene nanoribbons are another topic covered in this thesis. Chapter 7 thoroughly investigates the effects of surface area, defects and functional groups to the performance of graphene nanoribbons. Such controllable properties makes graphene nanoribbons promising candidate for other types of batteries such as lithium air batteries and sodium air batteries, which demand high surface area and controlled defects.

Appendices

Appendix I: PERMISSION FROM JOHN WILEY AND SONS

Dear Biwei,

We hereby grant permission for the requested use expected that due credit is given to the original source.

If material appears within our work with credit to another source, authorisation from that source must be obtained.

Credit must include the following components:

- Journals: Author(s) Name(s): Title of the Article. Name of the Journal. Publication year. Volume. Page(s). Copyright Wiley-VCH Verlag GmbH & Co. KGaA. Reproduced with permission.

If you also wish to publish your thesis in electronic format, you may use the article according to the Copyright transfer agreement:

3. Final Published Version.
Wiley-VCH hereby licenses back to the Contributor the following rights with respect to the final published version of the Contribution:
a. [...]
b. Re-use in other publications. The right to re-use the final Contribution or parts thereof for any publication authored or edited by the Contributor (excluding journal articles) where such re-used material constitutes less
than half of the total material in such publication. In such case, any modifications should be accurately noted.

Kind regards

Heike Weller
Rights Manager
Rights & Licenses

Wiley-VCH Verlag GmbH & Co. KGaA
Boschstraße 12
69469 Weinheim

https://creativecommons.org/licenses/by/4.0/legalcode

Appendix II: PERMISSION FROM AMERICAN SOCIETY OF CHEMISTRY

Copyright Clearance Center — RightsLink®

Home | Create Account | Help

ACS Publications
Most Trusted. Most Cited. Most Read.

Title: Graphene Nanoribbons Derived from the Unzipping of Carbon Nanotubes: Controlled Synthesis and Superior Lithium Storage Performance
Author: Biwei Xiao, Xifei Li, Xia Li, et al
Publication: The Journal of Physical Chemistry C
Publisher: American Chemical Society
Date: Jan 1, 2014
Copyright © 2014, American Chemical Society

LOGIN

If you're a copyright.com user, you can login to RightsLink using your copyright.com credentials. Already a RightsLink user or want to learn more?

PERMISSION/LICENSE IS GRANTED FOR YOUR ORDER AT NO CHARGE

This type of permission/license, instead of the standard Terms & Conditions, is sent to you because no fee is being charged for your order. Please note the following:

- Permission is granted for your request in both print and electronic formats, and translations.
- If figures and/or tables were requested, they may be adapted or used in part.
- Please print this page for your records and send a copy of it to your publisher/graduate school.
- Appropriate credit for the requested material should be given as follows: "Reprinted (adapted) with permission from (COMPLETE REFERENCE CITATION). Copyright (YEAR) American Chemical Society." Insert appropriate information in place of the capitalized words.
- One-time permission is granted only for the use specified in your request. No additional uses are granted (such as derivative works or other editions). For any other uses, please submit a new request.

BACK | CLOSE WINDOW

Curriculum Vitae

Name:	Biwei Xiao

**Post-secondary
Education and
Degrees:**
Sichuan University
Chengdu, Sichuan, China
2007-2011 B. Eng

The University of Western Ontario
London, Ontario, Canada
2012-2016 Ph.D.

**Honours and
Awards:**
Western Engineering Scholarship
2012-2016

**Related Work
Experience**
Teaching Assistant
The University of Western Ontario
2012-2016

Summer Intern
General Motors
2015, 2016

Research Assistant
Chengdu Green Energy and Green Manufacturing Techniques R&D
Centre
2011

Publications:

[1] **B. Xiao** and X. Sun, *Recent Progress of Graphene Nanoribbons Derived from Unzipped Carbon Nanotubes and the Application in Lithium-ion Batteries*, "Graphene Oxide: Synthesis, Mechanical Properties and Application", **Nova Sciences**, USA, (2014)

[2] **B. Xiao** and X. Sun et al., *Graphene Nanoribbons Derived from the Unzipping of Carbon Nanotubes: Controlled Synthesis and Superior Lithium Storage Performance*. **J. Phys. Chem. C** 118 (2014) 881

[3] **B. Xiao** and X. Sun et al., *Unravelling the Role of Electrochemically Active $FePO_4$ Coating by Atomic Layer Deposition for Increased High-voltage Stability of $LiNi_{0.5}Mn_{1.5}O_4$ Cathode Material*, **Adv. Sci.,** 2, 5 (2015) 1500022 (This paper was highlighted by *Materials Views* and *Materials Views China*)

[4] **B. Xiao** and X. Sun et al., *Atomic-scale Manipulation of Spinel Lithium Nickel Manganese Surface by Tetrahedrally-coordinated Ti as High Performance Cathode Material*, submitted

[5] **B. Xiao** and X. Sun et al., *Highly Stable Li$_{1.2}$Mn$_{0.54}$Co$_{0.13}$Ni$_{0.13}$O$_2$ Enabled by Novel Atomic Layer Deposited AlPO$_4$ Coating*, submitted

[6] **B. Xiao** and X. Sun *et al., Insight into the Structure Evolution of Li-rich NMC Cathode Material via In-situ X-ray Absorption Spectroscopy,* in preparation

[7] **B. Xiao** and X. Sun, *Surface Behaviors and Modifications of Cathode Materials for Lithium-ion Batteries*, to be submitted

[8] N. Cheng, S. Stambula, M. Banis, J. Liu, A. Riese, **B. Xiao** and X. Sun et al., *Pt Single-atomic/cluster Catalysis of the Hydrogen Evolution Reaction.* **Nat. Commun.**, 7 (2016) 13638

[9] B. Wang, J. Li, Q. Sun, **B. Xiao**, R. Li T.-K Sham and X. Sun, *Titanium Dioxide/Lithium Phosphate Nanocomposite Derived from Atomic Layer Deposition as a High-Performance Anode for Lithium-ion Batteries*. **Adv. Mater. Inter.,** (2016) 1600369

[10] X. Li, Q. Sun, J. Liu, **B. Xiao** and X. Sun, *Tunable Porous Structure of Metal Organic Framework Derived Carbon and the Application in Lithium-sulfur Batteries*. **J. Power Sources** 302 (2016) 174

[11] H. Yadegari, M. Banis, **B. Xiao** and X. Sun et al., *Three-dimensional Air Electrode for Sodium-oxygen Battery: A Mechanism Study toward the Cyclability of the Cell*, **Chem. Mater.,** 27 (2015) 3040

[12] J. Liu, M. Banis, **B. Xiao** and X. Sun et al., *Atomically Precise Growth of Sodium Titanates as Anode Materials for High-Rate and Ultralong Cycle-Life Sodium-Ion Batteries*. **J. Mater. Chem. A** 3 (2015) 24281

[13] Q. Sun, H. Yadegari, M. Banis, J. Liu, **B. Xiao** and X. Sun et al., *Self-stacked Nitrogen-Doped Carbon Nanotubes and Long-life Air Electrode for Sodium-Air Batteries: Elucidating the Evolution of Discharge Product Morphology,* **Nano Energy**, 12 (2015) 698

[14] J. Wang, N. Cheng, **B. Xiao** and X. Sun et al., *Comparative Study to Understand the Intrinsic Properties of Pt and Pd Catalysts for Methanol and Ethanol Oxidation in Alkaline Media*, **Electrochim. Acta,** 185 (2015) 267

[15] A. Lushington, J. Liu, M. Banis, **B. Xiao** and X. Sun, *A Novel Approach in Controlling the Conductivity of Thin Films using Molecular Layer Deposition*. **Appl. Surf. Sci.,** 357 (2015) 1319

[16] J. Liu, **B. Xiao**, M. Norouzi Banis and X. Sun et al., *Atomic Layer Deposition of Amorphous Iron Phosphates on Carbon Nanotubes as Cathode Materials for Lithium-ion Batteires*. **Electrochim. Acta.** 162 (2015) 275

[17] Q. Sun, H. Yadegari, J. Liu, **B. Xiao**, X. Li, C. Langford, R. Li and X. Sun, *Towards Sodium-"Air" Battery: Revealing the Critical Role of Humidity*. **J. Phys. Chem. C** 119 24 (2014) 13433

[18] X. Li, J. Liu, B. Wang, M. Banis, **B. Xiao** and X. Sun et al., *Nanoscale Stabilization of Li-Sulfur Batteries by Atomic Layer Deposited Al_2O_3*. **RSC Adv.** 4 (2014) 27126

[19] J. Yang, J. Wang, Y. Tang, D. Wang, **B. Xiao** and X. Sun et al., *In-situ Self-catalyzed Formation of Core-shell $LiFePO_4@CNTs$ Nanowire for Ultra-high Rate Performance Lithium-ion Batteries*. **J. Mater. Chem. A** 1 (2013) 7306

[20] J. Liu, Y. Tang, **B. Xiao** and X. Sun et al., *Atomic Layer Deposited Aluminium Phosphate Thin Films on N-doped CNTs*, **RSC Adv.,** 3 (2013) 4492

Conference Presentations:

[1] B. Xiao and X. Sun et al., *Graphene Nanoribbons Derived from Carbon Nanotubes: Controlled Synthesis and Superior Lithium Storage Performance*, 15th Tropical Meeting of the International Society of Electrochemistry, 2014, Niagara Falls, Canada

[2] B. Wang, J. Liu, **B. Xiao**, Y. Zhao, R. Li, T.K Sham and X. Sun, The Application of Atomic Layer Deposition in Lithium-Ion Batteries, *The 18th International Meeting on Lithium Batteries*, 2015, Chicago, US